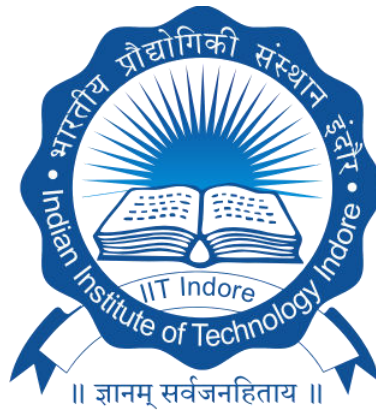


**Development of Metallic Materials for Knee
Implant Applications by Micro-Plasma Arc
Additive Manufacturing Process**

Ph.D. Thesis

by

Pankaj Kumar



**Department of Mechanical Engineering
Indian Institute of Technology Indore**

March 2023

**Development of Metallic Materials for Knee
Implant Applications by Micro-Plasma Arc
Additive Manufacturing Process**

A Thesis

*Submitted in partial fulfillment of the
requirements for the award of the degree*

of

DOCTOR OF PHILOSOPHY

by

Pankaj Kumar

(Roll No. 1801103003)



**Department of Mechanical Engineering
Indian Institute of Technology Indore**

March 2023



Indian Institute of Technology Indore

Candidate's Declaration

I hereby certify that the work which is being presented in the thesis entitled as “**Development of Metallic Materials for Knee Implant Applications by Micro-Plasma Arc Additive Manufacturing Process**” in the partial fulfillment of the requirements for the award of the degree of **DOCTOR OF PHILOSOPHY** and submitted in the **Department of Mechanical Engineering, Indian Institute of Technology Indore**, is an authentic record of my own work carried out during the time period from **July 2018 to March 2023** under the supervision of **Prof. Neelesh Kumar Jain** from the Department of Mechanical Engineering and **Dr. Sharad Gupta** from the Department of Biosciences and Biomedical Engineering.

The matter presented in this thesis has not been submitted by me for the award of any other degree of this or any other institute.

Pankaj Kumar

Pankaj Kumar

This is to certify that the above statement made by the candidate is correct to the best of our knowledge.

30th March 2023

(Prof. Neelesh Kumar Jain)

Signature of thesis supervisor #1 with date

30th March 2023

(Dr. Sharad Gupta)

Signature of thesis supervisor #2 with date

Pankaj Kumar has successfully given his Ph.D. Oral Examination held on _____

(Prof. Neelesh Kumar Jain)

Signature of thesis supervisor #1 with date

(Dr. Sharad Gupta)

Signature of thesis supervisor #2 with date

Acknowledgement

First and foremost, I would like to thank my thesis supervisors **Prof. Neesh Kumar Jain and Dr. Sharad Gupta** for providing me with the opportunity to complete my PhD thesis at **Indian Institute of Technology Indore**. As my supervisors, they have constantly forced me to remain focused towards achieving my goal. Their observations and comments helped me to establish the overall direction of the research and to move forward with investigation in depth. I am very grateful for their patience, motivation, enthusiasm, and immense knowledge in advanced machining processes and especially in additive manufacturing that taken together, make them as great mentors.

I express my deep gratitude to my PSPC members **Prof. I.A. Palani, Prof. Avinash Sonawane, and Prof. Srivathsan Vasudevan** for their guidance and cooperation. I am grateful to the faculty members of the Department of Mechanical Engineering for providing the essential facilities and guidance. I want to thank past scholar of the Advance Manufacturing Processes Lab **Dr. Mayur Sawant, Dr. Pravin Kumar, Dr. Vishal Kharka** for sharing their knowledge and expertise during my entire research work. I would also like to thank and express my gratitude towards my fellow PhD students **Sh. Vivek Rana, Sh. Bhavesh Chaudhary and Sh. Pradyumn Kumar Arya** for motivating me and helping me during the tough phases of my research. Special thanks to **Dr. Anshu Kumari and Dr. Saumya Jaiswal** for conducting cell viability experiment and **Sh. Mahesh Patel** for help in conducting experiments for bio-tribological characteristics. I would also like to thank my friends of IIT Indore **Dr. Anuj Kumar, Dr. Pavan Gupta, Sh. Anupam Kumar**, and others for their help, company, and comments despite of their busy schedules. I am thankful to **the Sophisticated Instrumentation Center (SIC), Advanced Manufacturing Processes (AMP) Lab, Additive and Micromanufacturing Lab (AMAL), BioPhysics & BioMedical Engineering Research Group, Advanced Welding Processes Lab, and Central Workshop of IIT Indore**. I express my gratitude to **Prof. Anand Parey, Dr. Satyajit Chatterjee, Dr. Dan Sathiaraj, Dr. Jayprakash Murugesan, and Dr. Girish Verma** to providing various characterization and testing facilities. I am also thankful to Lab staff of Mechanical Engineering Labs and Central Workshop especially **Dr. Anand Petare, Sh. Santosh Sharma, Sh. Sandeep Gour, Sh. Deepak Rathore, Sh. Vinay Mishra, and Sh. Umashankar Sharma** for their cooperation in fabrication of my experimental apparatus.

I express my sincere gratitude to **Ministry of Education** to pursue my doctoral studies.

Pankaj Kumar

Dedicated

This thesis is dedicated to the memory of my late mother Gulab Devi when I know I won't be able to say "hello" again.

This thesis is also dedicated to my father, brothers, and sisters, who taught me to be kind and keep on learning. To my beloved wife Kavita and my little champ Advik Anand, who taught me to live and who brought the real joy in my life. To my all-in laws for their respect, love, patience, and support in each step of my life. And of course, to my friends who inspires me all the time and have special place in social, professional, and personal life.

Abstract

This thesis reports on development of Co-Cr-Mo-xTi alloys and Ti-Ta-Nb-Mo-Zr high entropy alloy (HEA) by micro-plasma arc additive manufacturing (μ -PAAM) process and study of their *in-vitro* biocompatibility, microstructure, and mechanical properties for their possible knee implant applications. The experimental investigation was conducted in two-stages. Thirty pilot and 27 main experiments were conducted making *single-track-single-layer* depositions of Co-Cr-Mo-2Ti alloy and Ti-Ta-Nb-Mo-Zr HEA to identify optimum values of μ -PAAM process parameters for manufacturing their *multi-track multi-layer* depositions. In-vitro biocompatibility (in terms of cell viability using human cancerous (HeLa) cells, metallic ion release in PBS solution under pH value of 4.5, 5.5 and 7.5, and corrosion behaviour analysis under pH value of 7.4), density, porosity, microstructure, evolution of phases, microhardness, tensile and compression properties, and wear characteristic were studied for the samples of multi-layer deposition samples of Co-Cr-Mo-xTi alloys and Ti-Ta-Nb-Mo-Zr HEA. Additionally, bio-tribological characteristics of Ti-Ta-Nb-Mo-Zr HEA were studied in human body emulating biofluids by evaluating dry fretting wear characteristics, corrosion behaviour, and tribo-corrosion behaviour. Results indicated that avg. value of cell viability decreases with increase in incubation duration and increase in the prepared media concentration for all three variants of Co-Cr-Mo-xTi alloy. Overall avg. cell viability for Co-Cr-Mo-2Ti; Co-Cr-Mo-4Ti; and Co-Cr-Mo-6Ti alloys is found to be 92%; 95%; and 85% respectively. Overall avg. released amounts of metallic ions from them are 126; 41; 11, and 9 ppb for Co, Cr, Mo, and Ti ion respectively. Bulk density and relative density found to decrease with increase in Ti amount in the Co-Cr-Mo alloy due to smaller density of Ti than that Co-Cr-Mo alloy whereas porosity increased with Ti amount. Porous structure is beneficial for osseointegration of knee implant with the human bones. Microstructure and evolution of phase for Co-Cr-Mo-4Ti alloy indicated presence of α -Co phase having FCC crystal structure, ϵ -Co phase having HCP crystal structure, β -titanium phase having BCC crystal structure, and inter-metallic phases of CoTi_2 and lamellar chromium carbide (i.e., Cr_{23}C_6) at its grain boundaries. The Co-Cr-Mo-4Ti alloy is found to have max. values of tensile and compressive yield and ultimate strength, and moderate value of modulus of elasticity due to finer grains, more uniform porous structure, and absence of micro-cracks. Biocompatibility results for Ti-Ta-Nb-Mo-Zr HEA found that avg. % cell viability decreases with increase in prepared media concentration and its values for HeLa, HEK-293, and BHK cells are 90%; 88%; and 92% respectively. Absence of active-passive transition from cathodic to anodic reaction in Tafel polarization curves for Ti-Ta-Nb-Mo-Zr HEA under different pH values of SBF solution indicates its better corrosion resistance. Formation of phases indicated that it consists of fine dendritic and inter-dendritic structure having BCC major and BCC minor phases. Compressive yield and ultimate strength, compressive strain, elastic modulus for Ti-Ta-Nb-Mo-Zr HEA is found to be 1847 ± 25.8 MPa; 1892 ± 15.6 MPa; $13.5 \pm 1.6\%$; and 130 ± 4 GPa respectively which are better than the vacuum arc-melted Ti-Ta-Nb-Mo-Zr HEA. It is due to its solid solution strengthening enabled by its minimum elemental segregation. Its fractured surface morphology indicated brittle mode of failure. Study of its bio-tribological characteristics found that the presence of biofluids reduced coefficient of friction by almost 50%, significantly reduced depth of worn scar and specific wear rate than those in dry fretting wear due to their lubricating action and covering of uneven surfaces by the passive layers of oxides. Corroded surface micrographs found formation of a strong passive layer of TiO_2 , Ta_2O_5 , Nb_2O_5 , NbO_2 , and ZrO_2 on the exposed surface except for some marked regions. Coefficient of friction in tribo-corrosion remained constant for a large range of immersion duration for FPBS and for small ranges for PS and PBS biofluids implying no-fretting zone. The PS and FBPS biofluids resulted in max. and min. coefficient of friction respectively. It can be summarized that μ -PAAM process is an energy and material efficient, and environment friendly process that contributed immensely in development of Co-Cr-Mo-4Ti alloy and Ti-Ta-Nb-Mo-Zr HEA as the better knee

implant materials by minimizing the heat affect zone, thermal distortion, enhancing mechanical properties of their multi-layer depositions along with minimizing elemental segregation of Ti-Ta-Nb-Mo-Zr HEA and enhancing and its bio-tribological characteristics.

Keywords: Metallic biomaterials; Knee implant material; Co-Cr-Mo-xTi alloy; Equiatomic Ti-Ta-Nb-Mo-Zr; High entropy alloy; *In-vitro* biocompatibility evaluation; Dry fretting wear; Tribo-corrosion; Biofluids; Microstructure; Phase analysis; Knee implant; Micro-plasma arc additive manufacturing process

List of Patens and Publications

(A.1) Patent

1. **Magnetic Field Assisted Micro-Plasma Transferred Arc Powder Additive Layer Manufacturing Process** (Inventors: Mayur Sudhakar Sawant, **Pankaj Kumar**, Neelesh Kumar Jain) **Indian Patent Grant No. 464408** [Granted on 31th October 2023]

(A.2) Published Papers in Refereed Journals from PhD Thesis

1. **Pankaj Kumar**, Neelesh Kumar Jain, Sharad Gupta (2023), “Microstructure and mechanical characteristics of μ -plasma additively manufactured equiatomic Ti-Nb-Zr-Mo-Ta HEA” **Metals and Materials International**. <https://doi.org/10.1007/s12540-023-01540-5> (Impact Factor: 3.5)
2. **Pankaj Kumar**, Mayur S Sawant, Neelesh Kumar Jain, Anshu Kumari, Sharad Gupta (2023), “Development of Co-Cr-Mo-xTi alloys by micro-plasma-based 3D printing for knee implant applications and its biocompatibility assessment” **The International Journal of Advanced Manufacturing Technology**, 126, 2445–2459. <https://doi.org/10.1007/s00170-023-11277-5> (Impact factor: 3.56)
3. **Pankaj Kumar**, Mahesh Patel, Neelesh Kumar Jain, Sharad Gupta (2023), “Bio-tribological characteristics of 3D-printed Ti-Ta-Nb-Mo-Zr high entropy alloy in human body emulating biofluids for implant applications” **Journal of Bio- and Tribo-Corrosion**, 9, Article ID: 21 <https://doi.org/10.1007/s40735-022-00739-0> (March 2023)
4. **Pankaj Kumar**, Neelesh Kumar Jain, Saumya Jaiswal, Sharad Gupta (2023), “Development of Ti-Ta-Nb-Mo-Zr high entropy alloy by μ -plasma arc additive manufacturing process for knee implant applications and its biocompatibility evaluation”, **Journal of Materials Research and Technology**, 22, 541-555, <https://doi.org/10.1016/j.jmrt.2022.11.167> (Impact Factor: 6.3) (Jan-Feb 2023)
5. **Pankaj Kumar**, Mayur S Sawant, Neelesh Kumar Jain, Sharad Gupta (2022) “Study of mechanical characteristics of additively manufactured Co-Cr-Mo-2/4/6Ti alloys for knee implant material” **CIRP Journal of Manufacturing Science and Technology**, 39, 261-275, <https://doi.org/10.1016/j.cirpj.2022.08.015> (Impact factor: 3.6) (Nov 2022)
6. **Pankaj Kumar**, Mayur S Sawant, Neelesh Kumar Jain, Sharad Gupta (2022) “Microstructure characterization of Co-Cr-Mo-xTi alloys developed by micro-plasma based additive manufacturing for knee implants” **Journal of Materials Research and Technology**, 21, 252-266, <https://doi.org/10.1016/j.jmrt.2022.09.033> (Impact Factor: 6.3) (Nov 2022)
7. **Pankaj Kumar**, Mayur S Sawant, Neelesh Kumar Jain (2021) “Optimization of process parameters in micro-plasma transferred deposition process for cobalt-based alloy” **Materials Today: Proceedings**, 44(1), 1681-1686, <https://doi.org/10.1016/j.matpr.2020.11.840> (Jan 2021)
8. **Pankaj Kumar**, Neelesh Kumar Jain (2021) “Finite element analysis of femoral prosthesis using Ti-6Al-4 V alloy and TiNbZrTaFe high entropy alloy” **Materials Today: Proceedings**, 44(1), 1195-1201, <https://doi.org/10.1016/j.matpr.2020.11.239> (Jan 2021)

(B) Publications from the Collaborating Work

9. Pradyumn Kumar Arya, **Pankaj Kumar**, Neelesh Kumar Jain, Dan Sathiaraj, Girish Verma (2023) “3D Printing Parts: Mechanical Characterization, Applications, Challenges and Techniques” Chapter 5 in *Advances in Manufacturing and Processing of Materials* (Editors: Narender Kumar, Mohit Tyagi, Dilbagh Panchal, Ravi Pratap Singh), Apple Academic Press, Florida (USA)

Table of Contents

Details	Page No.
List of Figures	xvii-xxii
List of Tables	xxiii-xxiv
Nomenclature	xxv
Abbreviation	xxvii
Chapter 1: Introduction	1-28
1.1 Anatomy and Structure of Knee Joint	1
1.1.1 Biomechanics of Knee Joint	2
1.1.2 Causes for Failure of Knee Joint.....	4
1.2 Knee Replacement	6
1.2.1 Total Knee Replacement and Partial Knee Replacement	6
1.2.2 Types of Knee Implants	7
1.3 Assessment of Post-operative Rehabilitation of Knee Replacement	9
1.3.1 Patience Satisfaction Measurement Tool	9
1.3.2 Patient Dissatisfaction: Causes and Types	9
1.3.3 Internal Determinants of Patient Satisfaction	10
1.3.4 External Components of Patient Satisfaction	11
1.4 Materials for Knee Implants	12
1.4.1 Metallic Materials Knee Implants	14
1.4.2 Non-Metallic Materials for Knee Implants	16
1.5 Introduction to Additive Manufacturing	18
1.5.1 Classification of Additive Manufacturing Processes	19
1.5.2 Advantages of AM Processes	24
1.5.3 Limitations of AM Processes	25
1.5.4 Applications of AM Processes	25
1.5 Organization of the Thesis	26
Chapter 2: Review of Past Works and Research Objectives	29-38
2.1 Metallic Materials for Knee Implant Applications	29
2.2 High Entropy Alloys for Knee Implant Applications	31
2.3 Additive Manufacturing of Knee Implants	34
2.4 Summary of the Past Works	36
2.5 Identified Research Gaps	37
2.6 Research Objectives	37
2.7 Research Methodology	37

Chapter 3: Experimentation	39-66
3.1 Materials.....	39
3.1.1 Preparation of Powders for Co-Cr-Mo-xTi Alloys	39
3.1.2 Preparation of Powders for Ti-Ta-Nb-Mo-Zr High Entropy Alloy	42
3.2 Apparatus for μ -PAAM Process.....	44
3.3 Design and Planning of Experiments	45
3.3.1 Multi-layer Depositions of Co-Cr-Mo-xTi Alloys	48
3.3.2 Multi-layer Depositions of Ti-Ta-Nb-Mo-Zr HEA	50
3.4 Measurement of Responses for Co-Cr-Mo-xTi Alloys	51
3.4.1 In-vitro Biocompatibility Assessment	51
3.4.1.1 Cytotoxicity Assessment	51
3.4.1.2 Assessment of Release of Metallic Ions	52
3.4.1.3 Assessment of Corrosion Behavior	53
3.4.2 Aspect Ratio	54
3.4.3 Evaluation of Bulk Density, Relative Density, and Porosity	54
3.4.4 Microstructure, Formation of Phases, and Microhardness	55
3.4.5 Evaluation of Wear Characteristics	56
3.4.6 Tensile Testing and Fractography	56
3.4.7 Compression Testing and Fractography	57
3.4.8 Abrasion Resistance	58
3.5 Measurement of Responses for Ti-Ta-Nb-Mo-Zr HEA	58
3.5.1 In-vitro Biocompatibility Evaluation	58
3.5.1.1 Cell Viability Evaluation	59
3.5.1.2 Evaluation of Release of Metallic Ions	60
3.5.1.3 Study of Corrosion Behavior	60
3.5.2 Measurement of Aspect Ratio	61
3.5.3 Study of Microstructure, Evolution of Phases, and Microhardness	61
3.5.4 Compression Testing and Fractography	62
3.5.5 Evaluation of Wear Resistance	62
3.5.6 Evaluation of Abrasion Resistance	63
3.6 Bio-Tribological Characteristics of Ti-Ta-Nb-Mo-Zr HEA	63
3.6.1 Dry Fretting Wear	63
3.6.2 Study of Corrosion Behavior in Biofluids	64
3.6.3 Study of Tribo-Corrosion Behavior in Biofluids	65
Chapter 4: Results and Analysis for Co-Cr-Mo-xTi Alloys	67-104
4.1 Aspect Ratio Results	67

4.2 Findings from Biocompatibility Assessment	69
4.2.1 Cell Viability Results	69
4.2.2 Metallic Ions Release Results	73
4.2.3 Results for Corrosion Behavior	75
4.3 Density and Porosity Results	81
4.4 Analysis of Microstructure, Composition, and Phase Formation	84
4.5 Microhardness Results	91
4.6 Results for Wear Resistance	92
4.7 Results of Tensile and Compression Tests	94
4.8 Results of Tensile and Compression Fractography	97
4.9 Results for Abrasion Resistance	99
4.10 Concluding Remarks	102
Chapter 5: Results and Analysis for Ti-Ta-Nb-Mo-Zr HEA	105-148
5.1 Results for Aspect Ratio	105
5.2 Results of Biocompatibility Evaluation	107
5.2.1 Results for Cell Viability	107
5.2.2 Metallic Ion Release Results	111
5.2.3 Study of Corrosion Behavior	113
5.3 Study of Microstructure and Phase Evolution	118
5.4 Analysis of Microhardness	121
5.5 Results of Compression Test and Fractography	122
5.6 Wear Resistance Results	124
5.7 Results for Abrasion Resistance	128
5.8 Findings from Bio-Tribological Behavior of Ti-Ta-Nb-Mo-Zr HEA	129
5.8.1 Analysis of Dry Fretting Wear	129
5.8.2 Analysis of Corrosion Behavior in Biofluids	133
5.8.3 Analysis of Tribo-Corrosion Behavior in Biofluids	138
5.9 Closing Remarks	146
Chapter 6: Conclusions and Scope for Future Work	149-154
6.1 Significant Achievements	150
6.2 Conclusions	150
6.2.1 Development of Co-Cr-Mo-xTi Alloy	150
6.2.2 Development of Ti-Ta-Nb-Mo-Zr HEA	151
6.2.3 Bio-Tribological Characteristics of Ti-Ta-Nb-Mo-Zr HEA	152
6.3 Directions for Future Work	153
References	155-180
Appendix-A: Details of the Equipment Used in Evaluation and	181-186
Characterization of the Responses	
Appendix-B: Finite Element Analysis of Tibial Tray	187-190

Appendix C: SEM micrographs of Co-Cr-Mo-xTi alloys used for EDS analysis 191-191

List of Figures

Figure Number and Captions

	Page No.
Fig. 1.1: Anatomy of human knee joint.	2
Fig. 1.2: (a) Mechanical axis of a knee joint, and (b) anatomical planes of human body.	3
Fig. 1.3: Motions of a knee joint.	4
Fig. 1.4: Healthy knee joint (right), and damaged knee joint (left).	5
Fig. 1.5: Components of a knee implant	6
Fig. 1.6: (a) Uni-compartmental, (b) total knee replacement.	7
Fig. 1.7: Fixed bearing implant.	7
Fig. 1.8: Mobile bearing implant.	8
Fig. 1.9: (a) Posterior cruciate ligament (PCL) retaining, and (b) substituting implant.	8
Fig. 1.10: Failure of different metallic materials due to long term use in human body.	16
Fig. 1.11: Key developments in additive manufacturing since 1970s.	18
Fig. 1.12: Classification of AM processes.	20
Fig. 3.1: (a) Morphology of powder particles of Co-Cr-Mo-2Ti alloy, (b) statical distribution of size of powder particles.	40
Fig. 3.2: EDS obtained spectrum of the powder particles of Co-Cr-Mo-4Ti alloy: (a) before ball milling, and (b) after ball milling.	41
Fig. 3.3: Analysis of the prepared powder of Ti-Ta-Nb-Mo-Zr HEA: (a) size distribution of its particles, (b) SEM images showing morphology of it and its constituents, (c) at. % of its constituents by EDS, and (d) EDS mapping of it and its constituents.	43
Fig. 3.4: Working principle of μ -PAAM process.	44
Fig. 3.5: Photograph of 5-axis CNC machine developed for μ -plasma arc additive manufacturing (μ -PAAM) process.	45
Fig. 3.6: Photographs of the optimized single-track multi-layer depositions of: (a) Co-Cr-Mo-2Ti alloy, (b) Co-Cr-Mo-4Ti alloy, and (c) Co-Cr-Mo-6Ti alloy.	49
Fig. 3.7: Multi-track multi-layer deposition of Ti-Ta-Nb-Mo-Zr powder on the Ti-6Al-4V base plate by μ -PAAM process.	50
Fig. 3.8: Prepared samples of the optimized depositions Co-Cr-Mo-xTi alloys to study their corrosion behavior.	54
Fig. 3.9: Sample preparation for tensile testing and fractography: (a) dimensions as per ASTM E8 standard (b) schematic view of cut sample from the multi-track multi-layer deposition of Co-Cr-Mo-xTi alloy, and (c) photographs.	57
Fig. 3.10: Photographs of the (a) equipment used to study fretting wear, corrosion, and tribo-corrosion characteristics of Ti-Ta-Nb-Mo-Zr HEA and its attachments used for (b) fretting wear test, and (c) corrosion and tribo-corrosion tests.	64
Fig. 4.1: Photographs of 27 single-track single-layer depositions of Co-Cr-Mo-2Ti alloy obtained during the main experiments.	68

Fig. 4.2: Measurement of aspect ratio of single-track single-layer deposition of Co-Cr-Mo-2Ti alloy corresponding to experiment number: (a) 14; (b) 17; (c) 27.	68
Fig. 4.3: Average values of % cell viability in-vitro assessed by MTT assay for different values of incubation duration and concentration of media prepared for the optimized deposition samples of alloy: (a) Co-Cr-Mo-2Ti, (b) Co-Cr-Mo-4Ti, and (c) Co-Cr-Mo-6Ti.	71
Fig. 4.4: Morphology of HeLa cells treated for 72 hours of incubation duration with 106.6 μ l concentration of media of each optimized deposition sample of: (a) Co-Cr-Mo-2Ti, (b) Co-Cr-Mo-4Ti, (c) Co-Cr-Mo-6Ti, and (d) for untreated HeLa cells.	72
Fig. 4.5: Overall average of released amount of the Co, Cr, Mo, and Ti ions by the optimized deposition samples of Co-Cr-Mo-xTi alloys.	73
Fig. 4.6: Assessment results of corrosion behavior of the optimized deposition samples of Co-Cr-Mo-xTi alloys (a) open-circuit potential (OCP) curve, (b) Tafel polarization curve, (c) comparison of the measured and computed corrosion rates.	76
Fig. 4.7: SEM images of the corroded surfaces of the optimized deposition samples of: (a) Co-Cr-Mo-2Ti, (b) Co-Cr-Mo-4Ti, and (c) Co-Cr-Mo-6Ti alloy at 200X and 600 X magnification.	77
Fig. 4.8: (a) Elemental mapping of corroded surface of Co-Cr-Mo-4Ti alloy, and chemical composition of corroded surface of (b) Co-Cr-Mo-2Ti, (c) Co-Cr-Mo-4Ti, and (d) Co-Cr-Mo-6Ti alloy.	79
Fig. 4.9: (a) comparison of bulk density and relative density, and (b) average porosity, for optimized deposition of Co-Cr-Mo-2Ti; Co-Cr-Mo-4Ti; and Co-Cr-Mo-6Ti alloys.	83
Fig. 4.10: Porosity distribution in the optimized deposition of: (a) Co-Cr-Mo-2Ti alloy, (b) Co-Cr-Mo-4Ti alloy, and (c) Co-Cr-Mo-6Ti alloy.	83
Fig. 4.11: SEM micrographs for the optimized deposition of alloy: (a) Co-Cr-Mo-2Ti, (b) Co-Cr-Mo-4Ti, and (c) Co-Cr-Mo-6Ti.	85
Fig. 4.12: EDS spectrum used for chemical composition analysis of μ -PAAM deposited Co-Cr-Mo-xTi alloys.	85
Fig. 4.13: XRD patterns for Co-Cr-Mo; Co-Cr-Mo-2Ti; Co-Cr-Mo-4Ti; and Co-Cr-Mo-6Ti, alloys.	86
Fig. 4.14: Band contrast maps, phase maps and inverse pole figure maps obtained from EBSD for the optimized deposition of Co-Cr-Mo-2Ti alloy, Co-Cr-Mo-4Ti alloy, and Co-Cr-Mo-6Ti alloy.	89
Fig. 4.15: Pole figure obtained from EBSD for ϵ -Co (HCP), α -Co (FCC), Cr and β -Ti phases.	89
Fig. 4.16: Results of microhardness evaluation: (a) microhardness profile, and (b) average microhardness for the optimized depositions of Co-Cr-Mo-xTi alloys.	91
Fig. 4.17: (a) Variation of coefficient of friction for the optimized deposition (b) specific wear rate for the optimized depositions of Co-Cr-Mo-Ti alloys.	92
Fig. 4.18: Optical micrographs of wear track for the optimized deposition of: (a) Co-Cr-Mo-2Ti alloy, (b) Co-Cr-Mo-4Ti alloy, and (c) Co-Cr-Mo-6Ti alloy.	93

Fig. 4.19: (a) Tensile stress-strain diagram for Co-Cr-Mo-xTi alloys, (b) compressive stress-strain diagram for Co-Cr-Mo-xTi alloys, and (c) photograph of tensile fractured samples.	95
Fig. 4.20: SEM images showing fractography of tensile test samples of (a) Co-Cr-Mo-2Ti, (b) Co-Cr-Mo-4Ti, and (c) Co-Cr-Mo-6Ti alloy.	98
Fig. 4.21: SEM images showing fractography of compression testing samples of (a) Co-Cr-Mo-2Ti, (b) Co-Cr-Mo-4Ti, and (c) Co-Cr-Mo-6Ti alloy.	99
Fig: 4.22. Optical micrographs of scratches on the optimized deposition samples of (a) Co-Cr-Mo-2Ti, (b) Co-Cr-Mo-4Ti, and (c) Co-Cr-Mo-6Ti alloy.	100
Fig. 5.1: Photograph of the 27 single-track single-layer depositions of Ti-Ta-Nb-Mo-Zr HEA manufactured in the main experiments by the μ -PAAM process.	106
Fig. 5.2: Measured values of deposition height and width for single-track single-layer deposition samples of Ti-Ta-Nb-Mo-Zr HEA corresponding to: (a) exp. no. 6, (b) exp. no.11, (c) exp. no. 15, (d) exp. no. 18, (e) exp. no. 20, and (f) exp. no. 27.	106
Fig. 5.3: Viability of HeLa, HEK-293, and BHK cells in different concentration of the prepared media for the developed Ti-Ta-Nb-Mo-Zr HEA for incubation duration of (a) 24 hours; (b) 48 hours; and (c) 72 hours.	108
Fig. 5.4: Bright-field micrographs of (a) HeLa cells (b) HEK-293 cells (c) BHK cells treated with 100 μ l concentration of the prepared media for Ti-Ta-Nb-Mo-Zr HEA samples for incubation durations of 24; 48; and 72 hours; and for untreated cells.	110
Fig. 5.5: Released amounts of ions of constituent elements (a) Ti (b) Ta, (c) Nb, (d) Mo, and (e) Zr, from the multi-track multi-layer deposition samples of Ti-Ta-Nb-Mo-Zr HEA in SBF solution of 4.4, 5.4, and 7.4 pH value for immersion durations of 1, 2, and 3 weeks.	112
Fig. 5.6: (a) OCP curve plot, and (b) Tafel polarization curve for multi-track multi-layer deposition sample of Ti-Ta-Nb-Mo-Zr HEA in SBF solution of pH 4.4; 5.4; and 7.4 values.	114
Fig. 5.7: SEM Micrographs of the corroded surface of multi-track multi-layer deposition sample of Ti-Ta-Nb-Mo-Zr HEA in the SBF solution having pH value of (a) 4.4, (b) 5.4, and (c) 7.4.	115
Fig. 5.8: Results of EDS for corroded surface of multi-track multi-layer deposition sample of Ti-Ta-Nb-Mo-Zr HEA.	116
Fig. 5.9: Results of XRD for corroded surface of multi-track multi-layer deposition sample of Ti-Ta-Nb-Mo-Zr HEA.	116
Fig. 5.10: SEM image showing microstructure of multi-track multi-layer deposition sample of Ti-Ta-Nb-Mo-Zr HEA at 250x magnification.	119
Fig. 5.11: (a) SEM image at 500x magnification showing microstructure of multi-track multi-layer deposition sample of Ti-Ta-Nb-Mo-Zr HEA, and EDS results showing its (b) chemical composition, (c, d) chemical compositions for spectrum 1 belonging to minor BCC phase and spectrum 2 belonging to major BCC phase (marked in Fig. 5.11a), and (e) mapping of constituent elements.	120

Fig. 5.12: XRD plot for multi-track multi-layer deposition sample of Ti-Ta-Nb-Mo-Zr HEA.	120
Fig. 5.13: Microhardness profile of multi-track-multi-layer deposition sample of Ti-Ta-Nb-Mo-Zr HEA.	122
Fig. 5.14: Compressive stress-strain curve for multi-track multi-layer deposition of Ti-Ta-Nb-Mo-Zr HEA.	123
Fig. 5.15: SEM images of compression fractured surface morphology of multi-track multi-layer deposition sample of Ti-Ta-Nb-Mo-Zr HEA at different magnifications: (a) 500x magnification, (b) 1000x magnification for the red color region marked in Fig. 11a, (c) 2000x magnification for the yellow color region 'a' marked in Fig. 11b, and (d) 7000x magnification for the yellow color region 'b' marked in Fig. 11c.	124
Fig. 5.16: Results of sliding wear for multi-track multi-layer deposition sample of Ti-Ta-Nb-Mo-Zr HEA at different applied load showing: (a) change in COF with time, (b) avg. COF determined from Fig. 12a, (c) worn scar depth profile, (d) avg. worn scar depth computed from worn scar depth profile, and (e) computed values of specific wear rate.	126
Fig. 5.17: SEM images of the worn track of multi-track multi-layer deposition sample of Ti-Ta-Nb-Mo-Zr HEA for the applied load of: (a) 15 N, (b) 30 N, (c) 45 N.	127
Fig. 5.18: Optical micrographs of measurement of scratch track width at different applied load (a) 10 N, (b) 15 N, (c) 20 N.	129
Fig. 5.19: Fretting wear results for multi-track multi-layer deposition sample of Ti-Ta-Nb-Mo-Zr HEA under different applied load: (a) variation of coefficient of friction with number of cycles, (b) average coefficient of friction, (c) worn scar depth profile with probe travel length, (d) average worn scar depth, and (e) specific wear rate.	131
Fig. 5.20: 3D surface roughness profile of worn surface of multi-track multi-layer deposition sample of Ti-Ta-Nb-Mo-Zr HEA in dry fretting wear conducted at applied load of: (a) 10 N, (b) 20 N, (c) 30 N.	131
Fig. 5.21: SEM images of fretting wear track and worn scar morphology for multi-track multi-layer deposition sample of Ti-Ta-Nb-Mo-Zr HEA for applied load of: (a) 10 N, (b) 20 N, (c) 30 N.	132
Fig. 5.22: Results for corrosion behavior analysis of multi-track multi-layer deposition sample of Ti-Ta-Nb-Mo-Zr HEA: (a) open circuit potential (OCP) curve, and (b) Tafel polarization curve.	134
Fig. 5.23: SEM images of the corroded surface of multi-track multi-layer deposition sample of Ti-Ta-Nb-Mo-Zr HEA in different biofluids: (a) PS, (b) PBS, (c) FPBS, and (d) marked spectrum for its chemical compositions using EDS analysis.	136
Fig. 5.24: Results for tribo-corrosion of multi-track multi-layer deposition sample of Ti-Ta-Nb-Mo-Zr HEA in different biofluids: (a) variation of coefficient of friction with number of cycles, (b) average coefficient of friction at applied load of	139

10 N, (c) change in worn scar depth with probe travel length, (d) average worn scar depth, (e) specific wear rate, (f) OCP curve, and (g) Tafel polarization curve.	
Fig. 5.25: 3D surface roughness profile of tribo-corroded surface of multi-track multi-layer deposition sample of Ti-Ta-Nb-Mo-Zr HEA at 10 N applied load in different biofluids: (a) PS, (b) PBS, and (c) FPBS.	142
Fig. 5.26: SEM images of tribo-corroded surface of multi-track multi-layer deposition sample of Ti-Ta-Nb-Mo-Zr HEA depicting tribo-corrosion wear track and morphology of worn track at 200x and 400x magnification and corroded area in different biofluids: (a) PS, (b) PBS, and (c) FPBS.	144
Fig. B1: 3D model of tibial tray used in its finite element analysis.	187
Fig. B2: Von-Mises equivalent stress predicted by FEA for tibial tray made of (a) Co-Cr-Mo-2Ti, (b) Co-Cr-Mo-4Ti, and (c) Co-Cr-Mo-6Ti alloy.	188
Fig. B3: Total deformation predicted by FEA for tibial tray made of (a) Co-Cr-Mo-2Ti, (b) Co-Cr-Mo-4Ti, and (c) Co-Cr-Mo-6Ti alloy.	189
Fig. C1: SEM micrographs of Co-Cr-Mo-xTi alloys used for EDS analysis.	191

List of Tables

Table Number and Captions

	Page No.
Table 1.1: Motions of knee joint about different planes and axes along with examples.	4
Table 1.2: Required properties for knee implant material and consequences of not having it.	13
Table 1.3: Classification of AM processes according to the ASTM F-42 standard.	20
Table 1.4: Advantages and limitations of AM processes.	21
Table 2.1: Comparison of mechanical properties of the commonly used materials for knee implants with that of human bone.	31
Table 2.2: Identified research objectives (RO) for the present work and the methodology used to meet them.	38
Table 3.1: Chemical compositions of base plate and Co-Cr-Mo-2/4/6Ti alloys.	40
Table 3.2: Chemical compositions of powder particles of Co-Cr-Mo-4Ti alloy obtained from its EDS spectrum	41
Table 3.3: Values of μ -PAAM process parameters, and design of experiments approach used in different phases of experiments.	46
Table 4.1: Parametric combination utilized in 27 main experiments as well as associated measured and observed responses.	69
Table 4.2: Released amounts of metallic ions in ppb by the optimized deposition samples of Co-Cr-Mo-xTi alloys in the PBS solution different values of its pH and immersion times.	73
Table 4.3: Corrosion related parameters determined from Tafel polarization curve for optimized deposition samples of Co-Cr-Mo-xTi alloys.	76
Table 4.4: Chemical composition (by wt.%) of multi-layer depositions of Co-Cr-Mo-xTi alloys obtained from their EDS spectrum.	86
Table 4.5: Presence of different phases in optimized deposition samples of Co-Cr-Mo-Ti alloys.	89
Table 4.6: Mean values and standard deviation of yield strength, ultimate strength, % elongation, and elastic modulus of Co-Cr-Mo-2/4/6Ti alloys obtained from their tensile and compressive tests, tensile properties of cast and forged Co-Cr-Mo (i.e., ASTM F75) alloy.	96
Table 4.7: Mean values and standard deviation (SD) of scratch track width and coefficient of friction, and computed values of scratch hardness number for the optimized deposition samples of Co-Cr-Mo-xTi alloys.	100
Table 4.8a: Summary of results of different tests conducted on the μ -PAAM manufactured Co-Cr-Mo-2/4/6Ti alloys and available data for Co-Cr-Mo alloy.	101
Table 4.8b: Comparison of elastic modulus of Co, Cr, and Mo based alloys fabricated by different processes along with μ -PAAM manufactured Co-Cr-Mo-2/4/6Ti alloys.	101
Table 5.1: Computed values of aspect ratios and visually observed deposition quality of 27 single-track single-layer depositions of Ti-Ta-Nb-Mo-Zr HEA	107

manufactured in the main experiments and corresponding parameters of μ -PAAM process.	
Table 5.2: Corrosion parameters obtained from the Tafel polarization curve for the multi-track multi-layer deposition sample of Ti-Ta-Nb-Mo-Zr HEA in the SBF solution.	114
Table 5.3: Comparison of sliding wear characteristics of the multi-track multi-layer sample of Ti-Ta-Nb-Mo-Zr HEA with present HEAs and Ti-6Al-4V alloy.	127
Table 5.4: Results of abrasion resistance test for Ti-Ta-Nb-Mo-Zr HEA.	129
Table 5.5: Corrosion parameters obtained from the Tafel polarization curve for multi-track multi-layer deposition sample of Ti-Ta-Nb-Mo-Zr HEA in three biofluids.	135
Table 5.6: Chemical compositions (by at. %) of marked spectrums of corroded surface of Ti-Ta-Nb-Mo-Zr HEA in FPBS biofluids.	136
Table 5.7: Comparison of parameters of corrosion and tribo-corrosion behavior of multi-track multi-layer deposition sample of Ti-Ta-Nb-Mo-Zr HEA in different biofluids determined from their corresponding Tafel polarization curves.	140
Table 5.8: Comparison of bio-tribological characteristics of the multi-track multi-layer deposition sample of Ti-Ta-Nb-Mo-Zr HEA with existing HEA and Ti based alloys.	145
Table B1: Material properties used in FEM analysis for tibial tray.	187
Table B2: Maximum values of Von-Mises equivalent stress and total deformation predicted by FEA of tibial tray made of Co-Cr-Mo-2/4/6Ti alloys.	190

Nomenclature

A_i	Exposed area of a sample (cm ²)
at. %	Atomic percentage
E_{corr}	Corrosion potential
F_N	Applied load
H_{sn}	Scratch hardness number
i_{corr}	Corrosion current density
K	Constant for dimensional consistency (= 8.76×10^4)
M_a	Average masses of a sample measured in air
M_w	Average masses of a sample measured in water
Nl/min	Normal liter per minute
P	Normal load
p_c	Computed corrosion rate
p_t	Determined corrosion rate
s	Relative slip distance
T_e	Exposure time for corrosion (hours)
V	Wear volume
v_s	Specific fretting wear rate
w	Average width of scratch track
W_m	Weight loss of a corroded sample
wt.%	Weight percentage
ρ	Density of the sample material (g/cm ³)
ρ_b	Bulk density
ρ_r	Relative density
ρ_w	Density of water

Abbreviation

ACL	Anterior cruciate ligament
AM	Additive manufacturing
ASTM	American Society for Testing and Materials
BHK	Baby hamster kidney
CAD	Computer aided design
CAM	Computer aided manufacturing
CNC	Computer numerical control
CT	Computerized tomography
DC	Direct current
DED	Direct energy deposition
DLF	Directed light fabrication
DMD	Direct metal deposition
DMEM	Dulbecco's modified eagle medium
DMSO	Dimethyl sulfoxide
DNA	Deoxyribonucleic acid
EBF3	Electron beam freeform fabrication
EBS	Electron backscattered diffraction
EDS	Energy dispersive spectroscopy
FBAM	Fusion based additive manufacturing
FBS	Fetal bovine serum
FEA	Finite element analysis
FPBS	1% FBS mixed with the PBS solution
GMA	Gas metal arc
GTA	Gas tungsten arc
HA	Hydroxyapatite
HAZ	Heat affected zone
HEA	High entropy alloy
HEK-293	Human embryonic kidney 293

HeLa	Henrietta lacks
HSS	High-speed steel
ICP-AES	Inductively coupled plasma-atomic emission spectrophotometer
JCPDS	Joint Committee on Powder Diffraction Standards
LBMD	Laser-based metal deposition
LCL	Lateral collateral ligament
LENS	Laser engineered net shaping
LFF	Laser freeform fabrication
L-PBF	Laser-based powder bed fusion
MCL	Medial collateral ligament
MIG	Metal inert gas
MTT	Standard 3-(4, 5-dimethylthiazol-2-yl)-2, 5-diphenyltetrazolium bromide
OCP	Open-circuit potential
OFAT	One-factor-at-a-time
PBS	Phosphate buffered saline
PCA	Porous coated anatomical
PCL	Posterior cruciate ligament
PEEK	Polyether ether ketone
PKR	Partial knee replacement
PMMA	Polymethyl-methacrylate
PPAD	Pulsed plasma arc deposition
ppb	Parts per billion
PS	Physiological saline
SBF	Simulated body fluid
SCE	Saturated calomel electrode
SEM	Scanning electron microscopy
SOD	Stand-off Distance
SS316L	Stainless steel

SSAM	Solid-state additive manufacturing
STL	Stereolithography
TIG	Tungsten inert gas
TKR	Total Knee replacement
UHMWPE	Ultra-high molecular weight polyethylene
WSEM	Wire spark erosion machining
XRD	X-ray diffraction
μ-PAAM	Micro-plasma arc additive manufacturing
μ-WAAM	Micro-wire and arc additive manufacturing

Chapter 1

Introduction

This chapter provides a brief overview of anatomy and structure of human knee joint, its biomechanics, causes of its failure, types of knee replacement and implants, desired characteristics of materials for knee implants, and presently used metallic and non-metallic materials for knee implants. It also provides details about additive manufacturing (AM), their classification based on melting of the feedstock material and heat source type, their advantages, limitations, and applications. It concludes with organization of the thesis.

1.1 Anatomy and Structure of Knee Joint

Knee is the largest and strongest joint in the human body which is made up of bones, cartilage, ligaments, and tendons. It consists of lower end of the femur (i.e., thighbone), upper end of the tibia (i.e., shinbone), and the patella (i.e., kneecap) as shown in Fig. 1.1. The joint in the knee between the tibial and the femoral bones is known as *tibiofemoral* joint and the joint between the patella and femur is known as *patellofemoral* joint. The underside of the patella sits in a groove within the femur called the patella-femoral groove. Within this groove, the patella moves largely lengthwise, but it has some sideways movement and can tilt and rotate as well. Ends of three bones of the knee joint are covered with articular cartilage which is a smooth and slippery substance that helps knee bones to glide smoothly during the knee movement. Two wedge-shaped meniscal cartilages act as shock absorbers between femur and tibia. They are tough and rubbery to help cushion and stabilize the knee joint. Ligament is the fibrous tissue that connects bones to other bones to form a joint. The stability of the knee joint is achieved by four ligaments and strong muscles as shown in Fig. 1.1. The four ligaments are [i.e., medial collateral ligament (MCL), lateral collateral ligament (LCL), anterior cruciate ligament (ACL), and posterior cruciate ligament (PCL)] which function similar as strong ropes to hold the knee bones together and provide stability to knee.

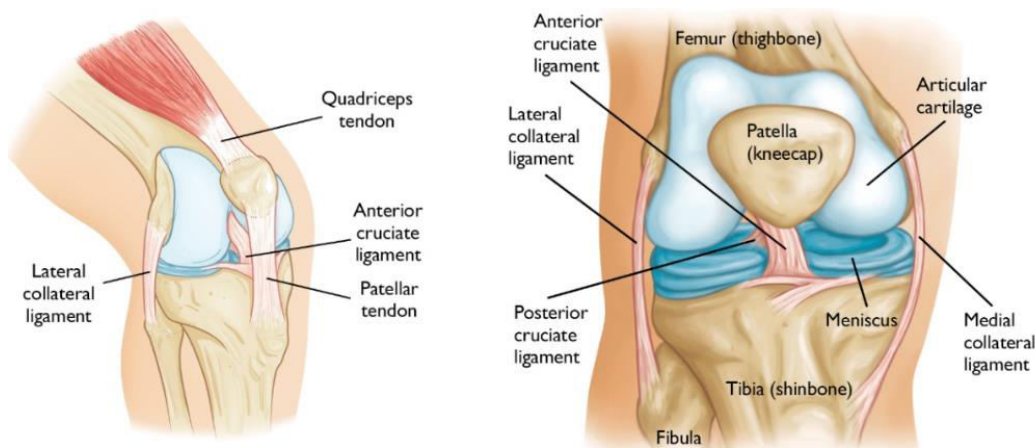


Fig. 1.1: Anatomy of human knee joint.

Source: <https://orthoinfo.aaos.org/en/treatment/knee-replacement-implants>

The MCL is located inside the knee joint. It extends from the medial femoral epicondyle to the tibia, and it prevents excessive abduction of the knee. The LCL is located outside the knee joint. It extends from the lateral femoral epicondyle to the head of the fibula. It prevents excessive adduction of the knee. The ACL extends postero-laterally from the tibia and inserts on the lateral femoral condyle. It prevents excessive posterior movement of the femur on the tibia. The PCL extends antero-medially from the tibia posterior to the medial femoral condyle. It prevents excessive anterior movement of the femur on the tibia. Quadriceps tendon connects the muscles in front of thigh to patella and patellar tendon, below the kneecap, runs from patella to the front of the tibia bone. On the back of the thigh, the hamstring muscles flex the knee normally to a maximum of 135 degrees and extends to 0 degree (i.e., straight position). The knee joint is surrounded by synovial membrane which releases a lubricating fluid for the cartilage and to reduce friction. The meniscus is a thickened cartilage pad between the femur and tibia. It acts as a smooth surface for motion of knee joint and in the standing position it absorbs the load of the body above the knee joint. The knee joint is surrounded by fluid-filled sacs called bursae, which serve as gliding surfaces for the tendons and reduce the friction between the tendons. There are large blood vessels passing through the area behind the knee (referred to as the popliteal space). The knee can also rotate slightly under guidance of specific muscles of the thigh. Functioning of the knees allows movement of the legs which is critical to normal walking (Festas *et al.* 2019).

1.1.1 Biomechanics of Knee Joint

Human knee joint is a modified hinge joint whose biomechanics can be understood in terms of its mechanical axis and motions, and anatomical planes of human body. Mechanical axis of the knee joint refers to the angle formed by a line drawn from the center of the femoral head to the medial tibial spine and a line drawn from the medial tibial spine

to the center of the ankle joint as shown in Fig. 1.2a. This line is practically perpendicular to the ground. There are three anatomical planes of the human body namely sagittal plane, coronal plane, and transverse plane. An axis is a straight line around which an object can rotate, and movement at any joint take place in a plane about an axis. There are three axes of rotation namely sagittal axis, frontal axis, and vertical axis. Fig. 1.2b explains these planes and axis which are defined as follows:

- **Sagittal plane:** Sagittal plane is a vertical plane which passes from anterior (front) to posterior (rear) dividing the body into right and left halves.
- **Coronal or frontal plane:** A coronal or frontal plane is any vertical plane that divides the body into ventral and dorsal (or belly and back) sections.
- **Transverse or axial plane:** It lies horizontally and divides the body into superior (or upper) and inferior (or lower) parts.
- **Sagittal axis:** The sagittal axis passes horizontally from posterior to anterior and is formed by the intersection of the sagittal plane and transverse plane.
- **Frontal axis:** The frontal axis passes horizontally from left to right and is formed by the intersection of the frontal plane and transverse plane.
- **Vertical or longitudinal axis:** The vertical axis passes vertically from inferior to superior and is formed by the intersection of the sagittal plane and frontal plane.

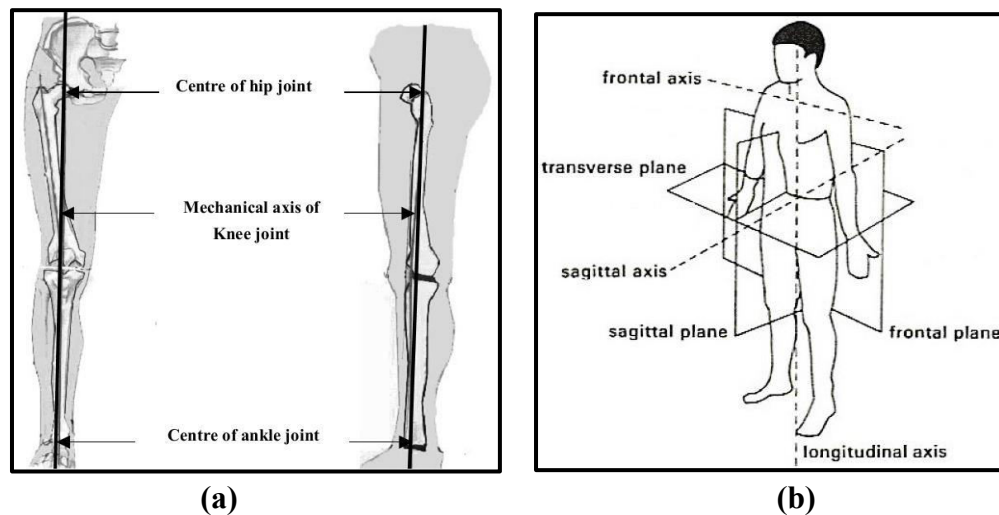


Fig. 1.2: (a) Mechanical axis of a knee joint, and (b) anatomical planes of human body (Sato et al. 2010).

Source: <http://www.spineuniverse.com/anatomy/anatomical-planes-body>

Motions of a knee joint are shown in the Fig. 1.3 and tabulated in Table 1.1. The active movements of the knee joint are described as flexion, extension, medial rotation, and lateral rotation as described below:

- **Flexion:** When the knee is flexed or bent, the cruciate ligament is taut, and the collateral ligaments are relaxed. Maximum flexion of the knee is 120-150 degrees.
- **Extension:** When the knee is extended or straightened, the lateral and medial collateral ligaments as well as the ACL are taut. Maximum extension of the knee is 5-10 degrees.
- **Medial Rotation:** This movement can only be achieved while the knee is in flexion. The cruciate ligaments control medial rotation of the tibia by twisting around each other to enable this movement. Maximum internal rotation is 30-40 degrees.
- **Lateral Rotation:** This movement also requires the knee to be flexed in order to rotate laterally. The cruciate ligaments control lateral rotation of the tibia by untwisting around each other to enable this movement. Maximum external rotation is 30-40 degrees.

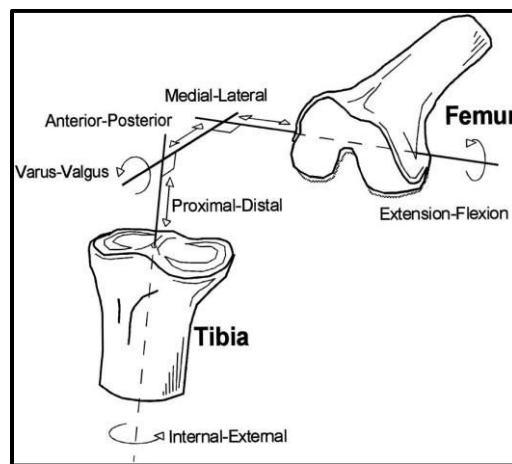


Fig. 1.3: Motions of a knee joint.

Source: <http://ajs.sagepub.com/content/27/4/533/F1.expansion>

Table 1.1: Motions of knee joint about different planes and axes along with examples.

Plane	Axis	Motion	Example
Sagittal	Frontal	Rotation: Flexion/Extension Translation: Medial/Lateral	Walking, Squatting
Coronal	Sagittal	Rotation: Adduction/Abduction Translation: Anterior/Posterior	Side bending
Transverse	Vertical	Rotation: Axial Translation: Superior/Inferior	Turning either left or right side

1.1.2 Causes for Failure of Knee Joint

Arthritis is the inflammation of one or more joints in a human body. Its primary symptoms are swelling, pain, stiffness, reduced range of motion which can worsen with age (Hylkema et al. 2019; Twiggs et al. 2019). Any joint can be affected by the arthritis, but knee arthritis is more prominent. Common types of knee arthritis are: (i) gout, (ii) post-traumatic arthritis, (iii) rheumatoid arthritis, (iv) osteoarthritis. Gout is accumulation of uric acid in knee joint causing sudden and sharp pain. Post-traumatic arthritis is

developed after knee injury, knee fracture, or severe ligament tearing of knee joint which may damage the articular cartilage over time, causing pain in knees and limiting their functioning. Rheumatoid arthritis is an autoimmune disease in which synovial membrane becomes thickened and inflamed, producing too much synovial fluid, which over-fills the joint space. This chronic inflammation can damage the cartilage and eventually cause cartilage loss, pain, and stiffness which can lead to serious knee injury. Osteoarthritis is the most common type of knee arthritis affecting around 5 million people globally (**Kloppenburg and Berenbaum 2020**). It usually occurs after the age of 50 and often in an individual with a family history of arthritis. It is caused due to gradual wear and tear of knee cartilages that are vital for load bearing and friction reduction. It decreases the protective space between the bones resulting in their rubbing with each other causing severe pain and stiffness (**Wallace et al. 2017; Cui et al. 2020; Hunter and Zeinstra 2019**). Figure 1.4 depicts healthy knee joint (right) and damaged knee joint (left). If the knee joint is severely damaged by arthritis or injury, it may be hard to perform even simple activities such as walking or climbing stairs. The patient may begin to feel pain while sitting or lying down. If physiotherapy, medication, changing activity level, and use of walking supports are no longer helpful then total knee replacement (TKR) surgery is only option to restore normal functioning of knees (**Lee et al. 2017; Taunton 2021; Liu et al. 2021**). The TKR surgery through resurfacing the damaged and worn surfaces of the affected knee joint can relieve knee pain, correct leg deformity, and allow the patient to resume her/his normal activities. It costs approx. Rs. 5-10 Lacs in India with exact cost depending on knee implant material.



Fig. 1.4: Healthy knee joint (right), and damaged knee joint (left).

Source: <http://www.aclsolutions.com/anatomy.php>

1.2 Knee Replacement

Knee implants are designed to replace the natural knee parts that have been damaged. A knee implant (as shown in Fig. 1.5) consists of (i) **Femoral component:** It is generally made of metallic material. It is fixed to the end of femur (thigh bone). There is a groove down the center of this part of the implant which allows the patella (or kneecap) to move up and down as the knee bends and straightens, (ii) **Tibial component:** It consists of two subcomponents i.e., One is flat metallic platform, and another is ultra-high molecular weight polyethylene (UHMWPE) spacer to provide cushioning effect which is placed over the flat metallic surface, and (iii) **Patellar component:** It is made of metallic material. It is like dome shaped piece. It is used in some of the TKR surgeries (**Merola and Affatato 2019**).

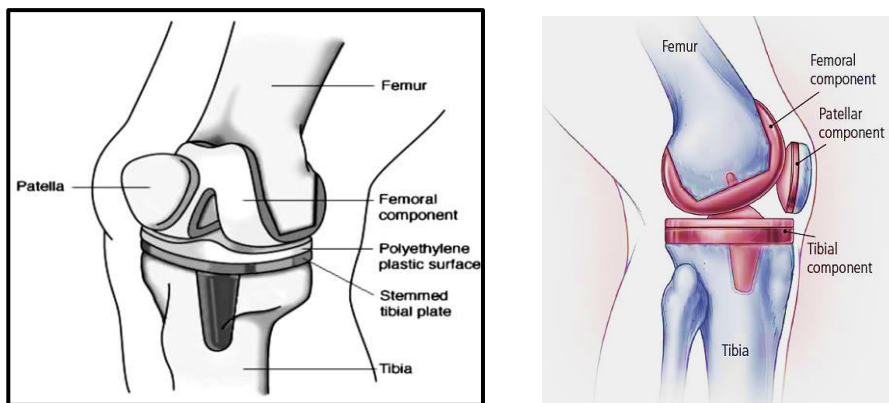


Fig. 1.5: Components of a knee implant (**Chu 1999**).

The first knee implant model was developed in late 1950s by **Mckeever (1985)**. It was a tibial plateau prosthesis consisting of a single metallic component. Two design approaches were introduced in late 1960s (i.e., anatomical and functional models) to manufacture the knee implants. Anatomical models are planned to preserve and evade the posterior cruciate ligament (PCL) and the anterior cruciate ligament (ACL) if it is engaged. The fixed surface of anatomical design contains a cut-out slot that provides a passageway through the joint for the cruciate ligaments. Functional design allowed non-anatomical joint surface geometries anticipated to maximize surface area and reduce polyethylene stress (**Robinson 2005**). Knee implants are not one-size-fit or one-style-fit. They may vary according to design, fixation, and materials.

1.2.1 Total Knee Replacement and Partial Knee Replacement

Failed knee joint may be repaired either totally or partially replacing its failed components. They are known as total knee replacement and partial knee replacement respectively as shown in Fig. 1.6. Total knee replacement means that all components of knee joint are replaced by artificial components such as femoral, tibial and patellar

components. A partial knee replacement (PKR) also called uni-compartmental knee replacement, is performed in which either damaged femoral or tibial component is replaced.

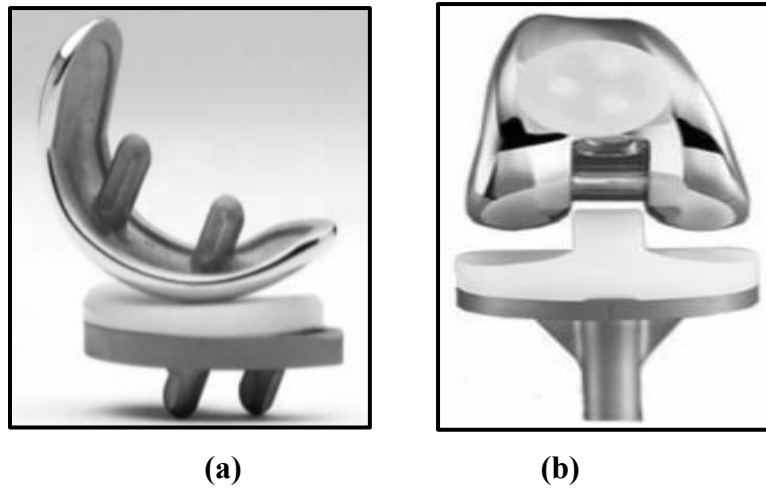


Fig. 1.6: (a) Uni-compartmental, (b) total knee replacement
Source: <http://bonesmart.org/joint-replacement-surgery/knee>

1.2.2 Types of Knee Implants

Following types of knee implants are used to restore the functions of the damaged human knee joint:

- **Fixed bearing implant:** It is the most common type of implant in TKR surgery. It is termed as fixed bearing implant because the polyethylene cushion is firmly fixed to the tibial tray as shown in Fig. 1.7 and the femoral component slides over it. This implant provides good range of motion. Its failure occurs due to excessive activity or additional weight which causes pain, loosening of the implant, and ultimately its failure.

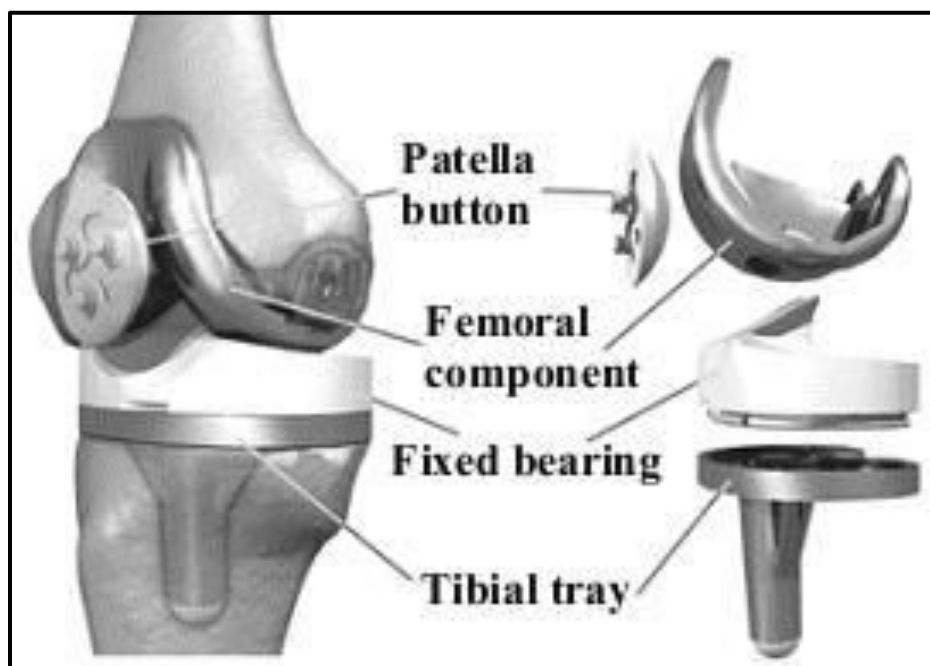


Fig. 1.7: Fixed bearing implant.
Source: <http://bonesmart.org/joint-replacement-surgery/knee>

- **Mobile bearing implants:** It is a special type of knee implant designed for younger, more active, and overweight persons for longer performance with less wear. The polyethylene cushion has protrusion which is inserted in corresponding hole made in the metallic tibial tray as shown in Fig. 1.8. This enables the femoral component to rotate by few degrees which allows the patient to move medial and lateral sides of the knee.

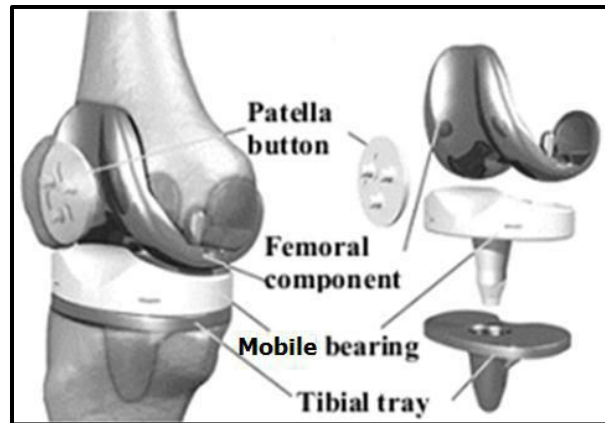


Fig. 1.8: Mobile bearing implant.

Source: <http://bonesmart.org/joint-replacement-surgery/knee>

- **Medial pivot implants:** This implant look like a natural knee as it rotates, twists, bends, flexions, and stables. Its design is more stable during normal knee motion.
- **Posterior cruciate ligament (PCL) retaining or substituting implant:** The PCL is an important ligament that stabilizes the knee joint. In some TKR, the PCL is found defective therefore it is removed while in other cases it is left intact. If PCL is removed, then a special knee implant that simulates the function of the PCL by ‘cam and post’ mechanism, is implanted for stabilization of the knee implant. Fig. 1.9 depicts the photographs of PCL retaining and PCL substituting implants. The ACL is usually removed in TKR and left intact in PKR.

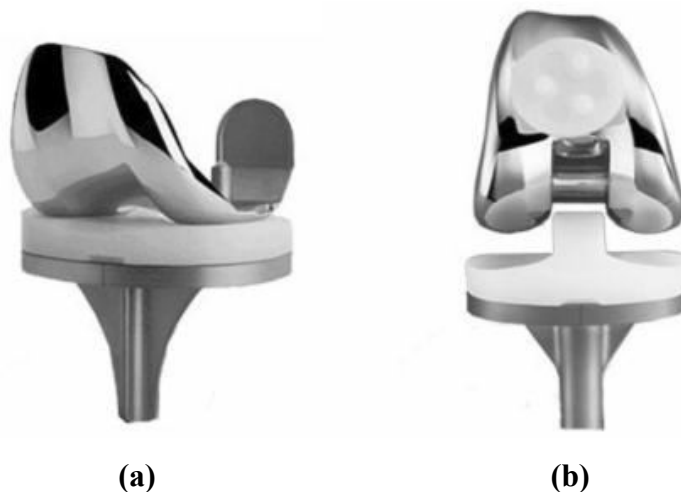


Fig. 1.9: (a) Posterior cruciate ligament (PCL) retaining, and (b) substituting implant.

Source: <http://bonesmart.org/joint-replacement-surgery/knee>

- **Cemented and cement-less implant:** This type of implants depends on the type of fixation i.e., cemented, cement-less or hybrid (combination of both). Most implants use a special type of bone cement namely polymethyl-methacrylate (PMMA) at the time of implantation to hold the implants in place. The cementless implants have a textured surface or coated with porous material at the bone/implant interface so that it allows bone growth on the implant surface. In some cases, knee screws may be used to stabilize the implant until the bone growth occurs.

1.3 Assessment of Post-operative Rehabilitation of Knee Replacement

Total knee arthroplasty (TKA) is one of the most popular elective operations performed globally, with an annual rate of over 5% between 1998 and 2008 (Culliford *et al.* 2015; Naylor *et al.* 2017). Recent initiatives have been undertaken to enhance patient outcomes, such as changes to implant design, patient optimization, and perioperative pain control. Shorter hospital stays, fewer problems, and a lower need for follow-up care have all been a result of postoperative therapies, particularly rehabilitation. Rehabilitation strategies are intended to increase quadriceps strength and range of motion, ease daily living tasks, and support the execution of increasingly difficult exercises. Numerous surgical therapies, including continuous passive motion, high velocity contractions, fast rehabilitation, and telerehabilitation, have been studied in recent years. These interventions modify the technique with which patients perform specific exercises, while telerehabilitation utilizes remote devices to provide standard rehabilitation (Doerfler *et al.* 2016; Moffet *et al.* 2015).

1.3.1 Patience Satisfaction Measurement Tool

The Knee Society Clinical Rating System has been widely used since 1989 as a scoring system for the assessment of TKA outcomes. The new Knee Society Knee Scoring System was introduced in 2011 to incorporate patient-reported outcome assessment scales (satisfaction, expectations, and physical activities). Other popular PROMs include the 36-item Short Form Health Survey (SF-36), the 12-item Short Form Health Survey (SF-12), the Western Ontario and McMaster Universities Arthritis Index (WOMAC), the Knee injury and Osteoarthritis Outcome Score (KOOS) and the Oxford knee score (OKS). Pain, mobility, physical function, and mental health are known as primary factors influencing patient satisfaction (Scuderi *et al.* 2012; Van Hove *et al.* 2015).

1.3.2 Patient Dissatisfaction: Causes and Types

The most common causes of patient dissatisfaction after TKA are residual pain and limited function. Postoperative pain is associated with the preoperative diagnosis and mental status, while functional recovery is affected by age and gender. Scott *et al.* (2012) noted that a high percentage of patients was not satisfied with their ability to kneel, squat,

and climb stairs after TKA. **Parvizi et al. (2014)** found that 89% of the patients were satisfied with their ability to perform daily living activities and 91% were satisfied in terms of pain relief, but only 66% reported their knees felt normal, 33% had lingering pain, 41% suffered from stiffness, 33% complained of bothering noise, swelling, or tightness, and difficulty in getting in and out of a car, getting up and down from a chair, and climbing up and down stairs.

1.3.3 Internal Determinants of Patient Satisfaction

Age, gender, personality, expectations, physical and psychological comorbidities, TKA diagnosis, and the degree of arthropathy are some potential intrinsic factors of patient satisfaction. These determinants

- **Age:** According to **Noble et al. (2006)** and **Scott et al. (2012)**, patients were more satisfied with the outcome of TKA when they were 60 years or younger. **Williams et al. (2013)** reported that patient satisfaction was significantly low among patients less than 55 years of age. **Parvizi et al. (2014)** described residual symptoms and functional deficits more prevalent in younger patients. **Von Keudell et al. (2014)** documented that satisfaction with postoperative pain, ROM, and kneeling was higher after unicompartmental knee arthroplasty in patients less than 55 years of age, whereas TKA provided greater satisfaction in patients more than 65 years of age.
- **Gender:** Residual pain and stiffness are likely to be more prevalent in female TKA patients (**Bonnin et al. 2011**). However, it has not been sufficiently established as to whether gender is a predictive factor of patient satisfaction.
- **Personality of Patients:** **Gong and Dong (2014)** retrospectively investigated the relationship between the outcomes of TKA and patient's personality classified into 4 types: patients with extroverted personality were more satisfied than those with introverted or anxious personality after TKA. In our opinion, however, the influence of personality on the outcome of TKA is not straightforward to determine due to the difficulty of categorizing various human personalities.
- **Expectations of Patients:** **Bourne et al. (2010)** and **Scott et al. (2010)** found that unmet expectations were the strongest predictor of dissatisfaction after TKA. However, patient's expectations tend to be higher than the surgeons, and it is important for the surgeon to inform the patient of the possibility of unmet expectations. Recent systemic reviews have shown that there is no significant association between patient's expectations and postoperative satisfaction, suggesting the need for more objective measures of assessment.

- **Comorbidities:** Preoperative back pain or pain in the other joints is a major predictor of postoperative dissatisfaction after TKA. Studies have shown that patients with medical or psychological comorbidities are more likely to experience pain or functional disability after TKA. Patients with low preoperative mental health based on the SF-12 and SF-36 scores are more likely to experience poor outcomes in terms of pain relief and functional improvement. Patients with diabetes or pulmonary disease are more likely to experience limited mobility after TKA. Preoperative depression does not affect postoperative function, but patients with preoperative depression appear to obtain higher levels of satisfaction after TKA than those without (**Singh and Lewallen 2013; Fisher et al. 2007**).
- **Diagnosis for total knee arthroplasty:** Rheumatoid arthritis patients have been reported to have greater satisfaction than patients with other indications for surgery. This can be attributed either to 1) the fact that the most important expectation among rheumatoid arthritis patients is pain relief, whereas patients with other diseases are more concerned with functional improvement or to 2) the relatively low expectation among patients with rheumatoid arthritis (**Bullens et al. 2001**).
- **Severity of arthropathy:** **Bourne et al. (2010)** and **Maratt et al. (2015)** found that patients with severe pain or dysfunction before surgery were more likely to be satisfied after surgery. **Kim et al. (2009)** found that dissatisfaction with TKA was associated with poor preoperative WOMAC score, suggesting that end-stage arthritis patients are likely to have a low level of satisfaction.
- **Other factors:** **Fisher et al. (2007)** found that high body mass index, previous history of knee surgery, disabilities, low social support, poverty, living alone, and postoperative varus knee alignment can lead to poor satisfaction after TKA. **Mann et al. (2013)** observed improvements in outcome scores after revision TKA when performed by a different surgeon.

1.3.4 External Components of Patient Satisfaction

External components that can be associated with patient satisfaction include anaesthesia, postoperative pain management, surgical technique, implant type, and postoperative rehabilitation.

- **Anaesthesia and postoperative pain management:** Studies have linked anaesthesia and postoperative pain management with patient satisfaction. Regional anaesthesia appears to result in greater patient satisfaction, but a study by **Harsten et al. (2013)** found that the general anaesthesia group obtained more favourable results than the spinal anaesthesia group in terms of early recovery, pain relief, dizziness/nausea, and

early ambulation. A variety of attempts have been made for initial pain relief and improved patient satisfaction, but narcotic analgesics are less frequently used due to the risk of complications.

- **Surgical technique:** Minimally invasive TKA has been expected to improve patient satisfaction, but **Hernandez-Vaquero *et al.* (2010)** found no significant differences in satisfaction between the two techniques. Therefore, further research is needed to investigate the influence of surgical technique on patient satisfaction.
- **Type of implant:** TKA has evolved to better accommodate patients' desire for functional improvement. Research has shown a relationship between the type of implant and postoperative satisfaction. **Hamilton *et al.* (2015)** conducted a prospective, double-blind randomized control trial for comparison of Kinemax TKA and Triathlon TKA, which showed that the outcome of TKA could be influenced by the prosthesis design.
- **Postoperative rehabilitation:** **Levine *et al.* (2013)** and **Kim *et al.* (2009)** reported that rehabilitation managed by a physical therapist did not improve patient satisfaction or functioning compared to neuromuscular electrical stimulation performed at home without therapist's supervision. However, systematic rehabilitation guided by a physical therapist would be beneficial for a faster return to normal daily activities.

1.4 Materials for Knee Implants

Success for any knee implants depends on the correct choice of biomaterials used to manufacture them. A biomaterial is defined by the European Society for Biomaterials as “a material that interacts with the biological system to evaluate, treat, reinforce or replace a tissue, organ or function of an organism” (**Williams 1987**). Though lifespan of knee implants is 10 to 20 years, but they often fail due to wear of their components, infection caused due to poor osseointegration, and stress shielding effect which is caused due to improper transfer of load between the human bones and knee implants (**Straumal *et al.* 2021; Lu *et al.* 2021; Cheng *et al.* 2022**). Wear of knee implant components is a continuously persistent problem irrespective of its material. Higher coefficient of friction or low wear resistance results in loosening of the knee implants. Release of wear debris to the blood causes severe allergic reactions to the human body (**Sawy and Shaarawy 2014; Ali *et al.* 2020**). All this necessitate revision surgery, extended stay in hospital, and increased cost of knee surgery (**Bairagi and Mandal 2022**). Table 1.2 presents the required properties for knee implant material that will help longer life of knee implants in the human body and they described in the following paragraphs:

Table 1.2: Required properties for knee implant material and consequences of not having it (Carr and Goswami 2009, Bergschmidt et al. 2016; Xiang et al. 2019).

Required property for knee implant material	Consequences of not having the required property
Biocompatibility	Response of human body; Adverse effects on the immune system
Osseointegration	Inadequate integration between knee implant and human tissues and bones
Higher corrosion resistance	Releasing non-compatible metallic ions to human blood, Allergic reactions
Modulus of elasticity closer to human bones	Stress shielding effect due to loosening of implant components Severe inflammatory response Destruction of healthy bones
Adequate yield and compressive strength	Implant failure, pain to patient and revision surgery
Higher wear resistance	Mixing of wear debris in human blood leading to carcinogenicity
Longer fatigue life	Mechanical failure of knee implant, Need of revision surgery

- Biocompatibility:** It is the most important requirements for knee implant materials which are expected to be highly non-toxic and should not cause any inflammatory or allergic reactions in the human body. It is not only associated to toxicity, but to all the adverse effects of a material in a biological system (Geetha et al. 2009; Navarro et al. 2008). Success of knee implant materials is mainly dependent on the reaction of the human body to the knee implant, and this measures the biocompatibility of a material (Williams 2008). The two main factors that influence the biocompatibility of a material are the host response induced by it and its degradation in the human body environment. When knee implants are exposed to human tissues and fluids, several reactions take place between the host and the knee implant material and these reactions dictate the acceptability of implant materials by the human body.
- Osseointegration:** Osseointegration is direct functional and structural correlation between the human bones and tissues and load-carrying surface of an implant. It is an important requirement for stability and long-term clinical success of knee implants (Ryu et al. 2021). Sola et al. (2019) mention that structural pores are intentionally introduced in knee implant material to improve its osseointegration and reduce its total density without affecting its load carrying capacity. Inability of a knee implant to join with the adjacent bones and tissues due to micromotions, results in the formation of a fibrous tissue around the implant which promotes its loosening. Surface chemistry, roughness and topography influence both the osseointegration and biocompatibility (Mirhosseini et al. 2007).
- Higher corrosion resistance:** Lower corrosion resistance of the knee implant materials in the human body fluids results in the release of toxic metallic ions to the human body

which are found to cause allergic and toxic reactions (**Hallab et al. 2005**). Corrosion can reduce the life of an implant and consequently may impose revision surgery. Life span of knee implants is mainly determined by their material abrasion and wear resistance. Thus, high corrosion resistance of knee implant materials is of prime importance for their longevity in the human body.

- **Modulus of elasticity closer to that of human bone:** Elastic modulus of human bones varies from 4 to 30 GPa depending on the type of the bone and the measurement direction (**Katz 1980**). **Au et al. (2007)** and **Geetha et al. (2009)** have emphasized that large difference in the elastic modulus between implant material and the surrounding bone cause severe stress concentration, namely load shielding from natural bone, that may weaken the bones and deteriorate the implant/bone interface, loosening and consequently failure of knee implant. Elastic modulus is considered as a main factor in selection of knee implant materials.
- **Adequate yield and compressive strength:** Inadequate strength of knee implant materials influence their fracture (**Alvarado et al. 2003; Geetha et al. 2009**). This causes pain to the patient. After a certain time, the pain becomes unbearable which leads to revision surgery.
- **Higher wear resistance:** Low wear resistance or high coefficient of friction results in loosening of knee implants (**Alvarado et al. 2003; Ramsden et al. 2007**). Wear debris are found to be biologically active and make severe inflammatory response that leads to destruction of the healthy bones. Tribo-corrosion behavior of knee implant material is another concern because it releases non-compatible metallic ions to human body. It is also worth mentioning that mechanical loading can also result in corrosion fatigue and accelerate wear of the implants.
- **Longer fatigue life:** The fatigue strength is related to the response of a material to the repeated cyclic loading. Fatigue characteristics of a material strongly depend on its microstructure which can be altered by its processing and heat treatment (**Niinomi et al. 2007**). Fatigue fracture of knee implant causes their loosening, stress-shielding, and their premature failure (**Teoh, 2000**).

1.4.1 Metallic Materials for Knee Implants

Knee implant materials are divided into categories of metallic and nonmetallic materials (i.e., polymers, ceramics, and composites). A knee implant has three major components: femur, tibia (includes tibial tray and tibial insert) and patella or kneecap. The tibial insert and the patellar components are usually made of plastics such as ultra-high molecular weight polyethylene (UHMWPE) or crosslinked polyethylene. The femoral component and

tibial tray are made of metallic materials such stainless steel, cobalt-chromium alloys, and titanium alloys (Carr and Goswami 2009). It is important to know the physical and chemical properties of these metallic materials as well as their interaction with the tissue of the human body which are discussed below.

- **Stainless steel:** Stainless steel is a generic name for several steels due to their resistance to a wide range of corrosive media due to their high Cr content which has great affinity towards oxygen. This causes formation a film of chromium oxide on stainless steel surface which is passive, adhesive, and self-healing (Alvarado et al. 2003; Navarro et al. 2008). Austenitic stainless-steel SS 316L is the mostly used for manufacturing knee implants due to its easier availability, good biocompatibility and strength, excellent fabrication properties, and lower cost. But its wear resistance is relatively poor which causes rapid loosening of implants due to generation of more wear debris. Though stainless-steel corrosion resistance can be modified by lowering the nickel content and alloying them with Mn or N but stainless-steel implants often degrade due to pitting, crevice, corrosion fatigue, fretting corrosion, stress corrosion cracking, and galvanic corrosion in the human body (Singh and Dahotre, 2007). Poor corrosion resistance and danger of allergic reactions restrict use of stainless steel as knee implant material (Navarro et al. 2008; Gradzka-Dahlke et al. 2007). Moreover, elastic modulus of stainless steel is approx. 200 GPa which is much higher than that of human bones.
- **Cobalt Chromium based alloy:** Cobalt chromium alloys can be basically categorized into two types; one is the Co-Cr-Mo alloy (which is usually used to cast a product) and the second one is Co-Ni-Cr-Mo alloy, (which is usually wrought by hot forging). The castable Co-Cr-Mo alloy has been used in dentistry for long time and recently being used in making the knee implants. The wrought Co-Ni-Cr-Mo alloy is a relative new material which is now being used for knee implants (Alvarado et al. 2003). Cobalt-based alloys have high resistance to corrosion even in chloride environment due to spontaneous formation of passive oxide layer in the human body environment (Alvarado et al. 2003; Ramsden et al. 2007; Navarro et al. 2008;). These materials also have high resistance to fatigue and cracking caused by corrosion and good wear resistance. Also, they are not brittle because they have a minimum of 8% elongation. But these materials have a high elastic modulus (220-230 GPa) comparable to that of stainless steel (approx. 200 GPa) which is higher than the cortical bones (20–30 GPa) (Alvarado et al. 2003; Ramsden et al. 2007). Toxic elements such as Ni, Cr and Co are found to be released from stainless steel and Co-Cr alloys due to their corrosion in the human body (Okazaki and Gotoh 2005).

- Titanium and its alloys:** There are three types of phases are presents in titanium (Ti)-alloys namely alpha (α), alpha-beta (α - β), and beta (β) phases. The β -phase in Ti alloys tends to exhibit a much lower modulus than the α -phase, and also it satisfies most of the other requirements for knee implant material (**Eisenbarth et al. 2004; Nag et al. 2009**). Ti-alloys are excellent choice as knee implant material due to their excellent characteristics such as high strength, low density (approx. 4.7 g/cm^3), good resistance to corrosion (due to the formation of TiO_2 passive oxide layer at the surface), complete inertness to human body environment, enhanced biocompatibility, and moderate elastic modulus of approximately 110 GPa. Better osseointegration of Ti-alloys improves life of the knee implants thus minimizing the risks of its loosening and failure. Commercially pure Ti (CP-Ti) and Ti-6Al-4V are most commonly used for knee implant applications. Ti-6Al-V4 is slowly replacing CP-Ti due to its higher mechanical strength (**Eisenbarth et al. 2004**). Fig. 1.10 summaries drawbacks of different metallic materials for the knee implants which ultimately leads to premature failure of knee implants thus necessitating the revision surgery.

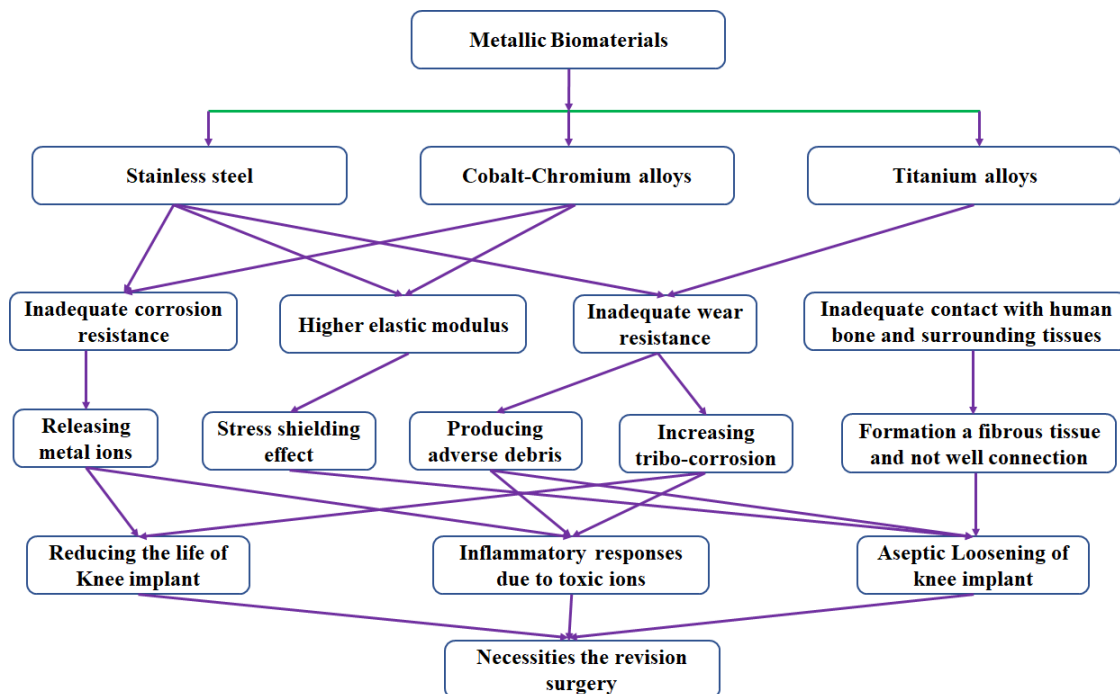


Fig. 1.10: Failure of different metallic materials due to long term use in human body.

1.4.2 Non-metallic Materials for Knee Implants

Non-metallic materials for knee implants are further divided into two subcategories of polymers and ceramics. They are used in the tibial insert and patellar components.

- Polymers:** Currently the most widely used polymers for knee implants are ultrahigh molecular weight polyethylene (UHMWPE) and thermoplastic polyether ether ketone (PEEK). The UHMWPE consists of long-chains of polymerized alkene and ethylene. It

is a semi-crystalline polymer having both crystalline and amorphous structure. It contains a set of ordered crystalline lamellae with tightly packed randomly orientated macromolecules embedded in a disordered amorphous structure. Increased molecular weight and degree of cross-bond formation between chains increase the strength and wear resistance of UHMWPE. These properties combined with a low coefficient of friction, higher abrasive wear and corrosion resistance, and higher impact strength and toughness have made it a good choice of knee implant material. The PEEK is a bioinert thermoplastic polymer used in knee implant. However, when combined with hydroxyapatite (HA), it shows increased bioactivity and greater tensile strength (**Ma et al. 2014**). Furthermore, often a bioactive solute is required because native PEEK has shown to exhibit poor osseointegration (**Evans 2015**).

- **Ceramics:** Ceramics gained popularity in the 1970's as the bearing materials. They consist of metallic elements such as aluminum, zirconium and silicon bonded with non-metallic elements. These ceramics are chemically inert after binding to oxygen imparting excellent biocompatibility. They also possess low surface roughness and high hardness, highest modulus of elasticity of any other biomaterial used in knee implant. But ceramics are brittle thus leading to catastrophic failure. The first ceramic bearing used in hip implant in 1971 were marred by catastrophic failure due to acute debonding at the implant-cement interface of cemented ceramic sockets resulting in aseptic loosening and implant fracture. Ceramics can be classified as non-oxides, oxides, and composites. Oxide ceramics such as alumina (Al_2O_3) and zirconia (ZrO_2) are preferred choice for orthopedic implant applications such as acetabular and femoral components.

Alumina (Al_2O_3) was developed as a biomaterial in the 1960s, making it a well characterized biomaterial. Modern alumina is processed using hot isostatic pressing, a process which reduces inclusions, grain size and grain boundaries, increasing hardness and increasing scratch resistance. Alumina also possesses a very low coefficient of friction due to low surface roughness, resulting from its low grain size. This excellent tribological performance is further compounded by high wettability of alumina and resulting film-fluid lubrication, which reduces in-vitro wear. Retrieval studies have demonstrated alumina-on-alumina wear rates of a few microns per year (**Willmann 2000**). Biologically the typical response to alumina wear debris is fibrocystic with no giant cell formation and little induction of macrophages, reducing osteolysis (**Hannouche et al. 2005**). The estimated lifetime risk of catastrophic failure of alumina femoral heads is estimated to be 0.004% (**Willmann 2000**).

Zirconium (ZrO_2) was introduced to reduce the catastrophic failure rates associated with alumina while retaining the desirable wear characteristics of smaller femoral heads on polyethylene (Bal et al. 2007). Pure zirconia is not used as a bearing material as it undergoes phase transformation between its three crystalline arrangements (monoclinic, cubic, tetragonal). This can result in volume and shape changes that increases its susceptibility to fracture. As a result, pure zirconia, requires stabilization through a process known as transformation toughening. Zirconia can be stabilized with CaO, Y_2O_3 or MgO which control the phase transformations.

1.5 Introduction to Additive Manufacturing

American Society for Testing and Materials (ASTM) standard ISO/ASTM 52900/2021 defines additive manufacturing (AM) as “a process of joining materials to make objects from the data of 3D computer aided design (CAD) model, usually layer upon layer, as opposed to subtractive manufacturing processes”. AM process is also referred to as 3D printing, freeform manufacturing, additive fabrication, or toolless manufacturing process. A CAD model is created using a design software and exported to stereolithography (STL) file format that is read by the AM equipment. Figure 1.11 depicts key moments of 3D printing showing progress of AM from the 1970s. In the 1980s, rapid prototyping was initially applied to the development of prototypes, enabling individuals to quickly construct a scale model of the final object. As AM processes improved, their applications grew to include rapid tooling, which was used to make molds for final products. By the early 2000s, use of additive manufacturing started to create the functional products.

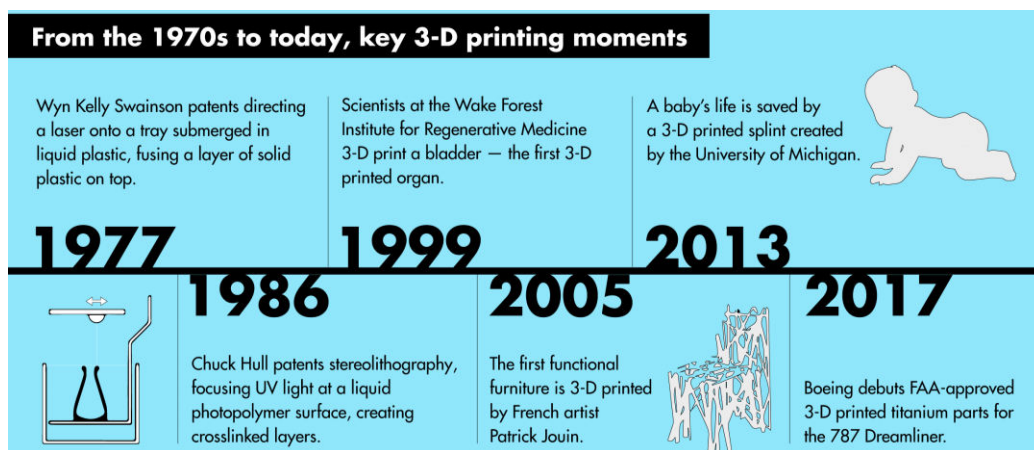


Fig. 1.11: Key developments in additive manufacturing since 1970s.

Source: <https://mitsloan.mit.edu/ideas-made-to-matter/additive-manufacturing-explained>

Nowadays, metal additive manufacturing is gaining a lot of attention for aerospace, biomedical, oil & gas, marine, automobile, sports, and luxury applications due to its features such as part design flexibility, component complexity, light weigh, part consolidation, and

design for function. AM is interdisciplinary in nature, utilizes CAD and computer aided manufacturing (CAM), advanced materials, robotics, joining, sensing, monitoring, and control. It is one of key enablers of Industry 4.0.

1.5.1 Classification of Additive Manufacturing Processes

The AM process is classified into seven major categories according to the ASTM F-42 standard. Table 1.3 describes the seven major AM processes, their brief description, associated technology with each AM processes, and raw material can be used for the making the components. These AM processes are powder bed fusion, direct energy deposition, Material extrusion, vat photo polymerization, binder jetting, materials jetting, and sheet lamination. The advantages and limitations of these processes is summarized in table 1.4. AM processes offers the potential to produce intricate geometric parts, and even parts that would be impractical to manufacture using any other production method. This comes with significant time and material savings compared to traditional processes like machining. However, it is important to note that the mechanical properties of additively parts are constrained, which presents clear disadvantages when compared to parts produced using the traditional manufacturing methods mentioned. On one hand, the size of the manufactured parts is still constrained and is contingent on the size of the additive manufacturing equipment. On the other hand, production costs are quite favorable and economically attractive, especially for polymeric materials. However, when it comes to metallic materials, the manufacturing cost remains high due to the complexity of obtaining the material for its transformation and the transformation process itself. Additionally, the price of metallic materials is higher in comparison to basic polymers.

On the other side, the AM processes can also be classified according to the requirement of melting of the deposition or feedstock material and type of heat source as shown in Fig. 1.12. Accordingly, the AM processes are divided into following two major categories: (i) fusion based additive manufacturing (FBAM) processes which melt the feedstock material, is also referred as direct energy deposition (DED) process and (ii) solid-state additive manufacturing (SSAM) processes which do not require melting of the feedstock material. FBAM has unique multi-functional capabilities of freeform manufacturing of complicated parts, coating, cladding, surface texturing, surface alloying, repairing, remanufacturing, rapid prototyping, and rapid tooling for various industrial applications. Their typical applications include biomedical, post-injury rehabilitation, aerospace, automobile, marine, power generation, gas turbines, oil, and gas extraction, and sports equipment.

Table 1.3: Classification of AM processes according to the ASTM F-42 standard.

AM Processes	Brief Description	Related Technology	Materials
Powder Bed Fusion	Thermal energy selectively fuses regions of a powder bed	Electron beam melting (EBM), Selective laser sintering (SLS), Selective laser melting (SLM), Multi jet fusion (MJF), and Direct metal laser sintering (DMLS)	Metals, Polymers
Direct Energy Deposition	Focused thermal energy is used to fuse materials by melting as the material is being deposited	Laser Engineering Net Shape (LENS) Wire-arc Additive Manufacturing (WAAM) Micro-plasma Arc Additive Manufacturing (μ -PAAM)	Metals
Material Extrusion	Material is selectively dispensed through a nozzle or orifice	Fused deposition modelling (FDM)	Polymers
Vat Photo Polymerization	Liquid photopolymer in a vat is selectively cured by light-activated polymerization	Stereo lithography (SLA), Digital light processing (DLP)	Photopolymers
Binder Jetting	A liquid bonding agent is selectively deposited to join powder materials	Powder bed and inkjet head (PBIH), plaster-based 3D printing (PP)	Polymers, Foundry sand, Metals
Material Jetting	Droplets of build material are selectively deposited	Multi-jet modelling (MJM)	Polymers, Waxes
Sheet Lamination	Sheets of material are bonded to form an object	Laminated object manufacturing (LOM), ultrasonic consolidation (UC)	Paper, Metals

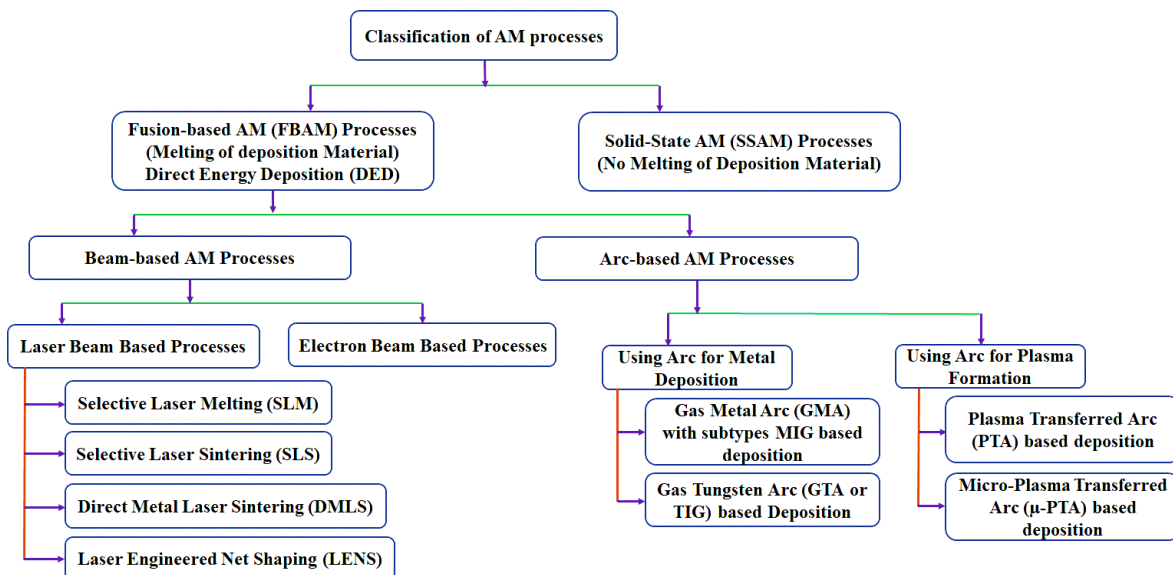


Fig. 1.12: Classification of AM processes.

Table 1.4: Advantages and limitations of AM processes.

AM Processes	Advantages	Limitations
Powder Bed Fusion	Ability to integrate into small scale; Office size machine; Powder support structure; Large material options	Relatively slow speed; Lack of structural properties in materials; Size limitations; High power usage; Surface finish dependent on powder grain size
Direct Energy Deposition	High quality; Functional parts; Speed often sacrificed for high accuracy	May require post processing for desired effect; Limited material
Material Extrusion	Widespread; Inexpensive ABS plastic can be used; Relatively inexpensive; Suitable for visual models and prototypes	Nozzle radius limited; Low accuracy and speed; Required constant pressure of material
Vat Photo Polymerization	Relatively quick process; Large build areas	Relative expensive; High post processing time; Limited material; Required support structure
Binder Jetting	Different colors; High range of materials; Fast process; Allows two materials	Not always suitable for structural parts; Due to the use of binder material; High time post processing
Material Jetting	High accuracy; Low waste; Multiple material parts and colors under one process	Support often required; Limited materials
Sheet Lamination	High speed; Low cost; Ease of material handling; High level of accuracy and good finish	Fusion processes required more research

The FBAM processes can be further classified into the following two subcategories based on the type of heat source used for melting of the deposition material: (a) Beam based AM processes namely *laser beam-based processes* (i.e., selective laser melting (**Zhou et al. 2019**), selective laser sintering (**Lupone et al. 2021**), direct metal laser sintering (**Ishfaq et al. 2021**), and laser engineered net shaping (**Zhang et al. 2023**)) and *electron beam based processes* (i.e., electron beam melting, **Galati and Iuliano, 2018**), and (b) Arc-based AM processes which use arc for material deposition generally in wire form and referred to as wire arc additive manufacturing (WAAM) i.e., gas metal arc or gas tungsten arc (**Ren et al. 2020**), and the processes with use the arc for plasma formation such as plasma transferred arc and micro-plasma transferred arc (**Sawant and Jain; 2017 and 2018**) in which plasma/micro-plasma is used as the heat source.

Laser beam is the most commercialized energy source in FBAM and the process is named as Laser Engineered Net Shaping (LENS). It was developed in 1995 at Sandia National Laboratories and was commercialized by Optomec in 1998 (**Banerjee et al. 2005**). It is also referred as directed light fabrication (DLF), direct metal deposition (DMD), 3D

laser cladding, laser-based metal deposition (LBMD), laser freeform fabrication (LFF), laser direct casting (LDC), laser cast, and laser consolidation (**Calignano et al. 2017**). Different types of lasers used in commercial FBAM processes include CO₂ laser, Nd:YAG laser, Yb-fiber laser, and excimer laser. Laser based FBAM processes are generally applicable to powder form of the deposition material. High-intensity laser irradiation is focused to fuse the deposition material which solidifies to form a deposition on the substrate or previously deposited layer. Significant process parameters are spot size, beam power, beam focal offset, travel speed, powder flow rate, powder morphology, powder moisture level, inert gas flow (**DebRoy et al. 2018**). Deposition process is carried out with a coaxially flowing shielding gas to protect the melt pool or in a hermetically sealed chamber filled with argon gas to regulate the oxygen and moisture level. Electron beam is another beam based FBAM process developed by NASA Langley research center and named as Electron Beam Freeform Fabrication (EBF3) process. It uses a high-power electron beam with a vacuum environment (1×10^{-4} torr or lower) to melt the deposition material thus eliminating the need of a shielding gas as used in laser-based deposition process. The process can be used to build a complex part using wire form of the deposition material and found to have almost 100% efficient in consumption of deposition material and 95% efficient in power utilization. This process is suitable for wire form of the deposition material due to the complications of powder feeding in a vacuum. Since a carrier gas is used for powder delivery, gas will get ionized in the electron beam. This process is suitable only for any electrically conductive material including alloys with high reflectivity such as aluminum and copper.

Arc-based FBAM processes have low setup cost, lower built time, and superior deposition efficiency (**Geng et al. 2017**). Spencer and Dickens from University of Nottingham made feasibility study for gas metal arc (GMA) or metal inert gas (MIG) based FBAM process in 1998 by generating arc between the consumable wire electrode and substrate to fuse the electrode and form a deposition (**Spencer et al. 1998**). Deposition melt pool is protected by shielding gas flowing through the GMA torch and does not require any customized working environment for deposition. This process has low buy-to-fly ratios, higher deposition rates and unlimited built volume potential but it is limited for wire deposition only. However, heat accumulation, accuracy and surface roughness are major drawback associated with multi-layer deposition using GMA-based FBAM process. With the increase in number of the deposited tracks, shape of each track cannot be controlled easily because of more heat accumulation, especially melt pool located at the boundaries of components. Moreover, bubbles and cavities may generate in the melt pool at high

temperature due to an intense metallurgical reaction (**Zhang et al. 2003**). Gas tungsten arc (GTA) or tungsten inert gas (TIG) based FBAM is another arc-based deposition process where arc generated between the non-consumable tungsten electrode and metallic substrate is used to fuse the deposition material. The melt pool is protected by shielding gas flowing through the GTA torch. It does not require any customized working environment for deposition as required in case of laser or electron beam based FBAM processes. The tungsten electrode projects out of the torch and the formed arc is coned shaped and has an aperture angle of 45° resulting in lower energy density, lower deposition rate, higher heat affected zone (HAZ) and distortion. This process is limited for wire form of the deposition because powder particles adhere to the projected tungsten electrode and interrupt the deposition process. **Terakubo et al. (2005)** developed μ -GTA based FBAM process to overcome the overheating problem and successfully evaluated this process by depositing μ -bead of titanium using low amperage to reduce heat input and found that bead size increases from 1.1 to 3.3 mm with increase in peak current from 5A to 30A. Plasma arc based FBAM process is another arc-based process where plasma arc generated from a tungsten electrode within the nozzle is forced through a hole in it which constricts the arc resulting in its stability even at low current, higher energy density, smaller HAZ, and less thermal distortion as compared to GTA and GMA based FBAM processes. Since the electrode is inside the nozzle, deposition material refrains to encounter the deposition material enabling this process to use both powder and wire form of deposition material. Moreover, plasma deposition is adaptable to automatic operations because of more reliable arc for high production requirements. Higher heat input is a consistent problem incurred in arc-based FBAM processes and to curb this problem attempt were made by different researchers to lower it. **Xu et al. (2013)** used pulsed plasma arc deposition (PPAD) and noted out that PPAD has benefits of high production efficiency, low cost, fine microstructure, excellent mechanical properties, and high density. **Jhavar et al. (2014a)** developed a new process named as micro-plasma arc additive manufacturing (μ -PAAM) at IIT Indore (India) to reduce heat input during deposition. It has been successfully used for deposition of wire of AISI P20 tool steel on substrate of the same material (**Jhavar et al. 2014b**), repairing of dies and moulds (**Jhavar et al. 2016**), deposition of powder of Ti-6Al-4V on a substrate of the same material (**Sawant et al. 2018a**), coating of Stellite 6 powder on AISI 4130 steel substrate (**Sawant et al. 2018b**), and dimple and spot texturing on high-speed steel (HSS) cutting tool (**Sawant et al. 2018c**). These investigations have confirmed that μ -PAAM process is material and energy-efficient process.

1.5.2 Advantages of AM processes

Following are some unique advantages offered by the AM processes:

- **Free-form fabrication:** AM processes surpass the limitations of conventional manufacturing processes such as casting, forging, forming, and machining. They manufacture the parts regardless of machining constraints, which let the complex geometries become manufacturable.
- **Digital-driven fabrication is highly controllable and repeatable:** Optimized complex geometries of products generated by a computer program can be manufactured precisely by AM processes.
- **Controllable multi-material manufacturing:** Functionally graded, smart materials, and biomaterials can be developed by the AM processes using multi-materials in the desired proportion.
- **Personalized manufacturing at low cost:** Traditional large-scale production usually needs an expensive prefabricated mold, which is a time-consuming process. In comparison, AM processes allows solid realization directly from a CAD model without a mold, which is much more efficient and cheaper. This is favored by applications such as multi-functional surgical tools, customized bone replacement, and heritage replication and repair.
- **Automatic manufacturing process:** Computer designed part geometries and multi-material manufacturability of AM processes allow unmanned manufacturing of a complicated product and material-diverse object through a single machine.
- **Reduction of material waste:** In conventional manufacturing processes, material is typically removed from a larger piece; think timber milling or cutting shapes from sheets of steel. In contrast AM starts from scratch, adding material to create a component or part. By using only, the substance necessary to create a part, the AM ensures minimal waste. The AM also reduces the need for tooling, therefore limiting the amount of material needed to produce different components.
- **Environment benefits:** The environmental benefits of additive manufacturing are an advantage to businesses seeking to improve manufacturing sustainability. AM offers many positive environmental benefits in comparison to traditional manufacturing. The most notable of which are waste reduction and energy savings. The AM processes, compared to traditional manufacturing, are more efficient and significantly reduce the environmental impact of waste products. They offer greater material efficiency because they only use what is needed to create a product.

1.5.3 Limitations of AM processes

Although AM processes offer many significant advantages but they still suffer from the following limitations.

- **Material limitation:** Machine for an AM process is usually designed for a limited range of materials that have similar properties. Different materials can hardly be processed on an AM machine due to their different reshaping processes. As such, development of material science can largely contribute to the realization of AM technology.
- **Large manufacturing time for large-scale production:** Even though AM is good at making customized products, the technology is positioned in the small-scale production. Preferably, AM processes are frequently used to manufacture complex geometries that are usually unmanageable in traditional ways.
- **Poor manufacturing accuracy:** The layered manufacturing strategy of AM processes ignores the edge shape in a single layer in the spatial direction to fit the real surface curvature. The layered structure on the surface is not ignorable.
- **Post-processing requirements:** Generally, AM processes are not net-shape manufacturing processes but only a core step of the process. The AM manufactured component requires further processing to be a functional product.

1.5.4 Applications of AM processes

AM processes have been advancing technology since the late 1980s and has experienced widespread use in the past decade. The applications of AM processes have already vastly transformed the following industries:

- **Biomedical:** AM processes are revolutionizing the biomedical industry by providing functional prototypes, surgical grade components, and true to life anatomical models. They are also producing advancements in orthopedic implant and dental devices, as well as tools and instrumentation such as seamless medical carts, anatomical models, customized saw and drill guides, and customized surgical tools. Material development in the biomedical industry is critical, with certified biocompatible materials potentially revolutionizing the customized implants and life-saving devices and pre-surgical tools.
- **Aerospace:** The aerospace industry was one of the first to adopt additive manufacturing, as it requires flight-worthy components made from high-performance materials. Common AM applications include environmental control system ducting, customized cosmetic aircraft interior components, rocket engines components and combustor liners. Additive manufacturing helps deliver complex, consolidated parts with enhanced strength and reduced material and weight.

- **Consumer products:** Marketing teams, designers, and graphic artists use AM to form ideas and deliver products to market quickly, simulating the look and feel of the final product. AM has been beneficial for consumer goods such as sporting goods and consumer electronics, providing detailed iterations early in the product development life cycle. As AM technology advances, more consumer products will look to additive manufacturing for larger volume demands.
- **Energy:** Use of AM processes have been successful in the energy sector due to their ability to quickly create tailored components and environmentally friendly materials that can withstand extreme conditions. Key AM applications include control-valve components, pressure gauge pieces, turbine nozzles, rotors, flow meter parts, and pump manifolds. AM also has the potential to create customized parts for use under-water or harsh environments.
- **Transportation:** AM processes have enabled the transportation industry to develop lightweight components that can withstand extreme speeds and heat, while still being lightweight enough to avoid preventable drag. These applications include complex ductwork, resilient prototypes, customized interior features, grilles, and large paneling.

1.6 Organization of the thesis

This thesis is organized into six chapters which explain all the aspects of the present research work:

Chapter 2 describes the previous research work on the use of different metallic materials for the knee implant applications, development of high entropy alloys as knee implant material, manufacturing of knee implant by AM processes, summary of the relevant past works, identified gaps and research objectives, and the methodology used to meet the identified research objectives.

Chapter 3 presents details of preparation of powders to develop metallic materials for knee implants, design and planning of experiments, apparatus for μ -PAAM process, evaluation of different responses such as *in-vitro* biocompatibility, aspect ratio, microstructure, evolution of phases, mechanical characteristics of Co-Cr-Mo-xTi alloys and Ti-Ta-Nb-Mo-Zr HEA, and bio-tribological behavior of Ti-Ta-Nb-Mo-Zr HEA.

Chapter 4 describes results and their analyses of better knee implant materials developed by adding 2%; 4%; and 6% of titanium to Co-Cr-Mo alloy by μ -PAAM process. It covers *in-vitro* biocompatibility assessment using viability of HeLa cells, release of metallic ions in PBS solution of different pH values and for different immersion durations, corrosion behavior study in PBS solution of 7.4 pH at 37⁰C. It also covers

evaluation of aspect ratio, density and porosity, microstructure analysis, formation of phases, inter-diffusion zone analysis, microhardness, tensile and compression tests and their fractography, abrasion resistance, and wear characteristics of the optimized depositions.

Chapter 5 presents results and their analyses on development of equiatomic Ti-Ta-Nb-Mo-Zr HEA for knee implant applications by the μ -PAAM process. This includes study of multi-track-multi-layer depositions of Ti-Ta-Nb-Mo-Zr HEA by means of *in-vitro* biocompatibility evaluation using cell viability, released amounts of ions of the constituents, corrosion behavior, microstructure, phase formation, microhardness, compressive stress-strain relation, sliding wear characteristics, and abrasion resistance. It also describes the results and analysis of dry fretting wear, corrosion, and tribo-corrosion characteristics of μ -PAAM manufactured Ti-Ta-Nb-Mo-Zr HEA with an objective to demonstrate it as a better knee implant material.

Chapter 6 summarizes the outcome of the present research by presenting its significant achievements, concluding remarks from findings on development of Co-Cr-Mo-xTi and equiatomic Ti-Ta-Nb-Mo-Zr HEA, and some identified directions for the future research.

Chapter 2

Review of Past Work and Research Objectives

This chapter describes the previous research work on the use of different metallic materials for the knee implant applications, development of high entropy alloys as knee implant material, manufacturing of knee implant by AM processes, summary of the relevant past works, identified gaps and research objectives, and the methodology used to meet the identified research objectives.

2.1 Metallic Materials for Knee Implant Applications

Knee implants are commonly manufactured from metallic biocompatible materials such as stainless steel (SS 316L), cobalt-based Co-Cr-Mo alloy, and titanium-based Ti-6Al-4V alloy (**Mukherjee et al. 2015; Zahoor et al. 2019**) due to their good biocompatibility, reasonable elastic modulus and compressive strength, wear, and corrosion resistance. Major drawbacks of these materials are lower corrosion resistance, and higher release of metallic ions in the human body necessitating revision surgery, more extended stay in hospital, and increased cost of surgery (**Li and Zheng 2016**). Use of stainless steel has almost been abandoned primarily due to release of its constituent nickel to the human blood which causes allergy and carcinogenicity (**Wang et al. 2016**). Moreover, it has poor resistance to fatigue, corrosion, and wear. Therefore, it has been replaced by Co-Cr-Mo, and Ti-6Al-4V alloys which have better biocompatibility and corrosion resistance. However, some patients with knee implants of Co-Cr-Mo alloy have shown slightly increased levels of cobalt and chromium ions in their blood (**Li et al. 2022**). Limited work is available on use of Co-Cr-Ti and Co-Cr-Mo-Ti alloys for biomedical applications. **Matkovi'c et al. (2006)** developed Co-Cr-Ti alloy by the casting method in which they varied titanium in a range from 4 to 12% for dental applications. **Ghiban et al. (2014)** highlighted the possibility for using Co-Cr-Mo-Ti alloy for dental applications. **Neto et al. (2006)** explored use of Ni-Cr and Co-Cr-Ti alloys for biomedical applications. **Okazaki et al. (2005)** studied osteo-compatibility of the implants manufactured from SS 316L, Co-Cr-Mo, Ti-6Al-4V, and Ti-15Zr-4Nb-4Ta alloys by implanting them into rat femur and tibia for 48 weeks. Their study revealed that bone contact rate of the implant made of Ti alloys was significantly higher as compared to the implants made of SS 316L and Co-Cr-Mo alloys. **Espallargas et al. (2015)** reported that metallic particulates and their byproducts might be associated with cytotoxicity, damage to the deoxyribonucleic acid (DNA), and metal hypersensitive reactions based on *in-vitro* and *in-vivo* studies. Titanium and its alloys are used for making knee implants due to their higher biocompatibility, corrosion resistance, and lower metallic ions release in the human

body. Majority of the knee implants are made of Ti-6Al-4V alloy, but its constituent aluminum results in neurological problems such as Alzheimer disease and vanadium results in cytotoxicity (Fikeni et al. 2019). Internal environment of a human body is physically and chemically different from the outside environments. Therefore, a metallic substance that works well the outside environments may suffer from severe corrosion in the human body. One of primary considerations for selecting metallic materials for knee implants in the human body environment is their strong corrosion resistance. Presence of a passive layer on a metallic implant boosts its corrosion resistance significantly, but passive layers are not entirely inert in the human body. Continuous contact of an oxide layer present on an implant surface with body fluids may result in the undesired biological responses. Increased release of metallic ions may eventually result in failure of a metallic implant. It can change pH value and oxygen level in the human body which disturb behavior of human cells and metabolism (Ruiz and Romanos 2018). Knee implants are unavoidably subjected to fretting wear and tribo-corrosion during their use in the human body (Mu et al. 2021; Afzali et al. 2019). Small amplitude of relative motion occurring between orthopedic implant and human bones leads to phenomenon of *fretting wear*. It releases worn debris to human blood and surrounding tissues and stimulates cell reactions leading to tissue inflammation. It affects bone regeneration and stability of an orthopedic implant and eventually leading to its aseptic loosening (Wang et al. 2019; Oladokun et al. 2015). Degradation of an orthopedic implant in the physiological environment is intensified by synergistic combination of fretting wear and corrosion known as *tribo-corrosion* which is caused by simultaneous presence of an aggressive environment and micromotions. It degrades the implant material and causes release of worn material debris to human body which may cause severe pain, inflammatory response, locking of joints, an irreversible deterioration and ultimate failure of an orthopedic implant (Sivakumar et al. 2018; Fallahnezhad et al. 2022). In many cases, fretting wear is accelerated by corrosion and vice versa. Researchers have mentioned challenges in understanding and prediction of occurrence fretting wear and tribo-corrosion in orthopedic implants (Billi et al. 2010; Amuzuga et al. 2018). Table 2.1 presents mechanical properties of commonly used biocompatible materials for knee implants along with that of human bone (Festas et al. 2019; Kim et al. 2020; Tian et al. 2019).

Table 2.1: Comparison of mechanical properties of the commonly used materials for knee implants with that of human bone.

Material	Mechanical properties				
	Density (gm/cm ³)	Modulus of elasticity (GPa)	Yield strength (MPa)	Strength to weight ratio	Poisson's ratio
Stainless steel 316L	8.00	210	240	30	0.27
Co-Cr-Mo	8.29	225	525	63	0.30
Ti-6Al-4V	4.43	110	900	203	0.34
Human bone	1.1	10-30	50-150	136	0.30
Ultra-high molecular weight polyethylene (UHMWPE)	0.945	0.6-1.8	60	63	0.46

Overall, it is summarized that stainless steel (180-210 GPa), cobalt-based alloys (220-240 GPa), and titanium-based alloys (55-110 GPa) have much higher elastic modulus than the natural human bones (10-30 GPa). Higher elastic modulus of these metallic knee implants materials implies higher stiffness i.e., higher resistance to elastic deformation, which will enable them to endure higher stress. It varies from patient to patient because knee implants are not manufactured patient specific in their mechanical and structural properties. Therefore, a good metallic material for knee implant must have higher biocompatibility and corrosion resistance, low modulus of elasticity which is comparable to that of human bone (to avoid stress shielding effect by proper load distribution between bones and implant material), higher hardness (to resist wear and permanent deformation such as scratch and rubbing particularly when articulation is involved), high yield strength (to resist plastic deformation under load), and fatigue strength (to sustain cyclic loads).

2.2 High Entropy Alloys for Knee Implant Applications

Knee implants require revision surgeries due to the implant deterioration, accidents, and illness of the patient. These procedures are painful to the patients, necessitate stay in the hospital, and monetary expenses (Von Hintze et al. 2021). Additionally, there are substantial complications associated with clinical use of the currently existing biocompatible metallic materials due to the stress-shielding-effect caused by their higher elastic modulus (above 110 GPa) than the human bones (about 10-30 GPa) (Asgharzadeh et al. 2017; Gueye et al. 2020). It leads to aseptic loosening and reabsorption of peri-prosthetic bone (Rahimizadeh et al. 2018). It can be observed that the currently available metallic materials do not satisfy demands of orthopedic implant industry and patients. Therefore, there is a prerequisite to develop new generation of metallic materials for knee implants having better biocompatibility and mechanical properties, lower elastic modulus, and tailor made for patient-specific needs.

Consequently, a unique category of multi-component material known as high entropy alloys (HEAs) have been developed recently. They comprise of five or more metallic elements in approximately equal atomic proportions to stabilize the solid solution phase and to optimize the configuration entropy. HEAs can be effective and promising knee implant materials owing to their excellent wear resistance, biocompatibility, higher hardness and strength, and greater structural stability (**Castro et al. 2021**). Ti-based HEAs having constituents such as Zr, Ta, Mo, and Nb have shown promising results in biomedical applications because of smaller value of their elastic modulus, and non-toxic and non-allergic nature (**Li et al. 2020; Acharya et al. 2019**). Therefore, HEAs such as Ti-Zr-Hf-Nb (**Ye et al. 2018**), Ti-Ta-Hf-Nb-Zr (**Tüten et al. 2019**), and Ti-Ta-Zr-Nb (**Ozan et al. 2020**) have been found suitable for biomedical applications. **Laheurte et al. (2010)** designed β -Ti alloy Ti-29Nb-xTa-5Zr (where, x=13 and 6 Wt. %) and manufactured it by the *vacuum arc melting* process. Their results revealed that elastic modulus decreased from 60 GPa to 43 GPa as Ta content decreased from 13% to 6%. **Raducanu et al. (2011)** developed Ti-10Zr-5Nb-5Ta alloy, with non-toxic elements, by *cold crucible semi-levitation melting* technique for bone substitute. **Zhao et al. (2011)** added higher Zr content to Ti-based alloys to develop implant material having low elastic modulus and reported that such alloys are good choice for removable bone tissue implants due to presence of stable and protective zirconium oxide layer. **Wang and Xu (2017)** developed Ti-Ta-Nb-Mo-Zr HEA for the orthopedic implants by the *casting* process and studied its microstructure evolution and mechanical characteristics. **Mathiou et al. (2018)** developed Ti-Nb-Zr-Mo-Ta by the *vacuum arc melting* process and studied its microstructure and wear behavior and found that it consisted of dendritic structure consisting of body centered cubic (BCC) and hexagonal-closed-packed (HCP) crystal structures and micro-segregation in its inter-dendritic structure. **Popescu et al. (2018)** developed Ti-Zr-Nb-Ta-Fe HEA by the *powder metallurgy* process, studied its microstructure, and mechanical and corrosion characteristics, and found its biocompatibility and mechanical characteristics better. **Motallebzadeh et al. (2018)** performed microstructural, mechanical, and electrochemical characterization of bio-HEA Ti-Zr-Hf-Nb-Ta and Ti_{1.5}-Zr-Ta_{0.5}-Hf_{0.5}-Nb_{0.5} for biomedical applications. They reported that equiatomic bio-HEA Ti-Zr-Hf-Nb-Ta has exceptional biocompatibility and mechanical qualities as compared to Ti-6Al-4V alloy. **Nagase et al. (2018)** used *vacuum arc melting* to synthesize Ti-Zr-Hf-Cr-Mo and Ti-Zr-Hf-Co-Cr-Mo HEA as metallic biomaterials and found their biocompatibility comparable to pure titanium. **Hori et al. (2019)** designed a non-equiatomic Ti-Nb-Ta-Zr-Mo alloy using thermodynamic calculations and a binary phase diagram. They suggested that it may be utilized as a biomaterial. **Yuan et al. (2019)**

performed tests on all elements of Ti-Zr-Hf-Nb-Ta HEA and found that none were allergic. They also studied the microstructure and characteristics of bio-HEA Ti-Zr-Hf-Nb-Ta. **Hua et al. (2021)** developed $Ti_x-Zr-Nb-Ta-Mo$ ($x = 0.5, 1, 1.5, \text{ and } 2$, molar ratio) using arc melting and studied their mechanical, corrosion, and wear characteristics. They reported that $Ti_{0.5}-Zr-Nb-Ta-Mo$ HEA exhibited high strength, hardness, good plasticity, better corrosion, and wear properties than Ti-6Al-4V alloy. **Łukaszczyk et al. (2021)** investigated tribo-corrosion behavior of oxygen hardened Ti-13Nb-13Zr alloy and found that alloy hardened at 700°C has good wear-resistant in a corrosive environment. **Zareidoost and Yousefpour (2021)** studied corrosion behavior and mechanical properties of cast Ti-Zr-Nb-Ta alloys for biomedical applications. Oxidation of an HEA makes it passivating that helps to reduce release of metallic ions in the simulated human body environment which is advantageous for life span of the implants. The *in-vitro* findings of **Okazaki and Gotoh (2005)** and **Kong et al. (2021)** support it. **Okazaki and Gotoh (2005)** investigated the amount of released metallic ions from SS 316L, Co-Cr-Mo alloy, commercially pure Ti, Ti-6Al-4V alloy, Ti-6Al-7Nb alloy, Ti-15Zr-4Nb-4Ta HEA in calf serum, 0.9% NaCl, artificial saliva, phosphate buffer saline (PBS) and fetal bovine serum (FBS) solutions. They concluded that Ti-15Zr-4Nb-4Ta HEA yielded minimum amount of released metallic ions which is an advantageous for life span of the implants. **Kong et al. (2021)** investigated on release of metallic ions from Ti-Nb-Ta-Zr HEA developed by the SLM process in minimal essential medium using immersion duration up to 180 days. Their results revealed that amount of released metallic ions is less than 10 parts per million (ppm) and passive oxide layers formed on Ti-Nb-Ta-Zr HEA was stable after 30 days of immersion duration.

It can be summarized that different HEAs have been developed by the conventional processes namely arc melting, powder metallurgy, and casting. These processes have poor form customizability and also results in increased elemental segregation during solidification of HEAs which results in a heterogeneous distribution of HEA constituents. It adversely affects desirable biocompatibility and mechanical characteristics for the knee implant materials. Researchers have explored use of different AM processes such as SLM process (**Wegener et al. 2021; Ishimoto et al. 2021**), electron-beam-melting (EBM) process (**Tamayo et al. 2021**), laser engineered net shaping (LENS) process (**Narayanan et al. 2022**), and laser-based-powder-bed-fusion (L-PBF) process (**Cabrini et al. 2022**) to minimize the drawbacks of the conventional processes. **Ishimoto et al. (2021)** used SLM process to develop Ti-Ta-Nb-Mo-Zr HEA as biocompatible material and found that it minimized its elemental segregation. The developed HEA showed excellent corrosion

resistance, biocompatibility, strength, and deformability indicating that AM process could minimize HEA element segregation tendency.

2.3 Additive Manufacturing of Knee Implants

Manufacturing process used for knee implants affects their evolved microstructure and attained mechanical and tribological characteristics, surface finish, and surface integrity which affect their life span. Conventional processes such as casting, machining, forging, and forming have been used to manufacture knee implants but these processes gave poor surface quality and mechanical characteristics of the manufactured implants (**Paris et al. 2016; Ingarao and Priarone 2020; Cheng et al. 2020**). Moreover, these processes are inflexible for near net-shape and productive manufacturing of the complex shaped and customized knee implants. Therefore, implant manufacturing industry is looking for a new near net-shape, productive and sustainable manufacturing processes. AM processes such as SLM (**Vrancken et al. 2014**), EBM (**Liu et al. 2017**), LENS (**Shaik et al. 2021**), and L-PBF (**Cabrini et al. 2022**) have shown considerable potential and sparked a lot of expectations in quality manufacturing of knee implants. They offer many advantages such as customization for complex geometries of femoral and tibial components of knee implants without use of expensive tooling, near net-shape manufacturing minimizing post-processing, more material and energy efficiency, and reduced cost (**Kajima et al. 2021; Xiang et al. 2022; Hazlehurst et al. 2013; Davids et al. 2021**). Therefore, they can help in overcoming limitations of conventional processes for implant manufacturing.

Lyons et al. (2021) reviewed various AM and conventional manufacturing process and concluded that parts with more complex geometry such as femoral and tibial components of knee implants are preferred to be manufactured through AM processes than conventional processes due to large amount of wastage of implant material. **Krishna et al. (2007)** used LENS to manufacture porous commercially pure (CP) Ti with low stiffness for load-bearing implant applications. **Xin et al. (2012)** investigated the biological responses of Co-Cr samples made by SLM and casting in artificial saliva solution using a seven-day immersion test. They found that the SLM-built parts showed significantly less release of Co ions and exhibited higher biocompatibility as compared to the cast specimen. **Tan et al. (2015)** studied microstructure and mechanical characteristics of Ti-6Al-4V alloy made by EBM process and found that microhardness, yield strength, and ultimate tensile strength increases, and elongation decreases as deposition height increases due to increase in interspacing of β -Ti phase which primarily occurs due to decrease in cooling rate. **Liu et al. (2016)** investigated impact of porosity variation on mechanical characteristics of β -type Ti2448 alloy manufactured by EBM and SLM processes. They revealed that porous

deposited samples of Ti2448 alloy have higher fatigue strength than Ti-6Al-4V deposited sample. **Surmeneva et al. (2017)** fabricated Ti-6Al-4V lattice scaffolds by EBM and achieved mechanical properties near to that of trabecular bones. **Yan et al. (2018)** fabricated Ti-6Al-4V mandibular prosthesis by EBM process using 3D-model obtained from computerized tomography (CT) scan. They considered important aspects such as porosity and pore size in the geometry of their 3D-model and obtained an optimum geometry using finite element analysis (FEA). **Tang et al. (2018)** manufactured hip stents, ankle implants, and cervical and sacral cages from Ti-6Al-4V alloy by the selective EBM process and successfully implanted them to some patients. An ankle implant used in a patient was found to have an adequate functioning after two years of surgery. **Li et al. (2020)** used SLM process and aging heat treatment to study their influence on tribological characteristics of Co-Cr-Mo alloys. Their results revealed that scratch resistance decreased due to homogenized recrystallization and ϵ -phase formation at high temperature (1150°C).

Oliveira et al. (2022) discussed importance of micro-AM process such as micro-wire and arc additive manufacturing (μ -WAAM) by exploring the size limits of arc-based additive manufacturing. They fabricated single wall using a wire diameter of 250 μm with higher deposition rate. But μ -AM process using powder, wire and combined forms of deposition material is not reported. Therefore, **Jhavar et al. (2014a)** developed μ -plasma arc additive manufacturing (μ -PAAM) process using deposition material in wire form. **Sawant and Jain (2018a)** and **Kumar and Jain (2020)** added capability to use deposition material in powder and combined powder and wire form in this process. The μ -PAAM process uses maximum direct current (DC) up to 20 A (whereas plasma-based AM process uses current from 250 to 300 A), maximum DC power up to 440 W, and gives deposition rate from 10 to 50 g/min (beam-based and arc-based AM processes give deposition rate 2-10 g/min and 50-300 g/min. It offers advantages such as concentrated heat source which gives high energy density, arc stability even at low current, smaller heat affected zone and thermal distortion, homogeneous defect-free deposition having dense structure, low dilution, and ability to achieve deposition layer thickness less than 1 mm (**Jhavar et al. 2014a and 2014b**). These characteristics enable μ -PAAM process to fill the existing wide gaps between capabilities of beam-based and arc-based AM processes thus making it suitable for meso-scale AM applications. **Sawant and Jain (2017)** studied the deposition and wear characteristics of single-layer and multi-layer depositions of Stellite 6 powder made by μ -PAAM process on AISI 4130 substrate and they (**2018b**) compared Stellite6 coatings made by μ -PAAM process with those made by laser-beam based AM and plasma arc AM processes in terms of deposition quality and cost-effectiveness. They concluded that

the μ -PAAM process is a cost-effective, energy-efficient, material efficient, and environment-friendly process for meso-scale AM applications. Hence, μ -PAAM process seems to have great potential for material development and manufacturing of knee implants. Consequently, it was selected for the experimental investigations in the present work.

2.4 Summary of the Past Works

Following conclusions can be drawn from the review of the relevant past work described in the previous sections:

- Stainless steel, Co-Cr-Mo alloys and Ti-6Al-4V alloy have major drawbacks such as occurrence of *stress shielding effect* (caused due to significant difference in their modulus of elasticity and human bones), lower cell viability and corrosion resistance, and release of metallic ions and their byproducts to human body. They lead to cytotoxicity, damage to the DNA, metallic hypersensitive reactions, and neurological problems such as Alzheimer disease.
- Addition of titanium will have a favorable alloying impact on Co-Cr-Mo alloy to develop better knee implant material because it offers excellent biocompatibility, low elastic modulus (which will minimize the stress shielding effect), high corrosion resistance, near bio-inert response in the human body environment, high specific strength [due to low density of Ti (i.e., 4.5 g/cm³) which is almost half of density of Co-Cr-Mo alloy (i.e., 8.29 g/cm³)], and better capacity to join with the surrounding bones and tissues (**Geetha et al. 2009**). Addition of Ti to Co-Cr alloys has also been found to reduce release of metallic ions (**Kassapidou et al. 2020; Hjalmarsson et al. 2011**).
- Development of Ti-Ta-Nb-Mo-Zr HEA by additive manufacturing process will offer advantages such as excellent biocompatibility, near bio-inert response in the human body, and excellent corrosion resistance because elements such as Ti, Ta, Nb, Mo, and Zr are non-toxic and non-allergic nature in human body environment, smaller value of elastic modulus, high strength and hardness, excellent wear resistance and corrosion resistance (**Acharya et al. 2019; Li et al. 2020; Hua et al. 2021**).
- AM processes such as SLM, EBM, and LENS have shown promising potential to manufacture good quality knee implants, but they suffer from higher thermal distortion, heat affected zone, higher dilution, low deposition material utilization, poor energy conversion efficiency, and higher costs of equipment, energy consumption, operation, and maintenance (**Vrancken et al. 2014; Liu et al. 2017; Ingarao and Priarone 2020; Cheng et al. 2020; Shaik et al. 2021; Cabrini et al. 2022**).
- The μ -PAAM process is a cost-effective, energy-efficient, material efficient, and environment-friendly process because it uses maximum value of DC current up to 20 A

(as against plasma-based AM process which use current $\sim 250\text{-}300$ A), maximum DC power up to 440 W, gives 10-50 g/min deposition rate, and fills the wide existing gaps between capabilities of beam-based and arc-based AM processes making it suitable for meso-scale AM applications.

2.5 Identified Research Gaps

Following research gaps are identified based upon review of the relevant past work on development of metallic materials for knee implant:

- No work has been reported on development of Co-Cr-Mo-xTi alloys by μ -PAAM process as better knee implants and its study of microstructure, *in-vitro* biocompatibility evaluation and mechanical characteristics.
- No work has been reported on development of Ti-Ta-Nb-Mo-Zr HEA by μ -PAAM process as better knee implants and its study of microstructure, *in-vitro* biocompatibility evaluation and mechanical characteristics.

2.6 Research Objectives

Following research objectives were identified based on the existing research gaps:

- Alloying 2/4/6 wt.% of titanium to Co-Cr-Mo alloy by μ -PAAM process and studying its effects on *in-vitro* biocompatibility, microstructure, and mechanical properties of the resultant alloys so as to explore them as better metallic materials for the knee implant applications.
- Development of equiatomic Ti-Ta-Nb-Mo-Zr high entropy alloy by μ -PAAM process and study its *in-vitro* biocompatibility, microstructure, mechanical properties, and bio-tribological characteristics with an objective to assess it as a better metallic material for the knee implant applications.

2.7 Research Methodology

Table 2.2 presents the research methodology used in the present work to achieve the identified research objectives giving details of different stages of experimentation, constant and variable parameters used in them, and different characterization methods used to study the different responses.

The *next chapter* presents details of preparation of the powders to develop metallic materials for the knee implant applications, design and planning of experiments, apparatus for μ -PAAM process, evaluation of *in-vitro* biocompatibility, aspect ratio, microstructure, evolution of phases, mechanical properties of Co-Cr-Mo-xTi alloys and Ti-Ta-Nb-Mo-Zr HEA, and bio-tribological characteristics of Ti-Ta-Nb-Mo-Zr HEA.

Table 2.2: Identified research objectives (RO) for the present work and the methodology used to meet them.

RO-1: Alloying 2/4/6 wt. of Ti to Co-Cr-Mo alloy by μ-PAAM process for the knee implant applications: Pilot, and main experiments manufacturing <i>single-track-single-layer depositions</i> of Co-Cr-Mo-xTi alloys. Identification of optimum combinations of Co-Cr-Mo-xT alloys by studying density, porosity, microstructure, and formation of phases, in-vitro biocompatibility assessment, and mechanical characteristics.			
Stage of experimentation	Pilot experiments [No. of experiments: 30, DOE: One-factor-at-a-time]: To identify optimum values/ranges of μ -PAAM process parameters for good and continuous deposition of Co-Cr-Mo-2Ti alloy using one-factor-at-a-time approach.	Main experiments [No. of experiments: 27, DOE: Full factorial]: To identify optimum values of the 3 variable parameters using criteria of uniform and continuous deposition, and lower aspect ratio (i.e., ratio of deposition width to deposition height)	
Input parameters and responses for single-track single-layer depositions	Variable input parameters: μ -plasma power: 120-440 W; Mass flow rate of deposition material powder: 0.7-5.0 (g/min); Deposition head travel speed: 30-200 (mm/min); Flow rate of μ -plasma forming gas: 0.1-0.5 Normal litre per minute (NI/min); Flow rate of shielding gas: 2-9 (NI/min); Stand-off distance (SOD): 3-15 mm Responses: Visual examination for continuous deposition	Variable input parameters: μ -plasma power: 264; 275; 286 W; Mass flow rate of deposition material powder: 2.0; 2.5; 3.0 g/min; Deposition head travel speed: 45; 50; 55 mm/min Constant input parameters: Flow rate of μ -plasma forming gas: 0.25 NI/min; Flow rate of shielding gas: 3.6 NI/min; SOD: 9 mm Responses: Measurement of aspect ratio and visual examination for uniform and continuous deposition	
Input parameters for multi-track multi-layer depositions of Co-Cr-Mo-xTi alloys: The main experiments identified optimum values of 264 W for μ -plasma power, 2.5 g/min for mass flow rate of deposition material powder, and 50 mm/min for deposition head travel speed. This parametric combination was used to manufacture 150 mm long <i>multi-track-multi-layer</i> deposition of prepared powders of Co-Cr-Mo-2Ti, Co-Cr-Mo-4Ti, and Co-Cr-Mo-6Ti alloys on Co-Cr-Mo base plate by μ -PAAM process.			
Responses and characterization of multi-track-multi-layer deposition	<ul style="list-style-type: none"> Analysis of microstructure and evolution of phases, elemental and phase mapping 	<ul style="list-style-type: none"> In-vitro biocompatibility assessment: Cell viability using MTT Assay, Metallic ion release, Corrosion behaviour in PBS 	<ul style="list-style-type: none"> Mechanical characteristics: Microhardness, Tensile and compressive properties; Wear characteristics Finite element simulation of tibial tray
RO-2: Development of Ti-Ta-Nb-Mo-Zr HEA for the knee implant applications through pilot, and main experiments manufacturing <i>single-track-single-layer depositions</i> of Ti-Ta-Nb-Mo-Zr HEA. Study of <i>multi-track-multi-layer depositions</i> of Ti-Ta-Nb-Mo-Zr HEA by studying microstructure, formation of phases, in-vitro biocompatibility assessment, and mechanical characteristics.			
Stage of experimentation	Pilot experiments [No. of experiments: 30, DOE: One-factor-at-a-time]: To identify optimum values/ranges of μ -PAAM process parameters for uniform and continuous deposition of Ti-Ta-Nb-Mo-Zr HEA using one-factor-at-a-time approach.	Main experiments [No. of experiments: 27, DOE: Full Factorial]: To identify optimum values of 3 variable parameters for using criteria of uniform and continuous deposition, and lower aspect ratio	
Input parameters	Variable input parameters: μ -plasma power: 150-440 W; Mass flow rate of deposition material powder: 0.8-5.0 (g/min); Deposition head travel speed: 30-150 (mm/min); Flow rate of μ -plasma forming gas: 0.1-0.5 (NI/min); Flow rate of shielding gas: 3-9 (NI/min); SOD: 3-10 mm Responses: Visual examination for continuous deposition	Variable input parameters: μ -plasma power: 396; 407; 418 W; Mass flow rate of deposition material powder: 1.7; 2.2; 2.7 g/min; Deposition head travel speed: 47; 53; 59 mm/min Constant input parameters: Flow rate of μ -plasma forming gas: 0.3 NI/min; Flow rate of shielding gas: 5 NI/min; SOD: 9 mm Responses: Measurements of aspect ratio and visual examination for uniform and continuous deposition	
Responses and characterization of multi-track-multi-layer deposition	<ul style="list-style-type: none"> Analysis of microstructure and evolution of phases, elemental and phase mapping 	<ul style="list-style-type: none"> In-vitro biocompatibility assessment: Cell viability using MTT Assay, Metallic ion release, Corrosion behaviour in SBF 	<ul style="list-style-type: none"> Mechanical characteristics: Microhardness, Compressive properties; Wear characteristics
Input parameters for multi-track multi-layer depositions of Ti-Ta-Nb-Mo-Zr HEA: Main experiments identified optimum values of μ -plasma power: 418 W; mass flow rate of deposition material powder: 1.7 g/min; deposition head travel speed: 53 mm/min. This parametric combination was used to manufacture an 80 mm long <i>multi-track-multi-layer depositions</i> of Ti-Ta-Nb-Mo-Zr HEA			
RO-3: Bio-tribological characteristics of Ti-Ta-Nb-Mo-Zr HEA in human body emulating biofluids	Characterization:		
	<ul style="list-style-type: none"> ❖ Dry fretting wear characteristics: Applied load: 10; 20; 30 N, number of cycles: 2.7×10^4; Total relative slip displacement: 13.5 m ❖ Corrosion behavior: physiological saline (PS), phosphate buffered saline (PBS) solution, and 1% fetal bovine serum (FBS) mixed with the PBS solution (FPBS) pH value: 7.4 at $37 \pm 1^\circ\text{C}$, ❖ Tribo-corrosion behavior: applied load: 10 N, number of cycles: 4.5×10^4; biofluids: PS, PBS, and FPBS, pH value: 7.4 at $37 \pm 1^\circ\text{C}$ 		

Chapter 3

Experimentation

This chapter presents details of preparation of powders to develop metallic materials for knee implants, design and planning of experiments, apparatus for μ -PAAM process, evaluation of different responses such as *in-vitro* biocompatibility, aspect ratio, microstructure, evolution of phases, mechanical characteristics of Co-Cr-Mo-xTi alloys and Ti-Ta-Nb-Mo-Zr HEA, and bio-tribological behavior of Ti-Ta-Nb-Mo-Zr HEA. It also describes finite element analysis of tibial tray of Co-Cr-Mo-xTi alloys.

3.1 Materials

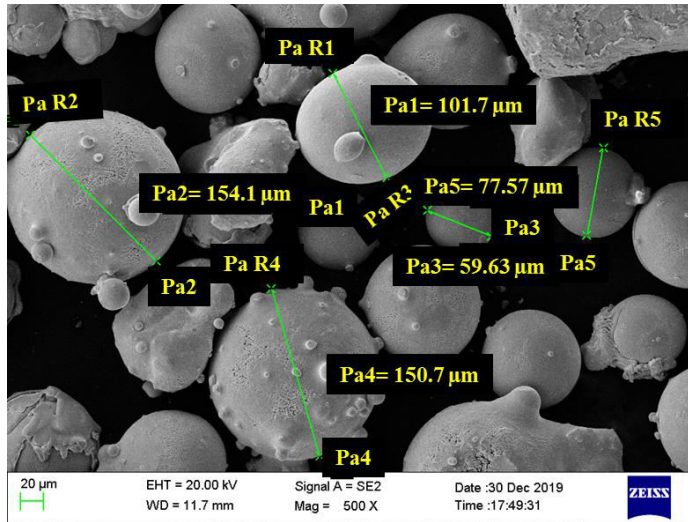
This section describes details of preparation of powders to develop Co-Cr-Mo-xTi alloys and Ti-Ta-Nb-Mo-Zr HEA, their chemical composition, distribution of powder particle size, and powder morphology.

3.1.1 Preparation of Powders for Co-Cr-Mo-xTi Alloys

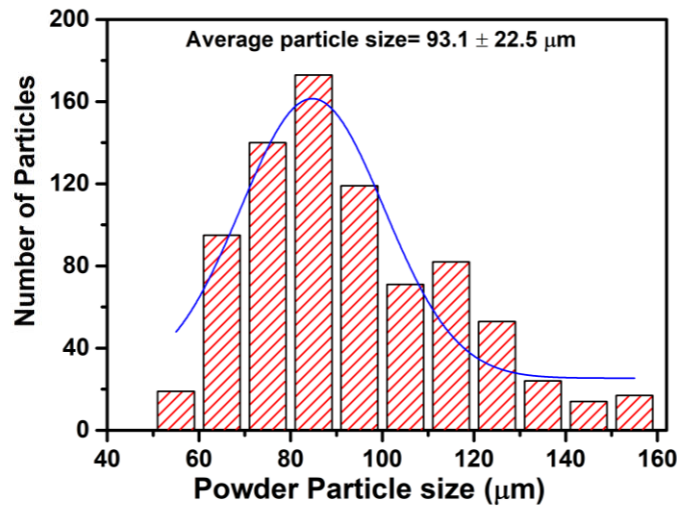
Table 3.1 presents chemical compositions of the Co-Cr-Mo-xTi alloys to be developed for knee implant applications by adding 2; 4; and 6 wt.% of titanium powder to Co-Cr-Mo alloy without changing wt.% of Cr and Mo. It also presents composition of the base plate of Co-Cr-Mo alloy on which the Co-Cr-Mo-xTi alloys to be developed by the μ -PAAM process. The base plate was ground by a surface grinder and cleaned using acetone before making any deposition on it. Powder of each Co-Cr-Mo-2/4/6Ti alloy was prepared by mixing the desired % (as mentioned in Table 3.1) of procured powders of Co, Cr, Mo, and Ti (from Sigma Aldrich with 99.9% purity and having particle size in a range from 60 to 160 μ m) in the tungsten carbide vials of a planetary ball milling machine (*Pulverisette 6* from *Fritsch, Germany*). The mixing was carried out for 20 hours at 250 rpm using tungsten carbide balls of 15 mm diameter and maintaining ball to powder ratio as 10:1. The mixed powders of Co-Cr-Mo-xTi alloys were de-moisturized for 2 hours in the oven at 80 $^{\circ}$ C and were vacuum sealed before their single-layer and multi-layer depositions. Figure 3.1a presents scanning electron microscopy (SEM) image (taken by *JEOL-JSM 7610F Plus*, Japan) of Co-Cr-Mo-2Ti alloy powder depicting its morphology and size of its particles. Figure 3.1b presents statistical distribution for the size of powder particles by a bar diagram and Gaussian curve. Figure 3.1a shows that the particle size ranges from 59 to 154 μ m whereas Fig. 3.1b reveals that mean particle size is 93.1 μ m with 22.5 μ m standard deviation.

Table 3.1: Chemical compositions of base plate and Co-Cr-Mo-2/4/6Ti alloys.

Type	Alloy type	Wt.% of constituents									
		Cr	Mo	Ti	Ni	Fe	W	Mn	Si	C	Co
Base plate	Co-Cr-Mo	28.5	1.0	0	2.0	2.0	4.6	1.02	1.09	1.2	Bal.
Co-Cr-Mo-2/4/6Ti alloys	Co-Cr-Mo-2Ti	29	4	2	0.5	0.75	0	1	0	0.35	Bal.
	Co-Cr-Mo-4Ti	29	4	4	0.5	0.75	0	1	0	0.35	Bal.
	Co-Cr-Mo-6Ti	29	4	6	0.5	0.75	0	1	0	0.35	Bal.



(a)



(b)

Fig. 3.1: (a) Morphology of powder particles of Co-Cr-Mo-2Ti alloy, (b) static distribution of size of powder particles.

Figures 3.2a-3.2b present EDS spectrum used for chemical composition analysis of Co-Cr-Mo-4Ti alloy before ball milling (Fig. 3.2a) and after ball milling (Fig. 3.2b). Table 3.2 present the chemical composition of Co-Cr-Mo-4Ti alloy powder before and after ball milling. It can be observed from table 3.2 that the oxygen was present as trace amount before and after ball milling i.e., $< 0.01 \pm 0.005$ wt.% and $< 0.03 \pm 0.02$ wt.% respectively.

Tungsten was present in an amount of 0.52 ± 0.36 wt.% after the ball milling. It is possibly due to mixing of the powders in tungsten carbide vials of the ball milling machine.

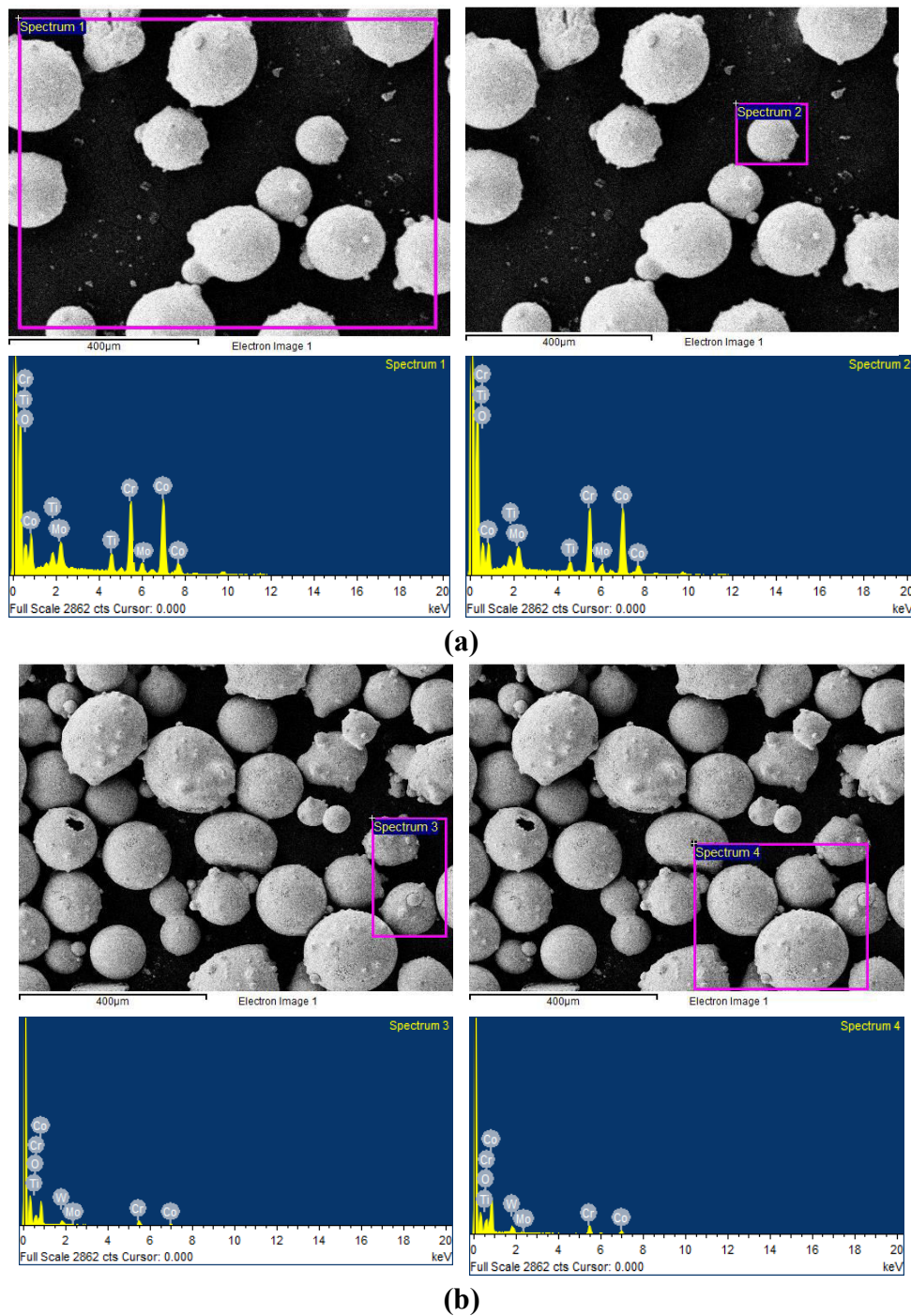


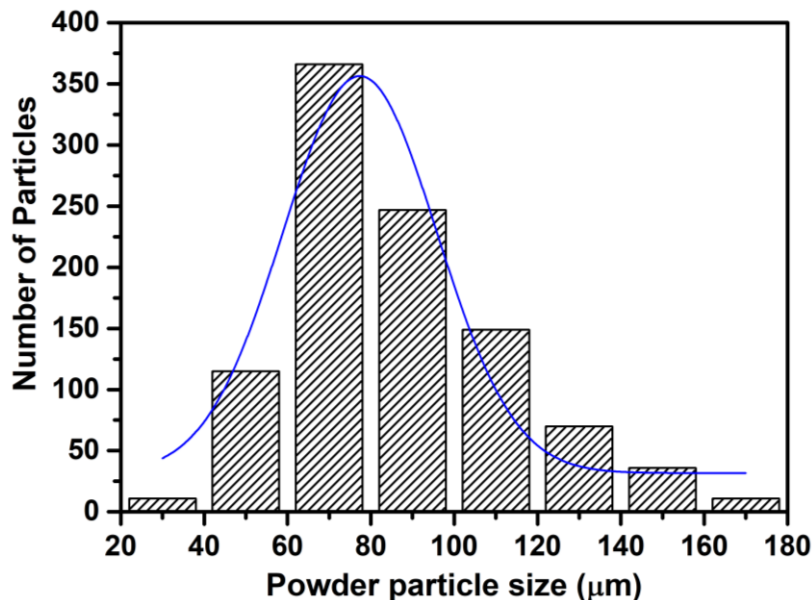
Fig. 3.2: EDS obtained spectrum of the powder particles of Co-Cr-Mo-4Ti alloy: (a) before ball milling, and (b) after ball milling.

Table 3.2: Chemical compositions of powder particles of Co-Cr-Mo-4Ti alloy obtained from its EDS spectrum.

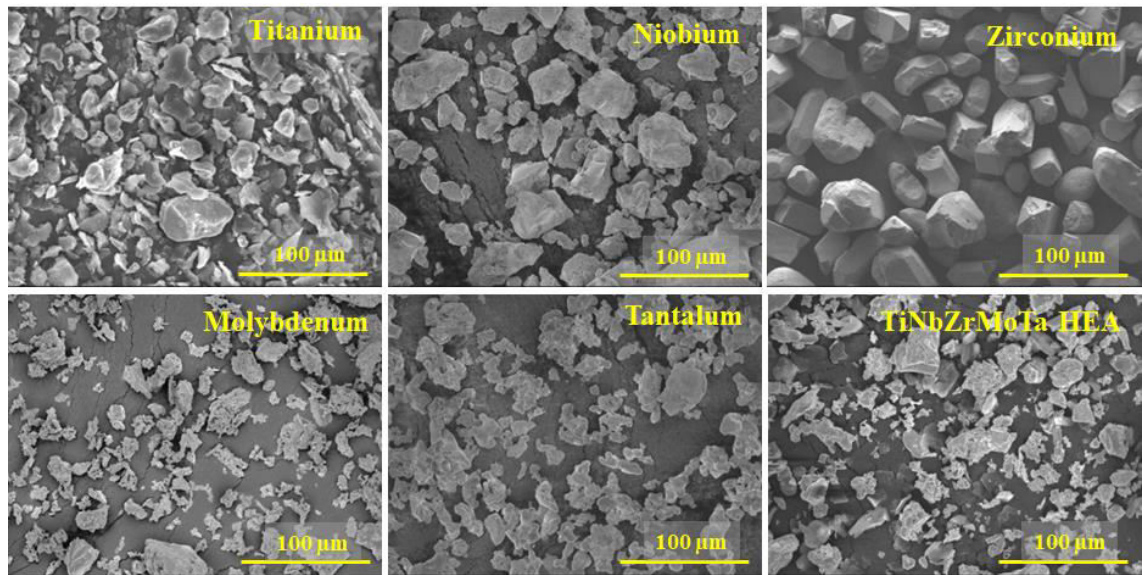
Condition	Co	Cr	Mo	Ti	O	W
Before ball milling	62.9 ± 0.07	29.03 ± 0.05	4.05 ± 0.03	4.01 ± 0.03	0.02 ± 0.01	-
After ball milling	62.6 ± 0.35	29.02 ± 0.07	4.05 ± 0.07	4.02 ± 0.05	0.03 ± 0.02	0.52 ± 0.36

3.1.2 Preparation of Powders for Ti-Ta-Nb-Mo-Zr High Entropy Alloy

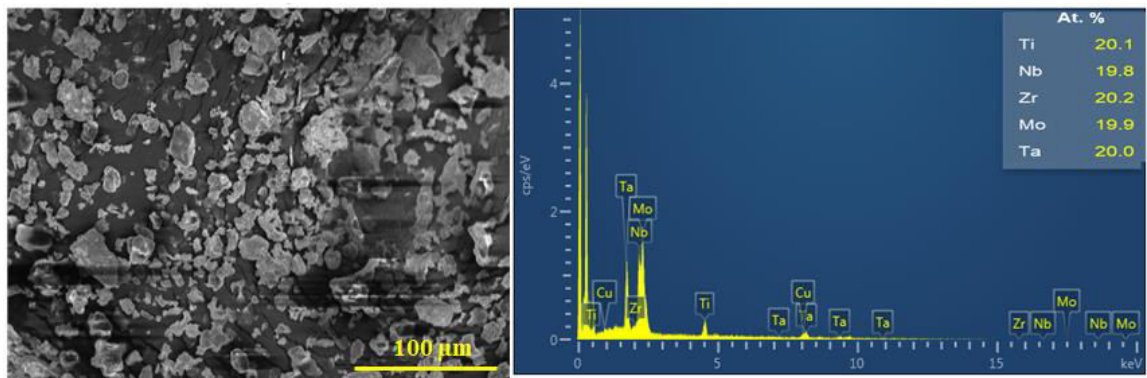
Powder of Ti-Ta-Nb-Mo-Zr HEA was prepared by mechanically mixing the as-received powders of Ti, Nb, Zr, Mo, and Ta (*Loba Chemie Pvt. Ltd.* from Bengaluru, India having randomly oriented particles having size of $67.5 \pm 37.5 \mu\text{m}$) in a planetary ball milling for 10 hours at 250 rpm in tungsten carbide vials using balls of 10 mm diameter and ball-to-powder ratio of 10:1. The prepared powder of Ti-Ta-Nb-Mo-Zr HEA was de-moisturized for 2 hours in the oven at 80°C and was vacuum sealed before for its single-layer and multi-layer depositions. The oxygen content was not found in the as-received powders and the alloyed powders prepared using ball milling. Whereas, argon was used as shielding gas to protect the molten pool from outside environment during the deposition by μ -PAAM process. Figures 3.3a-3.3d present analysis of the prepared powder of Ti-Ta-Nb-Mo-Zr HEA showing its particle size distribution (Fig. 3.3a), SEM images depicting morphology of it and its constituents (Fig. 3.3b), its energy dispersive spectroscopy (EDS) showing at.% of its constituents (Fig. 3.3c), and EDS mapping of it and its constituents (Fig. 3.3d). It can be seen from Fig. 3.2 that (i) size distribution of Ti-Ta-Nb-Mo-Zr HEA powder particles is gaussian with most of particles having their size in a range from 50 to $110 \mu\text{m}$ (Fig. 3.3a), (ii) the powder particles are randomly oriented (Fig. 3.3b), (iii) at.% of Nb and Mo is slightly lower than their desired values; at.% of Ti and Zr is slightly higher than their desired values; and at.% of Ta is the desired one (Figs. 3.3c and 3.3d). The prepared powder of Ti-Ta-Nb-Mo-Zr HEA was used to manufacture its single-track single-layer depositions and subsequently multi-track multi-layer depositions by the μ -PAAM process on a base plate of Ti-6Al-4V alloy. Prior to Ti-Ta-Nb-Mo-Zr HEA deposition, the base plate was ground, washed with acetone, and then washed with the distilled water.



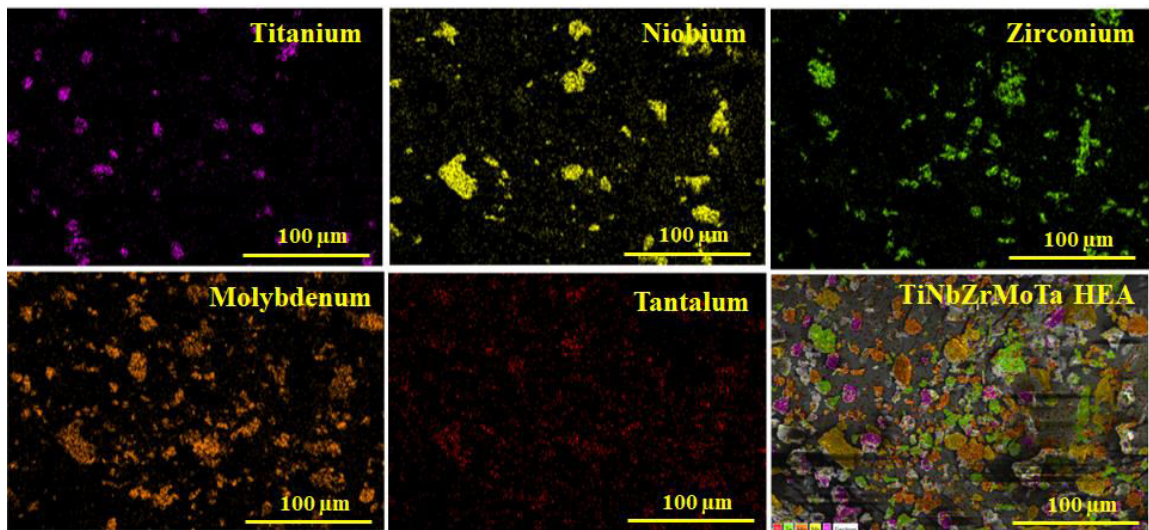
(a)



(b)



(c)



(d)

Fig. 3.3: Analysis of the prepared powder of Ti-Ta-Nb-Mo-Zr HEA: (a) size distribution of its particles, (b) SEM images showing morphology of it and its constituents, (c) at. % of its constituents by EDS, and (d) EDS mapping of it and its constituents.

3.2 Apparatus for μ -PAAM Process

Figure 3.4 presents working principle of micro-plasma arc additive manufacturing (μ -PAAM) process in which a direct current (DC) power supply of 440 watt is used to supply a low DC current in the range of 0.1 to 20 A to ionize the plasma forming gas to generate μ -plasma arc inside the nozzle and between non-consumable tungsten electrode and the base plate. The generated μ -plasma arc is used as a heat source to melt the incoming feedstock material and to fuse it with the base plate or previously deposited layer. It is forced through a fine hole in the nozzle which constricts it resulting in its stability even at low current, higher energy density, less heat affected zone, thermal distortion and dilution. The μ -PAAM process uses a coaxially fed inert gas (i.e., argon) to shield the molten deposition from the surrounding environment. Since the electrode is inside the nozzle, feedstock material refrains to encounter it enabling this process to use deposition or feedstock material in powder, wire and combined powder-wire form.

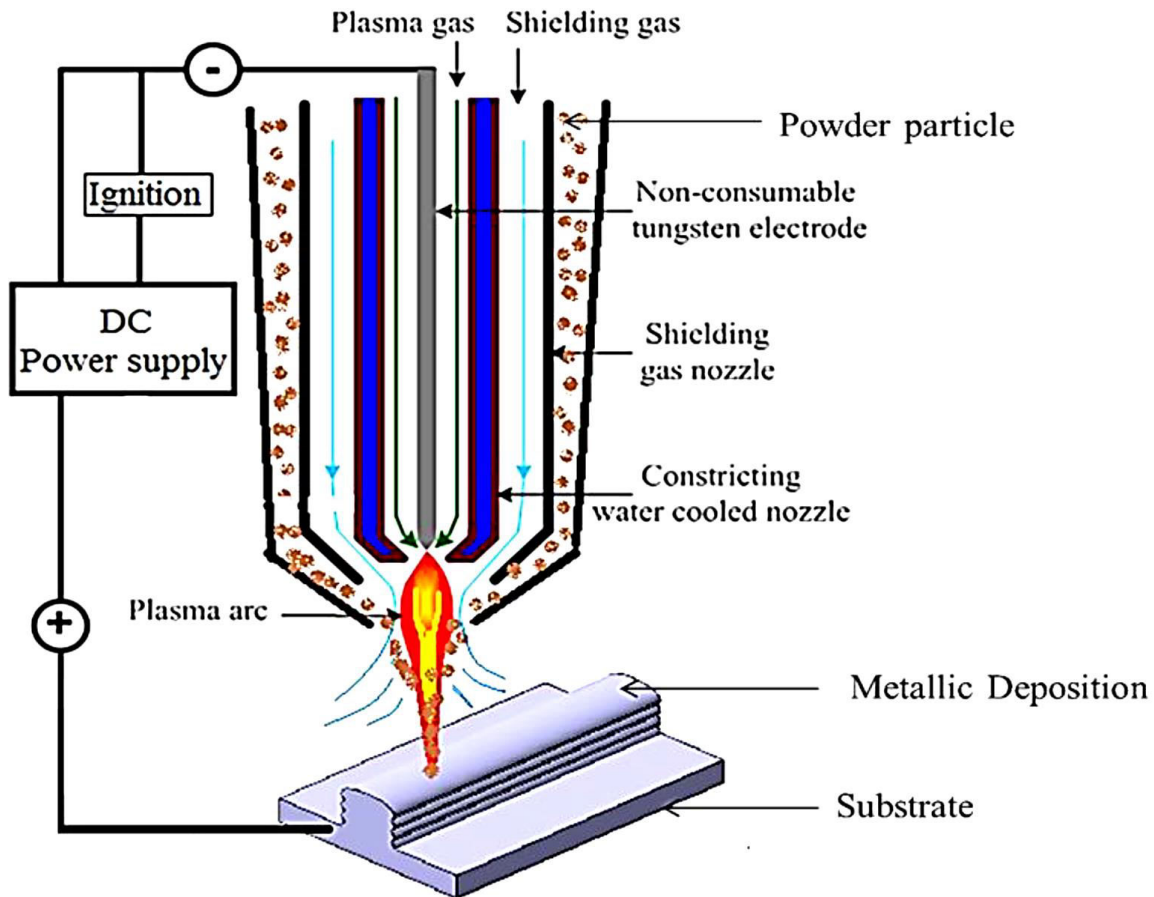


Fig. 3.4: Working principle of μ -PAAM process.

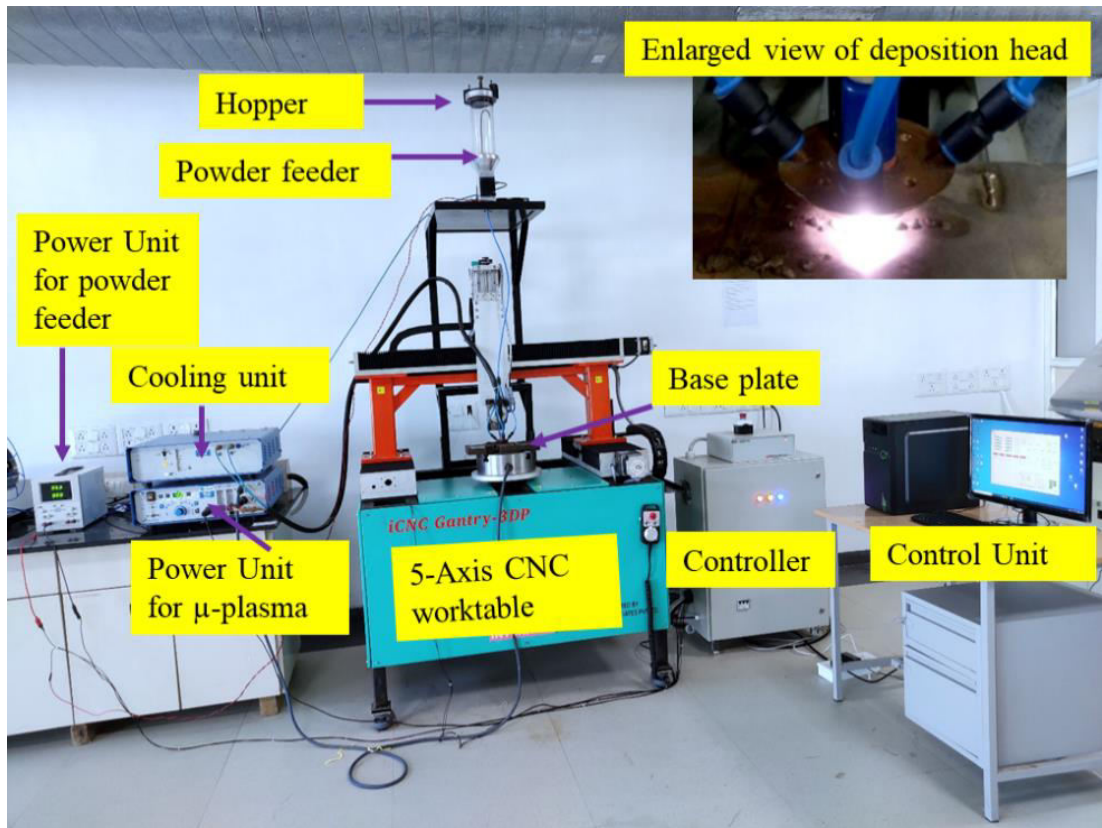


Fig. 3.5: Photograph of 5-axis CNC machine developed for μ -plasma arc additive manufacturing (μ -PAAM) process.

Figure 3.5 shows photograph of the developed 5 axis computer numerical controlled (CNC) machine for μ -PAAM process. It was developed by integrating following five units: (i) 5-axis CNC worktable for mounting the base plate. Its controller is programmed in G and M codes through a dedicated computer, (ii) 440 W power supply unit (*Dual Arc 82* from *Elderfield & Hall Inc. USA*) with option of operating either in continuous or pulsed mode and with capacity of supplying DC current up to 20 A with an increment of 0.1 A for formation of μ -plasma arc. It also has a cooling unit, (iii) feeding system to supply powder of feedstock material to the deposition head at the required flow rate. It has hopper, powder feeder, and DC power unit to supply power to the powder feeding system, (iv) system to supply plasma forming gas and melt pool shielding gas (both argon) to the deposition head, and (v) indigenously developed deposition head consisting of μ -plasma torch at its centre, and 4 nozzles inclined at 60° to vertical axis and placed circumferentially at equal intervals (enlarged view shown in Fig. 3.5) to supply feedstock material powder to base plate.

3.3 Design and Planning of Experiments

Experiments were planned, designed and conducted in two different phases namely pilot experiments and main experiments to identify optimum process parameters of μ -PAAM process by manufacturing single-track single-layer depositions of Co-Cr-Mo-2Ti powder on Co-Cr-Mo alloy base plate (having 120 mm length; 120 mm width and 50 mm thickness)

and equiatomic Ti-Ta-Nb-Mo-Zr HEA powder on Ti-6Al-4V alloy base plate (having 160; 120; and 30 mm length, width and thickness respectively) in both the phases of experiments. Table 3.3 presents ranges and values of μ -PAAM process parameters, and approach for design of experiments used in different phases of experiments whose details are described in the following paragraphs.

Table 3.3: Values of μ -PAAM process parameters, and design of experiments approach used in different phases of experiments.

Parameter	Unit	Values/Ranges used for pilot experiments	Values used for main experiments
Number of experiments	-	30	27
Approach for design of experiments	-	One-factor-at-a-time	Full factorial
μ-PAAM process parameters for Co-Cr-Mo-xTi alloys			
μ -plasma power	W	120-440	264; 275; 286
Mass flow rate of feedstock material powder	g/min	0.7-5.0	2.0; 2.5; 3.0
Deposition head travel speed	mm/min	30-200	45; 50; 55
Flow rate of μ -plasma forming gas	NI/min	0.1-0.5	0.3
Flow rate of shielding gas	NI/min	2-9	4
Stand-off distance	mm	3-15	9
μ-PAAM process parameters for Ti-Ta-Nb-Mo-Zr HEA			
μ -plasma power	W	150-440	396; 407; 418
Mass flow rate of feedstock material powder	g/min	0.8-5.0	1.7; 2.2; 2.7
Deposition head travel speed	mm/min	30-150	47; 53; 59
Flow rate of μ -plasma forming gas	NI/min	0.1-0.5	0.3
Flow rate of shielding gas	NI/min	3-9	5
Stand-off distance	mm	3-10	9

- Pilot experiments for Co-Cr-Mo-xTi alloys:** Primary objective of pilot experiments was to identify optimum values/ranges of six important parameters of μ -PAAM process for the main experiments using criterion of continuous deposition (through visual examination) by varying them in their following ranges: (a) μ -plasma power: 120-440 W; (b) mass flow rate of feedstock material powder: 0.7-5.0 (g/min); (c) deposition head travel speed: 30-200 (mm/min); (d) flow rate of μ -plasma forming gas: 0.1-0.5 Normal liter per minute (NI/min); (e) flow rate of shielding gas: 2-9 (NI/min); and (f) stand-off distance (SOD): 3-15 mm. Pilot experiments were conducted using one-factor-at-a-time (OFAT) experimental design approach in which one parameter was varied in its considered range and other parameters were kept constant at minimum values of their respective ranges. It was found that 0.3 NI/min is the minimum required flow rate of μ -plasma forming gas to produce μ -plasma arc and transmit it to the base plate. Its higher

values caused melt pool to expand leaving a dimple-like imprint on top surface of a deposition. Flow rate of shielding gas 4 Nl/min was found to protect molten pool from the contamination from the atmospheric air. Its greater values caused melt pool to expand leaving a dimple-like imprint on top surface of deposition. It was observed that 9 mm of SOD was adequate to assure supply of powdered material to center of the melt pool. Its values less than or more than 9 mm resulted in wastage of the deposition material. It was found that minimum μ -plasma power of 264 W was required to melt Co-Cr-Mo-2Ti powder hence 264; 275; and 286 W were chosen as values for the main experiments. Mass flow rate of feedstock material powder more than 2 g/min allowed smooth powder feeding and continuous deposition of Co-Cr-Mo-2Ti powder but its value greater than 3 g/min resulted in non-uniform and partially melted deposition. Therefore, values of 2.0; 2.5; and 3.0 g/min were selected for the main experiments. Discontinuous depositions were formed when deposition head travel speed exceeded 55 mm/min whereas its value less than 45 mm/min resulted in a larger heat affected zone. Consequently, 45; 50; and 55 mm/min were chosen for the main experiments. Summarily, the pilot experiments identified 0.3 Nl/min as flow rate of μ -plasma forming gas; 4.0 Nl/min as flow rate of shielding gas; and 9 mm as SOD as their optimum values, and 264; 275; and 286 W for μ -plasma power, 2.0; 2.5; and 3.0 g/min for feedstock material powder mass flow rate, and 45; 50; and 55 mm/min for deposition head travel speed as their optimum ranges for conducting 27 main experiments.

- **Main experiments for Co-Cr-Mo-xTi alloys:** Twenty-seven full factorial main experiments were conducted by manufacturing single-track single-layer depositions (each having 50 mm length) of Co-Cr-Mo-2Ti alloy powder on Co-Cr-Mo alloy base plate to identify optimum values of μ -plasma power, feedstock material powder mass flow rate, and deposition head travel speed for further experimentation using criteria of good quality continuous deposition and lower aspect ratio (i.e., ratio of deposition width to deposition height). These experiments identified optimum values of 264 W for μ -plasma power, 2.5 g/min for mass flow rate of feedstock material powder, and 50 mm/min for deposition head travel speed for manufacturing multi-track multi-layer depositions of Co-Cr-Mo-2Ti alloy.
- **Pilot experiments for Ti-Ta-Nb-Mo-Zr HEA:** The one-variable-at-a-time experimental design approach was used for the pilot experiments, in which one parameter was varied within its considered ranges while other parameters were maintained constant at minimal values of their respective ranges. Their prime goal was to find out optimum values/ranges of six variables of μ -PAAM process for the main

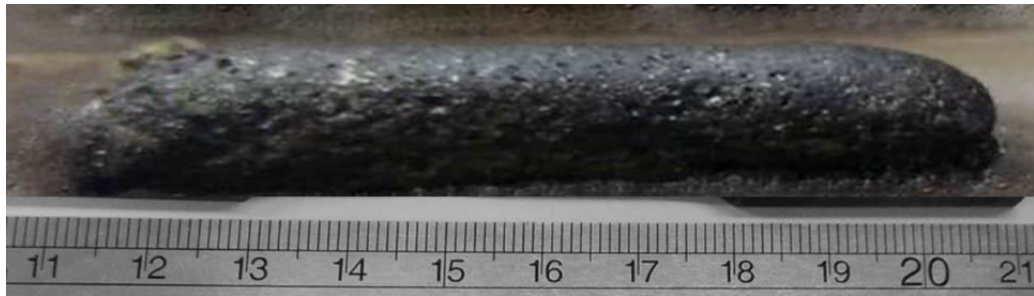
experiments using the criterion of uniform and continuous deposition (determined through visual inspection) by changing them in their the following ranges: (a) μ -plasma-power: 150-440 W; (b) mass flow rate of feedstock material powder: 0.8-5.0 (g/min); and (c) deposition head travel speed: 30-150 (mm/min); (d) flow rate of μ -plasma forming gas: 0.1-0.5 (NI/min); (e) flow rate of shielding gas: 3-9 (NI/min); and (f) SOD: 3-10 mm. Outcome of these experiments are: (i) minimum μ -plasma-power of 396 W was essential to melt Ti-Ta-Nb-Mo-Zr HEA powder hence 396; 407; and 418 W were selected for the main experiments, (ii) mass flow rate of feedstock material powder over 1.7 g/min produced continuous deposition of Ti-Ta-Nb-Mo-Zr HEA powder and its value beyond 2.7 g/min caused non-uniform and partially melted deposition. Therefore, values of 1.7; 2.2; and 2.7 g/min were selected for the main experiments, (iii) Discontinuous depositions were formed when the deposition head travel speed exceeded 59 mm/min while its value less than 47 mm/min resulted in a larger heat-affected-zone. Consequently, 47; 53; and 59 mm/min were chosen for main experiments, (iv) 9 mm of SOD is found as adequate to supply feedstock material to the center of the melt pool. Its values less than or more than 9 mm resulted in wastage of the deposition-material, (v) 0.3 NI/min is the minimum required flow rate of μ -plasma forming gas to form μ -plasma arc and transmit it to the base plate. Its higher values caused the melt pool to expand leaving a dimple-like impression on top surface of a deposition, and (vi) flow rate of shielding gas 5 NI/min was found to protect the molten pool from atmospheric air contamination. Its greater value caused the melt pool to expand leaving a dimple-like mark on a deposition top surface.

- **Main experiments for Ti-Ta-Nb-Mo-Zr HEA:** Twenty-seven full factorial main experiments were performed to produce single-track single-layer depositions of Ti-Ta-Nb-Mo-Zr HEA powder on Ti-6Al-4V alloy base plate by varying μ -plasma power (at 396; 407; and 418 W), mass flow rate of feedstock material powder (at 1.7; 2.2; and 2.7 g/min), and deposition head travel speed (at 47; 53; and 59 mm/min) at three levels each. These experiments identified optimum values of 418 W for μ -plasma-power, 1.7 g/min for mass flow rate of feedstock material powder, and 53 mm/min for deposition head travel speed to manufacture multi-track multi-layer depositions of Ti-Ta-Nb-Mo-Zr HEA powder using criteria of good quality of continuous deposition having lower aspect ratio.

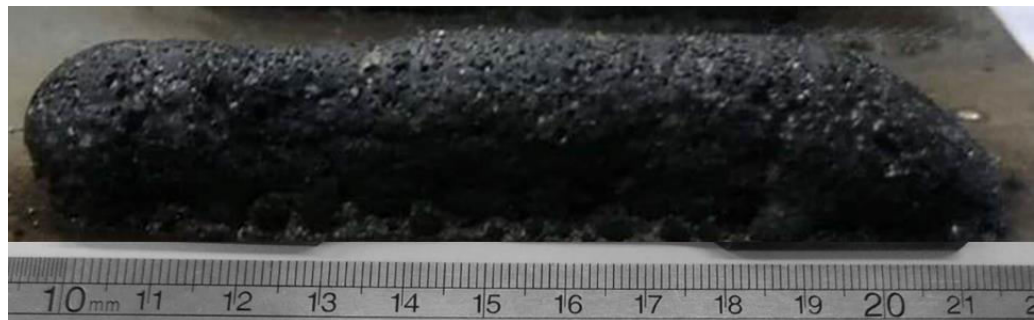
3.3.1 Multi-layer Depositions of Co-Cr-Mo-xTi Alloys

The identified optimum values of μ -plasma power (264 W), mass flow rate of feedstock material powder (2.5 g/min), and deposition head travel speed (50 mm/min) from the main

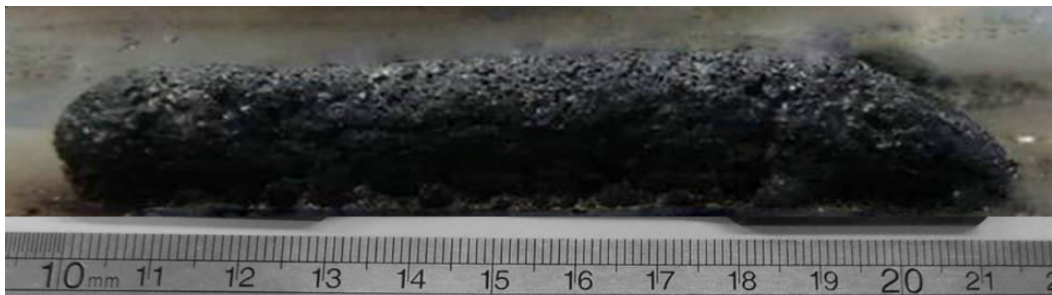
experiments were used to make 100 mm long single-track multi-layer depositions (consisting of 10 layers) and 150 mm long multi-track multi-layer depositions (consisting of 15 layers and 8 tracks) of the prepared powders of Co-Cr-Mo-2Ti, Co-Cr-Mo-4Ti, and Co-Cr-Mo-6Ti alloys on Co-Cr-Mo base plate by μ -PAAM process. Figure 3.6 depicts the photographs of the single-track multi-layer deposited samples of Co-Cr-Mo-2Ti alloy (Fig. 3.6a), Co-Cr-Mo-4Ti alloy (Fig. 3.6b), and Co-Cr-Mo-6Ti alloy (Fig. 3.6c). They are referred to as the optimized depositions in the subsequent text. Bulk density, relative density, porosity, microstructure, evolution of phases, and microhardness were studied for these samples. Aspect ratio was studied for single-track single-layer deposition samples. Whereas *in-vitro* biocompatibility in terms of cell viability, metallic ion release and corrosion behavior, tensile and compression properties and their fractography, wear characteristics, and abrasion resistance were studied for the samples of optimized multi-track multi-layer depositions of Co-Cr-Mo-2Ti, Co-Cr-Mo-4Ti, and Co-Cr-Mo-6Ti alloys.



(a)



(b)

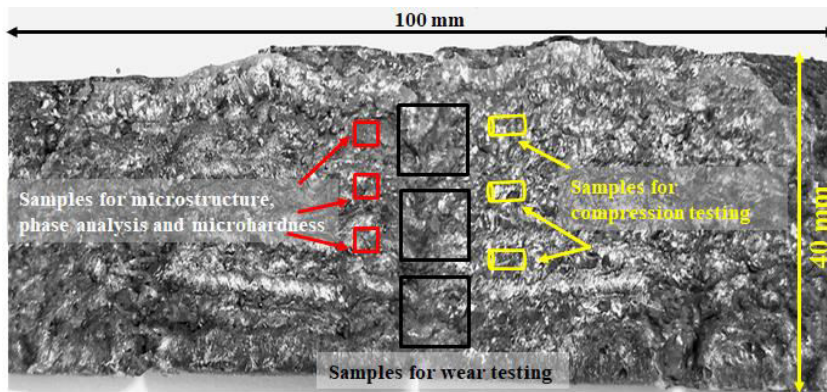


(c)

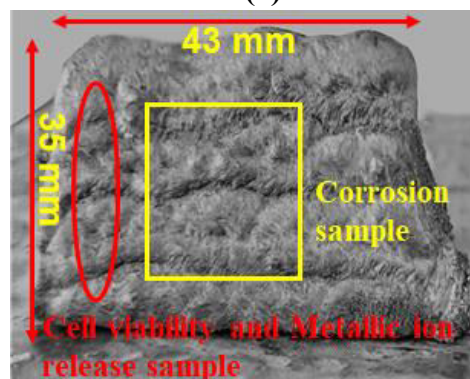
Fig. 3.6: Photographs of the optimized single-track multi-layer depositions of: (a) Co-Cr-Mo-2Ti alloy, (b) Co-Cr-Mo-4Ti alloy, and (c) Co-Cr-Mo-6Ti alloy.

3.3.2 Multi-layer Depositions of Ti-Ta-Nb-Mo-Zr HEA

The optimum values of μ -plasma-power (418 W), mass flow rate of feedstock material powder (1.7 g/min), and deposition head travel speed (53 mm/min) identified from the main experiments were used to manufacture two multi-track multi-layer depositions (each consisting of 20 deposition layers, 10 deposition tracks, and their lengths were 100 mm and 43 mm) of Ti-Ta-Nb-Mo-Zr HEA powder on Ti-6Al-4V alloy base plate by the μ -PAAM process using 0.3 mm overlap between the two consecutive deposition tracks. The measured height of each deposition layer and measured width of each deposition track are found as 2 ± 0.3 mm and 1.5 ± 0.6 mm respectively thus giving approximately 40 mm as total deposition height, and 12 mm total deposition width. Figure 3.7a and 3.7b depict the photographs of the manufactured multi-track multi-layer depositions of Ti-Ta-Nb-Mo-Zr HEA. These figures also show locations from where the samples have been cut to study their microstructure, formation of phases and microhardness (shown in red color in Fig. 3.7a) wear characteristics (shown in black color in Fig. 3.7a), *in-vitro* biocompatibility using cell viability and release of metallic ions (shown in red color in Fig. 3.7b) and corrosion behavior (shown in yellow color in Fig. 3.7b), and compression test (shown in yellow color in Fig. 3.7a). Aspect ratio was studied on the samples from single-track single-layer depositions.



(a)



(b)

Fig. 3.7: Multi-track multi-layer deposition of Ti-Ta-Nb-Mo-Zr powder on the Ti-6Al-4V base plate by μ -PAAM process.

3.4 Measurement of Responses for Co-Cr-Mo-xTi Alloys

Following sections describe procedure used to study *in-vitro* biocompatibility, bulk density, relative density, porosity, aspect ratio, microstructure, evolution of phases, microhardness, tensile and compression properties and their fractography, wear characteristics, and abrasion resistance of Co-Cr-Mo-2Ti, Co-Cr-Mo-4Ti, and Co-Cr-Mo-6Ti alloys along with the details of corresponding sample preparation.

3.4.1 *In-vitro* Biocompatibility Assessment

Biocompatibility of any new developed material for implants is generally evaluated *in-vitro* then *in-vivo* to ensure its biological safety before its clinical use. MTT assay [standard 3-(4, 5-dimethylthiazol-2-yl)-2, 5-diphenyltetrazolium bromide] is pretended to be the gold standard for *in-vitro* evaluation of cell viability of a newly developed material for orthopedic implants due to its easier implementation in cell culture growth in suspension and rapidity in evaluation (Delgado-Ruiz and Romanos 2018; Priyadarshini et al. 2019; Reiner et al. 2020). In the present work, *in-vitro* biocompatibility was evaluated by means of cytotoxicity assessment, metallic ion release, and corrosion behavior analysis of the developed materials for knee implants

3.4.1.1 Cytotoxicity Assessment

Three cylindrical samples of 3 mm diameter and 6 mm length were cut from each optimized depositions of Co-Cr-Mo-2Ti; Co-Cr-Mo-4Ti; and Co-Cr-Mo-6Ti alloys (i.e., total 9 samples were cut) by the wire spark erosion machining (WSEM) machine (EcoCut model from Electronica India Ltd.) *in-vitro* assessment of cytotoxicity and metallic ions release. The cut 9 samples were cleaned in an ultrasonic cleaner and then dried. Pretreatment was given to these samples by the sterilization method in which they were immersed in 70% alcohol for 12 hours and then dried after removing them. Then the samples were exposed to UV light for 3 hours.

Subsequently, they were incubated in 2 ml cell culture in Dulbecco's Modified Eagle Medium (DMEM) for the time durations of 24; 48; and 72 hours (i.e., 1st sample from Co-Cr-Mo-xTi alloy was incubated for 24 hr; 2nd sample for 48 hr; and 3rd sample was incubated for 72 hr) at 37°C for their cytotoxicity assessment in the presence of Henrietta Lacks (HeLa) cell (procured from *National Centre for Cell Science Pune, India*). Each sample after its incubation duration was removed from the media and such prepared media (i.e., total 9 media corresponding to 9 samples of the optimized depositions) were used for *in-vitro* cytotoxicity assessment of the corresponding sample by the MTT assay. For this, HeLa cells were cultured and maintained in DMEM media supplemented with 10% fetal bovine serum (FBS) and 100 units/ml penicillin-streptomycin (pen-strep) and incubated at

37°C with 5% CO₂ in an incubator. Then the HeLa cells were trypsinized and were seeded in 96 well plates with seeding density of approximately 10,000 cells per well. The seeded cells after 24 hours were observed under the microscope and the HeLa Cell media was removed. Then the HeLa cells were treated in triplicate with 16.6; 33.3; 66.6; and 106.6 µl concentration of the prepared media for each sample of an optimized deposition (i.e., HeLa cells were treated thrice in the prepared media of an optimized deposition sample for its each concentration and average value was used in the analysis) and were incubated for time duration 24; 48; and 72 hours. After each treatment, the corresponding media was aspirated from its well and the well plate was washed with the phosphate buffer saline (PBS) solution of 1X concentration. Subsequently 0.5 mg/ml fresh MTT was added to the well plates containing the HeLa cells and incubated them for 4 hours followed by their aspiration. The insoluble formazan crystals produced by the viable cells were dissolved in 200 µl dimethyl sulfoxide (DMSO). Absorbance of the dissolved solution was measured by a microplate reader (BioTek SynergyH1 from *Agilent, USA*) at the wavelength of 570 nm. Untreated HeLa cells were used as control and the relative cell viability of an optimized deposition sample was estimated using Eq. 3.1.

$$\text{Cell viability (\%)} = \frac{\text{Absorbance of the treated cells}}{\text{Absorbance of the control cells}} \times 100 \quad (3.1)$$

Bright field micrographs of HeLa cell were captured using an inverted microscope (Eclipse Ti-U from *Nikon*) for the control cells and for 106.6 µl concentration of the media of each optimized deposition sample after 72 hours of incubation duration.

3.4.1.2 Assessment of Release of Metallic Ions

Some researchers have investigated the metallic ions release of different metallic implants materials such as SS316L, Co-Cr-Mo, and Ti-6Al-4V in various body fluids by changing pH value from 2 to 8 because continuous interaction of implant material with the body fluids (whose pH value is 7.4) changes its pH value (**Espallargas et al. 2015; Ruiz and Romanos 2018; Fikeni et al. 2019**). Amount of release of metallic ions varies with different types of corrosion (e.g., corrosion caused by cells concentration, galvanic corrosion, tension, and pitting corrosion). Chemical composition of corrosive solution, artificial saliva, cell culture medium, and serum also significantly impact the composition of the released metallic ions (**Espallargas et al. 2015**). Therefore, released amounts of metallic ions from optimized deposition samples (same as used in in-vitro cell viability evaluation) were assessed *in-vitro* in the PBS solution (its composition was 9 g per liter NaCl; 7.4 g per liter K₂HPO₄; and 1 g per liter KH₂PO₄) by varying its pH values at 4; 5.5; and 7.5 and varying immersion duration as 1; 3; and 7 weeks. The PBS solution of the desired pH value

was prepared by adding HCl for an acidic solution (i.e., pH < 7.0) or NaOH for alkaline solution (i.e., pH > 7.0). After the standard metallographic preparation and ultrasonic cleaning, the optimized depositions samples were kept in a centrifuge glass tube with 5 ml PBS solution at 37°C in 5% CO₂ incubator. Concentration of the released ions from the optimized depositions was measured after one, three and seven weeks using the inductively coupled plasma-atomic emission spectrophotometer (IC-PAES) which performs elemental analysis with high sensitivity using argon plasma as ionization source. It can concurrently determine concentrations of most of elements of the Periodic table. Mean quantities of various elements released from the optimized depositions of Co-Cr-Mo-xTi alloys were measured on the basis of parts per billion (ppb) with a detection limit of 6 ppb.

3.4.1.3 Assessment of Corrosion Behavior

One sample (having dimensions of 20 mm × 20 mm × 5 mm as shown in Fig. 3.8) from cross-section of each optimized deposition was cut by the WSEM machine. All 3 samples were polished with 1500 grit SiC emery paper and cleaned using ultrasonic cleaner prior to their corrosion behavior study following the ASTM G1-90 standard. Corrosion behavior of the prepared samples was studied on an Electrochemical Workstation (*CH instrument 604E* from *CH Instruments, Inc. USA*). It has a cell consisting of three electrodes i.e., saturated calomel electrode (SCE) as a reference electrode, platinum foil as a counter electrode, and test sample as the working electrode. The test was performed in 7.4 pH value PBS solution in the thermostatic bath maintaining temperature at 37±1⁰C. Surface area of 1 cm² of each prepared sample was exposed in the PBS solution for 1 hour to achieve steady condition of open-circuit potential (OCP) which is defined as the potential of working electrode relative to the reference electrode when no voltage is applied to the Electrochemical Workstation. Stabilized OCP was used to define range of potential for Tafel polarization curve using 0.1 mV/s scanning rate in the potential range from -0.8 to 0.6 volts. Tafel polarization curve gives essential information about corrosion behavior and corrosion rate in the solution prepared using the standard procedure. Corrosion current density '*i_{corr}*' (μA/cm²) was computed using Tafel extrapolation method maintaining maximum possible linearity. It is used to determine corrosion rate '*p_t*' (mm/year) using standard equation i.e., $p_t = 22.85 i_{corr}$ (**Shi et al. 2010**). Corrosion rate '*p_c*' was also computed from Eq. 3.2 using weight loss of a corroded sample '*W_m*' as per ASTM G31-72 standard (**ASTM International 2012**):

$$p_c = \frac{K}{\rho} \frac{W_m}{A_i T_e} \left(\frac{mm}{year} \right) \quad (3.2)$$

where, '*K*' is a constant for dimensional consistency (= 8.76×10⁴); '*W_m*' is weight loss of a corroded sample (g); '*A_i*' is exposed area of the sample (cm²); '*T_e*' is exposure time for

corrosion (hours); and ' ρ ' is density of the sample material (g/cm^3). Corroded surfaces of the optimized deposition samples were inspected using an SEM and its chemical compositions measured using EDS. Values of ' p_t ' and ' p_c ' were compared. To support the results of corrosion rate of Co-Cr-Mo-xTi alloys, oxidative mass loss/gain using thermogravimetric analysis (TGA) was conducted for its multi-layer multi-track deposition samples. Three square samples of dimension 3 mm and 0.25 mm thickness of each optimized depositions were cut by WSEM machine. Each cut sample was hand polished by SiC emery papers up to 2000 grit size followed by ultrasonic cleaning. The TGA analysis was performed on TGA equipment (model: METTLER TOLEDO TGA/DSC 1 STARe System) in the nitrogen environment over the temperature range from room temperature to 800°C with a heating rate of 5°C per minute.

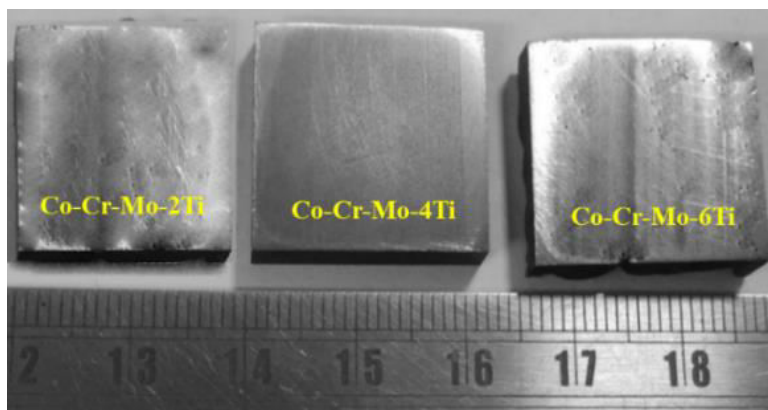


Fig. 3.8: Prepared samples of the optimized depositions Co-Cr-Mo-xTi alloys to study their corrosion behavior.

3.4.2 Aspect Ratio

Samples of 27 single-track single-layer depositions of main experiments were prepared by cutting each deposition at its center by the WSEM machine. The cut samples were hot mounted in a polymeric resin, ground, and polished up to 1500 grit size silicon carbide emery papers. Width and height of the prepared sample of each deposition were measured using the stereo zoom microscope (*EZ4 HD* from *Leica*) and aspect ratio was computed by dividing width to height of the respective deposition.

3.4.3 Evaluation of Bulk Density, Relative Density, and Porosity

Five cylindrical samples each having 3 mm diameter and 6 mm length were cut from each optimized deposition of Co-Cr-Mo-xTi alloy by WSEM machine for measurement of their bulk and relative density, and porosity. These samples were cleaned in an ultrasonic cleaner and then dried. Bulk density of each sample ' ρ_b ' was determined measuring its mass on a microbalance system (*CX-265* from *Citizen* having an accuracy of 0.01 mg), computing its volume (i.e., 42.4 mm^3), and computing ratio of its mass to volume. Relative density of

each optimized deposition sample was determined as per the ASTM B311-13 standard using Archimedes buoyancy principle (i.e., ‘an object partially or wholly immersed in a fluid medium is buoyed up by a force which is equal to the weight of the fluid displaced’) (Yuan et al. 2019). It implies that volume of displaced fluid by an object is equal to the immersed volume of it which assists in measuring the volume of an object and hence its relative density. Therefore, weight of each sample was measured in air and then in water using the microbalance system. Relative density ‘ ρ_r ’ was calculated using Eq. 3.3.

$$\text{Relative density } (\rho_r) = \left(\frac{M_a}{M_a - M_w} \right) \times \rho_w \quad (3.3)$$

where, ‘ M_a ’ and ‘ M_w ’ are average masses of a sample measured in air and in water respectively, and ‘ ρ_w ’ is density of water (1.0 g/cm³). Porosity was estimated from measurement of relative density of a sample using Eq. 3.4:

$$\text{Porosity} = \left(1 - \frac{\rho_r}{\rho_b} \right) \times 100\% \quad (3.4)$$

Measurements were taken over five samples of each optimized deposition for computation of bulk density, relative density, and porosity and their average values have been used for the analysis.

3.4.4 Microstructure, Formation of Phases, and Microhardness

Samples from the optimized depositions of Co-Cr-Mo-xTi alloy were prepared by transversely cutting them by the WSEM machine to study their microstructure, formation of phases and microhardness. The cut samples were hot mounted in a polymeric resin, ground, and polished up to 2000 grade using silicon carbide emery paper. Then cloth polishing was done with diamond pastes with the fineness of 6, 3, and 1 μm respectively. Polished samples were kept at 50⁰C temperature for 300s in the freshly prepared etchant solution consisting of 50 ml of HCl, 5 mm of HNO₃, and 50 ml of H₂O. Microstructure of the prepared sample of each optimized deposition was obtained by field-emission SEM (*supra 25* from *Carl Zeiss*). Their chemical composition was determined using the energy dispersive spectroscopy (EDS). Their inter-diffusion zones were studied by electron backscattered diffraction (EBSD) images obtained by SEM (*NovaNano SEM 450*) using 20 kV accelerating voltage, 1⁰ minimum tolerance angle, and 0.5 μm step size for orientation imaging microscopic (OIM) analysis. Samples for EBSD were prepared by electropolishing the cloth polished samples of the optimized depositions in 8:2 volumetric ratio mixture of methanol and perchloric acid at 20 volts DC voltage and 238K temperature. Since EBSD alone cannot distinguish between the phases having similar crystal structure therefore chi-scan (chemical indexing) was used (Rogal et al. 2020). Formation of phased in an optimized deposition sample was analyzed by x-ray diffraction (XRD) (*D₂-Phaser* from

Bruker, USA) using 40 kV voltage, 30 mA current, 2Θ range of 10-100° with 0.02 step size, 1s dwell time, and $CuK\alpha$ radiation ($\lambda = 1.5418 \text{ \AA}$). Different phases present in an optimized deposition sample and their crystal structures were identified by matching the characteristic peaks present in their XRD with the Joint Committee on Powder Diffraction Standards (JCPDS) database.

Microhardness of the optimized deposition samples were measured on Vickers's microhardness measuring machine (*VMH 002V* from *Walter UHL Germany*) applying 300 g load on each sample for 15 seconds duration as per ASTM E92-82 standard. Total fifteen measurements were taken at different locations with 0.1 mm interval from the top surface of each optimized deposition sample to obtain its microhardness profile.

3.4.5 Evaluation of Wear Characteristics

Three samples (each having 15 mm length, 15 mm width, and 4 mm thickness) were cut from each optimized deposition by the WSEM machine as per ASTM G133 standard to evaluate the wear characteristics. Wear test was performed on a linear reciprocating wear testing machine (*CM9104* from *Ducom, USA*) under dry condition at room temperature by sliding 6 mm diameter tungsten carbide ball (950 HV hardness) for 6 mm distance with 15 Hz frequency for 15 minutes time duration under 15 N normal load. Wear test for each optimized deposition was repeated thrice (i.e., for each prepared sample from optimized deposition of Co-Cr-Mo-xTi alloy). Wear volume was calculated by taking difference in the mass of a sample before and after its wear test on the microbalance and then dividing by the relative density of the sample. Specific wear rate (mm^3/Nm) was calculated by Eq. 3.5.

$$v_s = \frac{V}{F_N s} \left(\frac{\text{mm}^3}{\text{Nm}} \right) \quad (3.5)$$

where ' V ' is the material volume loss during the sliding wear (mm^3); ' F_N ' is the applied load (N), and ' s ' is total sliding distance (m).

3.4.6 Tensile Testing and Fractography

Three rectangular samples (to ensure repeatability) were cut by the WSEM machine from each multi-track multi-layer deposition of Co-Cr-Mo-2Ti, Co-Cr-Mo-4Ti, and Co-Cr-Mo-6Ti alloys along their deposition length. Each sample has length of 100 mm; 25 mm gauge length; 6 mm gauge width; and 3 mm thickness as shown in Fig. 3.9a as per ASTM E8 standard to ensure same elongation before failure in the tensile testing. Schematic view of cut samples from the multi-layer depositions is shown in Fig. 3.9b. Then these samples were ground and fine polished. Figure 3.9c depicts photographs of the prepared samples for the tensile testing. Tensile tests were carried out at room temperature using 0.001/s strain rate on the tensile testing machine (*H50KL, Tinius Olsen from USA*) to evaluate yield

strength, ultimate tensile strength, strain, and modulus of elasticity of the prepared samples. One fractured sample of each alloy was selected to study its tensile fractography using the SEM.

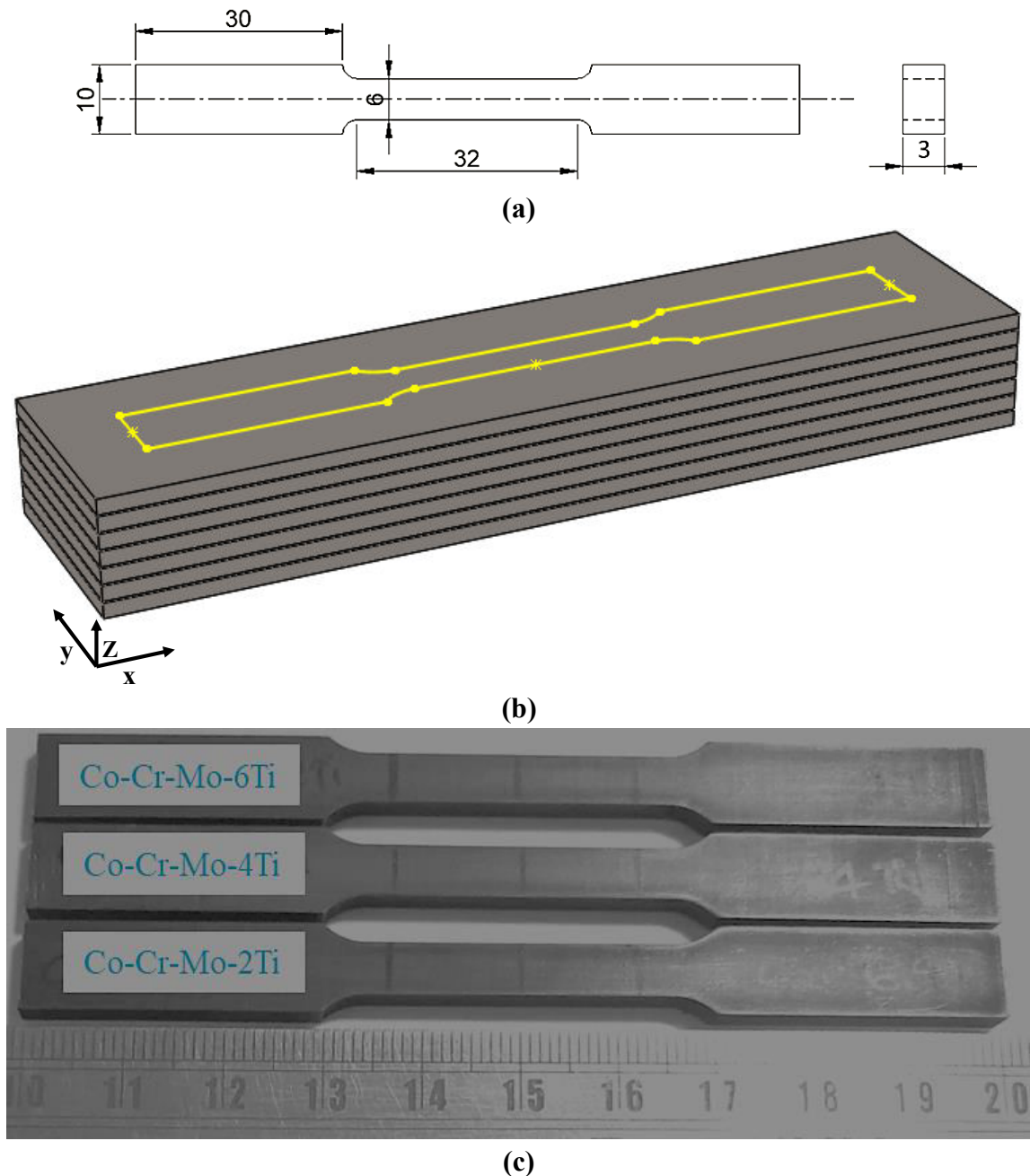


Fig. 3.9: Sample preparation for tensile testing and fractography: (a) dimensions as per ASTM E8 standard (b) schematic view of cut sample from the multi-track multi-layer deposition of Co-Cr-Mo-xTi alloy, and (c) photographs.

3.4.7 Compression Testing and Fractography

Three cylindrical samples (to ensure repeatability) were cut by the WSEM machine from each multi-track multi-layer deposition of Co-Cr-Mo-2Ti, Co-Cr-Mo-4Ti, and Co-Cr-Mo-6Ti alloys along their deposition length. Each cylindrical sample has 4 mm diameter and 8 mm length to maintain length to diameter ratio as 2 as per ASTM E9 standard to

ensure same increase in cross-section area before failure in the compression testing. These samples were ground and fine polished. Compression tests were performed at room temperature using 0.001/s strain rate on the precision universal testing machine (*AGX-V series*, Shimadzu from Japan) to evaluate compressive yield strength, ultimate compressive strength, compressive strain, and modulus of elasticity of the prepared samples. One fractured sample of each alloy was selected to study its compressive fractography using the SEM.

3.4.8 Abrasion Resistance

Primary reason for loosening of knee implants is the friction generated between knee implant components by rubbing action against each other and destruction of natural bones due to wear of the implants. Scratch test is based on hardness measurement that assesses abrasion resistance of a material to its permanent or plastic deformation. It is measured using the scratches made by a diamond stylus on the surface of the developed implant material along a linear route at a continuous normal force and speed (**Ben-Nissan et al. 2015**). Scratch test was conducted on the samples of the optimized deposition prepared for microstructure examination to determine their abrasion resistance in terms of scratch hardness number ' H_{sn} ', and mean value of coefficient of friction. It was conducted on the scratch testing machine (*TR-101* from *Ducom Instruments, India*) by sliding the conical shaped diamond stylus (having apex angle of 120° and $200\ \mu\text{m}$ tip radius) for 7 mm sliding distance with 20 mm/s sliding speed under normal load ' P ' of 10 N with as per ASTM G171-03 standard. Each optimized deposition sample was tested thrice using identical conditions to ensure repeatability of results. Average width of scratch track ' w ' was measured using an optical microscope (*DM2500M* from *Leica*) and scratch hardness number was computed using Eq. (3.6) as per ASTM standard G171-03.

$$H_{sn} = \frac{8P}{\pi w^2} \text{ (MPa)} \quad (3.6)$$

3.5 Measurement of Responses for Ti-Ta-Nb-Mo-Zr HEA

Following sections describe procedure used to evaluate aspect ratio of Ti-Ta-Nb-Mo-Zr HEA single-track single-layer depositions, and microstructure, microhardness, compressive stress-strain relationship, fractography, and sliding wear characteristics of multi-track multi-layer deposition of Ti-Ta-Nb-Mo-Zr HEA along with the details of corresponding sample preparation.

3.5.1 *In-vitro* Biocompatibility Evaluation

Internal environment of the human body is physically and chemically different from the outside environment. Therefore, a biocompatible metallic material that functions well

outside environment may experience severe corrosion in the human body (**Tower et al. 2021**). Although presence of passive oxide layers on metallic implants considerably increases its corrosion resistance but they are not completely inert in the human body. Release of metallic ions in the human bloods alters its pH value and oxygen level which changes human cells behavior and metabolism. Adverse effects of different metallic ions in various solutions and the human body have been reported by different researchers (**Delgado-Ruiz and Romanos 2018; Priyadarshini et al. 2019; Reiner et al. 2020; Tower et al. 2021; Schoon et al. 2019; Garcia-Mendez et al. 2021**). Knee implants may eventually fail due to increase in the released amount of different metallic ions allergic and toxic to the human body.

3.5.1.1 Cell Viability Evaluation

Three cylindrical shaped samples of 4 mm diameter and 8 mm length (shown in red color in Fig. 3.6b) were cut from multi-track multi-layer deposition of Ti-Ta-Nb-Mo-Zr HEA by WSEM machine for *in-vitro* evaluation of cell viability and release of metallic ions. The cut samples were cleaned in an ultrasonic cleaner and then dried. Pre-treatment was given to the prepared samples by the sterilization method in which they were immersed in 70% alcohol for 12 hours, removed from the solution and then they were dried. The dried samples were exposed to UV light for 4 hours for further sterilization. Subsequently they were incubated in sterile tubes containing 2 ml DMEM for the time duration of 24; 48; and 72 hours at 37°C. Such incubation allowed the time-dependent release of metallic ions from Ti-Ta-Nb-Mo-Zr HEA to the cell culture media which tends to *in-vitro* mimic the biological environment. Prepared three culture media (corresponding to 24; 48; 72 hours incubation duration) were used for treating them with HeLa cells, human embryo kidney (HEK-293) cells, and baby hamster kidney (BHK) cells using MTT assay to evaluate cell viability of Ti-Ta-Nb-Mo-Zr HEA. The used HeLa, HEK-293, and BHK cell lines were procured from the National Centre for Cell Science Pune, India. They were further sub-cultured and preserved in DMEM enriched with 10% fetal bovine serum (FBS) and 1x penicillin-streptomycin at 37°C with 5% CO₂ incubator. Each cell line was trypsinized and was seeded in 96 well plates with seeding density of ~10,000 cells per well. Then the cell preserving solution was removed after 16-18 hours from each cell line well plate. Each cell type attached to its well plate was treated with 20; 40; 60; and 100 µl in triplicate for 24 hours duration with each of the prepared cell culture media of the developed Ti-Ta-Nb-Mo-Zr HEA. Total volume of each well was maintained as 100 µl by adding fresh DMEM for the remainder volume while using 20; 40; and 60 µl of cell culture media. After the treatment, the corresponding cell culture media (containing the leached-out metallic ions) was

withdrawn, and the cells were gently washed with 1x-PBS solution. Then 100 μ l MTT stock of 0.5 mg per liter concentration was added to each well for 4 hours. The MTT stock with 5 mg/ml concentration was prepared in 1x-PBS solution and it was diluted up to 0.5 mg per liter by adding the DMEM media for the treatment with a cell line. After four hours, the MTT stock was aspirated from the wells and 100 μ l of Dimethyl sulfoxide was added to each well. Each well plate was then kept in a horizontal shaker for 5-10 minutes, and the absorbance of each cell type was recorded by a 570 nm wavelength microplate reader. The untreated HeLa, HEK-293, and BHK cells were used as the control cell for the corresponding treated cells. Cell viability of each type of treated cells was computed by Eq. 3.1. Bright-field micrographs of untreated and treated HeLa, HEK-293, and BHK cells were captured using an inverted microscope.

3.5.1.2 Evaluation of Release of Metallic Ions

The samples of multi-layer deposition of Ti-Ta-Nb-Mo-Zr HEA used for cell viability evaluation were also used to evaluate released metallic ions after carefully polishing them with SiC emery papers up to 1200 grit size followed by ultrasonic cleaning. Then they were placed in 5 ml polypropylene tubes and separately sterilized in an autoclave for 30 minutes. These tubes were carefully cleaned with 5 vol.% concentrated HNO₃ solutions and ultrapure water to remove the impurities and, and then again sterilized in an autoclave. Released amounts of metallic ions by Ti-Ta-Nb-Mo-Zr HEA samples were assessed in simulated body fluid (SBF) solution by varying its pH values at 4.4; 5.4; and 7.4 and immersion duration as 1; 2; and 3 weeks. Chemical composition of the prepared SBF solution is: 8 g/l NaCl; 0.4 g/l KCl; 0.14g/l CaCl₂; 0.35 g/l NaHCO₃; 1 g/l glucose; 0.1 g/l MgCl₂.6H₂O; 0.06 g/l MgSO₄.7H₂O; 0.06 g/l KH₂PO₄; and 0.06 g/l Na₂HPO₄.12H₂O. This is equivalent to average saline content of human body fluid. Desired pH value of the prepared SBF solution was maintained by adding HCl for an acidic solution (i.e., pH < 7.0) or NaOH for alkaline solution (i.e., pH > 7.0). Each prepared SBF solution of a particular pH value was poured into the 5 ml polypropylene tube containing sample of Ti-Ta-Nb-Mo-Zr HEA and then the sample is incubated for duration 1; 2; and 3 weeks at 37°C. Concentrations of the released ions from Ti-Ta-Nb-Mo-Zr HEA after one, two, and three weeks were measured using the IC-PAES which performs elemental analysis with high sensitivity using argon plasma as the ionization source. Mean quantities of various elements released from Ti-Ta-Nb-Mo-Zr HEA were measured based on ppb with a detection limit of 6 ppb.

3.5.1.3 Study of Corrosion Behavior

Three samples cut from multi-track multi-layer deposition of Ti-Ta-Nb-Mo-Zr HEA were polished up to 1500 grit SiC emery papers and cleaned ultrasonically prior to their

corrosion behavior study on an Electrochemical Workstation (Vertex Potentiostat from Ivium Technologies, Netherlands). This workstation has a cell consisting of three electrodes i.e., SCE as a reference electrode, platinum foil as the counter electrode, and test sample as the working electrode. Sometimes pH value of human blood may change due to different diseases or circumstances. Therefore, influence of pH values of test solutions on the corrosion behavior should be considered during the knee implant material evaluation and selection. Therefore, corrosion behavior of the developed Ti-Ta-Nb-Mo-Zr HEA was evaluated in three SBF solutions having 4.4; 5.4; and 7.4 pH values in the thermostatic bath maintaining temperature of $37\pm 1^\circ\text{C}$. Surface area of 1 cm^2 of each prepared sample was exposed to each SBF solutions for 30 minutes to achieve a steady condition of OCP, which is defined as the potential of the working electrode relative to the reference electrode when no voltage is applied and no current is flowing. Stabilized OCP was used to determine range of potential for the Tafel polarization curve using 0.1 mV/s scanning rate in the potential range from -1V to 2V . Corrosion parameters were obtained from the Tafel polarization curve using equivalent weight and density as 19.955 g and 7.683 g/cm^3 respectively for Ti-Ta-Nb-Mo-Zr HEA and their corroded surfaces were examined using SEM. Phase mapping and chemical composition of the corroded surface of the sample was analyzed using EDS detector attached to the SEM. Phase analysis of oxides of the constituent elements formed on the corroded surface was analyzed on the XRD equipment using 40 kV voltage, 30 mA current, 2θ range of $10\text{-}100^\circ$ with 0.02 step size, 1 s dwell time, and $\text{CuK}\alpha$ radiation ($\lambda = 1.5418\text{ \AA}$). Different oxide phases present in the corroded sample were identified by matching the characteristic peaks present in the XRD with the JCPDS database.

3.5.2 Measurement of Aspect Ratio

Twenty-seven samples were prepared by cutting the twenty-seven single-track single-layer depositions of Ti-Ta-Nb-Mo-Zr HEA (obtained in the main experiments) at middle of their deposition length by the WSEM machine. The cut samples were ground and polished using SiC emery sheets up to a grit size of 2000 after being hot mounted in a polymeric resin. The stereo-zoom microscope was used to measure the width and height of each prepared sample. The aspect ratio of a deposition was computed as the ratio of the measured width of the deposition to the height of the deposition.

3.5.3 Study of Microstructure, Evolution of Phases, and Microhardness

Three cubic samples (each sample having 5 mm dimension) were cut from the middle of multi-track multi-layer deposition (location shown in Fig. 3.6a) of Ti-Ta-Nb-Mo-Zr HEA using WSEM machine. The cut samples were ground and polished by the SiC emery sheets up to a grit size of 2000 after being hot mounted in a polymeric resin. Then, they were

finely polished with cloth using successively finer diamond pastes (6, 3, and 1 μm). The freshly made Kroll's reagent solution, which contains 100 ml H_2O , 6 ml HNO_3 and 3 ml HF, was applied to their fine-polished surface to reveal their microstructure. Of these three samples, one sample was used to study its microstructure through SEM equipment and chemical composition using the EDS facility of the SEM equipment. The second sample was used to analyze evolution of phases through XRD equipment using 40 kV voltage, 30 mA current, 2θ range of $10\text{-}100^\circ$ with 0.02 step size, 1s dwell-time, and $\text{Cu-K}\alpha$ radiation ($\lambda = 1.5418 \text{ \AA}$). Different phase formed in the Ti-Ta-Nb-Mo-Zr HEA deposition sample were identified by comparing the distinctive peaks in their XRD with the JCPDS database.

The third sample was used to evaluate Vicker's microhardness by applying 300 g load for a dwell-time of 15 seconds in accordance with ASTM E92-82 standard. Fifteen distinct measurements were noted down at various locations at 0.1 mm intervals from the top surface to get microhardness profile of Ti-Ta-Nb-Mo-Zr HEA. Three measurements were taken at each location to confirm the reproducibility.

3.5.4 Compression Testing and Fractography

Three cylindrical samples (each having 2 mm diameter and 4 mm length as per ASTM E9 standard) were cut by the WSEM machine from the middle of multi-track multi-layer deposition of Ti-Ta-Nb-Mo-Zr HEA (location shown in Fig. 3.6a) to evaluate its compressive yield strength, ultimate compressive strength, and compressive strain. The cut samples were ground and fine-polished up to 1500 grit size using SiC emery paper. The compression tests were carried out at room temperature using 0.001/s strain rate on the precision universal testing machine (*AGX-V series*, Shimadzu from Japan). The fractured samples were used to study their compressive fractography by the SEM images.

3.5.5 Evaluation of Wear Resistance

Three samples (each having $15 \times 15 \times 4$ mm dimension as per ASTM G133 standard) were cut from the mid-section of multi-track multi-layer deposition of Ti-Ta-Nb-Mo-Zr HEA (location shown in Fig. 3.6a) to evaluate its sliding wear characteristics under dry conditions. The sliding wear test was performed on the ball-on-disc tribometer (*DUCOM TR-20LE*, from the USA) using 6 mm diameter silicon nitride ball (having 1200 HV hardness), applying 15, 30, and 45N load for the duration of 30 minutes each, and rotating the sample mounting disc at 300 rpm. Each wear test was repeated thrice to ensure the repeatability of the results. The sliding wear characteristics of Ti-Ta-Nb-Mo-Zr HEA sample were evaluated in terms of specific wear rate, worn scar depth, worn track analysis, and average coefficient of sliding friction for each value of the applied load. The specific wear rate ' v_s ' was computed using Eq. 3.5. The worn-scar depth was measured using the

3D-surface roughness-cum-contour-tracing equipment (*LD 130 MarSurf* from *Mahr Metrology*, Germany). The worn tracks were analyzed using SEM images. Average coefficient-of-friction at an applied load was computed from its time dependent profile.

3.5.6 Evaluation of Abrasion Resistance

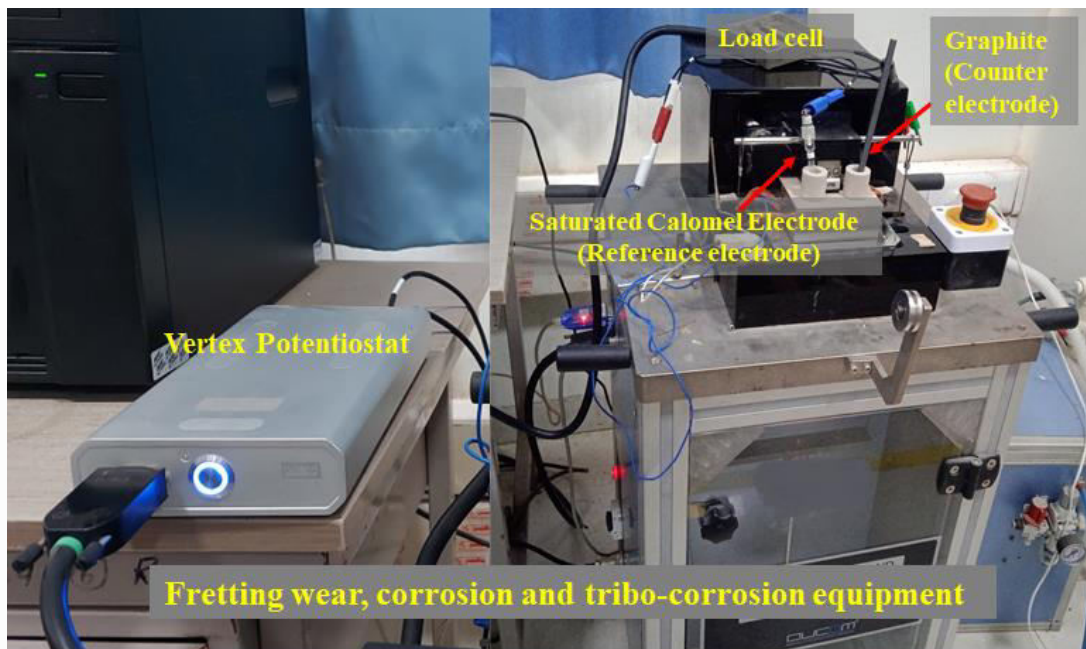
Scratch test was conducted on the prepared sample of Ti-Ta-Nb-Mo-Zr HEA to determine its abrasion resistance in terms of scratch hardness number ' H_{sn} ' and mean value of coefficient of friction. It was conducted on the scratch testing machine by sliding the conical shaped diamond stylus (having an apex angle of 120° and $200\ \mu\text{m}$ tip radius) for 6 mm sliding distance with 0.1 mm/s sliding speed under normal load of 10; 15; and 20 N with as per ASTM G171-03 standard. Experiments were performed thrice at each load using identical conditions to ensure repeatability of results. Average width of scratch track was measured using an optical microscope and scratch hardness number was calculated using Eq. (3.6) as per ASTM standard G171-03.

3.6 Bio-Tribological Characteristics of Ti-Ta-Nb-Mo-Zr HEA

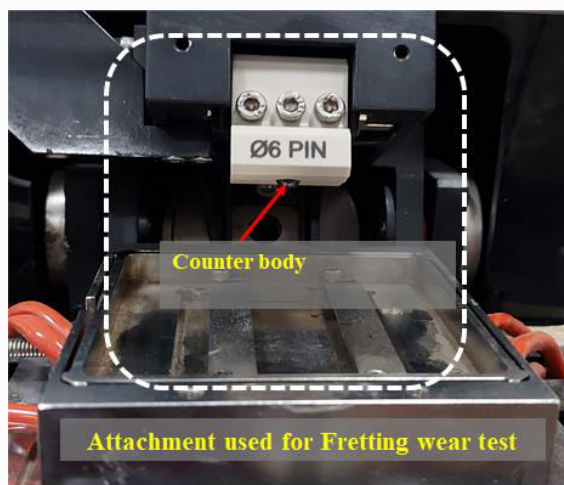
This section describes procedure used to study dry fretting wear, corrosion, and tribo-corrosion characteristics of multi-track multi-layer deposition sample of Ti-Ta-Nb-Mo-Zr HEA in human body emulating biofluids of 7.4 pH value at 37°C .

3.6.1 Dry Fretting Wear Study

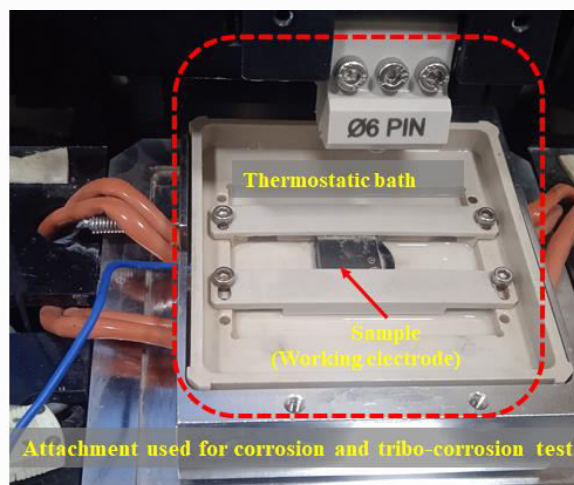
Dry fretting wear test was performed on the prepared samples of Ti-Ta-Nb-Mo-Zr HEA using the fretting wear and tribo-corrosion equipment (from *Ducom Instruments, India*) shown in Fig. 3.10a and its dry fretting wear attachment shown in Fig. 3.10b. It was conducted by reciprocating 6 mm diameter tungsten carbide pin [having Rockwell hardness on 'C' scale (HRC) as 85] with $250\ \mu\text{m}$ stroke length under three different loads of 10; 20; and 30 N and for 2.7×10^4 number of cycles. Total relative slip displacement is 13.5 m for dry fretting wear test. Experiments were performed thrice at each load using identical conditions to ensure repeatability of results. Fretting worn scar depth was measured using 3D surface roughness cum contour tracing equipment. Three-dimensional profile of worn scar was obtained through an optical profilometer (*NT9080* from *Veeco, USA*). The worn tracks were analyzed using the SEM.



(a)



(b)



(c)

Fig. 3.10: Photographs of the (a) equipment used to study fretting wear, corrosion, and tribo-corrosion characteristics of Ti-Ta-Nb-Mo-Zr HEA and its attachments used for (b) fretting wear test, and (c) corrosion and tribo-corrosion tests.

3.6.2 Study of Corrosion Behavior in Biofluids

The cut samples were polished up to 1500 grit by SiC emery papers and cleaned ultrasonically to study their corrosion characteristics on the electrochemical workstation attached to the fretting wear and tribo-corrosion equipment as shown in Fig. 3.10a. It has a cell consisting of 3 electrodes namely SCE as the reference electrode, graphite as the counter electrode, and the sample as the working electrode. Corrosion characteristics was studied in three human body emulating biofluids namely physiological saline (PS), PBS solution, and 1% fetal bovine serum (FBS) mixed with the PBS solution (FPBS). Their pH value was maintained as 7.4 and temperature in the thermostatic bath of the electrochemical

workstation was kept at $37\pm 1^\circ\text{C}$ thus emulating the human body conditions. Surface area of 1 cm^2 of each prepared sample was exposed to each biofluid for 30 minutes to achieve a steady state condition of OCP, which is the potential of the working electrode relative to the reference electrode when no voltage is applied. Potential range from -1 to 2 volts at scanning rate of 0.1 mV/s was used to obtain Tafel polarization curve. Corrosion parameters (i.e., corrosion potential ' E_{corr} ', corrosion current density ' i_{corr} ', and corrosion rate) were determined from the Tafel polarization curve using equivalent weight and density of Ti-Ta-Nb-Mo-Zr HEA as 19.955 g and 7.683 g/cm^3 respectively. The corroded surfaces were studied by the SEM images.

3.6.3 Study of Tribo-Corrosion Behavior in Biofluids

Samples of Ti-Ta-Nb-Mo-Zr HEA deposition were used to study tribo-corrosion characteristics after polishing them up to 1500 SiC emery papers. Electrochemical workstation, thermostatic bath, and fretting wear attachment of the equipment (depicted in Fig. 3.10c) were used to study tribo-corrosion characteristics. It was done using 10 N applied load and 4.5×10^4 number of cycles in the presence of three biofluids (i.e., PS, PBS, and FPBS) maintaining their pH as 7.4 and temperature as $37\pm 1^\circ\text{C}$. Total relative slip displacement is 22.5 m for tribo-corrosion test. Equation 3.5 was used to compute specific wear rate in tribo-corrosion and the worn scar depth was measured in the same manner as in case of dry fretting wear. Experiments were performed thrice using identical conditions to ensure repeatability of results. Three-dimensional profile of worn scar was obtained through an optical profilometer. Values of OCP, ' E_{corr} ', ' i_{corr} ', and corrosion rate were determined from the Tafel polarization curve obtained from tribo-corrosion study using equivalent weight and density of Ti-Ta-Nb-Mo-Zr HEA as 19.955 g and 7.683 g/cm^3 respectively. The worn tracks and tribo-corroded surfaces were studied using the SEM images.

The *next chapter* describes results and their analyses of better knee implant materials developed by adding 2%; 4%; and 6% of titanium to Co-Cr-Mo alloy by μ -PAAM process. It covers *in-vitro* biocompatibility assessment using viability of HeLa cells, release of metallic ions in PBS solution of different pH values and for different immersion durations, corrosion behavior study in PBS solution of 7.4 pH at 37°C . It also covers evaluation of aspect ratio, density and porosity, microstructure analysis, formation of phases, inter-diffusion zone analysis, microhardness, tensile and compression tests and their fractography, abrasion resistance, and wear characteristics of the optimized depositions.

Chapter 4

Results and Analysis for Co-Cr-Mo-xTi Alloys

This chapter describes results and analysis for Co-Cr-Mo-xTi alloys covering their *in-vitro* biocompatibility assessment, aspect ratio, density, porosity, microstructure, formation of phases, inter-diffusion zone, microhardness, tensile and compression tests and their fractography, abrasion resistance test and wear characteristics.

4.1 Aspect Ratio Results

Figure 4.1 shows photographs of 27 depositions of Co-Cr-Mo-2Ti alloy manufactured during the main experiments. Table 4.1 presents aspect ratio computed as ratio of measured deposition width to deposition height and observed deposition quality in terms of continuous and consistent deposition (CCD) and non-uniform deposition (NUD) along with parametric combinations for 27 main experiments. Figure 4.2 illustrates measurement of aspect ratio for experiment numbers 14 (Fig. 4.2a), 17 (Fig. 4.2b), and 27 (Fig. 4.2c) for single-track single-layer deposition of Co-Cr-Mo-2Ti alloy. It can be observed from Fig. 4.1 and Table 4.1 that 21 depositions out of the 27 depositions are CCD whereas depositions corresponding to experiment number 1, 2, 3, 7, 8, and 17 were found to be NUD.

It can be observed from Table 4.1 that (i) NUD occurred due to lower values of deposition material powder mass flow rate and μ -plasma power while CCD occurred at their optimum value, (ii) aspect ratio is varying in a range from 1.11 to 1.91, and (iii) experiment No. 5 yielded minimum value of aspect ratio of 1.11 and continuous and consistent deposition which has lower μ -plasma power (264 W), and moderate values of powder mass flow rate (2.5 g/min) and deposition head travel speed (50 mm/min). Therefore, this parametric combination was identified as the optimum for manufacturing multi-track multi-layer depositions of powder of Co-Cr-Mo-2Ti, Co-Cr-Mo-4Ti, and Co-Cr-Mo-6Ti alloys.

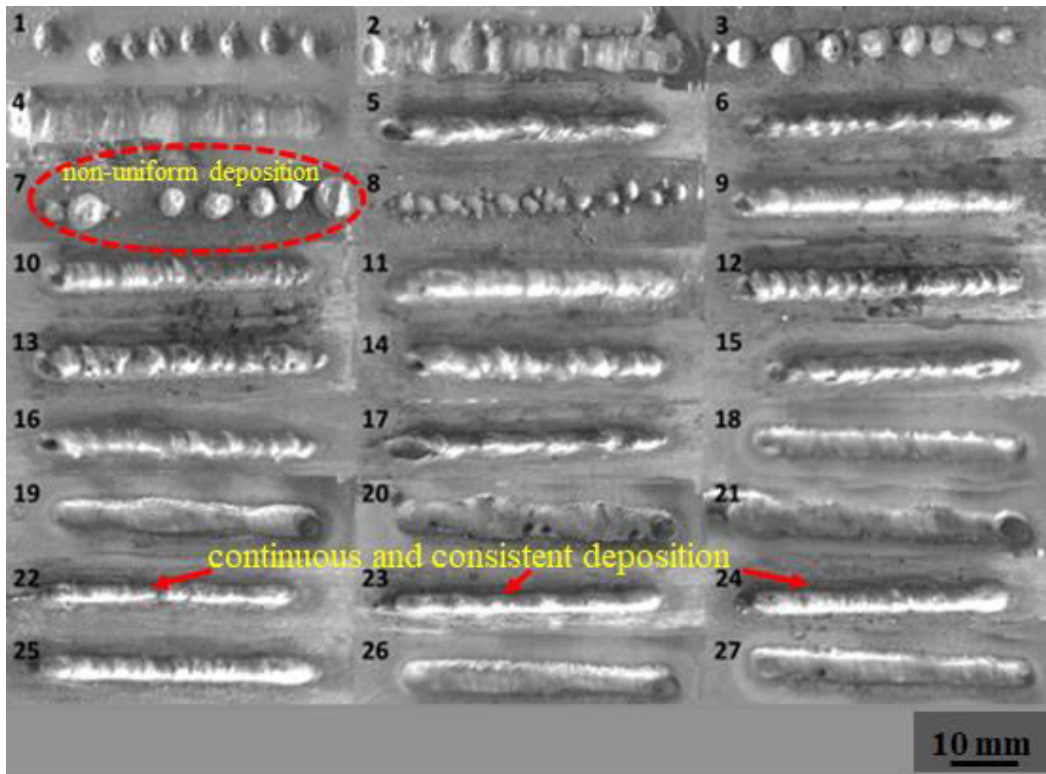


Fig. 4.1: Photographs of 27 single-track single-layer depositions of Co-Cr-Mo-2Ti alloy obtained during the main experiments.

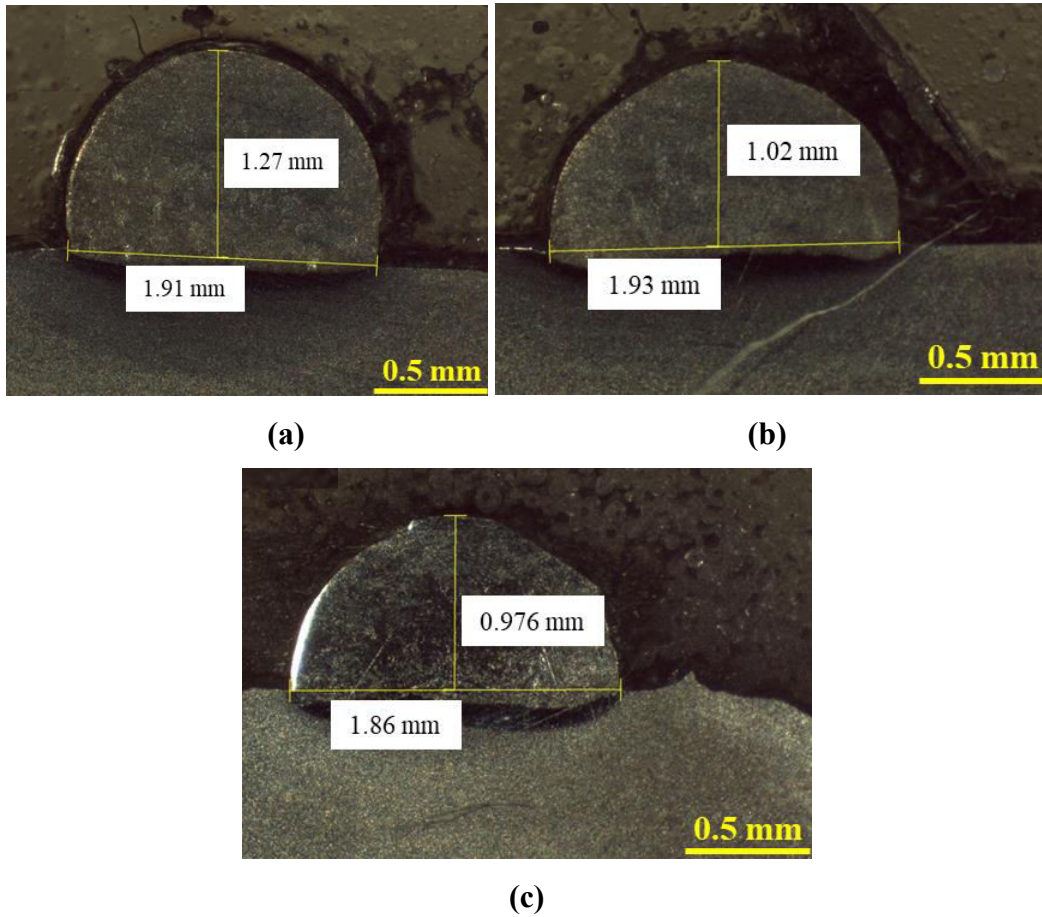


Fig. 4.2: Measurement of aspect ratio of single-track single-layer deposition of Co-Cr-Mo-2Ti alloy corresponding to experiment number: (a) 14; (b) 17; (c) 27.

Table 4.1: Parametric combination utilized in 27 main experiments as well as associated measured and observed responses.

Exp. No.	Variable input parameters			Measured responses	
	μ -plasma power (W)	Mass flow rate of feedstock material powder (g/min)	Deposition head travel speed (mm/min)	Aspect ratio	Deposition quality
1	264	2.0	45	1.27	NUD
2	264	2.0	50	1.18	NUD
3	264	2.0	55	1.30	NUD
4	264	2.5	45	1.31	CCD
5	264	2.5	50	1.11	CCD
6	264	2.5	55	1.30	CCD
7	264	3.0	45	1.54	NUD
8	264	3.0	50	1.47	NUD
9	264	3.0	55	1.44	CCD
10	275	2.0	45	1.44	CCD
11	275	2.0	50	1.43	CCD
12	275	2.0	55	1.44	CCD
13	275	2.5	45	1.51	CCD
14	275	2.5	50	1.50	CCD
15	275	2.5	55	1.52	CCD
16	275	3.0	45	1.65	CCD
17	275	3.0	50	1.89	NUD
18	275	3.0	55	1.59	CCD
19	286	2.0	45	1.37	CCD
20	286	2.0	50	1.34	CCD
21	286	2.0	55	1.37	CCD
22	286	2.5	45	1.61	CCD
23	286	2.5	50	1.55	CCD
24	286	2.5	55	1.54	CCD
25	286	3.0	45	1.70	CCD
26	286	3.0	50	1.68	CCD
27	286	3.0	55	1.91	CCD

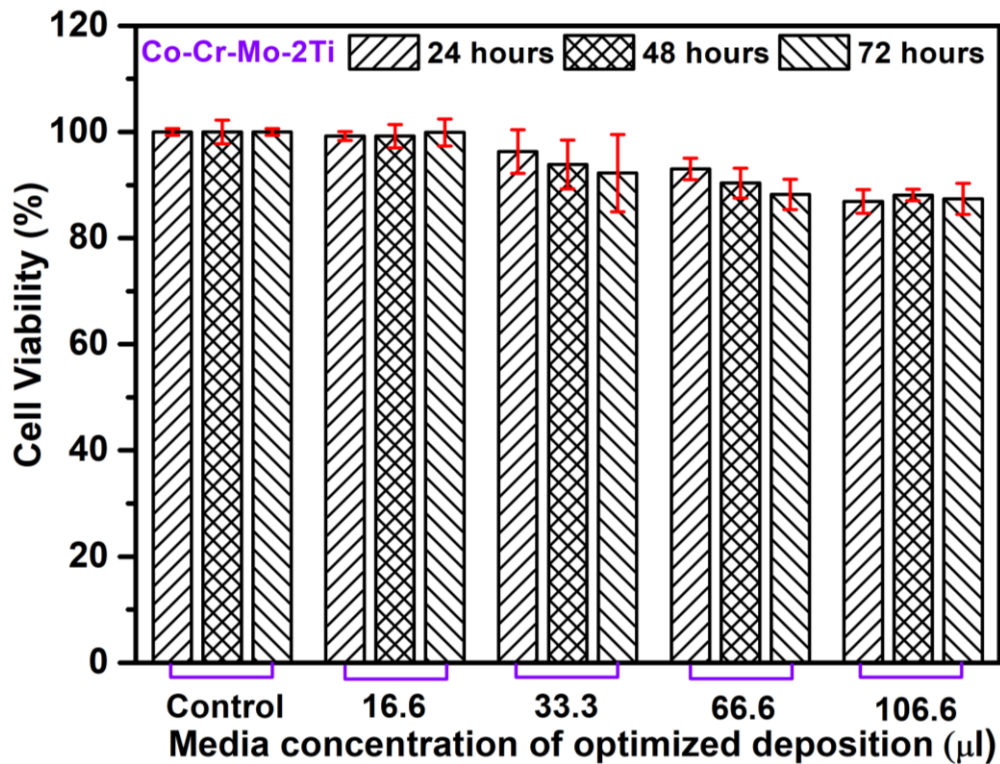
4.2. Findings from Biocompatibility Assessment

This section presents findings from *in-vitro* assessments of biocompatibility of multi-track multi-layer deposition samples of Co-Cr-Mo-xTi alloys in terms of cell viability results for different values of incubation duration and concentration of media, amounts of metallic ions released by them in the PBS solution of different pH values at 4; 5.5; and 7.5 and different immersion duration of 1; 3; and 7 weeks, and results for corrosion behavior of in PBS solution of 7.4 pH value at 37°C.

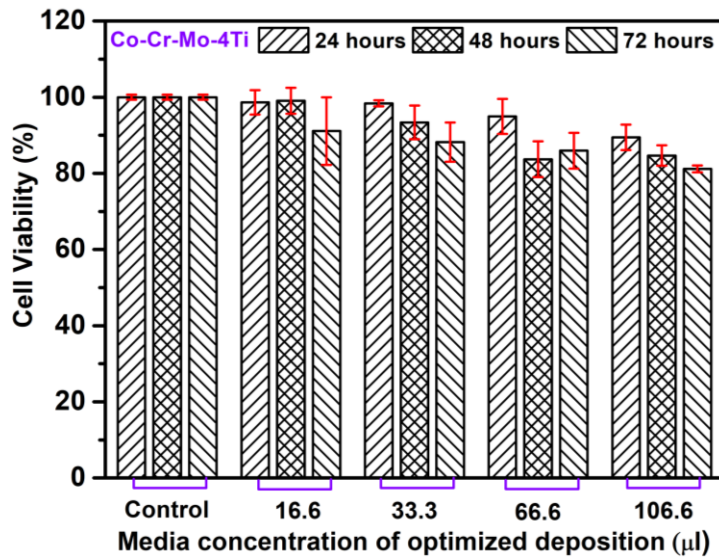
4.2.1. Cell Viability Results

Figure 4.3 presents bar diagram depicting average values of % cell viability assessed by MTT assay for different values of incubation duration and concentration of media prepared for the optimized deposition samples of Co-Cr-Mo-2Ti (Fig. 4.3a), Co-Cr-Mo-4Ti (Fig.

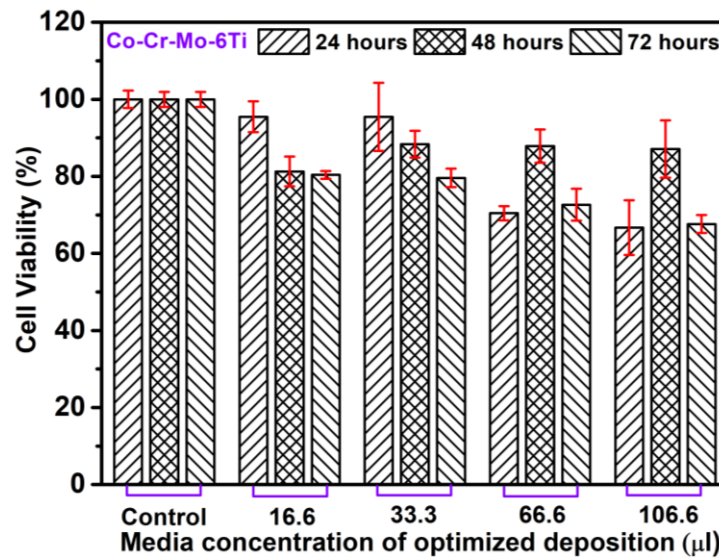
4.3b), and Co-Cr-Mo-6Ti (Fig. 4.3c) alloys. It can be noted from these figures that average value of cell viability decreases with increase in incubation duration and increase in the prepared media concentration for all three variations of Co-Cr-Mo-Ti alloy except for 48 hours incubation duration for 66.6 and 106.6 μl concentration of media of sample of Co-Cr-Mo-6Ti alloy (Fig. 4.3c). Overall average values of cell viability for the optimized deposition samples of Co-Cr-Mo-2Ti; Co-Cr-Mo-4Ti; and Co-Cr-Mo-6Ti alloys are 92%; 95%; and 85%, respectively. It implies that Co-Cr-Mo-4Ti optimized deposition sample has maximum cell viability which is 10% and 3% more than that of Co-Cr-Mo-6Ti and Co-Cr-Mo-2Ti samples respectively. Addition of Ti to Co-Cr-Mo alloy is advantageous due to formation of intermetallic phase CoTi_2 which is non-cytotoxic to human body and more active in cell growth mechanism (Hasani 2020). Lesser cell viability of Co-Cr-Mo-6Ti might be due to larger porous structure and its non-uniform distribution (shown in Fig. 4.9c). This observation is supported by the findings in which it has shown that Co-Cr-Mo-6Ti alloy has larger size pores and non-uniform distribution of porosity. It increases contact area between the synovial fluid present in knee joint and knee implant which obstruct cell growth rate and increase shrinkage rate of cells on knee implant surface.



(a)



(b)



(c)

Fig. 4.3: Average values of % cell viability in-vitro assessed by MTT assay for different values of incubation duration and concentration of media prepared for the optimized deposition samples of alloy: (a) Co-Cr-Mo-2Ti, (b) Co-Cr-Mo-4Ti, and (c) Co-Cr-Mo-6Ti.

Figure 4.4 depicts morphology of HeLa cells treated for 72 hours incubation duration with 106.6 µl concentration of media of each optimized deposition sample of Co-Cr-Mo-2Ti (Fig. 4.4a), Co-Cr-Mo-4Ti (Fig. 4.4b), Co-Cr-Mo-6Ti (Fig. 4.4c), and for untreated HeLa cell (Fig. 4.4d) i.e., without applying any media. It can be observed from Fig. 4.4d that the untreated HeLa cells are mutually connected, and they are not localized. They are in different shapes such as triangle, elongated, oval, flat, spindle. Fig 4.4a shows that HeLa cells in Co-Cr-Mo-2Ti sample media are not entirely scattered over the observation area whereas they are scattered over the observation area and mutually connected in the media of

samples of Co-Cr-Mo-4Ti (Fig. 4.4b) and Co-Cr-Mo-6Ti (Fig. 4.4c) alloys. It can also be observed from Fig. 4.4a that few cells are embossed and rounded cells which indicate that the cells are ready to divide or already divided. Once cells are divided then they again attach to the well plate. Round shaped and black colored cells visible in Figs. 4.4b and 4.4c are the dead cells. HeLa cells become more elongated, triangular, and spindle shape rather than round shape due to increase in amount of Co and Ti in the optimized deposition samples. Presence of cobalt enhances cell growth rate while presence of CoTi_2 intermetallic phase enables contact surface more active in the biofluids. Adding different wt.% of Ti to Co-Cr-Mo alloy has considerable effects on cells morphology after 72 hours incubation duration on cell growth rate and cell viability in the prepared media of optimized deposition samples. These findings are in accordance with the work of **Kassapidou et al. (2020)** and **Nath et al. (2018)**. Overall, it can be concluded that HeLa cells are metabolically active and shown insignificant adverse effects to the optimized deposition samples and optimized deposition of Co-Cr-Mo-4Ti alloy is better in terms of cell viability and morphology.

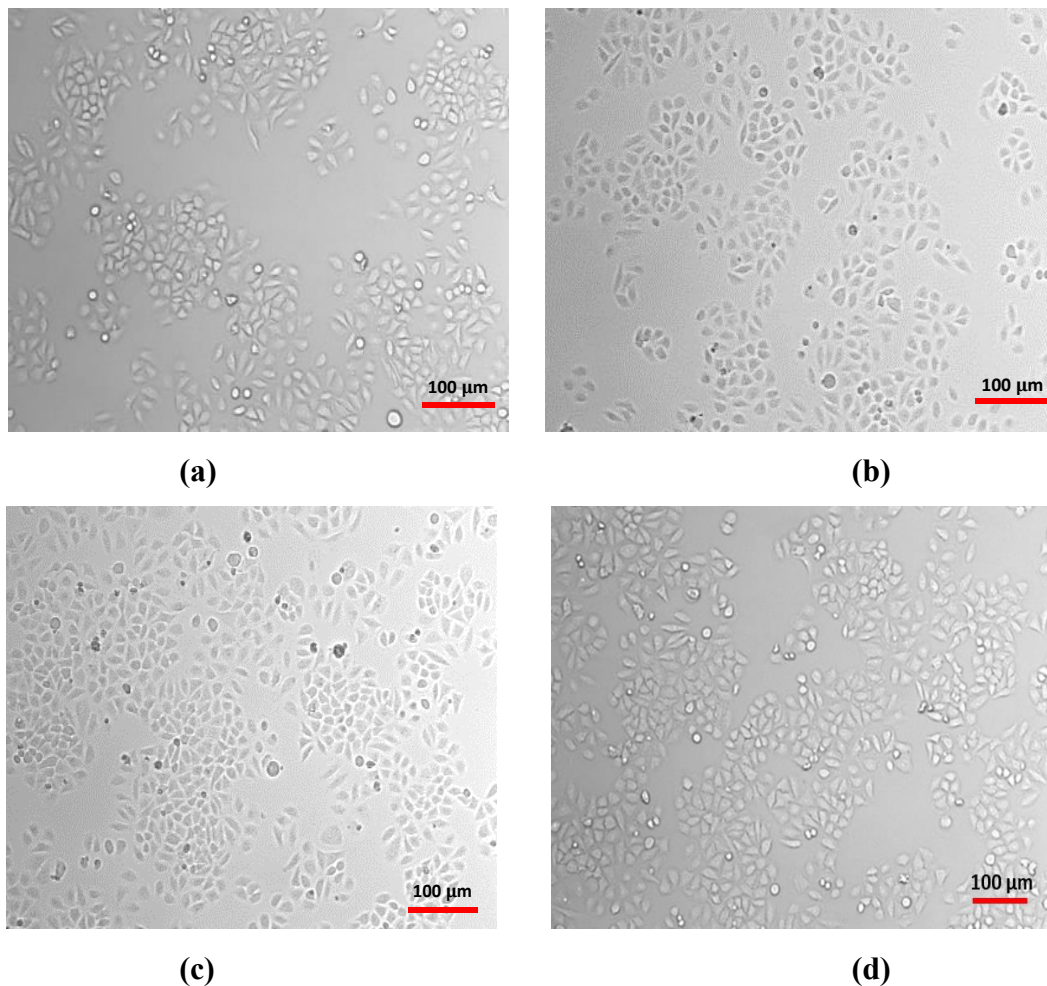


Fig. 4.4: Morphology of HeLa cells treated for 72 hours of incubation duration with 106.6 μl concentration of media of each optimized deposition sample of: (a) Co-Cr-Mo-2Ti, (b) Co-Cr-Mo-4Ti, (c) Co-Cr-Mo-6Ti, and (d) for untreated HeLa cells.

4.2.2 Metallic Ions Release Results

Released amounts of metallic ions by the optimized deposition samples were assessed *in-vitro* in the PBS solution by varying its pH values at 4; 5.5; and 7.5 and varying immersion duration as 1; 3; and 7 weeks. Table 4.2 presents released amounts of Co, Cr, Mo, and Ti ions in parts per billion (ppb) by the optimized deposition samples of Co-Cr-Mo-xTi in the PBS solution for different values of pH and immersion duration. Fig. 4.5 shows overall average amount of Co, Cr, Mo, and Ti ions released by the optimized deposition samples.

Table 4.2: Released amounts of metallic ions in ppb by the optimized deposition samples of Co-Cr-Mo-xTi alloys in the PBS solution different values of its pH and immersion times.

Alloy type	Metallic ion	Amount released (ppb) for different values of pH and immersion duration								
		4.0			5.5			7.5		
		After 1 week	After 3 weeks	After 7 weeks	After 1 week	After 3 weeks	After 7 weeks	After 1 week	After 3 weeks	After 7 weeks
Co-Cr-Mo-2Ti	Co	98.5	110.6	158.4	99.6	112.9	150.6	102.3	113.4	155.5
	Cr	39.6	25.1	52.7	37.9	28.0	55.7	34.3	31.3	57.5
	Mo	13.1	11.4	8.3	14.2	12.7	7.5	17.3	13.25	8.6
	Ti	9.6	9.5	10.9	10.0	10.0	11.2	10.9	10.9	12.0
Co-Cr-Mo-4Ti	Co	103.2	114.5	148.6	105.3	116.9	141.4	106.8	118.6	147.6
	Cr	41.4	20.4	38.7	44.6	23.58	42.5	45.7	28.6	45.4
	Mo	8.1	10.4	6.3	9.4	10.9	7.0	10.6	11.2	7.4
	Ti	6.2	6.4	7.7	7.1	7.13	8.0	7.9	7.9	8.3
Co-Cr-Mo-6Ti	Co	107.2	119.7	164.9	109.5	121.5	169.25	111.0	124.9	171.8
	Cr	47.4	27.4	57.4	49.6	28.6	62.6	53.0	29.6	67.4
	Mo	10.6	12.7	9.4	11.3	13.6	9.9	13.7	14.9	10.2
	Ti	8.2	7.3	8.4	8.98	8.98	8.97	9.42	9.26	9.4

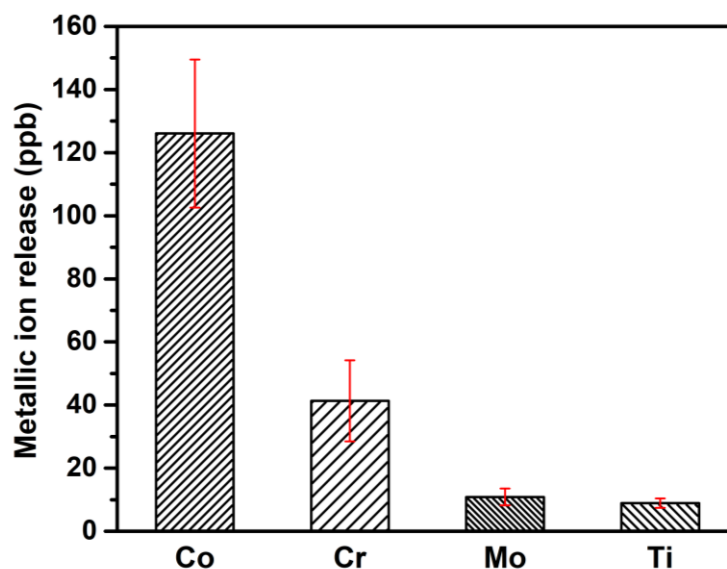


Fig. 4.5: Overall average of released amount of the Co, Cr, Mo, and Ti ions by the optimized deposition samples of Co-Cr-Mo-xTi alloys.

Following are the observations from Table 4.2 and Fig. 4.5.

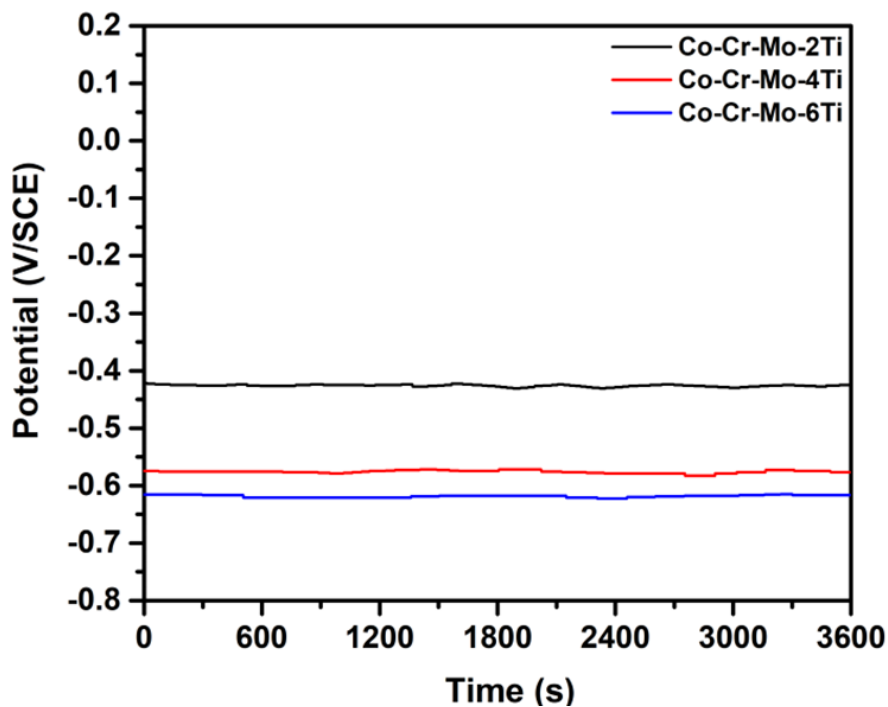
- Optimized deposition sample of Co-Cr-Mo-6Ti released maximum amount of cobalt and chromium ions (171.8 and 67.4 ppb) at 7.5 pH value of the PBS solution after 7 weeks of immersion duration,
- Optimized deposition sample of Co-Cr-Mo-2Ti released maximum amounts of molybdenum and titanium ions (17.3 and 12 ppb) at 7.5 pH value of the PBS solution after 1 and 7 weeks of immersion durations respectively,
- Majority of released amounts of Co, Cr, Mo, and Ti ions by Co-Cr-Mo-4Ti are in between that those by Co-Cr-Mo-2Ti and Co-Cr-Mo-6Ti samples,
- Released amount of Co ions increases with increase in immersion duration and pH value of the PBS solution and maximum released amount is found after 7 weeks of the immersion duration for the optimized deposition samples of all three alloys of Co-Cr-Mo-xTi.
- Released amount of Cr ion decreases from 1st to 3rd week of immersion duration and then increases after 7th week of immersion duration for the all three pH values of the PBS solution and for all three alloys Co-Cr-Mo-xTi optimized deposition samples.
- Released amount of Mo ion increases from 1st to 3rd week of immersion duration and then decreases after 7th week of immersion duration for the all three pH values of the PBS solution and for all three alloys Co-Cr-Mo-xTi optimized deposition samples
- Released amount of Ti ion increases with increase in pH value of the PBS solution for all three Co-Cr-Mo-xTi alloys optimized deposition samples. Its values are minimum for optimized deposition sample of Co-Cr-Mo-4Ti alloy.
- Overall average of released amounts of Co, Cr, Mo, and Ti ions by the optimized deposition samples of Co-Cr-Mo-xTi alloys are 126; 41;11, and 9 ppb respectively as shown in Fig. 4.5.

Overall, it can be observed that the released amounts of metallic ions depend on the pH value of the PBS solution, chemical composition of the test sample, and immersion duration. Released amount of Co ions is much higher than that of Cr, Mo, and Ti ions due to maximum amount of Co present in Co-Cr-Mo-xTi samples. This observation is supported by the findings of **Kassapidou et al. (2020)** who observed that addition of Ti to Co-Cr alloys in the implants may be advantageous since total release of metallic ions is reduced. **Hjalmarsson et al. (2011)** reported that when Co-Cr alloyed with Ti for knee implants then release of Co, Cr, and Ti ions are reduced. These findings might indicate that titanium passivates Co-Cr alloys thus reducing the ion releases. **Laitinen et al. (2017)** studied metallic ion levels in 22 patients with metal-on-metal hinge knee replacement and found

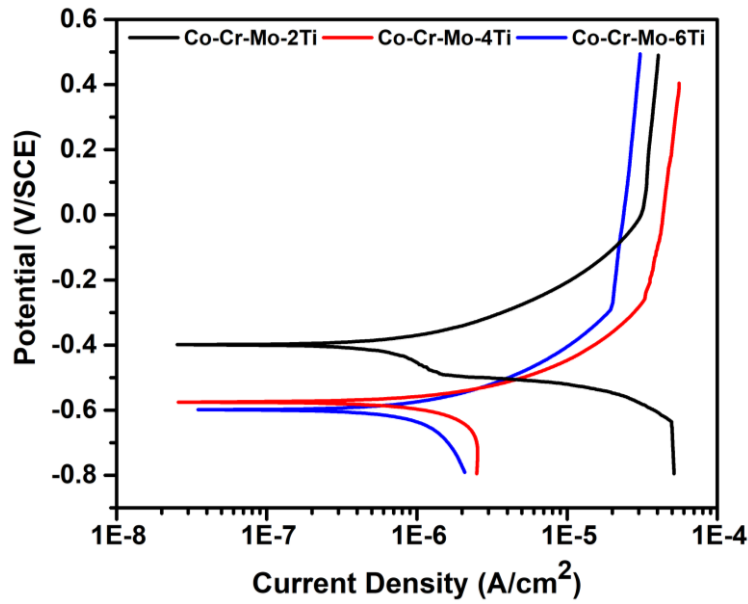
that 19 out of 22 patients had higher level of metallic ion released into their blood. They found maximum level of Co and Cr ions released in blood to be 77 ppb and 26 ppb respectively. They have mentioned that the released amount of cobalt ion less than 300 ppb is unlikely to cause adverse effects on neurological, cardiovascular, hematopoietic, and reproductive systems. Metallic ions released by knee implants into human blood is influenced by variation in pH value of blood and surrounding synovial fluid. Therefore, it can be concluded that the released amounts of metallic ions from the optimized deposition of Co-Cr-Mo-xTi alloys in the present work are within the physiological constraint of trace components in the human body.

4.2.3 Results for Corrosion Behavior

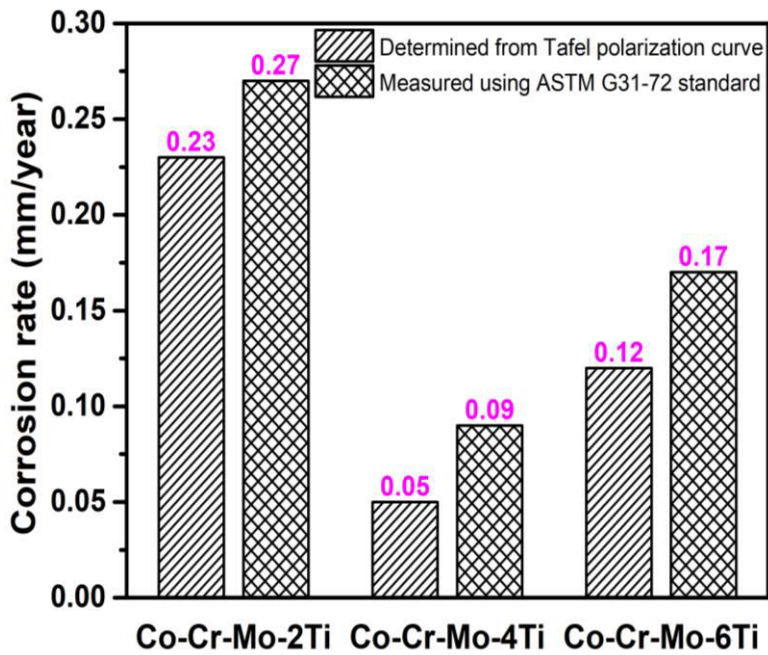
Figure 4.6 presents assessment results of corrosion behavior of the optimized deposition samples of Co-Cr-Mo-xTi alloys showing open circuit potential (OCP) curve (Fig. 4.6a), Tafel polarization curve, (Fig. 4.6b), and comparison between corrosion rate ' p_t ' determined from Tafel polarization curve and computed corrosion rate ' p_c ' using Eq. 3.2 as per ASTM G31-72 standard (Fig. 4.6c). Table 4.3 lists values of OCP, corrosion potential ' E_{corr} ', corrosion current density ' i_{corr} '; and corrosion rate ' p_t ' determined from the Tafel polarization curve of Fig. 4.6b. Figure 4.7 depicts SEM images of the corroded surfaces (after the corrosion assessment) of the optimized deposition samples of Co-Cr-Mo-2Ti alloy (Fig. 4.7a), Co-Cr-Mo-4Ti alloy (Fig. 4.7b), and Co-Cr-Mo-6Ti alloy (Fig. 4.7c) at 200X and 600X magnification.



(a)



(b)



(c)

Fig. 4.6: Assessment results of corrosion behavior of the optimized deposition samples of Co-Cr-Mo-xTi alloys (a) open-circuit potential (OCP) curve, (b) Tafel polarization curve, (c) comparison of the measured and computed corrosion rates.

Table 4.3: Corrosion related parameters determined from Tafel polarization curve for optimized deposition samples of Co-Cr-Mo-xTi alloys.

Alloy type	Open circuit potential (volts)	Corrosion potential ' E_{corr} ' (volts)	Corrosion current density ' i_{corr} ' ($\mu\text{A}/\text{cm}^2$)	Corrosion rate ' p_i ' (mm/year)
Co-Cr-Mo-2Ti	-0.43	-0.43	9.87	0.23
Co-Cr-Mo-4Ti	-0.58	-0.58	2.15	0.05
Co-Cr-Mo-6Ti	-0.62	-0.62	4.57	0.12

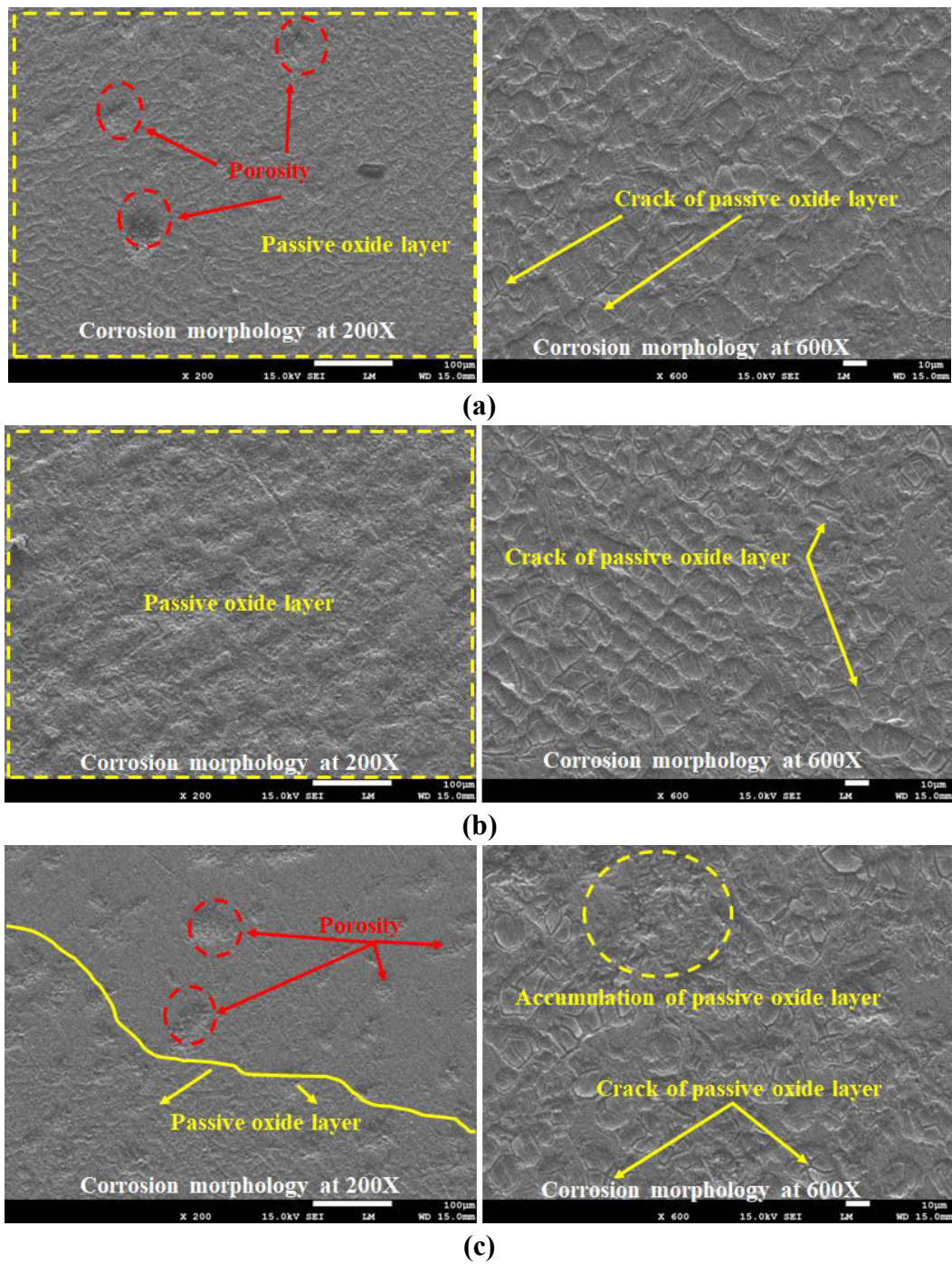
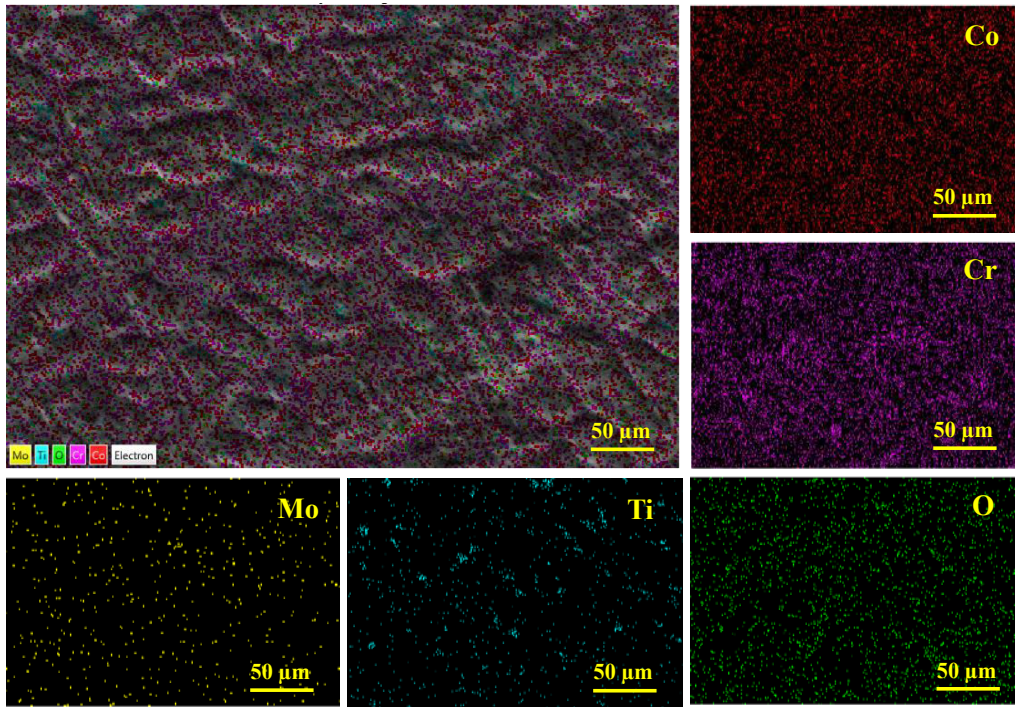
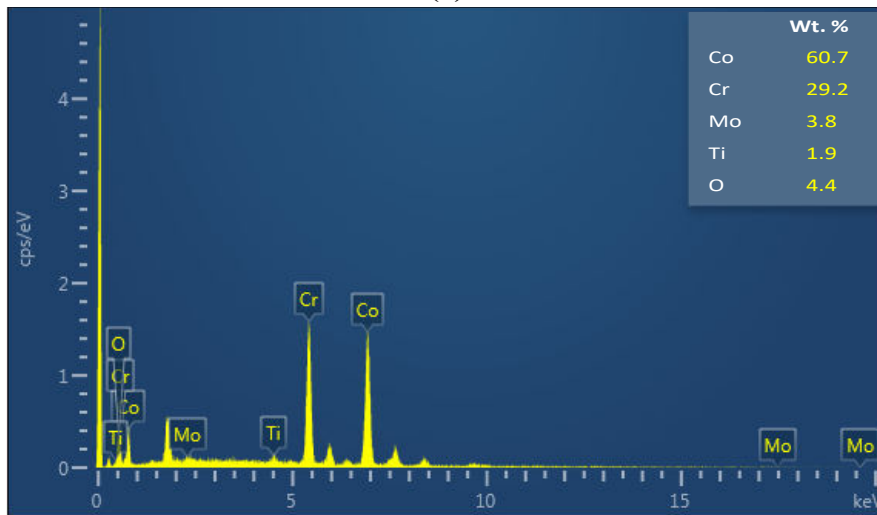


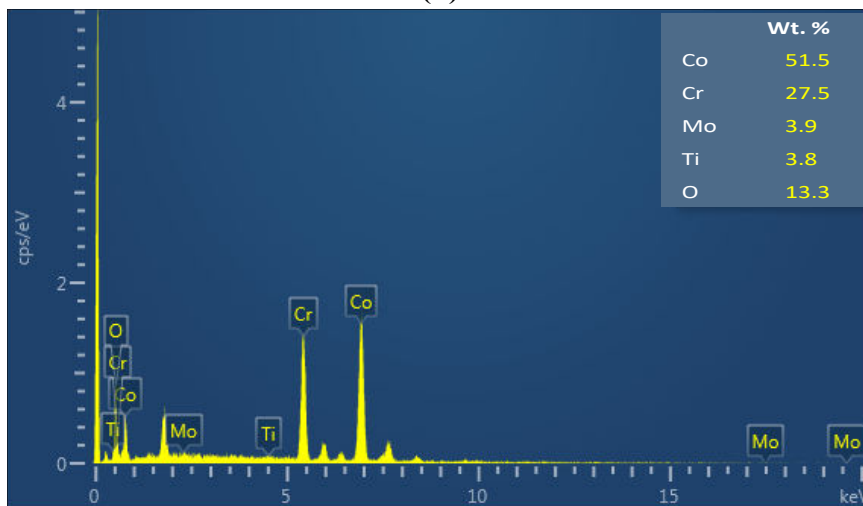
Fig. 4.7: SEM images of the corroded surfaces of the optimized deposition samples of: (a) Co-Cr-Mo-2Ti, (b) Co-Cr-Mo-4Ti, and (c) Co-Cr-Mo-6Ti alloy at 200X and 600 X magnification.



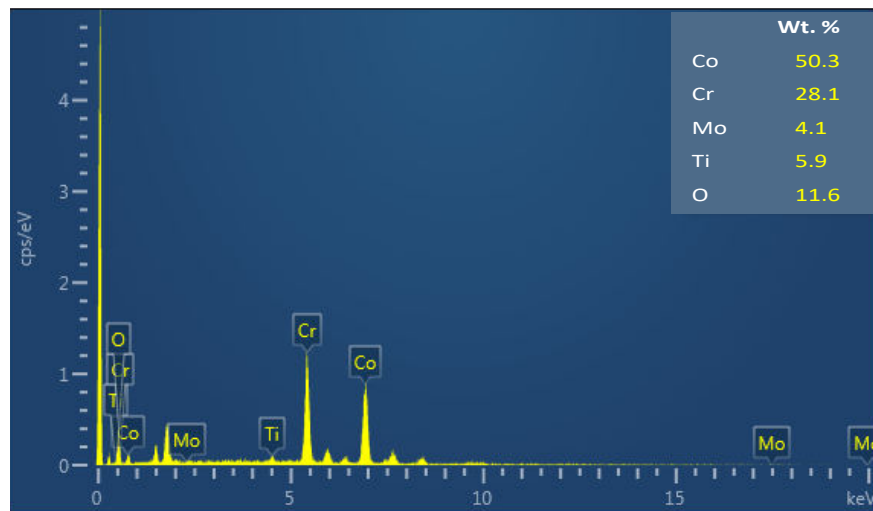
(a)



(b)



(c)



(d)

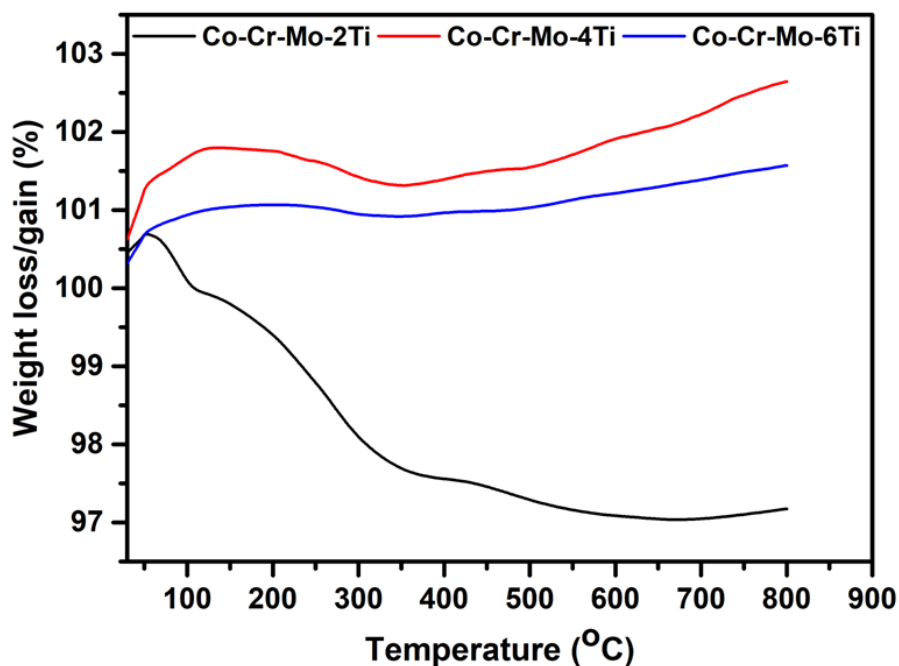


Fig. 4.8: (a) Elemental mapping of corroded surface of Co-Cr-Mo-4Ti alloy, and chemical composition of corroded surface of (b) Co-Cr-Mo-2Ti, (c) Co-Cr-Mo-4Ti, (d) Co-Cr-Mo-6Ti alloy, and (e) TGA plot of Co-Cr-Mo-xTi alloys.

Following are the observations from Fig. 4.6, Table 4.3, Fig. 4.7, and Fig. 4.8 and along with their interpretation:

- OCP curve for samples of all three alloys of Co-Cr-Mo-xTi are almost straight lines with very minor variations with time throughout the assessment duration (Fig. 4.6a) which might be due to instability in the formed passive oxide layer on their surfaces in the PBS solution.
- All the three Co-Cr-Mo-xTi alloys have negative values of their OCP (Fig. 4.6a) implying that they have higher corrosive tendency in the PBS solution and straight line of OCP indicates that these alloys may resist the electrolytic corrosive action which is due to formation of passive oxide layer on their surface during the exposure time

- Co-Cr-Mo-6Ti sample has minimum OCP value, Co-Cr-Mo-2Ti sample has maximum OCP value, and OCP value of Co-Cr-Mo-4Ti sample lies in between. It is confirmed by their respective values of their corrosion potential ' E_{corr} ' (Fig. 4.6b) determined from Tafel polarization curve (i.e., -0.62; -0.43; -0.58 volts) which have equal values of open-circuit potential and corrosion potential. OCP values of Co-Cr-Mo-4Ti alloy (i.e., -0.58) and Co-Cr-Mo-6Ti alloy (i.e., -0.62) are closer implying that these alloys have more corrosive tendency than Co-Cr-Mo-2Ti alloy.
- It can be observed from Fig. 4.6b that the optimized deposition samples of Co-Cr-Mo-xTi alloys show wide passive plateau up to 0.5 volts anodic side of Tafel polarization curve without pitting corrosion whereas slope of cathodic side is similar for Co-Cr-Mo-4Ti and Co-Cr-Mo-6Ti samples suggesting similar kinetics of cathodic reaction. Co-Cr-Mo-xTi alloys go through initial cathodic reaction followed by a decrease in corrosion current density ' i_{corr} ' with increase in corrosion potential ' E_{corr} ' until the anodic reaction begins. Change from cathodic to anodic reaction does not indicate active-passive transition. It indicates formation of strong passive oxide layers on the exposed surface of Co-Cr-Mo-xTi alloys in the PBS solution.
- It can be observed from Table 4.3 and Fig. 4.6c that corrosion current density ' i_{corr} ' (determined from Tafel polarization curve), corrosion rate, and measured corrosion rate (computed using Eq. 3.2) are minimum for Co-Cr-Mo-4Ti alloy sample (i.e., $2.15 \mu\text{A}/\text{cm}^2$; 0.05 mm/year; and 0.09 mm/year), and maximum for Co-Cr-Mo-2Ti alloy sample (i.e., $9.87 \mu\text{A}/\text{cm}^2$; 0.23 mm/year; and 0.27 mm/year), and in between for Co-Cr-Mo-6Ti alloy sample ($5.17 \mu\text{A}/\text{cm}^2$; 0.12 mm/year; and 0.17 mm/year). It implies that Co-Cr-Mo-4Ti alloy has minimum values of all important parameters of corrosion therefore it will offer maximum resistance to corrosion i.e., will have minimum corrosion as the knee implant material.
- It can be observed from the SEM micrographs of the corroded surfaces shown in Figs. 4.7a-4.7c that all samples of the optimized depositions do not have any localized corrosion. It implies that the released cobalt is completely dissolved in the PBS solution from their exposed surfaces. These findings are in agreement with the findings of **Lützner et al. (2020)** and **Liu et al. (2018)**.
- The SEM micrographs of corroded surfaces at 7.4 pH value of the PBS solution indicate that formation of a passive layer of oxides on the (i) entire exposed surface of Co-Cr-Mo-2Ti alloy with presence of some porosity (Fig. 4.7a), (ii) on the entire exposed surface of Co-Cr-Mo-4Ti alloy without presence of any porosity (Fig. 4.7b), and (iii) on some marked region on the exposed surface of Co-Cr-Mo-6Ti alloy with presence of

some porosity (Fig. 4.7c). Absence of any porosity on the corroded surface of Co-Cr-Mo-4Ti alloy (Fig. 4.7b) indicate formation of stronger passive layer of oxides imparting it better corrosion resistance or its less corrosion rate than Co-Cr-Mo-2Ti and Co-Cr-Mo-6Ti alloys. Some cracks can be seen in passive layer of oxides on the exposed surfaces of all three alloys.

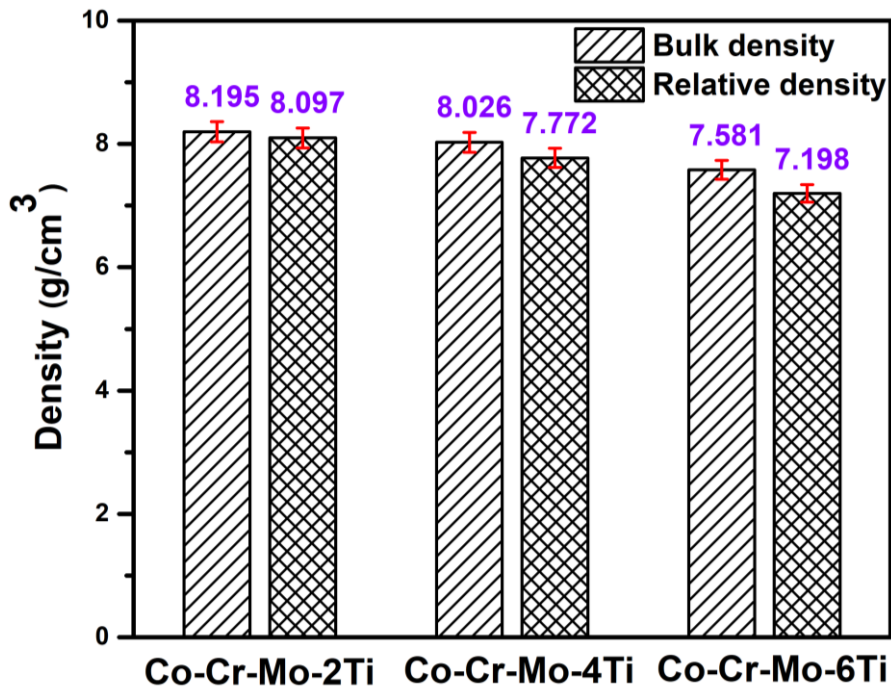
- It can be observed from the EDS analysis of the corroded surface of Co-Cr-Mo-xTi alloys (Figs. 4.8a-4.8d) that Co-Cr-Mo-4Ti alloy sample has maximum amount of oxygen (13.3 wt.% as depicted in Fig. 4.8c), Co-Cr-Mo-2Ti alloy sample has its minimum value (4.4 wt.% as shown in Fig. 4.8b), and Co-Cr-Mo-6Ti alloy sample has its value in between (11.6 wt.% as shown in Fig. 4.8d). Higher oxygen content in Co-Cr-Mo-4Ti alloy sample helps to possess it smaller value of corrosion rate than the other two alloys due to formation of the strong passive oxide layers on its corroded surface. The corrosion rate is further supported using TGA plot of Co-Cr-Mo-xTi alloys (Fig. 4.8e). It can be observed from Fig. 4.8e that there is a weight gain for Co-Cr-Mo-4Ti and Co-Cr-Mo-6Ti alloys as 1.3% and 0.6 % respectively, whereas Co-Cr-Mo-2Ti have weight loss of 3.6%. These observations signify the formation of strong passive oxide layer on Co-Cr-Mo-4Ti alloy, followed by Co-Cr-Mo-6Ti and Co-Cr-Mo-2Ti alloys. These observations are inline with the findings of corrosion rates of Co-Cr-Mo-xTi alloys shown in Fig. 4.6c and Table 4.3.

Based on the above findings, it can be concluded that Co-Cr-Mo-4Ti alloy has more resistance to corrosion than Co-Cr-Mo-2Ti and Co-Cr-Mo-6Ti alloys and could be potential alternative to metallic biocompatible materials currently used for knee implant application.

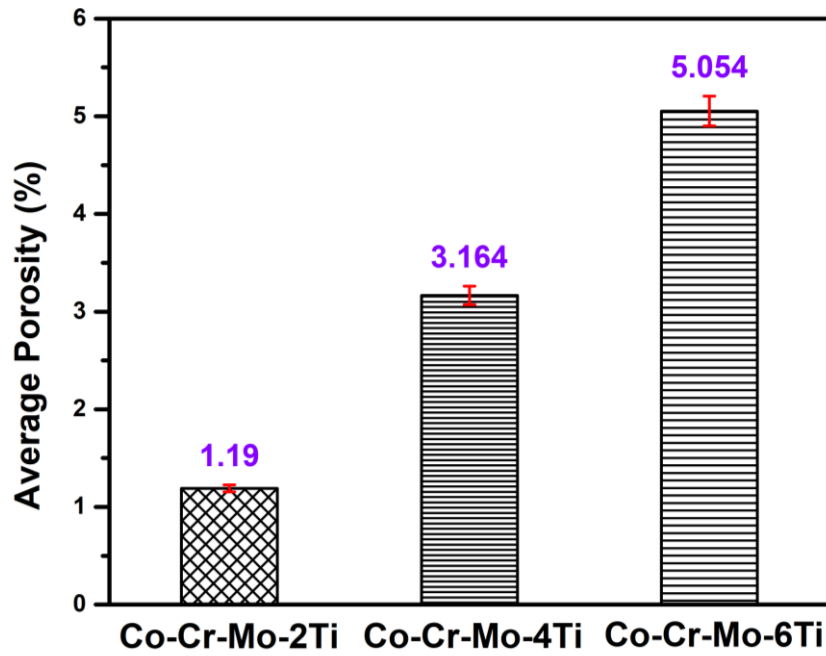
4.3 Density and Porosity Results

Figure 4.9a shows comparison of bulk density and relative density of the optimized depositions of Co-Cr-Mo-2Ti alloy; Co-Cr-Mo-4Ti alloy; and Co-Cr-Mo-6Ti alloy, Fig 4.9b depict values of their average porosity, and Fig. 4.10 presents micrographs of porosity distribution for them. It can be observed from Fig. 4.9a that bulk density and relative density decrease with increase in Ti amount in the Co-Cr-Mo alloy. It is due to the fact that density of Ti (4.5 g/cm^3) is much less than that density of Co-Cr-Mo alloy (8.29 g/cm^3). Ideally density of an implant material should be as close as possible to that of natural human bone because larger difference between their densities leads to improper transfer of loads between human bones and the implant causing stress shielding effect. It causes wear and tear of the implant and even its premature failure. Therefore, density of an implant very vital role in its life span. Fig. 4.9b illustrates that average porosity for Co-Cr-Mo-2Ti alloy; Co-Cr-Mo-4Ti alloy; and Co-Cr-Mo-6Ti alloy i.e., 1.19%; 3.16%; and 5.05% respectively. It is

due to increase in Ti amount in Cr-Co-Mo alloy which is evident from micrographs of Fig. 4.10. Titanium has smaller thermal conductivity than Co-Cr-Mo alloy. It leads to formation of pores due to shrinkage porosity during solidification of the molten alloy. Therefore, porosity in the optimized depositions increase with an increase in wt.% of titanium in the resultant Co-Cr-Mo-xTi alloy. Optimized deposition of Cr-Co-Mo-4Ti (Fig. 4.10b) shows more pores of smaller size and their more uniform distribution than the optimized depositions of Cr-Co-Mo-2Ti alloy and Cr-Co-Mo-6Ti alloy shown in Figs. 4.10a and 4.10c respectively. Such uniform porous structure is desirable for knee implant material as it allows better osseointegration with human bones and tissues (Lewallen et al. 2015; Frosch et al. 2021). However, further study regarding cell adhesion, proliferation, and in-vivo biocompatibility evaluation of Co-Cr-Mo-4Ti alloy is needed. Though Co-Cr-Mo-6Ti alloy has the higher porosity but it has larger size and smaller number of pores as compared to Co-Cr-Mo-4Ti alloy. It is due to more wt.% of titanium and corresponding decrease in wt.% of cobalt in it which decreases its thermal conductivity leading to its slower cooling rate during solidification of the molten alloy. It helps in increasing size of the pores caused by entrapment of unfused powder particles or air.

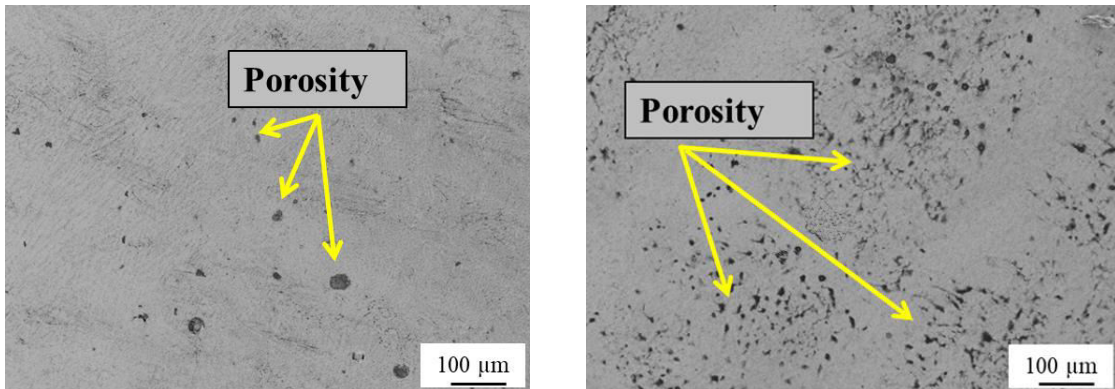


(a)



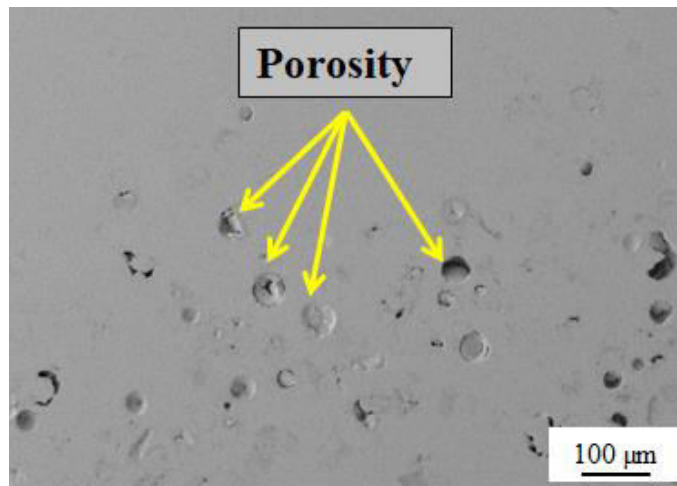
(b)

Fig. 4.9: (a) comparison of bulk density and relative density, and (b) average porosity, for optimized deposition of Co-Cr-Mo-2Ti; Co-Cr-Mo-4Ti; and Co-Cr-Mo-6Ti alloys.



(a)

(b)

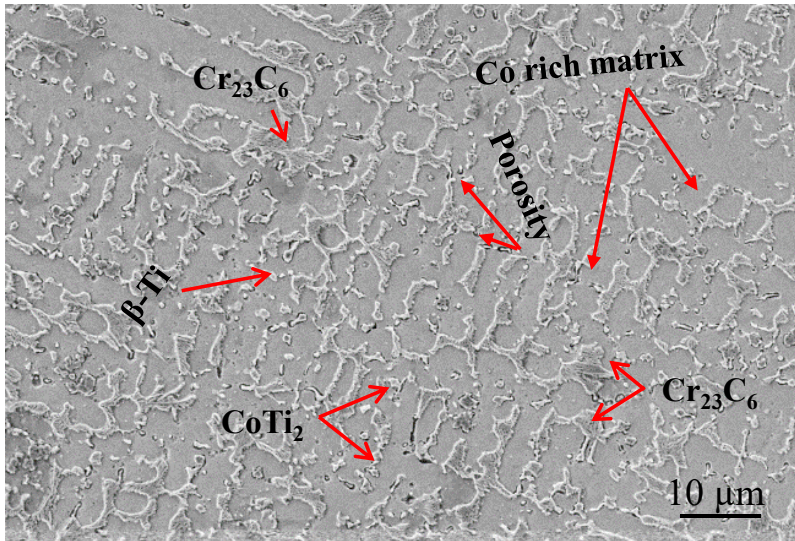


(c)

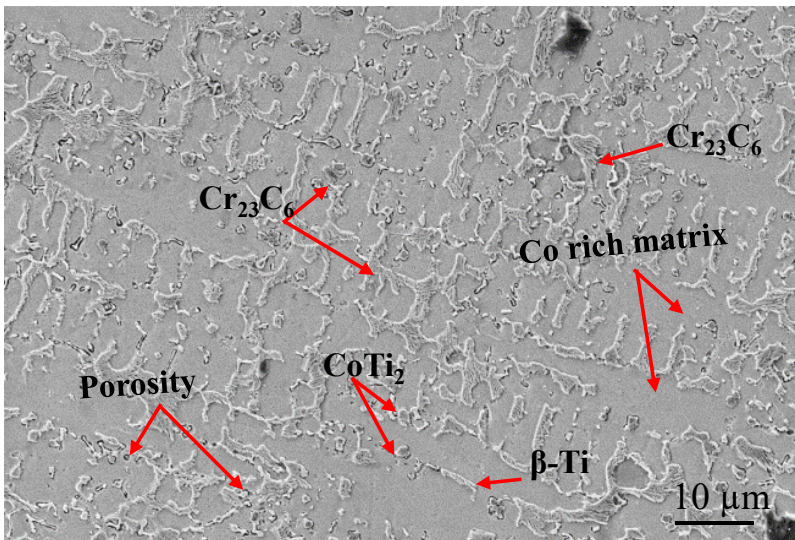
Fig. 4.10: Porosity distribution in the optimized deposition of: (a) Co-Cr-Mo-2Ti alloy, (b) Co-Cr-Mo-4Ti alloy, and (c) Co-Cr-Mo-6Ti alloy.

4.4 Analysis of Microstructure, Composition, and Phase Formation

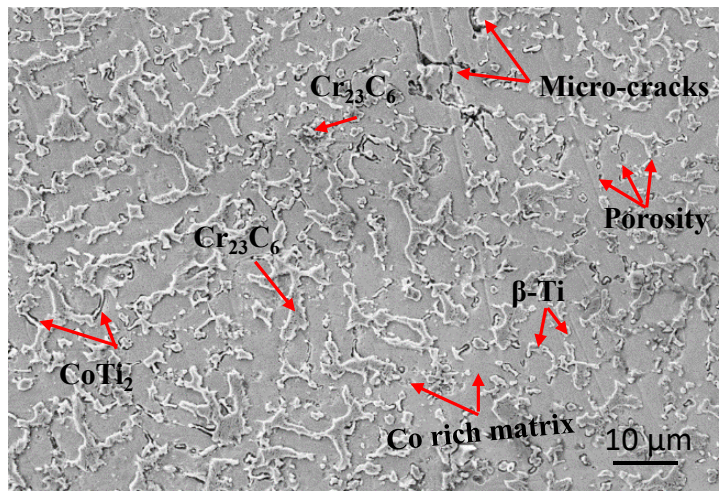
Figure 4.11 depicts SEM micrographs of the optimized depositions of Co-Cr-Mo-2Ti, Co-Cr-Mo-4Ti, and Co-Cr-Mo-6Ti alloys. Figure 4.12 presents EDS spectrum of selected region to obtained chemical composition of Co-Cr-Mo-xTi alloys (SEM micrographs of Co-Cr-Mo-xTi alloys used for EDS analysis has been shown in appendix 'C' for references) and table 4.4 depicts chemical composition of Co-Cr-Mo-xTi alloys to confirm their elemental composition with reference to measured chemical compositions after ball milling (shown in Fig. 3.2b and Table 3.2). Figure 4.13 shows the XRD peak patterns of Co-Cr-Mo, Co-Cr-Mo-2Ti, Co-Cr-Mo-4Ti, and Co-Cr-Mo-6Ti.



(a)



(b)



(c)

Fig. 4.11: SEM micrographs for the optimized deposition of alloy: (a) Co-Cr-Mo-2Ti, (b) Co-Cr-Mo-4Ti, and (c) Co-Cr-Mo-6Ti.

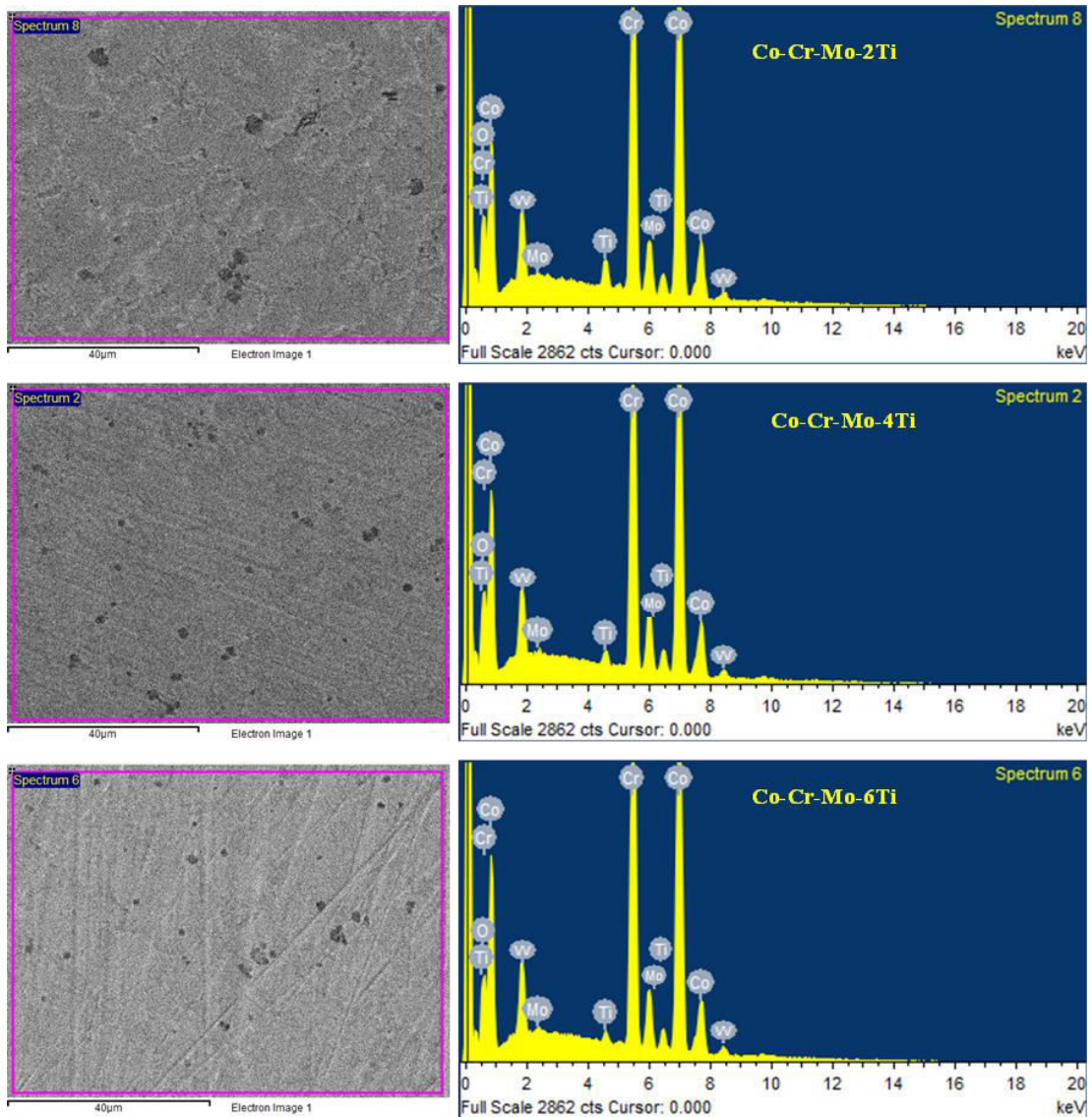


Fig. 4.12: EDS obtained spectrum of μ -PAAM deposited samples of Co-Cr-Mo-xTi alloys.

Table 4.4: Chemical composition (by wt.%) of multi-layer depositions of Co-Cr-Mo-xTi alloys obtained from their EDS spectrum.

Alloy	Co	Cr	Mo	Ti	O	W
Co-Cr-Mo-2Ti	64.1±0.7	29.1±0.1	4.06±0.1	2.08±0.1	0.12±0.1	1.09±0.1
Co-Cr-Mo-4Ti	61.1±0.2	29.2±0.1	4.05±0.01	4.03±0.1	0.16±0.2	1.44±0.6
Co-Cr-Mo-6Ti	59.9±0.8	29.05±0.1	4.07±0.1	6.01±0.1	0.13±0.1	1.32±0.4

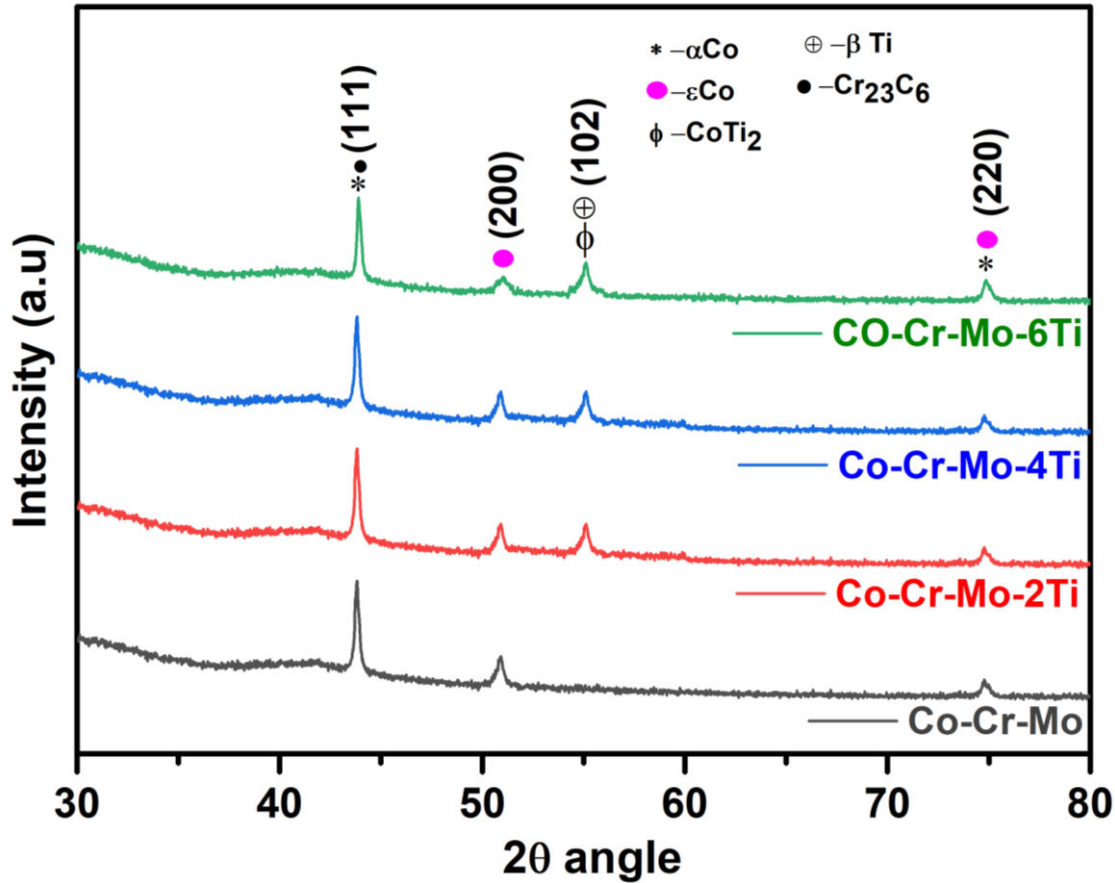


Fig. 4.13: XRD patterns for Co-Cr-Mo; Co-Cr-Mo-2Ti; Co-Cr-Mo-4Ti; and Co-Cr-Mo-6Ti, alloys.

Micrographs of Fig. 4.11 reveal that optimized depositions of Co-Cr-Mo-2Ti alloy (Fig. 4.11a) and Co-Cr-Mo-4Ti alloy (Fig. 4.11b) are porous and free from cracks. Whereas deposition of Co-Cr-Mo-6Ti alloy (Fig. 4.11c) is also porous but it shows micro-cracks which occur due to residual thermal stresses (**Wei et al. 2018**). Increase in Ti % in Co-Cr-Mo alloy increases solidification shrinkage due to its smaller thermal conductivity. Inadequate compensation for such solidification shrinkage after the deposition causes formation of micro-cracks. It can be observed from microstructure of Co-Cr-Mo-xTi alloys optimized deposition (Figs. 4.11a-4.11c) that they consist of Co-rich matrix, lamellar phases of chromium carbide at its grain boundaries, and inter-metallic phases of CoTi₂. EDS analysis of the optimized depositions of Co-Cr-Mo-xTi alloys in Fig. 4.12 reveal that wt.%

of their constituents are within the ranges as per Table 3.2. Table 4.4 depicts presence of tungsten 'W' varying in a range from 1.09 to 1.44 wt. % in the optimized depositions of Co-Cr-Mo-2/4/6Ti alloys respectively. Following are the three possible sources of tungsten: (i) ball milling in which alloy powders were mixed in the tungsten carbide vials using tungsten carbide balls, (ii) tungsten carbide electrode used in μ -PAAM process, and (iii) dilution of the base plate of Co-Cr-Mo alloy (which contains 4.6 wt.% of W) with the deposited Co-Cr-Mo-2/4/6 alloys. The following past works support that tungsten has insignificant influence on corrosion resistance with reference to biomedical applications. **Idil and Donaldson (2018)** reported use of tungsten for chronically implanted material due to its better corrosion resistance in the human body fluids enabled by the formation of protective passive layer of oxides on the exposed surface. **Naert (2011)** reported use of tungsten as an alloying element in Co-Cr-Mo alloys (61% Co; 26%Cr; 6% Mo; 5%W, and small amounts of Fe, Ce and C by wt.%) in prosthodontics applications by Wirobond® company (BEGO GmbH, Bremen, Germany). It helped to prevent corrosion failure. **Kohn (2011) and Hallab and Jacobs (2011)** reported use of cobalt-based wrought alloy Co-20Cr-15W-10Ni for the orthopaedic applications and it did not cause any corrosion failure. Biocompatibility evaluation of have found overall average values of cell viability for the optimized deposition samples of Co-Cr-Mo-2Ti; Co-Cr-Mo-4Ti; and Co-Cr-Mo-6Ti alloys as 92%; 95%; and 85%, respectively and overall average of the released amounts of Co, Cr, Mo, and Ti ions by the optimized deposition samples of Co-Cr-Mo-xTi alloys are 126; 41;11, and 9 ppb respectively (as shown in Fig. 4.5). It implies that presence of tungsten in Co-Cr-Mo-2Ti; Co-Cr-Mo-4Ti; and Co-Cr-Mo-6Ti alloys does not adversely affect their biocompatibility.

Peak positions of different phases in XRD patterns for optimized depositions of Co-Cr-Mo, Co-Cr-Mo-2Ti, Co-Cr-Mo-4Ti, and Co-Cr-Mo-6Ti alloys, as shown in Fig. 4.13, reveal presence of α -Co phase having face centered cubic (FCC) crystal structure (JCPDS#15-0806), ϵ -Co phase having hexagonal closed packed (HCP) crystal structure (JCPDS#05-0727), β -titanium phase having body centered cubic (BCC) crystal structure (JCPDS#44-1288), inter-metallic phases of CoTi_2 (JCPDS#07-0141), and lamellar chromium carbide (i.e., Cr_{23}C_6) (JCPDS#35-0783). Comparison of peak patterns of Co-Cr-Mo-xTi alloys with Co-Cr-Mo alloy reveals that the phases CoTi_2 and β -Ti are formed at 2θ angle of 55.5 degrees due to addition of Ti to Co-Cr-Mo alloy because peak corresponding to CoTi_2 phase is absent in Co-Cr-Mo alloy but present in Co-Cr-Mo-2/4/6Ti alloys as shown in Fig. 4.13. These results agree with the findings of μ -PAAM manufactured Co-Cr-Mo alloy (**Sawant and Jain 2017; 2018b, Kumar and Jain 2020**), and SLM-manufactured Co-Cr-W alloy (**Lu et al. 2015**) and Co-Cr-Mo alloy (**Barucca et**

al. 2015; AlMangour *et al.* 2020). Analysis of microstructures of the optimized depositions of Co-Cr-Mo-xTi alloys (Fig. 4.11 a-c), EDS results (Fig. 4.12), and XRD results (Fig. 4.13) lead to conclude that (i) Co-rich matrix is associated with peaks of ϵ -Co (HCP) and α -Co (FCC) phases, and (ii) peaks of precipitated intermetallic phases of CoTi_2 and Cr_{23}C_6 are associated with inter-dendritic phases. These results are in line with the findings for Co-Cr-Mo alloy (Gupta 2005) and Co-Cr-Ti alloy (Gupta 2001). Straumal *et al.* (2019) also revealed presence of two-phase cobalt rich matrix having dendritic microstructure, lamellar chromium carbide phase, and intermetallic phase of CoTi_2 from the phase diagram obtained from CALPHAD software as well as EDS and XRD analysis of microstructure. Cobalt phases ϵ -Co (HCP) and α -Co (FCC) are formed through a eutectic reaction at 1397°C (Gupta 2005; Gupta 2001). Alloying elements nickel and iron stabilize α -Co phase by decreasing its transformation temperature. Whereas, Mo increases transformation temperature and stabilizes ϵ -Co phase (Nová *et al.* 2017). Presence of Cr and carbon can initiate the precipitation process at 1000°C and form chromium rich carbide phases by eutectic reaction. Chromium carbide phase on grain boundaries impart more wear and corrosion resistance by precipitation hardening (Hirota *et al.* 2005). Addition of Ti in Co-Cr-Mo alloy formed β -Ti and intermetallic CoTi_2 phase. Titanium undergoes an allotropic transformation from 882°C to its melting temperature (i.e., 1668°C) in which α -Ti (HCP) phase converts to β -Ti (BCC) phase and remains stable up to its melting point. Phase β -Ti is stabilized by adding Co, Cr, Mo which retain it during rapid cooling from a range of 700°C to 1050°C . Phase β -Ti offers lower elastic modulus, higher ductility, good corrosion resistance, solid solution strengthening, low fusion temperature, and good weldability. Phases of intermetallic compound CoTi_2 are formed through a peritectic reaction occurring at 1058°C .

EBSD images of the optimized depositions of Co-Cr-Mo-xTi alloys (obtained from IIT Bombay) were studied to understand mechanisms of their phase changes and grain growth. EBSD data provided band contrast map, phase map, and inverse pole figure map which signify quantitative results of different crystal structure, their orientation, morphology of individual grains, collective texture of alloys, and crystallographic relationships between different phases present in the optimized depositions. Figure 4.14 present band contrast maps, phase maps, and inverse pole figure maps for the optimized depositions of Co-Cr-Mo-2Ti; Co-Cr-Mo-4Ti; and Co-Cr-Mo-6Ti alloys and Fig. 4.15 depicts pole figures of different phases presents in them. Table 4.5 shows quantitative summary of different phases present in them based on the image analysis of multiple EBSD scans performed at IIT Bombay.

Table 4.5: Percentage of different phases in the optimized deposition samples of Co-Cr-Mo-2/4/6Ti alloys.

Sample	ϵ -Co (HCP)	α -Co (FCC)	Chromium carbide	β -Ti
Co-Cr-Mo-2Ti	73%	8%	10%	9%
Co-Cr-Mo-4Ti	70%	9%	11%	10%
Co-Cr-Mo-6Ti	75%	8%	9%	9%

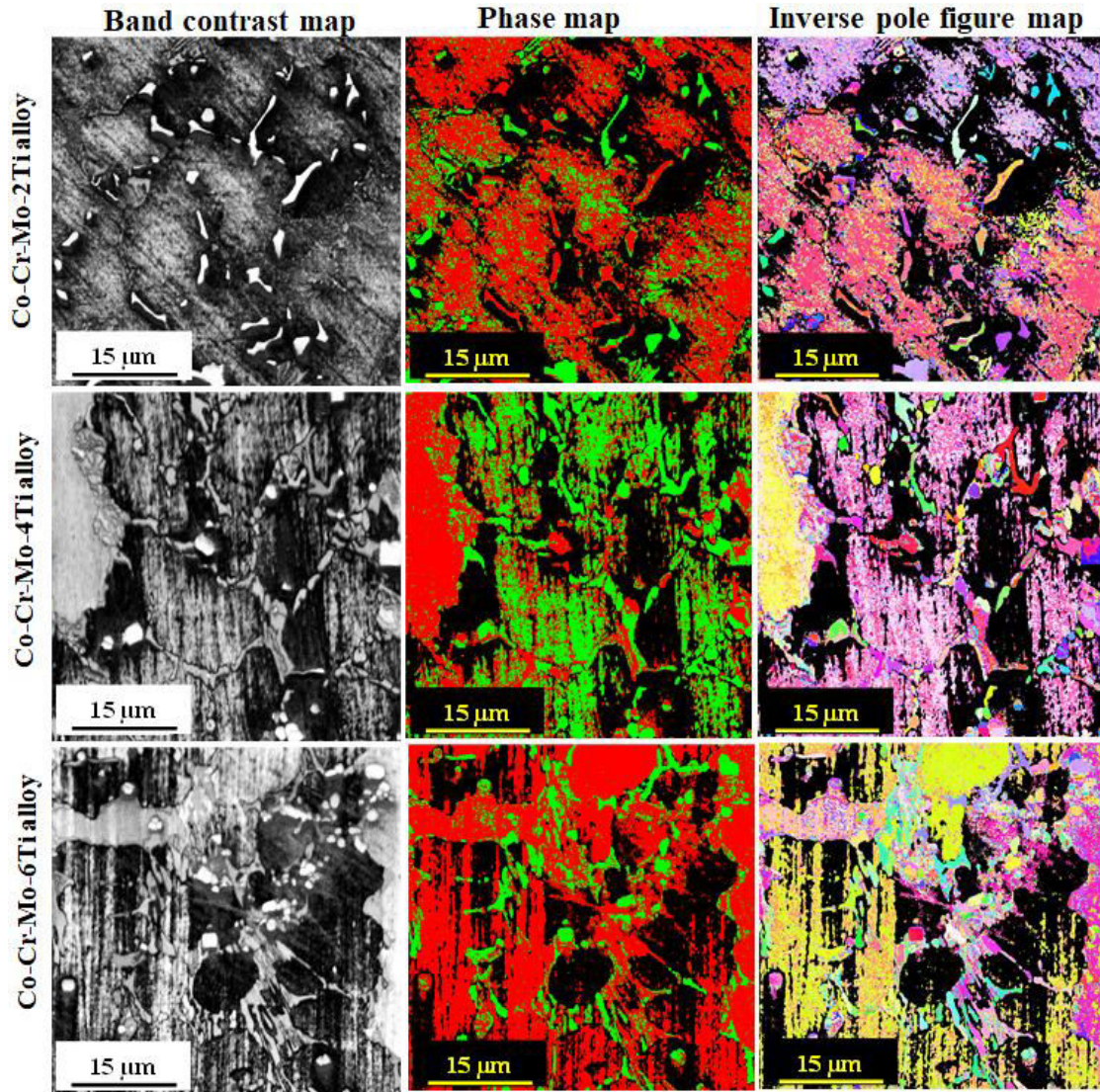


Fig. 4.14: Band contrast maps, phase maps and inverse pole figure maps obtained from EBSD for the optimized deposition of Co-Cr-Mo-2Ti alloy, Co-Cr-Mo-4Ti alloy, and Co-Cr-Mo-6Ti alloy.

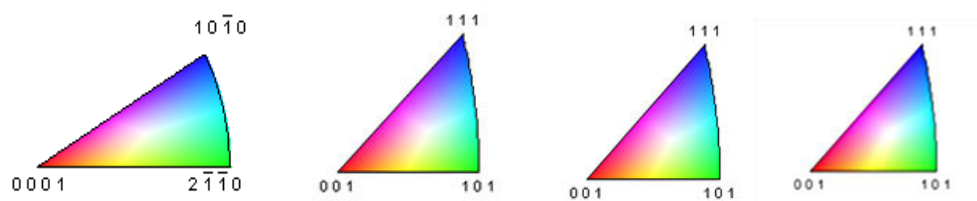
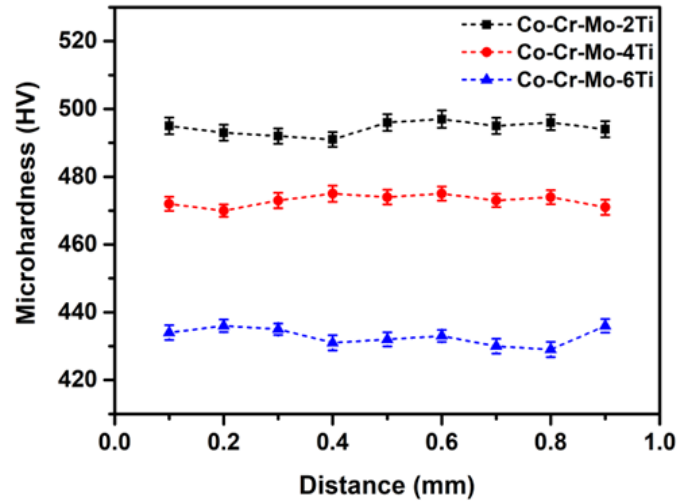


Fig. 4.15: Pole figure obtained from EBSD for ϵ -Co (HCP), α -Co (FCC), Cr and β -Ti phases.

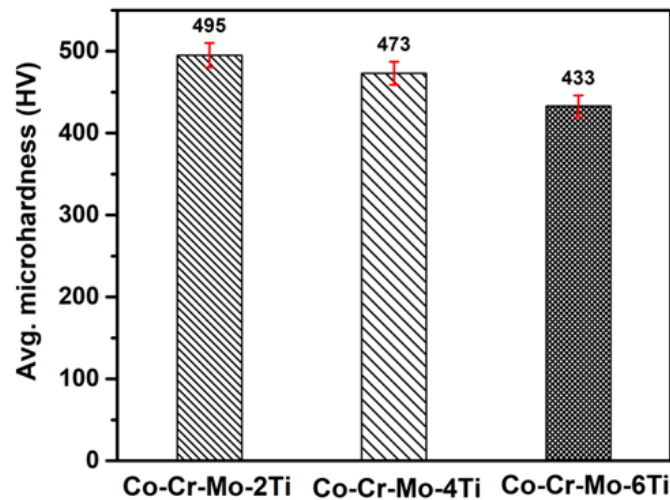
Phase map of optimized depositions of alloys Co-Cr-Mo-2Ti, Co-Cr-Mo-4Ti and Co-Cr-Mo-6Ti reveal presence of phases ϵ -Co (in red color), α -Co (in red color), β -Ti (in green color), and lamellar chromium carbide i.e., Cr_{23}C_6 (in green color) and intermetallic CoTi_2 (mixed green and black color). It agrees with the observations of their SEM micrographs (Figs. 4.11a-4.11c) and phase analysis by XRD (Fig. 4.13). This chromium carbide phase is commonly reported in EBSD analysis of cast Co-Cr-Mo alloy (Priya et al. 2020) and AM manufactured Co-Cr-Mo alloy (Wang et al. 2020). Inverse pole figure maps of the optimized depositions do not show preferential orientation of grains. Phase ϵ -Co is randomly distributed along with α -Co phase. EBSD results enables grain orientation which generate pole figures for the phases present in the test sample. Pole figures shown in Fig. 4.15 indicate orientation relation between HCP $\{0001\}$ and FCC $\{111\}$ phases of the optimized depositions. These results agree with the results of Wang et al. (2021) and Hedberg et al. (2014). Kwak et al. (2021) also analyzed phase map from EBSD, image quality map and inverse pole figure map of AM manufactured Ti layer on Co-Cr alloy for knee implant. They revealed that % of β -Ti phase increases as the annealing temperature increases due to enhanced diffusivity of Cr and Co into Ti at high temperature. Phase transformation of Co from FCC to HCP phase was observed in the Co-Cr base. However, transformation from FCC to HCP phase is lethargic, thus FCC phase typically persist after cooling at ambient temperature (Ocampo et al. 2002). It can be observed from Table 4.5 that ϵ -Co is present in higher % in the optimized deposition samples i.e., 73% in Co-Cr-Mo-2Ti; 70% in Co-Cr-Mo-4Ti; 75% in Co-Cr-Mo-6Ti alloy whereas % amount of Cr, α -Co phase, and β -Ti phase are almost equal in these alloys i.e., 8-10%. This observation can be attributed to porosity presence in Co-Cr-Mo-xTi alloys. Lu et al. (2015) reported that the presence of porosity results in a higher proportion of ϵ -Co phase in SLM manufactured Co-Cr-W alloy, which can also be observed in the EBSD analysis of μ -PAAM manufactured Co-Cr-Mo-xTi alloys (Fig. 4.14 and Table 4.5). Though presence of tungsten is indicated in EDS analysis of multi-layer deposition samples of Co-Cr-Mo-xTi alloys as presented in Fig. 4.12 and Table 4.4 but it is not indicated in their XRD plots (Fig. 4.13) and EBSD images (Fig. 4.14 and Table 4.5). Further investigations using transmission electron microscopy (TEM) or electron probe micro-analyzer (EPMA) based wavelength dispersive X-ray spectroscopy (WDS) may help in detailed analysis of chemical compositions of Co-Cr-Mo-xTi alloys. Unfortunately, these facilities are not available at IIT Indore at present.

4.5 Microhardness Results

Fig. 4.16a demonstrates microhardness profile and Fig. 4.16b depicts average microhardness of the optimized depositions of Co-Cr-Mo-2Ti alloy; Co-Cr-Mo-4Ti alloy; and Co-Cr-Mo-6Ti alloy.



(a)



(b)

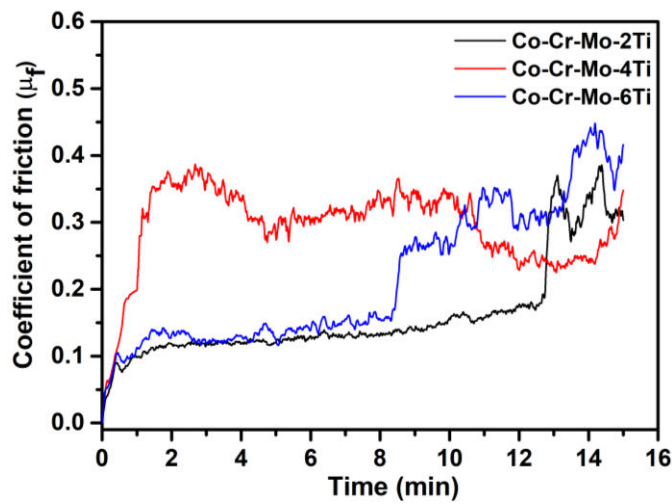
Fig. 4.16: Results of microhardness evaluation: (a) microhardness profile, and (b) average microhardness for the optimized depositions of Co-Cr-Mo-xTi alloys.

It can be observed from Fig. 4.16a that optimized deposition of Co-Cr-Mo-2Ti alloy has maximum microhardness followed by optimized depositions of Co-Cr-Mo-4Ti alloy; and Co-Cr-Mo-6Ti alloy. It is due to the facts that increasing % of Ti in Co-Cr-Mo alloy increases formation of β -Ti and intermetallic CoTi_2 phases which have less hardness than the carbide phases. Average microhardness of optimized deposition of Co-Cr-Mo-2Ti alloy is found to be the highest (i.e., 495 HV) followed by 473 HV for Co-Cr-Mo-4Ti alloy; and 433 HV for Co-Cr-Mo-6Ti alloy as shown in Fig. 4.16b. Decrease in average microhardness values with increase in % of Ti the optimized depositions is due to increase in porosity (Fig. 4.8b) because a dense material has higher microhardness and vice versa. Smaller difference

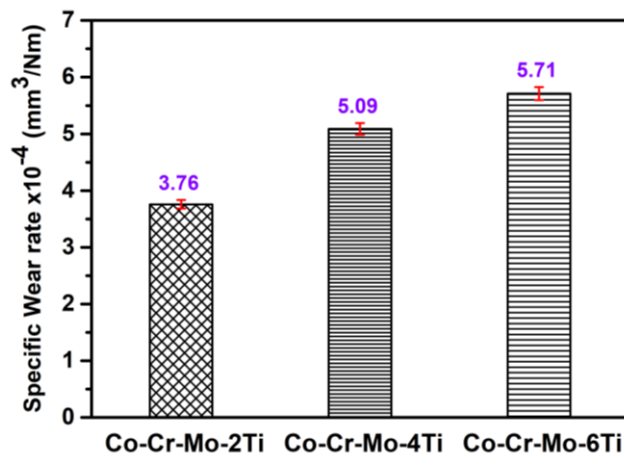
in average microhardness values of Co-Cr-Mo-4Ti alloy and Co-Cr-Mo-2Ti alloy (i.e., 22 HV) than that between Co-Cr-Mo-6Ti alloy and Co-Cr-Mo-2Ti alloy (i.e., 62 HV) again signifies the fact Co-Cr-Mo-4Ti alloy optimized deposition has smaller size pores and their more uniform distribution as highlighted in Fig. 4.10b.

4.6 Results for Wear Resistance

Biocompatible metallic materials used in knee implants suffer their failure due to their continuous wear. Moreover, mixing of the worn particles in the human blood causes allergic reactions. Therefore, higher wear resistance is an essential requirement for knee implant materials. It is determined by surface finish and surface integrity of the implant, and porosity and microhardness of the implant material. Figure 4.17a depicts fluctuation in coefficient of friction with wear time for the optimized depositions of Co-Cr-Mo-2Ti alloy; Co-Cr-Mo-4Ti alloy; and Co-Cr-Mo-6Ti alloy. Figure 4.17b presents specific wear rate for them and Figs. 4.18a-4.18c depicts optical micrographs of their wear track giving insights to their wear mechanisms.

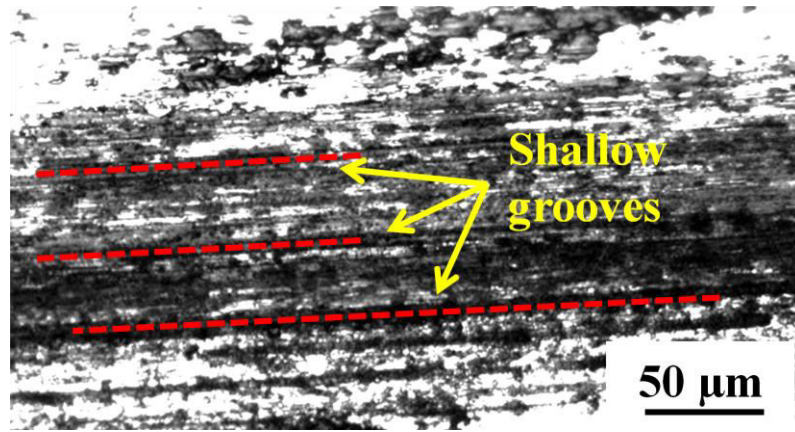


(a)

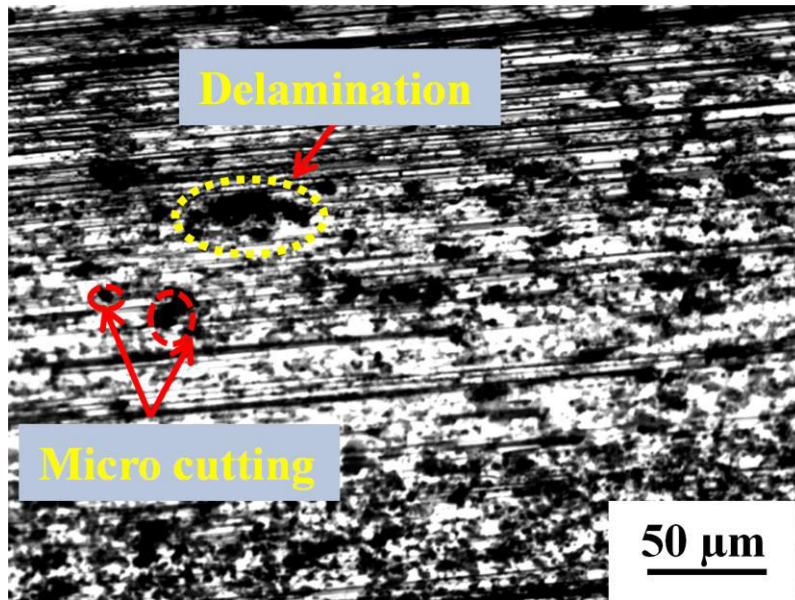


(b)

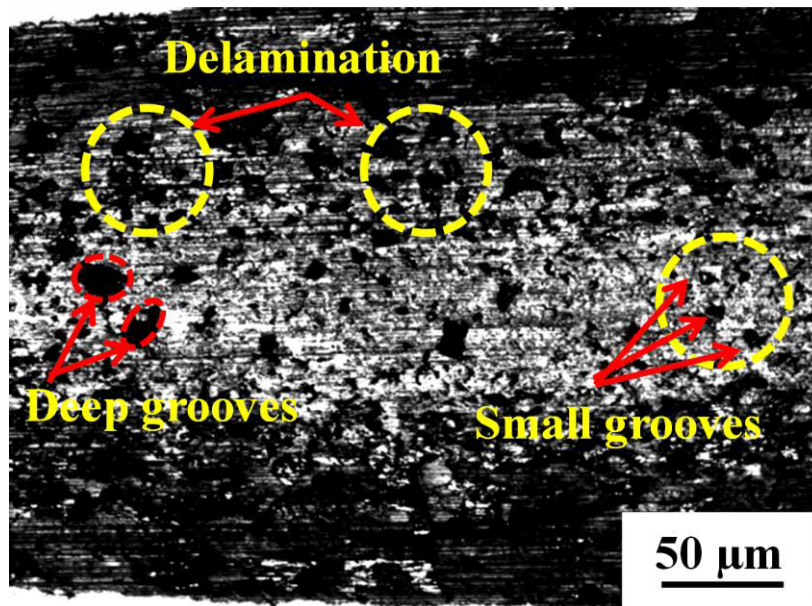
Fig. 4.17: (a) Variation of coefficient of friction for the optimized deposition (b) specific wear rate for the optimized depositions of Co-Cr-Mo-Ti alloys.



(a)



(b)



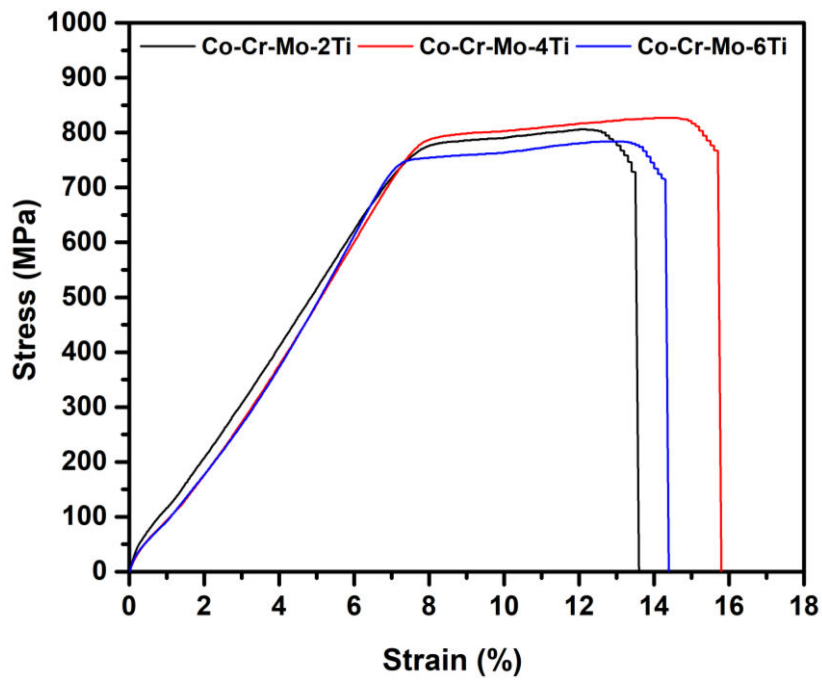
(c)

Fig. 4.18: Optical micrographs of wear track for the optimized deposition of: (a) Co-Cr-Mo-2Ti alloy, (b) Co-Cr-Mo-4Ti alloy, and (c) Co-Cr-Mo-6Ti alloy.

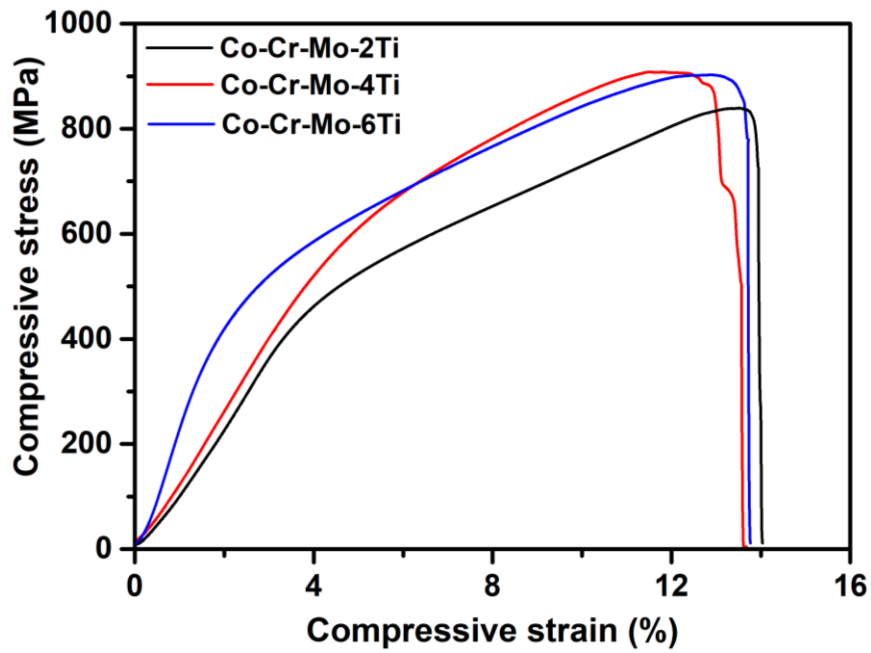
Fig. 4.17a shows that coefficient of friction for the optimized depositions of Co-Cr-Mo-2Ti; and Co-Cr-Mo-4Ti alloys have fewer fluctuations than that for Co-Cr-Mo-6Ti alloy. Fig. 4.17b depicts that Co-Cr-Mo-2Ti optimized deposition has minimum specific wear rate ($3.76 \times 10^{-4} \text{ mm}^3/\text{Nm}$), Co-Cr-Mo-6Ti optimized deposition has its maximum value ($5.71 \times 10^{-4} \text{ mm}^3/\text{Nm}$). Optical micrograph of worn track on optimized deposition of Co-Cr-Mo-2Ti alloy (Fig. 4.18a) shows micro-ploughing induced extremely shallow grooves resulting in less wear debris and hence greater wear resistance. Delamination and micro-cutting induced by recurrent ploughing that happened during wear of Co-Cr-Mo-4Ti optimized deposition can be seen in its optical micrograph (Fig. 4.18b). Micro-cutting occurs due to separation of material from the surface in the form of wear debris or microchips. Optical micrograph of worn surface of Co-Cr-Mo-6Ti optimized deposition (Fig. 4.18c) indicates establishment of deep grooves and delamination caused by repetitive ploughing resulting in increased material removal process by spalling. Formation of deep grooves is due to higher friction and poor wear resistance which leads to three-body abrasive wear during relative motion occurring between two layers by trapping the metallic wear debris. Observations of Figs 4.17-4.18 can be explained by change in microhardness (Fig. 4.16b) and porosity (Fig. 4.9b) of Co-Cr-Mo alloys with change in % of Ti. Decrease in microhardness and increase in porosity with increase in % of Ti in Co-Cr-Mo alloys increase coefficient of friction, specific wear rate, and wear volume. This is because ploughing, and delamination are caused by decreased microhardness and more porosity.

4.7 Results of Tensile and Compression Tests

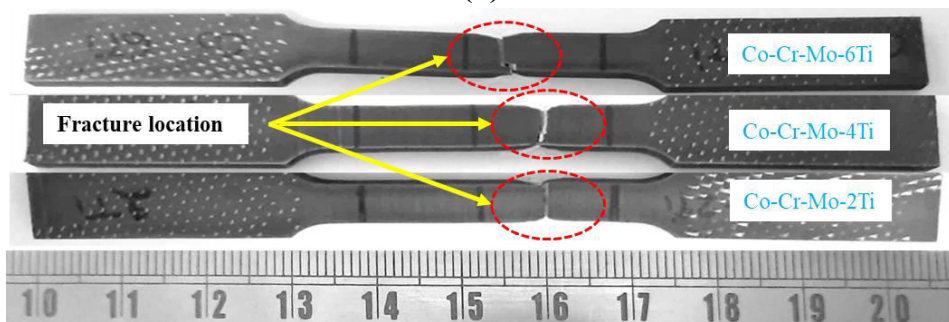
Figures 4.19a and 4.19b depict engineering stress-strain diagram for the optimized deposition samples of Co-Cr-Mo-2/4/6Ti alloys obtained in their tensile test and compression test respectively and Fig. 4.19c shows photograph of the tensile fractured samples. Table 4.6 presents mean values and standard deviation of yield strength, ultimate strength, % elongation, and elastic modulus of Co-Cr-Mo-xTi alloys obtained from their tensile and compressive tests. The tensile test results of Co-Cr-Mo-xTi alloys are compared with the values of cast and forged Co-Cr-Mo alloy (i.e., ASTM F75) used for orthopedic implant applications (**Tanzi et al. 2019**).



(a)



(b)



(c)

Fig. 4.19: (a) Tensile stress-strain diagram for Co-Cr-Mo-xTi alloys, (b) compressive stress-strain diagram for Co-Cr-Mo-xTi alloys, and (c) photograph of tensile fractured samples.

Table 4.6: Mean values and standard deviation of yield strength, ultimate strength, % elongation, and elastic modulus of Co-Cr-Mo-2/4/6Ti alloys obtained from their tensile and compressive tests, tensile properties of cast and forged Co-Cr-Mo (i.e., ASTM F75) alloy.

Alloy	Yield strength (its standard deviation) (MPa)		Ultimate strength (its standard deviation) (MPa)		% elongation (for tensile test) or % reduction in area (for compression test) and its SD)		Modulus of elasticity (its standard deviation) (GPa)	
	Tensile	Compressive	Tensile	Compressive	Tensile	Compressive	Tensile	Compressive
Co-Cr-Mo-2Ti	774 (6.7)	405 (4.7)	792 (9.4)	845 (5.7)	13.7 (1.8)	14.1 (1.3)	212 (7.1)	216 (5.3)
Co-Cr-Mo-4Ti	789 (7.9)	455 (5.8)	817 (10.2)	906 (7.8)	15.8 (1.2)	13.5 (1.1)	207 (7.9)	211 (4.5)
Co-Cr-Mo-6Ti	734 (5.8)	570 (6.1)	769 (8.7)	897 (3.7)	14.7 (0.9)	13.7 (1.5)	201 (6.5)	204 (6.5)
Cast Co-Cr-Mo (ASTM F75)	450	--	655	--	--	--	210	--
Forged Co-Cr-Mo (ASTM F75)	841	--	1277	--	--	--	253	--

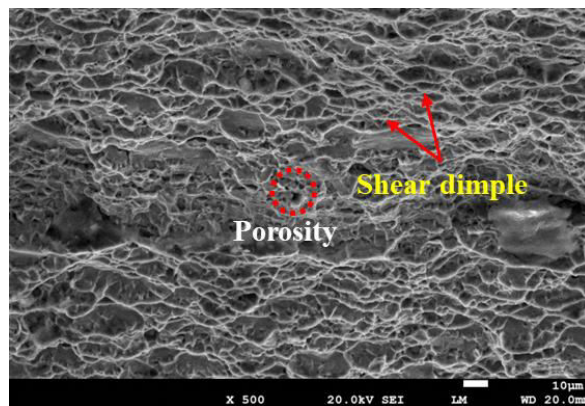
It can be observed from Fig. 4.19a that tensile stress increases almost linearly with tensile strain till yielding for the optimized deposition samples of all three Co-Cr-Mo-xTi alloys. There is no significant change in tensile stress with strain after the yielding therefore tensile stress-strain curves from yield to ultimate strength are almost horizontal lines and after that they become vertical lines indicating samples fracturing at ultimate tensile strength for all three Co-Cr-Mo-xTi alloys. It can also be observed from Fig. 4.19b that compressive stress increases linearly up to compressive yield point at almost same rate for Co-Cr-Mo-2 Ti and Co-Cr-Mo-4Ti alloys and at slightly higher rate for Co-Cr-Mo-6Ti alloy. The compressive stress increases linearly at a reduced rate from yield point to compressive ultimate strength for Co-Cr-Mo-2/4/6Ti alloys and become vertical lines indicating samples fracturing at ultimate compressive strength for all three Co-Cr-Mo-2/4/6Ti alloys. Fig 4.19c depicts that the tensile samples of Co-Cr-Mo-2/4/6Ti alloys fractured within the gauge length with slight localized necking indicating strain localization in a very small region before their ductile fracture.

Following are the observations from Table 4.6 along with their explanations: (i) Co-Cr-4Ti alloy has considerably higher values of tensile and compressive yield strength, tensile and compressive ultimate strength, and tensile strain (i.e., indicative of ductility) than Co-Cr-Mo-2Ti and Co-Cr-Mo-6Ti alloys. These differences may be attributed to differences in porosity and its distribution, presence of the micro-cracks (as shown in Fig. 4.11), cooling behavior during successive layers of deposition, and fraction of the phases formed during deposition by the μ -PAAM process, (ii) tensile and compressive modulus of elasticity of

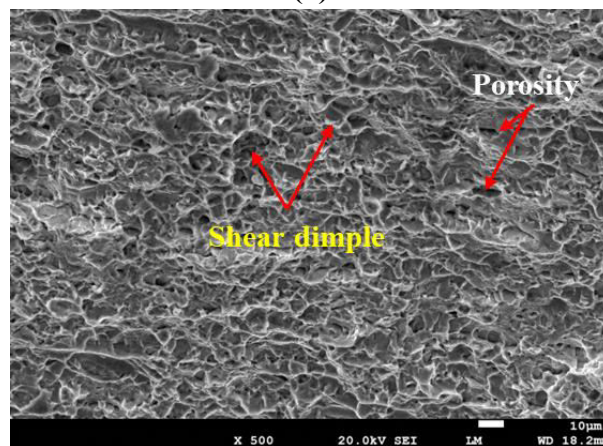
Co-Cr-Mo-xTi alloys decrease with increase in wt.% of titanium. This is due smaller value of modulus of elasticity of Ti (i.e., 120 GPa) than that of Co-Cr-Mo alloy (i.e., 220-240 GPa) i.e., increase in wt. of Ti will reduce modulus of elasticity of the resultant alloy. It implies that higher titanium containing alloy will minimize the stress-shielding effect due to reduced difference between elastic moduli of it and human bones (**Geetha et al. 2009**). Tensile and compressive modulus of elasticity vary in a range from 201 to 212 GPa and 204 to 216 GPa respectively. This is comparable with the cast Co-Cr-Mo alloy (i.e., 210 GPa) but much lower than the forged Co-Cr-Mo alloy i.e., 253 GPa (**Tanzi et al. 2019**), (iii) tensile yield strength is significantly higher than compressive yield strength whereas ultimate compressive strength is significantly higher than ultimate tensile strength for all three Co-Cr-Mo-2/4/6Ti alloys. This may be due to Bauschinger effect which is defined as a decrease in compressive yield strength of a material as a result of prior deformation in tension, (iv) tensile and compressive strain for all three Co-Cr-Mo-2/4/6Ti alloys are almost same indicating their same amount of ductility under tension and compression.

4.8 Results of Tensile and Compression Fractography

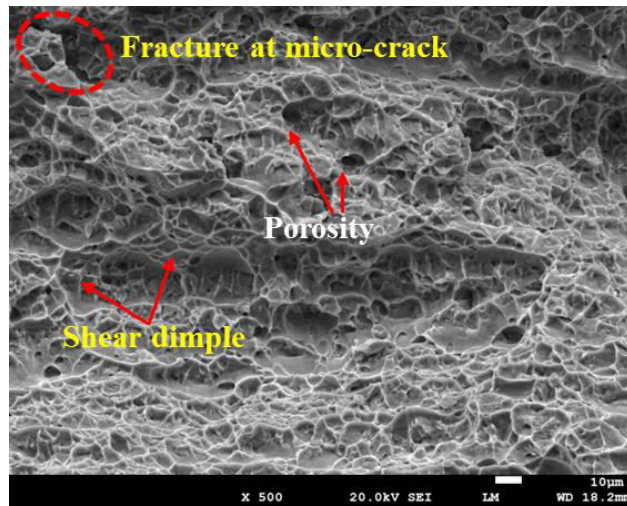
Figures 4.20 and 4.21 present SEM images depicting fractography of tensile and compression test specimen of Co-Cr-Mo-2Ti alloy (Figs. 4.20a and 4.21a), Co-Cr-Mo-4Ti alloy (Figs. 4.20b and 4.21b), and Co-Cr-Mo-6Ti alloy (Figs. 4.20c and 4.21c).



(a)

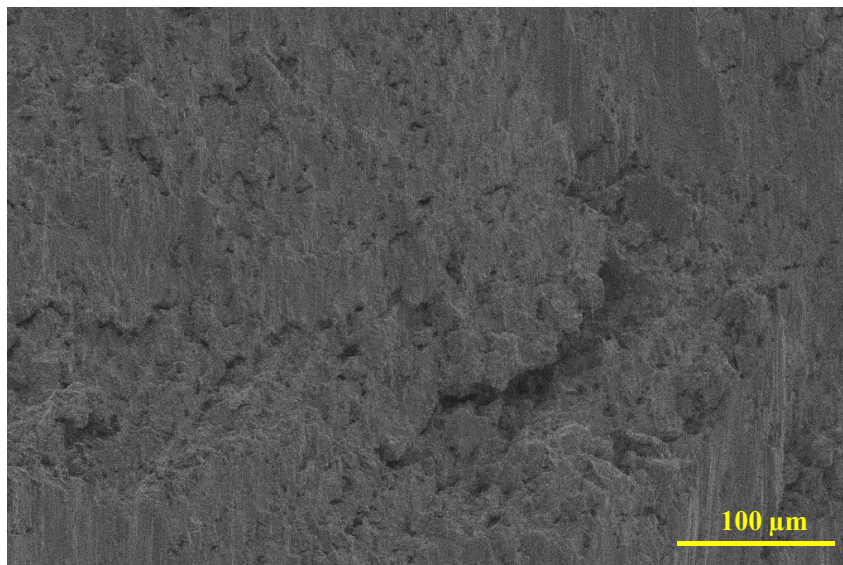


(b)

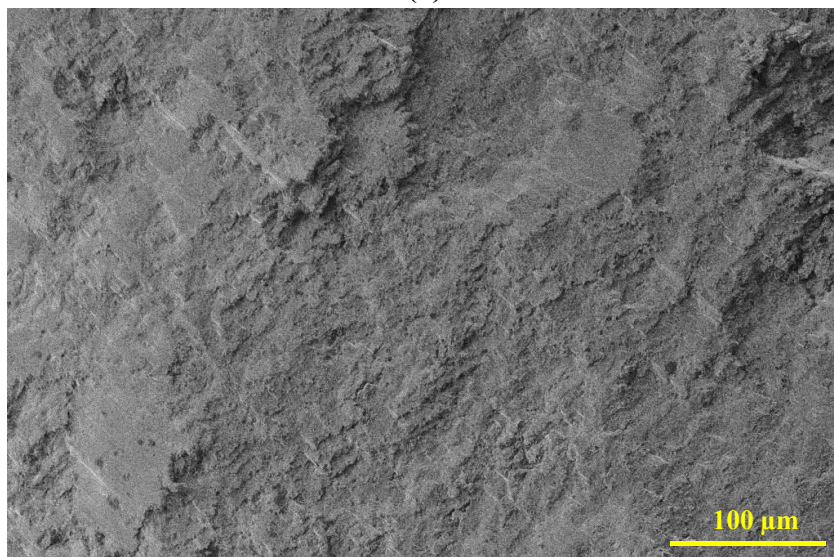


(c)

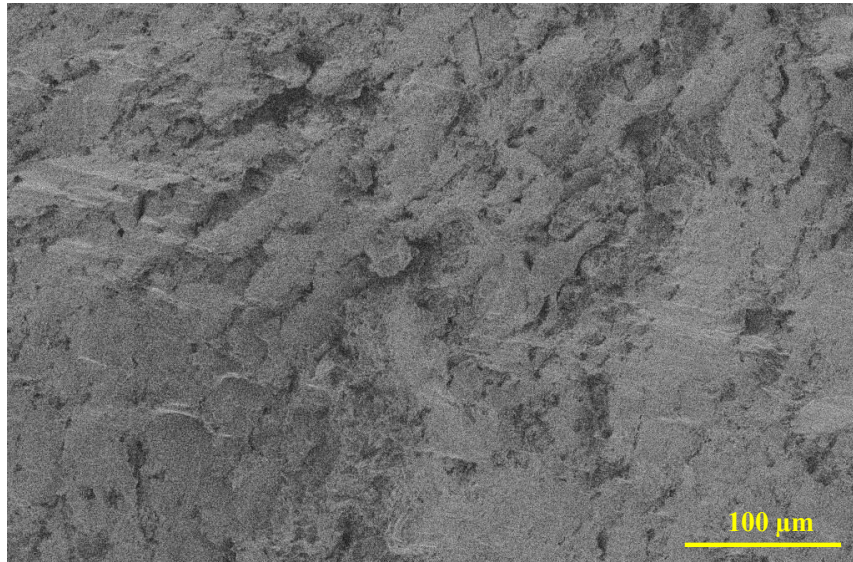
Fig. 4.20: SEM images showing fractography of tensile test samples of (a) Co-Cr-Mo-2Ti, (b) Co-Cr-Mo-4Ti, and (c) Co-Cr-Mo-6Ti alloy.



(a)



(b)



(c)

Fig. 4.21: SEM images showing fractography of compression testing samples of (a) Co-Cr-Mo-2Ti, (b) Co-Cr-Mo-4Ti, and (c) Co-Cr-Mo-6Ti alloy.

Shear dimples can be seen in fractography micrographs of tensile samples of Co-Cr-Mo-xTi alloys as shown in Figs. 4.20a-4.20c indicating their ductile mode of fracture which is supported by their % elongation values. Porosity is also seen in these images. Fractography micrographs of Co-Cr-Mo-6Ti (Fig. 4.20c) shows occurrence of fracture at micro-cracks which is also observed in its microstructure (Fig. 4.11c). Fractography of compression test samples of Co-Cr-Mo-xTi alloys as shown in Fig. 4.21 indicate presence of shear dimples suggesting their ductile mode of fracture. Tensile and compression test fractography images of Co-Cr-Mo-xTi alloys are similar to that of Co-Cr-Mo alloy (**Kilmametov et al. 2018**). Ductile mode of fracture of Co-Cr-Mo-xTi alloys under tension and compression may be due to metastable α -Co and β -Ti phases which play key role in influencing kinetic changes of α -Co phase during tensile and compression deformation, and fracture behavior in Co-Cr-Mo-xTi alloys. Cobalt and chromium are β -Ti phase stabilizing elements which increases β -Ti phase in Co-Ti based alloys. Therefore, their inclusion acts as the driving force for influencing kinetic changes of α -Co phase (**Gupta 2001; Gupta 2005; Straumal et al. 2019**). Similar results have been reported by other researchers also (**Mantrala et al. 2015; Mergulhão and Neves 2018; Amanov 2021**). Based upon results of tensile and compression tests, Co-Cr-Mo-4Ti alloy is found to be better material for knee implant.

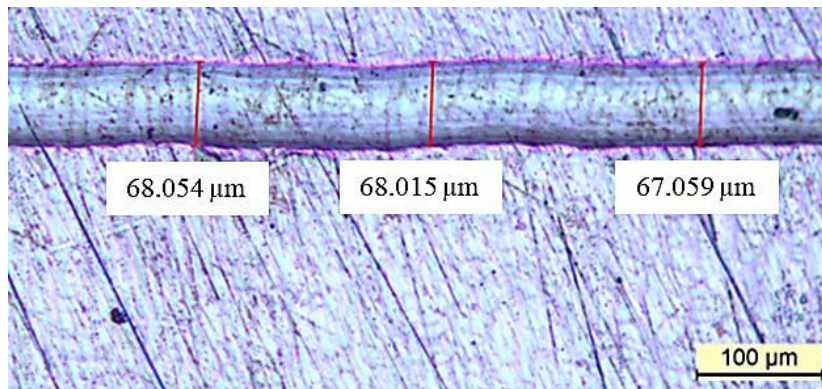
4.9 Results for Abrasion Resistance

Figures 4.22a, 4.22b, and 4.22c depict optical micrographs of scratch tracks developed on the optimized deposition samples of Co-Cr-Mo-2Ti, Co-Cr-Mo-4Ti, Co-Cr-Mo-6Ti alloys respectively during evaluation of their abrasive resistance. Table 4.7 presents mean

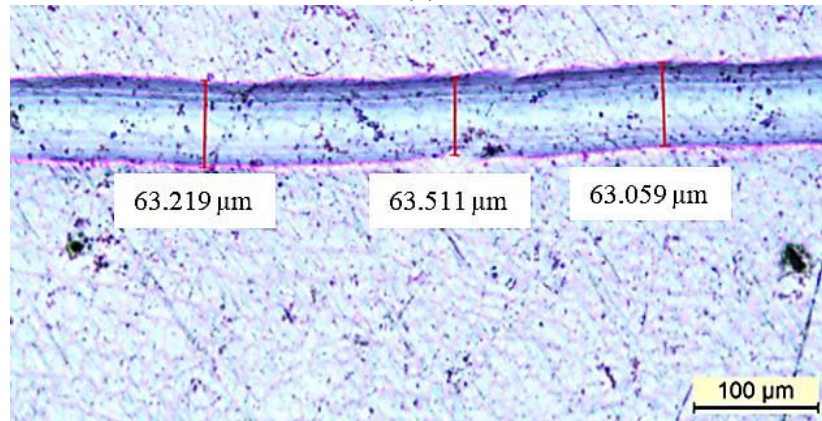
values (along with corresponding standard deviation) of scratch track width and coefficient of friction, and computed values of scratch hardness number for them.

Table 4.7: Mean values and standard deviation (SD) of scratch track width and coefficient of friction, and computed values of scratch hardness number for the optimized deposition samples of Co-Cr-Mo-xTi alloys.

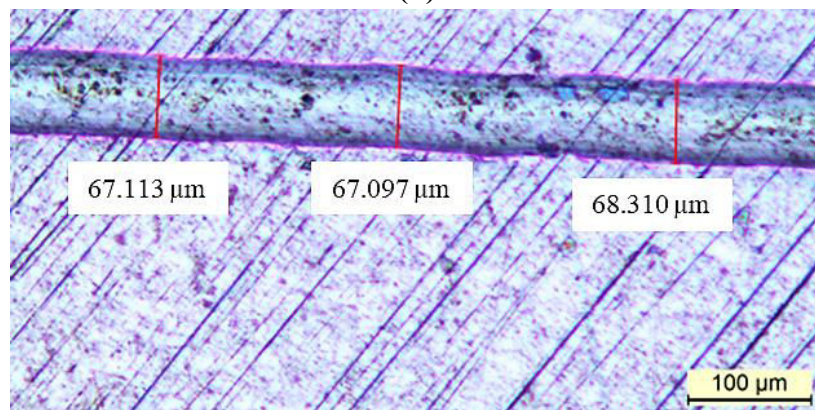
Alloy	Average scratch track width (SD) (μm)	Mean value of coefficient of friction (SD)	Scratch hardness number (GPa)
Co-Cr-Mo-2Ti	67.71 (0.460)	0.125 (0.039)	5.55
Co-Cr-Mo-4Ti	63.26 (0.187)	0.115 (0.038)	7.86
Co-Cr-Mo-6Ti	67.51 (0.568)	0.121 (0.040)	5.76



(a)



(b)



(c)

Fig: 4.22. Optical micrographs of scratches on the optimized deposition samples of (a) Co-Cr-Mo-2Ti, (b) Co-Cr-Mo-4Ti, and (c) Co-Cr-Mo-6Ti alloy.

It can be concluded from Fig. 4.22 and Table 4.7 that Co-Cr-Mo-4Ti (Fig. 4.22b) alloy has minimum value of avg. scratch track width and coefficient of friction and maximum value of scratch hardness number (i.e., 63.26 μm ; 0.115; and 7.86 GPa) imparting it better abrasion resistance to it due to presence of fine lamellar carbide phases. Co-Cr-Mo-2Ti alloy maximum value of avg. scratch track width and coefficient of friction and minimum value of scratch hardness number (i.e., 67.71 μm ; 0.125; and 5.55 GPa) imparting least abrasion resistance to it due to presence of coarse lamellar carbide phases. These values are in between for Co-Cr-Mo-6Ti alloy (i.e., 67.51 μm ; 0.121; and 5.76 GPa) alloy. Based upon results of abrasion resistance, Co-Cr-Mo-4Ti alloy is a better material for knee implant. Table 4.8a summarizes the results of cell viability, release of metallic ions, corrosion rate, density, porosity, type of pores, hardness, and tensile and compressive properties for the optimized deposition samples of Co-Cr-Mo-xTi alloys by the μ -PAAM process. Table 4.8b compares elastic modulus of Co, Cr, and Mo based alloys fabricated by different processes along with that by μ -PAAM process.

Table 4.8a: Summary of results for the μ -PAAM manufactured Co-Cr-Mo-2/4/6Ti alloys.

Parameters	Co-Cr-Mo-2Ti	Co-Cr-Mo-4Ti	Co-Cr-Mo-6Ti
Cell viability (%)	92 \pm 2	95 \pm 4	85 \pm 3
Overall maximum amount of release of metallic ions up to 7 weeks (ppb)	Co-158.4; Cr-57.5; Mo-17.3; Ti-12.0	Co-148.6; Cr-45.7; Mo-11.2; Ti-8.3	Co-171.8; Cr-67.4; Mo-14.9; Ti-9.42
Corrosion rate (mm/year)	0.23 \pm 0.03	0.05 \pm 0.02	0.12 \pm 0.04
Density (g/cm ³)	8.097 \pm 0.02	7.772 \pm 0.03	7.198 \pm 0.03
Porosity	1.19 \pm 0.5	3.16 \pm 0.8	5.05 \pm 0.2
Type of pores	Tiny pores	Uniform pores	Non-uniform pores
Hardness (HV)	495 \pm 4	473 \pm 7	433 \pm 9
Tensile yield strength (MPa)	774 \pm 6.7	789 \pm 7.9	734 \pm 5.8
Compressive yield strength (MPa)	405 \pm 4.7	455 \pm 5.8	570 \pm 6.1
Ultimate tensile strength (MPa)	792 \pm 9.4	817 \pm 10.2	769 \pm 8.7
Ultimate compressive strength (MPa)	845 \pm 5.7	906 \pm 7.8	897 \pm 3.7

Table 4.8b: Comparison of elastic modulus of Co, Cr, and Mo based alloys fabricated by different processes along with μ -PAAM manufactured Co-Cr-Mo-2/4/6Ti alloys.

Alloy	Process	Elastic modulus in GPa (reference)
Co-Cr-Mo	SLM	225.2 \pm 14.4 (Mergulhão et al., 2017, 2018)
Co-Cr-Mo	EBM	230 (Petit et al., 2016)
Co-Cr-Mo	Lost-wax casting	223 \pm 15.7 (Mergulhão et al., 2017, 2018)
Co-28Cr-6Mo (ASTM F75)	Casting	210 (Tanzi et al., 2019)
	Powder Metallurgy	253 (Tanzi et al., 2019)
Co-28Cr-6Mo (ASTM F799)	Hot Forging	210 (Tanzi et al., 2019)
Co-20Cr-10Mo-35Ni (ASTM F562)	Hot Forging	232 (Tanzi et al., 2019)
Co-28Cr-6Mo (ASTM F1537-20)	Cold Forging	232 (Tanzi et al., 2019)
	Hot forging	280 (https://www.astm.org/f1537-20.html)
Co-Cr-Mo-2Ti	μ -PAAM	212 (Tensile), 216 (Compressive)
Co-Cr-Mo-4Ti	μ -PAAM	207 (Tensile), 211 (Compressive)
Co-Cr-Mo-6Ti	μ -PAAM	201 (Tensile), 204 (Compressive)

Table 4.8a indicates that Co-Cr-Mo-4Ti alloy is a better material for knee implant applications than the other two alloys based on the overall combination of its cell viability, metallic ions release and corrosion rate in human body emulating biofluids, uniformity of pores, tensile yield and ultimate strength and compressive ultimate strength. Though it slightly higher density and elastic modulus than Co-Cr-Mo-6Ti alloy, and more pores than Co-Cr-Mo-2Ti alloy. It can also be noted from table 4.8a that the density and elastic modulus of Co-Cr-Mo-xTi alloys decrease with increase in Ti% in Co-Cr-Mo alloys. It can be observed from the Table 4.8b that μ -PAAM manufactured Co-Cr-Mo-2/4/6Ti alloys have smaller values of their elastic modulus as compared to other Co-based alloys fabricated by different processes. It will help them in reducing the stress shielding effect.

4.10 Concluding Remarks

This chapter presented influence of adding 2%; 4%; and 6% of Ti to Co-Cr-Mo alloy to develop Co-Cr-Mo-xTi alloys as better knee implant material by μ -PAAM process. Minimum value of aspect ratio of 1.11 and continuous and consistent deposition was obtained for lower μ -plasma power (264 W), and moderate values of powder mass flow rate (2.5 g/min) and deposition head travel speed (50 mm/min). Therefore, it was used for manufacturing multi-track multi-layer depositions of powder of Co-Cr-Mo-xTi alloys. Biocompatibility of Co-Cr-Mo-xTi alloys was assessed *in-vitro* using viability of HeLa cells, release of metallic ions in PBS solution of different pH values and for different immersion durations, and corrosion behavior study in PBS solution of 7.4 pH at 37⁰C along with studying their density, porosity, microstructural and evolution of phases, microhardness, tensile and compression tests and their fractography, abrasion resistance test, and wear characteristics. Overall average values of cell viability for the optimized deposition samples of Co-Cr-Mo-2Ti; Co-Cr-Mo-4Ti; and Co-Cr-Mo-6Ti alloys are 92%; 95%; and 85% respectively. Addition of Ti to Co-Cr-Mo alloy is found to be advantageous due to formation of intermetallic phase CoTi₂ which is non-cytotoxic to human body and more active in cell growth mechanism. Released amounts of metallic ions depend on the pH value of the PBS solution, chemical composition of the test sample, and immersion duration. Addition of Ti to Co-Cr-Mo alloy for implant material is advantageous as total release of metallic ions is reduced. Overall averaged released amounts of metallic ions by the optimized deposition samples of Co-Cr-Mo-xTi alloys are 126; 41;11, and 9 ppb for Co, Cr, Mo, and Ti ion respectively. They are within the physiological constraint of trace components in the human body as per findings of the past works. Co-Cr-Mo-4Ti alloy has minimum values of corrosion potential, corrosion current density, and measured and Tafel curve determined corrosion rates. SEM micrographs of corroded surface showed formation

of passive oxides layer on the exposed surface of Co-Cr-Mo-xTi alloys which may consist of TiO₂ formed due to presence of Ti in Co-Cr-Mo-xTi alloys imparting better corrosion resistance than Co-Cr-Mo alloy. Results revealed that bulk density and relative density decrease with increase in Ti amount in the Co-Cr-Mo alloy due to smaller density of Ti than that Co-Cr-Mo alloy. Porosity increases with increase of Ti amount which increases % difference between bulk and relative densities. Optimized deposition of Co-Cr-Mo-4Ti alloy showed more pores of smaller size and their more uniform distribution which is desirable for knee implant material because it will give better osseointegration with human bones and tissues. Its microstructure and phase evolution revealed presence of α -Co phase having FCC crystal structure, ϵ -Co phase having HCP crystal structure, β -titanium phase having BCC crystal structure, and inter-metallic phases of CoTi₂ and lamellar chromium carbide (i.e., Cr₂₃C₆) at its grain boundaries with relatively higher wt.% of chromium. Average microhardness of optimized deposition of Co-Cr-Mo-2Ti alloy is found to be the highest (i.e., 495 HV) followed by 473 HV for Co-Cr-Mo-4Ti; and 433 HV for Co-Cr-Mo-6Ti alloy optimized depositions. It can also be attributed to increase in porosity with %Ti in Co-Cr-Mo alloy. Coefficient of friction, specific wear rate, and wear volume are found to increase with increase in % of Ti in Co-Cr-Mo alloys due to decrease in microhardness and increase in porosity. Co-Cr-Mo-4Ti alloy has maximum values of tensile yield and ultimate tensile strength and ultimate compressive strength, and moderate value of tensile and compressive modulus of elasticity, finer grain size, and absence of micro-cracks. Co-Cr-Mo-4Ti alloy has minimum value of avg. scratch track width and coefficient of friction, and maximum value of scratch hardness number imparting it better abrasion resistance to it due to presence of fine lamellar carbide phases. It can be concluded from the findings of this chapter that Co-Cr-Mo-4Ti alloy is a better knee implant material owing to its less density, uniform porous structure, absence of cracks, moderate microhardness, higher yield tensile and compressive strength, and abrasion resistance, wear characteristics, cell viability, metallic ion release, and corrosion behavior.

The *next chapter* presents results and their analyses on development of equiatomic Ti-Ta-Nb-Mo-Zr HEA for knee implant applications by the μ -PAAM process. This includes study of *in-vitro* evaluation of biocompatibility, microstructure, phase formation, microhardness, compressive stress-strain relation, sliding wear characteristics, and abrasion resistance of multi-track multi-layer depositions of Ti-Ta-Nb-Mo-Zr HEA. It also describes the results and analysis of its dry fretting wear, corrosion, and tribo-corrosion characteristics with an objective to demonstrate it as a better knee implant material.

Chapter 5

Results and Analysis for Ti-Ta-Nb-Mo-Zr HEA

This presents results and their analyses on development of equiatomic Ti-Ta-Nb-Mo-Zr HEA for knee implant applications by the μ -PAAM process. This includes study of *in-vitro* evaluation of biocompatibility, microstructure, phase formation, microhardness, compressive stress-strain relation, sliding wear characteristics, and abrasion resistance of multi-track multi-layer depositions of Ti-Ta-Nb-Mo-Zr HEA. It also describes the results and analysis of its dry fretting wear, corrosion, and tribo-corrosion characteristics with an objective to demonstrate it as a better knee implant material.

5.1 Results for Aspect Ratio

Figure 5.1 depicts the photographs of the 27 single-track single-layer depositions of Ti-Ta-Nb-Mo-Zr HEA manufactured in the main experiments by the μ -PAAM process. Table 5.1 presents the computed values of their aspect ratios and visually observed deposition quality categorizing it as uniform and continuous deposition (UCD) and non-uniform deposition (NUD). Figure 5.2 shows the measured values of deposition height and width for the single-track single-layer deposition samples of Ti-Ta-Nb-Mo-Zr HEA corresponding to the exp. no. 6 (Fig. 5.2a); exp. no. 11 (Fig. 5.2b); exp. no. 15 (Fig. 5.2c); exp. no. 18 (Fig. 5.2d); exp. no. 20 (Fig. 5.2e); and exp. no. 27 (Fig. 5.2f). It can be observed from Fig. 5.1 and Table 5.1 that fifteen single-track single-layer depositions of Ti-Ta-Nb-Mo-Zr HEA are UCD, 11 are NUD, no deposition occurred in exp. no. 16. It can be summarized from Table 5.1 that (i) aspect ratio varies in a range from 0.62 to 1.44, (ii) NUD occurred for combinations of 396 and 407 W μ -plasma power and 47 and 53 g/min deposition material mass flow rate whereas UCD occurred at majority of 418 W μ -plasma power providing sufficient heat to melt the deposition material, and (iii) exp. no. 20 yielded UCD with minimum value of aspect ratio of 0.62 (Fig. 5.2e) corresponding to parametric combination of 418 W μ -plasma power, 1.7 g/min mass flow rate of feedstock material powder, and 53 mm/min deposition head travel speed. Therefore, this combination was used for manufacturing two multi-track multi-layer depositions of Ti-Ta-Nb-Mo-Zr HEA over which different investigations have been done and their results are discussed in this chapter.

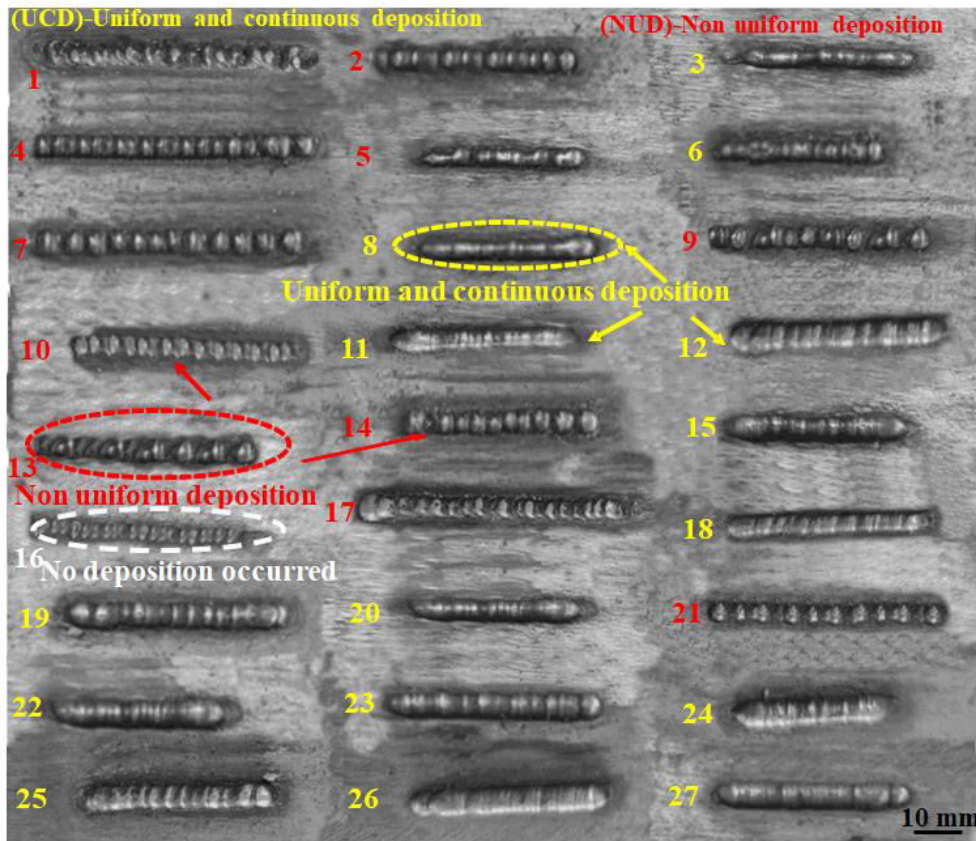


Fig. 5.1: Photograph of the 27 single-track single-layer depositions of Ti-Ta-Nb-Mo-Zr HEA manufactured in the main experiments by the μ -PAAM process.

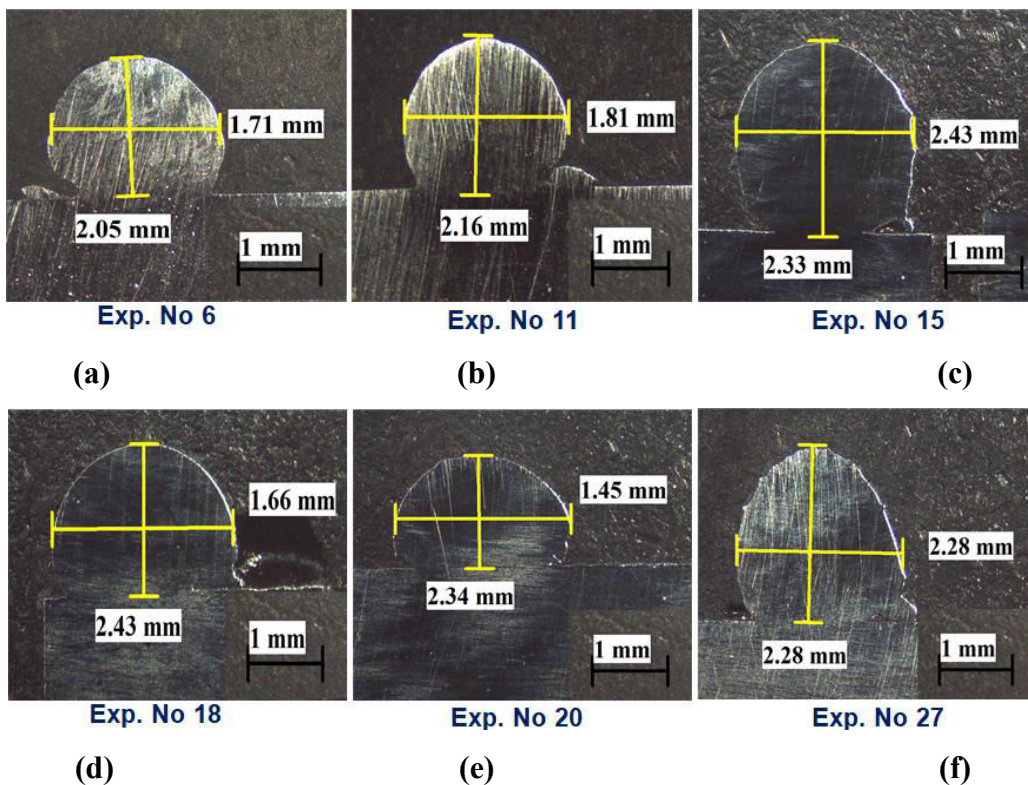


Fig. 5.2: Measured values of deposition height and width for single-track single-layer deposition samples of Ti-Ta-Nb-Mo-Zr HEA corresponding to: (a) exp. no. 6, (b) exp. no.11, (c) exp. no. 15, (d) exp. no. 18, (e) exp. no. 20, and (f) exp. no. 27.

Table 5.1: Computed values of aspect ratios and visually observed deposition quality of 27 single-track single-layer depositions of Ti-Ta-Nb-Mo-Zr HEA manufactured in the main experiments and corresponding parameters of μ -PAAM process.

Exp. No.	Variable input parameters			Measured responses	
	μ -plasma power (W)	Mass flow rate of feedstock material powder (g/min)	Deposition head travel speed (mm/min)	Aspect ratio	Deposition quality
16	407	2.7	47	---	No deposition
1	396	1.7	47	1.14	NUD
2	396	1.7	53	0.98	NUD
4	396	2.2	47	1.21	NUD
5	396	2.2	53	1.15	NUD
7	396	2.7	47	1.09	NUD
9	396	2.7	59	1.32	NUD
10	407	1.7	47	1.44	NUD
13	407	2.2	47	1.21	NUD
14	407	2.2	53	1.07	NUD
17	407	2.7	53	1.15	NUD
21	418	1.7	59	1.17	NUD
3	396	1.7	59	1.08	UCD
6	396	2.2	59	0.83	UCD
8	396	2.7	53	1.05	UCD
11	407	1.7	53	0.84	UCD
12	407	1.7	59	1.27	UCD
15	407	2.2	59	1.04	UCD
18	407	2.7	59	0.69	UCD
19	418	1.7	47	1.28	UCD
20	418	1.7	53	0.62	UCD
22	418	2.2	47	0.92	UCD
23	418	2.2	53	0.95	UCD
24	418	2.2	59	1.09	UCD
25	418	2.7	47	1.12	UCD
26	418	2.7	53	0.97	UCD
27	418	2.7	59	1.00	UCD

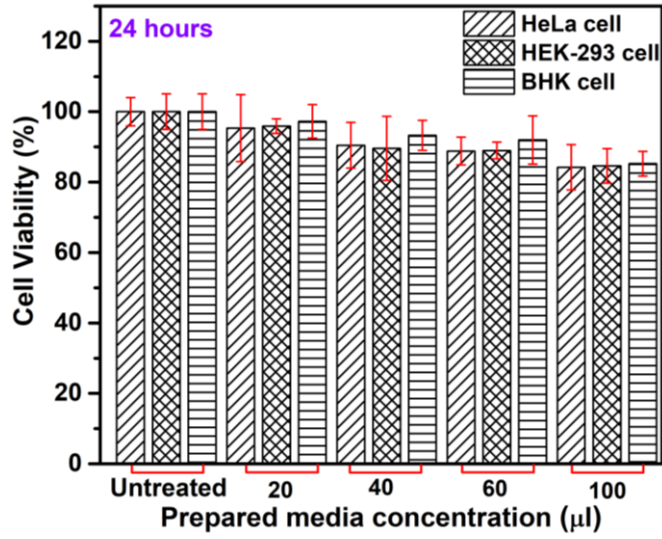
UCD: uniform and continuous deposition; NUD: non-uniform deposition

5.2 Results of Biocompatibility Evaluation

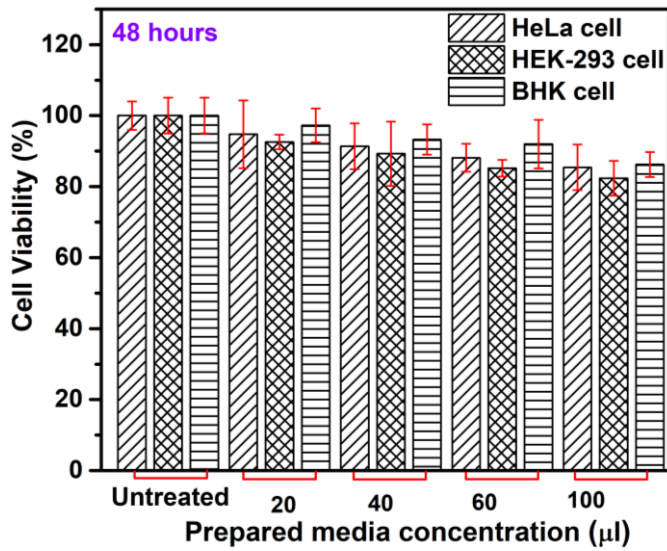
This section describes results and analysis of *in-vitro* evaluation of biocompatibility of μ -PAAM process manufactured Ti-Ta-Nb-Mo-Zr HEA multi-track multi-layer deposition through cell viability, released amounts of constituent ions, and corrosion behavior.

5.2.1 Results of Cell Viability

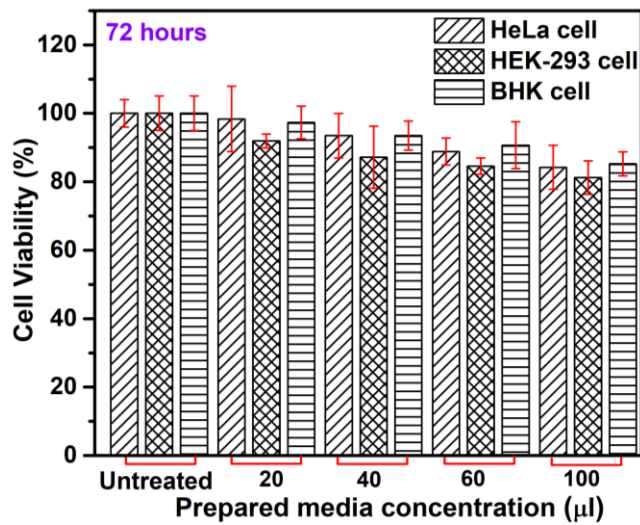
Figure 5.3 presents bar diagrams depicting average values of % cell viability of HeLa cells, human embryo kidney (HEK-293) cells, and baby hamster kidney (BHK) cells treated with the different concentration of the prepared media for the developed Ti-Ta-Nb-Mo-Zr HEA for incubation duration of 24 hours (Fig. 5.3a), 48 hours (Fig. 5.3b), and 72 hours (Fig. 5.3c) along with the untreated cells.



(a)



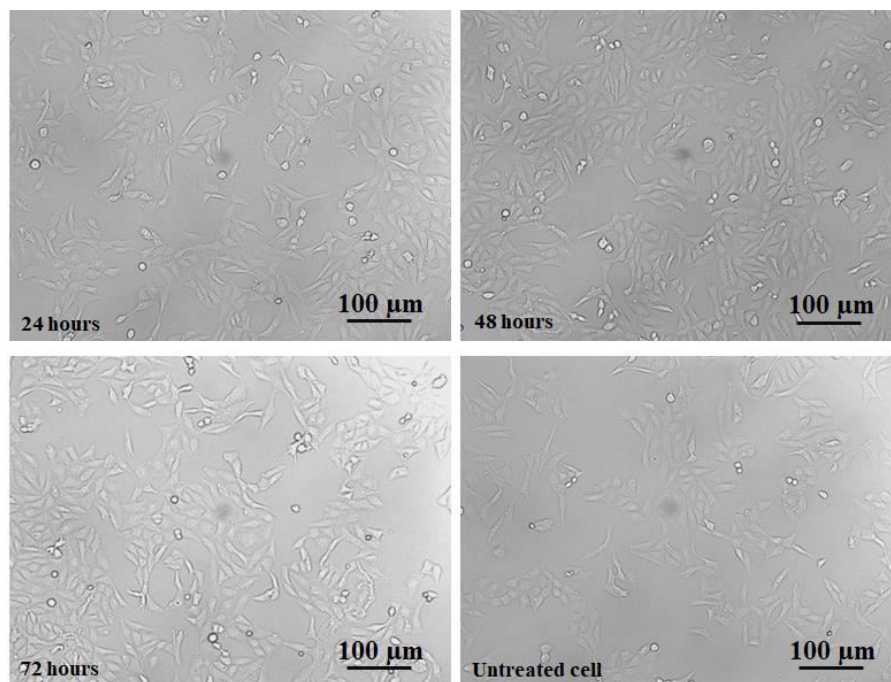
(b)



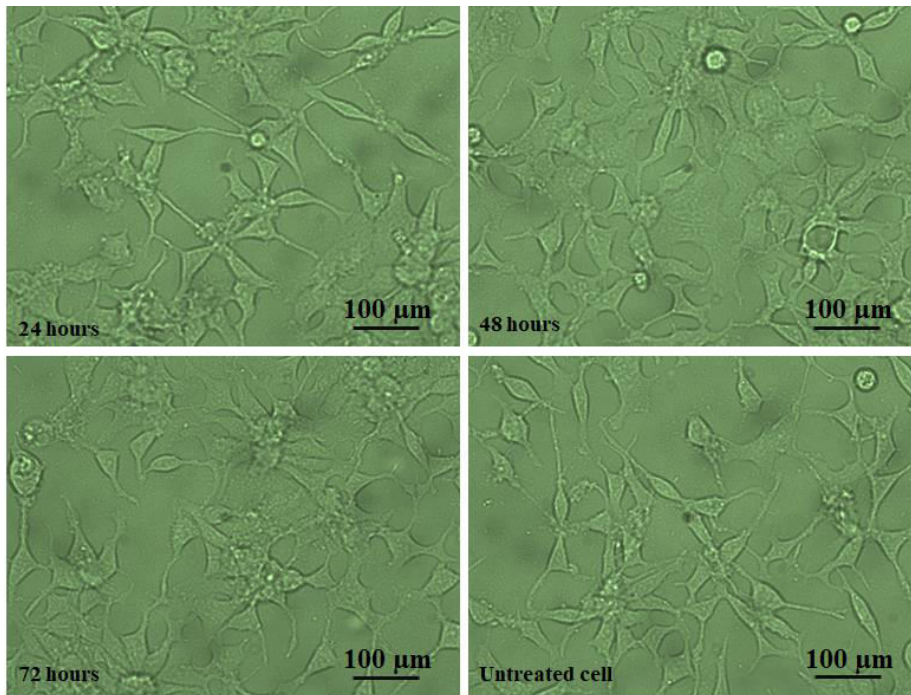
(c)

Fig. 5.3: Viability of HeLa, HEK-293, and BHK cells in different concentration of the prepared media for the developed Ti-Ta-Nb-Mo-Zr HEA for incubation duration of (a) 24 hours; (b) 48 hours; and (c) 72 hours.

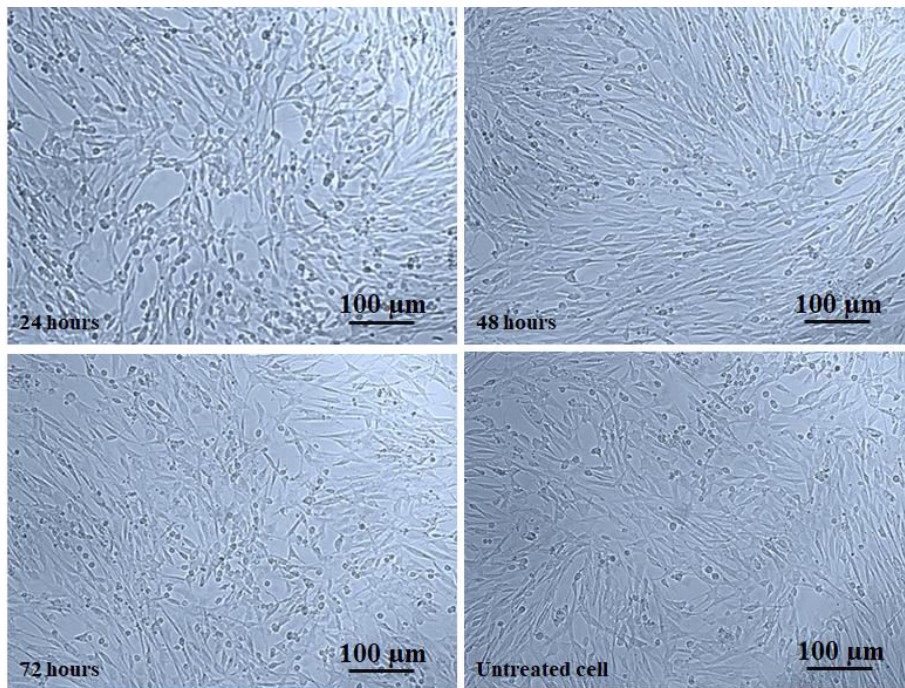
It can be observed from Fig. 5.3 that % cell viability of HeLa, HEK-293, and BHK cells continuously decreases with concentration of the prepared media for the developed Ti-Ta-Nb-Mo-Zr HEA attaining their minimum values at 100 μ l concentration for incubation durations of 24; 48; and 72 hours. However, BHK cell has maximum value of % cell viability at any concentration of the prepared media for the considered incubation durations. Overall average values of % cell viability of HeLa, HEK-293, and BHK cells are 90%; 88%; and 92% respectively in the prepared media for Ti-Ta-Nb-Mo-Zr HEA indicating its very good cell viability. It is due to (a) excellent corrosion resistance of Ti-Ta-Nb-Mo-Zr HEA which reduces release of ions of its constituent elements in the prepared media which is primary source for evaluating cell viability, (b) presence of Ta, Nb, and Zr elements form an extremely stable passive oxide layer on the exposed surface of Ti-Ta-Nb-Mo-Zr HEA which constrains release of ions of its constituent elements (Li et al. 2021), and (c) main alloying elements Nb, Ta, and Zr do not have adverse effects on cell viability. Bolmaro et al. (2019) reported similar results from *in-vitro* cell viability evaluation of the cast and annealed Ti-25Nb-10Zr alloy for orthopedic devices. Correa et al. (2020) reported that ions released from potential load bearing implant alloys Ti-15Zr-10Mo and Ti-15Zr-15Mo into the cell culture media did not have any toxic effect on cell growth and cell viability during the study period. Figure 5.4 depicts bright field micrographs for HeLa cells (Fig. 5.4a), HEK-293 cells (Fig. 5.4b), and BHK cells (Fig. 5.4c) treated with 100 μ l concentration of the prepared media for Ti-Ta-Nb-Mo-Zr HEA samples for incubation durations of 24; 48; and 72 hours, and for corresponding untreated cells.



(a)



(b)



(c)

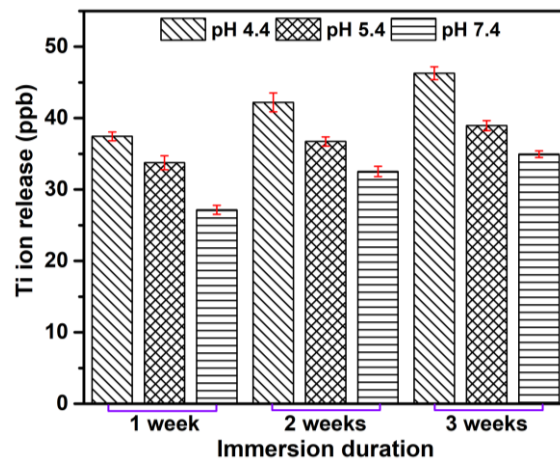
Fig. 5.4: Bright-field micrographs of (a) HeLa cells (b) HEK-293 cells (c) BHK cells treated with 100 μl concentration of the prepared media for Ti-Ta-Nb-Mo-Zr HEA samples for incubation durations of 24; 48; and 72 hours; and for untreated cells.

It can be observed that the HeLa cells (Fig. 5.4a) are round, triangle, and spindle shaped and are mutually connected. The rounded cells are slightly smaller than spindle shaped cells but are very well spread over the exposed surface. Micrographs of HEK-293 cells (Fig. 5.4b) show their epithelial like shape, and micrographs of BHK cells (Fig. 5.4c) illustrate

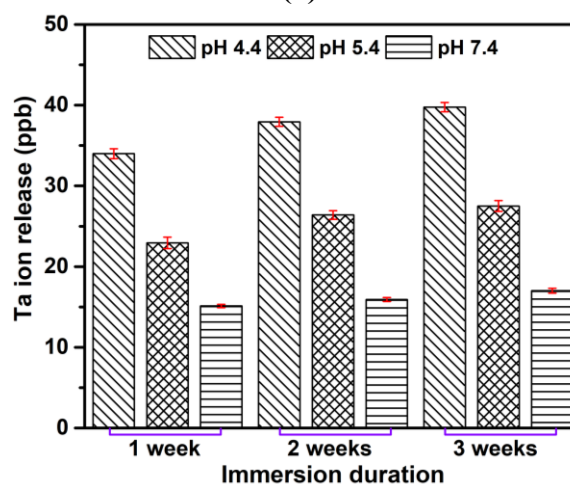
that their shape is of fibroblast in nature, and it changes from polygonal to elongated with incubation duration. These micrographs show voluminous nature of HeLa, HEK-293, and BHK cells indicating that these cells are metabolically active and healthy without any apparent physical change with increase in incubation duration of their treatment. It also leads to their overall average cell viability being 90% or more (Figs. 5.4a-5.4c). It is mainly due to addition of biocompatible elements Nb, Zr, and Ta as the main alloying elements in the development of Ti-Ta-Nb-Mo-Zr HEA. Similar study has been reported by **Hussein et al. (2016)** for the biocompatibility of Ti-Nb-Ta alloy using HeLa cells. Based on the *in-vitro* cell viability evaluation, it can be concluded that Ti-Ta-Nb-Mo-Zr HEA is an excellent biocompatible material for knee implants due to its main alloying elements such as Nb, Ta, Mo, and Zr.

5.2.2 Metallic Ion Release Results

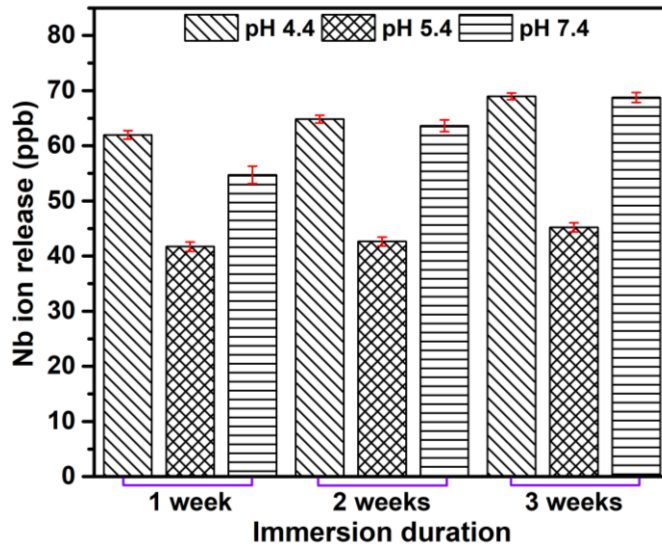
Figure 5.5 presents released amounts of ions of constituent element Ti (Fig. 5.5a); Ta (Fig. 5.5b); Nb (Fig. 5.5c); Mo (Fig. 5.5d), and Zr (Fig. 5.5e) from the multi-track multi-layer deposition samples of Ti-Ta-Nb-Mo-Zr HEA in the simulated body fluid (SBF) solution of 4.4; 5.4; and 7.4 pH values for immersion durations of 1; 3; and 7 weeks.



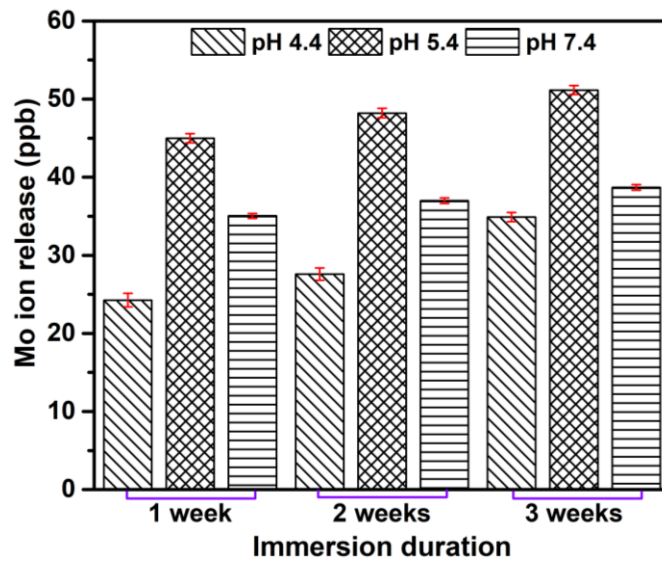
(a)



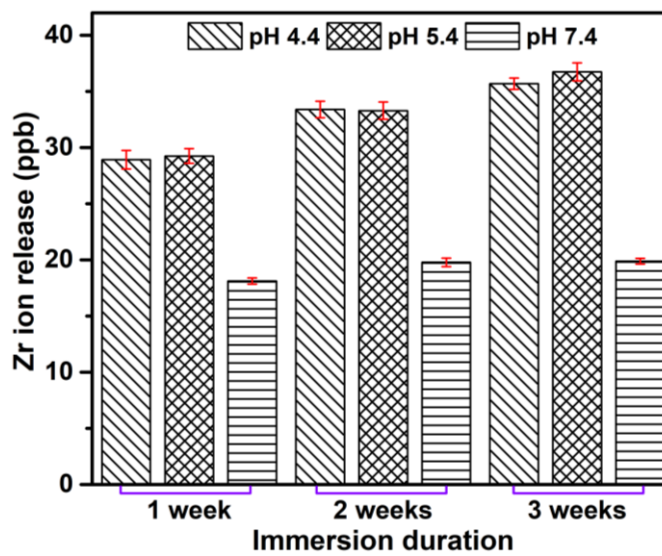
(b)



(c)



(d)



(e)

Fig. 5.5: Released amounts of ions of constituent elements (a) Ti (b) Ta, (c) Nb, (d) Mo, and (e) Zr, from the multi-track multi-layer deposition samples of Ti-Ta-Nb-Mo-Zr HEA in SBF solution of 4.4, 5.4, and 7.4 pH value for immersion durations of 1, 2, and 3 weeks.

It can be observed from Fig. 5.5 that released amounts of ions of Ti (Fig. 5.5a), Ta (Fig. 5.5b), Nb (Fig. 5.5c), Mo (Fig. 5.5d), and Zr (Fig. 5.5e) from the multi-track multi-layer deposition samples of Ti-Ta-Nb-Mo-Zr HEA increase with immersion duration for each pH value of the SBF. Released amounts of Ti, Ta, and Nb ions decrease with increase in pH value of the SBF solution and their maximum values (46; 40; and 67 ppb) are obtained at 4.4 pH value after 3 weeks immersion duration. Whereas released amount of Mo and Zr ions attain their maximum values (52 and 37 ppb) at 5.4 pH value of the SBF solution after 3 weeks immersion duration. Overall averaged released amounts of Ti, Ta, Nb, Mo, and Zr ions are 37; 26; 57; 38; and 28 ppb respectively. It implies that maximum released amount is 57 ppb for Nb ions which is much lower than the findings (i.e., 10,000 ppb for all the constituent elements) by **Kong et al. (2021)** for the SLM manufactured Ti-Nb-Ta alloy immersed in a minimal essential medium for more than 180 days. Overall, it can be concluded that the released amounts of metallic ions depend on the pH value of the SBF solution, chemical composition of the test sample, and immersion duration.

5.2.3 Study of Corrosion Behavior

Figure 5.6 presents results of corrosion behavior assessment of the multi-track multi-layer deposition sample of Ti-Ta-Nb-Mo-Zr HEA showing open circuit potential (OCP) curve (Fig. 5.6a) and Tafel polarization curve (Fig. 5.6b) for 4.4; 5.4; and 7.4 pH values of the SBF solution. The OCP measures potential of working electrode with respect to immersion duration whereas corrosion potential ' E_{corr} ' measures potential of working electrode with respect to corrosion current density ' i_{corr} ' when current is supplied to the corrosion system. OCP signifies tendency of corrosion of the working electrode in the test solution and its higher value indicates higher corrosion tendency and vice-versa. Values of OCP and corrosion potential ' E_{corr} ' may or may not have different values. Variations in the values of OCP and E_{corr} are attributed to working electrode, corrosion test solution and experimental apparatus. Table 5.2 lists corrosion potential ' E_{corr} ', corrosion current density ' i_{corr} '; and corrosion rate obtained from the Tafel polarization curve (Fig. 5.6b) using Tafel extrapolation method. Corrosion current density ' i_{corr} ' is a prominent parameter of corrosion analysis which is directly proportional to corrosion rate. Figure 5.7 illustrates the SEM micrographs of corroded surface of Ti-Ta-Nb-Mo-Zr HEA in SBF solution of pH 4.4 (Fig. 5.7a), pH 5.4 (Fig. 5.7b), and pH 7.4 (Fig. 5.7c). Figure 5.8 shows phase mapping and chemical composition of corroded surface and Fig. 5.9 presents phase analysis of oxides of the constituent elements of Ti-Ta-Nb-Mo-Zr HEA formed on its corroded surface.

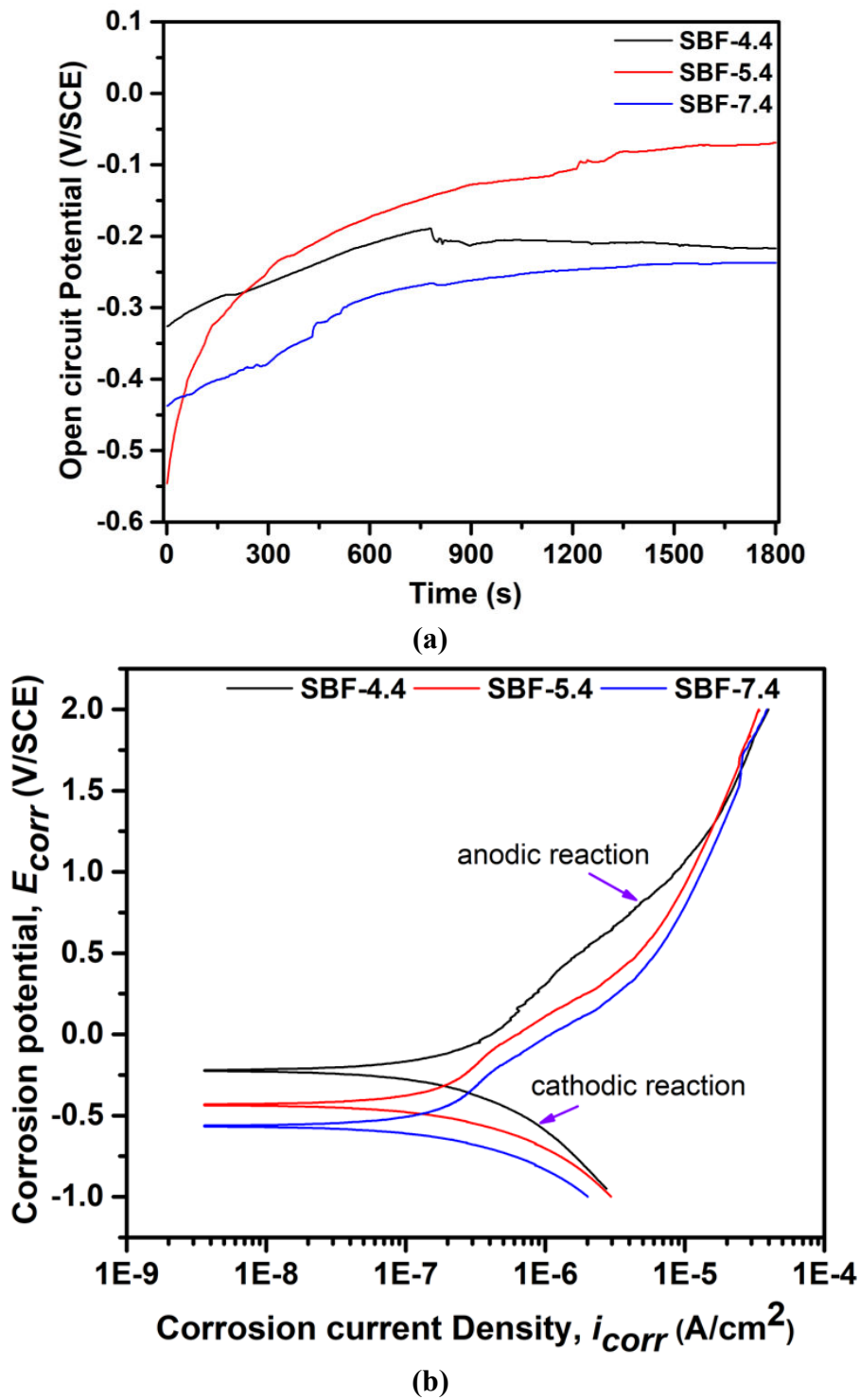
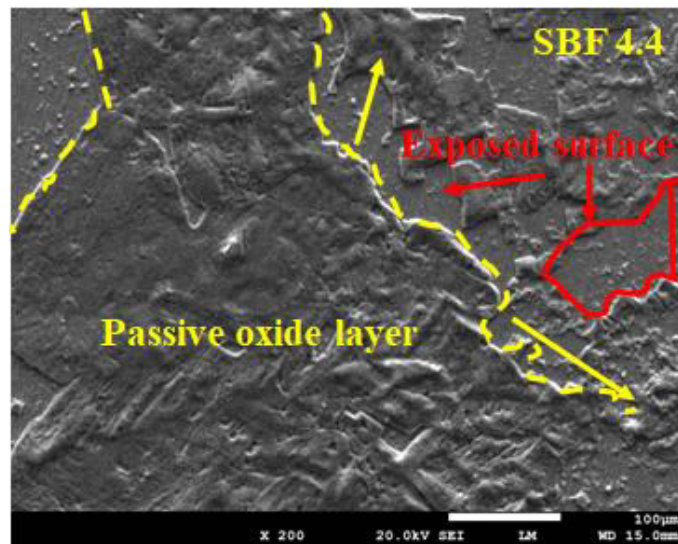


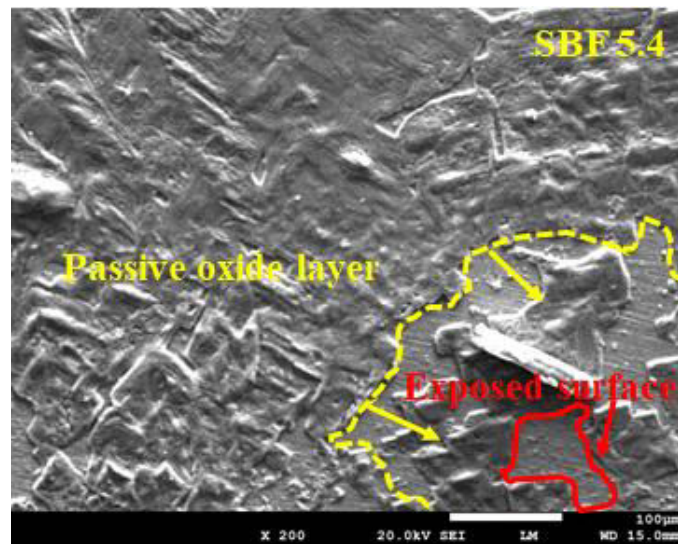
Fig. 5.6: (a) OCP curve plot, and (b) Tafel polarization curve for multi-track multi-layer deposition sample of Ti-Ta-Nb-Mo-Zr HEA in SBF solution of pH 4.4; 5.4; and 7.4 values.

Table 5.2: Corrosion parameters obtained from the Tafel polarization curve for the multi-track multi-layer deposition sample of Ti-Ta-Nb-Mo-Zr HEA in the SBF solution.

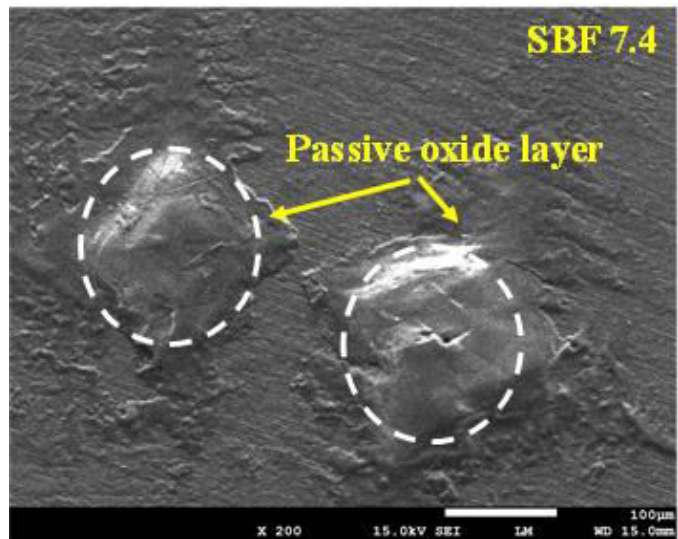
pH value of SBF solution	Avg. OCP (volts)	Corrosion potential ' E_{corr} ' (volts)	Corrosion current density ' i_{corr} ' ($\mu\text{A}/\text{cm}^2$)	Corrosion rate (mm/year)
4.4	-0.22	-0.23	8.49	0.08
5.4	-0.16	-0.44	10.4	0.09
7.4	-0.29	-0.57	14.2	0.12



(a)



(b)



(c)

Fig. 5.7: SEM Micrographs of the corroded surface of multi-track multi-layer deposition sample of Ti-Ta-Nb-Mo-Zr HEA in the SBF solution having pH value of (a) 4.4, (b) 5.4, and (c) 7.4.

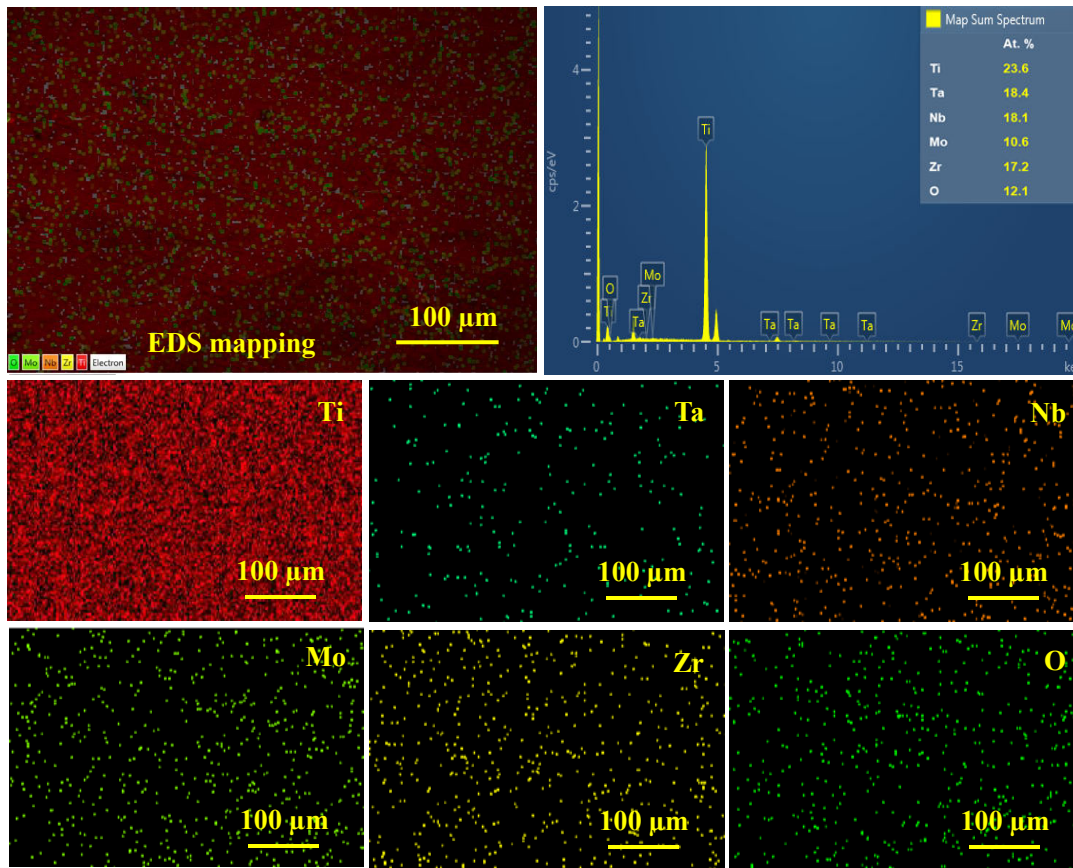


Fig. 5.8: Results of EDS for corroded surface of multi-track multi-layer deposition sample of Ti-Ta-Nb-Mo-Zr HEA.

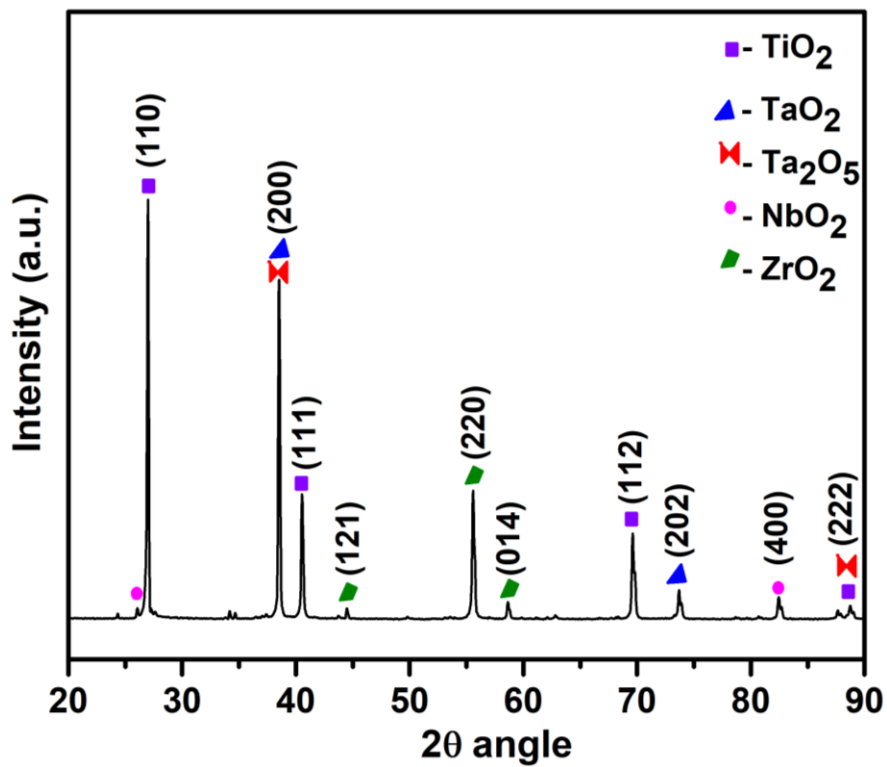


Fig. 5.9: Results of XRD for corroded surface of multi-track multi-layer deposition sample of Ti-Ta-Nb-Mo-Zr HEA.

The OCP curve of Ti-Ta-Nb-Mo-Zr HEA (Fig. 5.6a) has negative values for the considered immersion duration in the SBF solution for its considered pH values. The SBF solution of pH 7.4 value shows more negative OCP value (-0.29 V) than SBF solution of pH 4.4 (-0.22 V) and of pH 5.4 (-0.16 V). It indicates higher corrosive tendency of the exposed surface of the developed HEA. But OCP increases gradually with immersion duration and then becomes almost constant after immersion duration of 800 seconds for 4.4 and 7.4 pH values of the SBF solution and after 1500 seconds for 5.4 pH value of the SBF solution (Fig. 5.6a). Such increasing trend of OCP from negative values with immersion duration suggests formation of a passive oxide layer on the exposed surface of Ti-Ta-Nb-Mo-Zr HEA in the test solution. Passive layer formation tendency on the exposed surfaces is similar to the findings for Ti-16Nb alloy by **Yilmaz et al. (2019)**, for Ti-22Nb and Ti-22Nb-6Zr alloys by **Wang et al. (2009)**, and for Ti-Mo-Nb-Zr alloys by **Nnamchi et al. (2016)**. It is evident from Table 5.2 that corrosion potential decreases, and corrosion current density and corrosion rate increase with increase in pH value of the SBF solution implying that the developed HEA has better corrosion resistance at smaller pH values of the SBF solution. **Bolmaro et al. (2019)** have reported similar findings for corrosion behavior study of Ti-25Nb-10Zr alloy in 2, 5 and 7 pH value ringer solution at 37°C and found that this alloy has less corrosion resistance at 7 pH value. It can be seen in Fig. 5.6b that the Tafel polarization curves for developed Ti-Ta-Nb-Mo-Zr HEA are of similar nature for different pH values of the SBF solution with slight difference in their cathodic and anodic reaction parts. The Ti-Ta-Nb-Mo-Zr HEA go through initial cathodic reaction followed decrease in corrosion current density ' i_{corr} ' with increase in corrosion potential ' E_{corr} ' until the anodic reaction begins. Change from cathodic to anodic reaction does not indicate active-passive transition. It indicates formation of strong passive layers on the exposed surface of the developed Ti-Ta-Nb-Mo-Zr HEA except for some marked regions (where the passive layer is not formed) in the SBF solution for all its pH values. It is confirmed by the SEM micrographs of corroded surface (Figs. 5.7a-5.7c). Accumulation of passive oxide layers (marked as a circle) in the SBF of 7.4 pH value is seen in Fig. 5.7c. It can be correlated with the maximum value of corrosion rate (0.11 mm/year) at 7.4 value of the SBF solution from the Tafel polarization curve (Table 5.2). The EDS results for corroded surface of the Ti-Ta-Nb-Mo-Zr HEA (Fig. 5.8) reveal that strong passive layers consist of oxides of its constituent elements i.e., TiO₂, NbO₂, ZrO₂, Nb₂O₅, and Ta₂O₅. It is confirmed by presence of peaks corresponding to TiO₂ (JCPDS#79-1640), TaO₂ (JCPDS#65-1651), ZrO₂ (JCPDS#33-1483), NbO₂ (JCPDS#76-0682), and Ta₂O₅ (JCPDS#73-2323) in XRD plot of its corroded surface (Fig. 5.9). These observations are in accordance with the findings of **Yu et al. (2001)** and

Bocchetta et al. (2021). **Yu et al. (2001)** reported that alloying of Zr and Nb in the Ti matrix leads to formation of strong passive oxide layers in presence of different solutions due to formation of strong covalent bonds between the closely located Ti, Nb and Zr through completion of d-level of electrons. **Bocchetta et al. (2021)** have reported formation of passive layer consisting of TiO_2 , NbO_2 , ZrO_2 , Ta_2O_5 and Nb_2O_5 in corrosion behavior study of Ti-12Mo-5Ta and Ti-20Nb-10Zr-5Ta. Formation of strong passive layer of oxides of constituent of Ti-Ta-Nb-Mo-Zr HEA impart it excellent corrosion resistance in SBF solution. This finding is similar to findings of the past work by different researchers for Ti-Ta-Nb-Mo-Zr HEA albeit developed by different processes and for other alloys also. **Wang and Xu (2017)** reported that cast Ti-Zr-Nb-Ta-Mo HEA had better corrosion resistance than Ti-6Al-4V alloy in the PBS solution. **Cvijovic'-Alagic et al. (2019)** found that arc melted Ti-13Nb-13Zr alloy has better wear and corrosion resistance than Ti-6Al-4V alloy in the Ringer solution. **Hua et al. (2021)** observed that vacuum arc melted Ti-Zr-Nb-Ta-Mo HEA has good corrosion resistance than Ti-6Al-4V alloy in the PBS solution. The developed Ti-Ta-Nb-Mo-Zr HEA has better corrosion resistance than Ti-6Al-4V (**Yu et al. 2001**; **Wang and Xu 2017**; **Hua et al. 2021**), Ti-22Nb and Ti-22Nb-6Zr alloys (**Wang et al. 2009**), Ti-Mo-Nb-Zr alloy (**Nnamchi et al. 2016**), Ti-16Nb alloy (**Yilmaz et al. 2018**), Ti-25Nb-10Zr alloy (**Bolmaro et al. 2019**), and Ti-12Mo-5Ta and Ti-20Nb-10Zr-5Ta alloys (**Bocchetta et al. 2021**). Therefore, it could be a potential alternative to metallic biocompatible materials currently used for knee implant applications.

5.3 Study of Microstructure and Phase Evolution

Figure 5.10 illustrates SEM image at a magnification of 250x taken in the backscattered electron (BSE) mode showing microstructure of multi-track multi-layer deposition sample of Ti-Ta-Nb-Mo-Zr HEA. Figure 5.11a shows its SEM image at 500x magnification, and EDS results showing its chemical composition (Fig. 5.11b), chemical compositions for the spectrum 1 belonging to minor BCC phase (Fig. 5.11c) and spectrum 2 belonging to major BCC phase (Fig. 5.11d) marked in the SEM image at 500x magnification (as shown in Fig. 5.11a), and mapping of its constituent elements (Fig. 5.11e). Figure 5.12 depicts XRD plot of multi-track multi-layer deposition sample of Ti-Ta-Nb-Mo-Zr HEA showing formation of different phases in it.

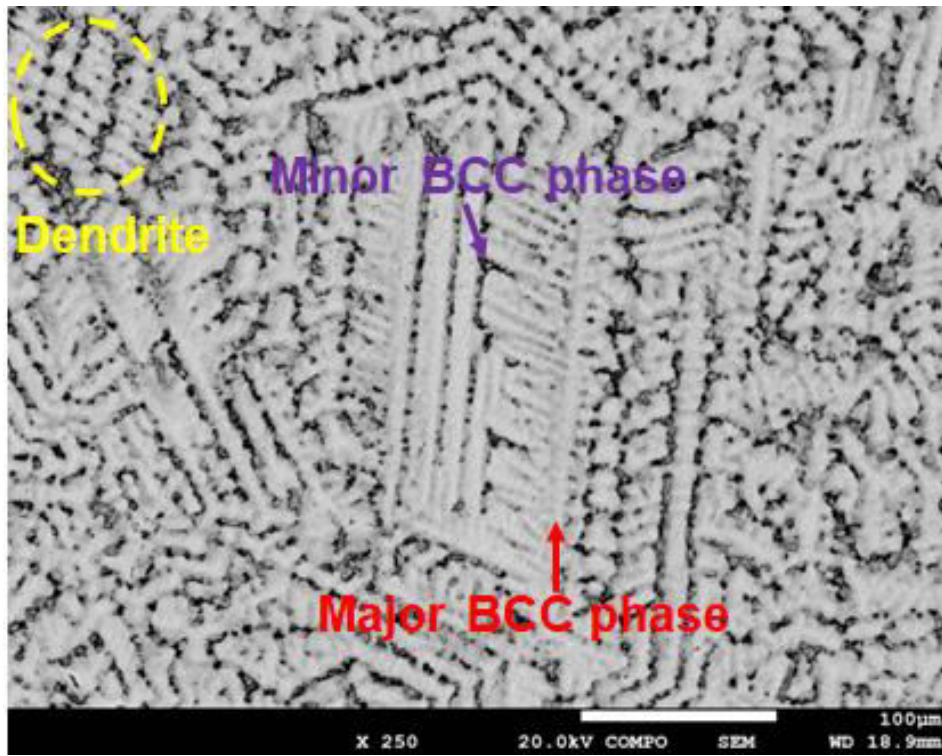
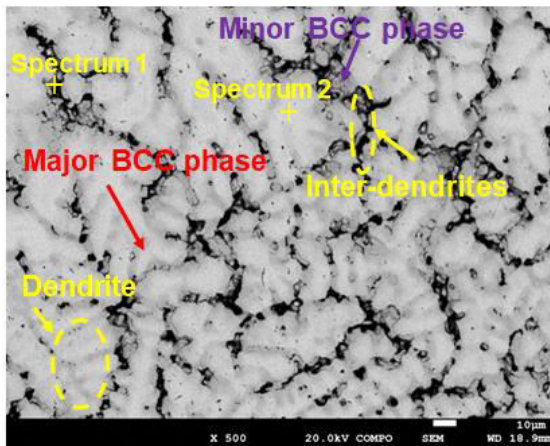
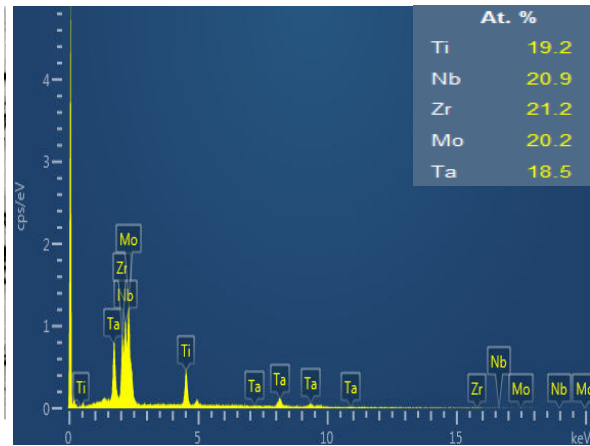


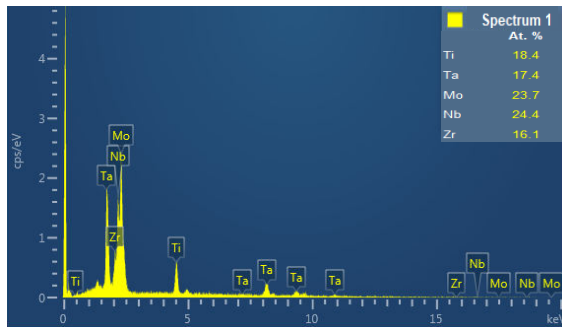
Fig. 5.10: SEM image showing microstructure of multi-track multi-layer deposition sample of Ti-Ta-Nb-Mo-Zr HEA at 250x magnification.



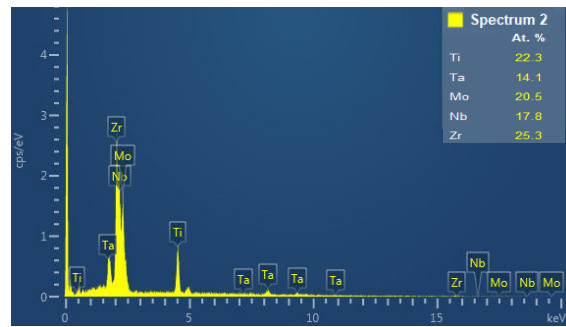
(a)



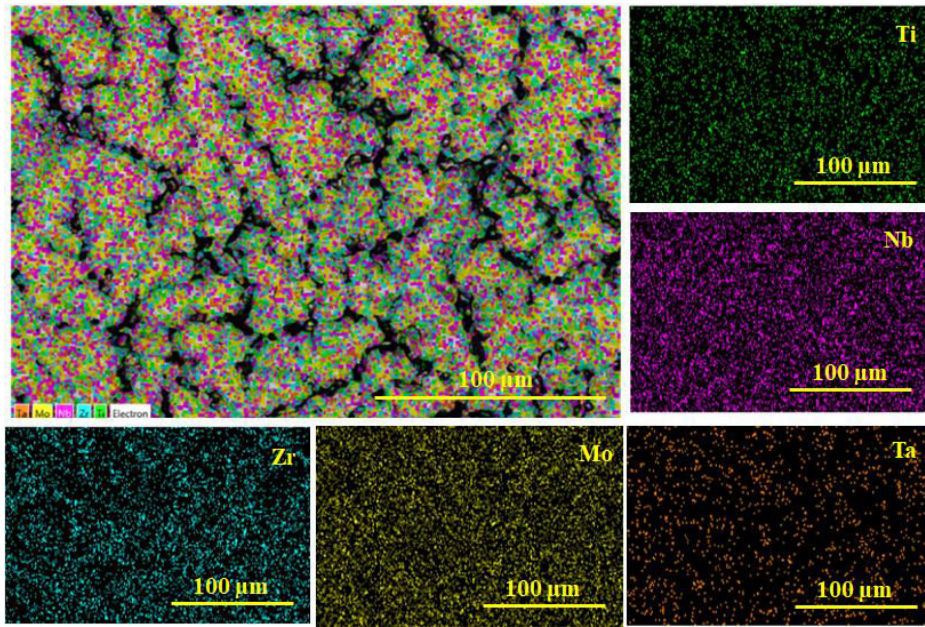
(b)



(c)



(d)



(e)

Fig. 5.11: (a) SEM image at 500x magnification showing microstructure of multi-track multi-layer deposition sample of Ti-Ta-Nb-Mo-Zr HEA, and EDS results showing its (b) chemical composition, (c, d) chemical compositions for spectrum 1 belonging to minor BCC phase and spectrum 2 belonging to major BCC phase (marked in Fig. 5.11a), and (e) mapping of constituent elements.

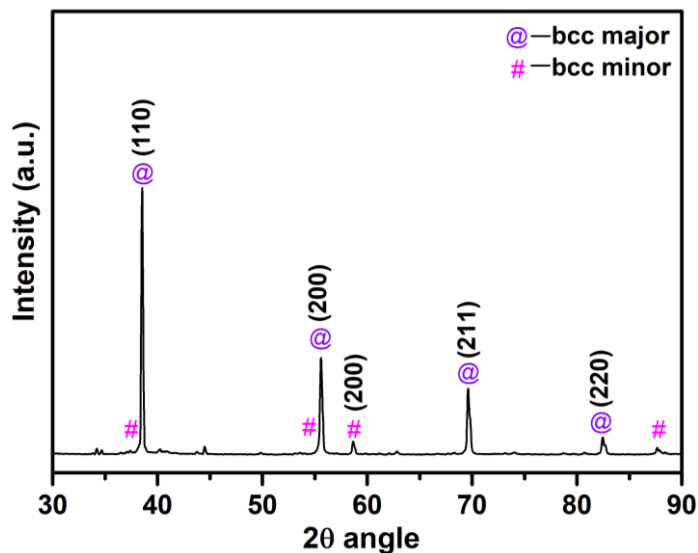


Fig. 5.12: XRD plot for multi-track multi-layer deposition sample of Ti-Ta-Nb-Mo-Zr HEA.

It can be observed from the SEM images in Figs. 5.10 and 5.11a that the multi-track multi-layer deposition sample of Ti-Ta-Nb-Mo-Zr HEA consists of two discrete phases i.e., major BCC phase (appearing in whitish color) having equiaxial fine dendritic structure and minor BCC phase (appearing in blackish color) having inter-dendritic structure. Dendritic microstructure specifies redistribution of the constituent elements during the solidification

process which results in formation of a mixture of fine dendritic and inter-dendritic phases. Their chemical composition (by at.%) obtained by EDS (Fig. 5.11b) reveal slight variation in the constituents of Ti-Ta-Nb-Mo-Zr HEA as compared to chemical composition of its alloyed powder (Fig. 3.2c). It indicates occurrence of minor segregation of constituents of Ti-Ta-Nb-Mo-Zr HEA in contrast to its as cast version developed by **Wang and Xu (2017)**. It is also confirmed by the mapping of its constituent elements as shown in Fig. 5.11e. It may be due to higher melting temperature of Ta (3020 °C), Mo (2623 °C), and Nb (2477 °C) than that of Zr (1855 °C) and Ti (1688 °C) which causes Ta, Mo, and Nb to solidify into a fine-dendritic structure and Zr and Ti to segregate into inter-dendritic structure (**Wang and Xu 2017**). It can be seen in Fig. 5.11c that spectrum 1 belonging to minor BCC phase has higher amount of Nb (24.4 at.%) and Mo (23.7 at.%) than that of Ti (18.4 at.%), Ta (17.4at.%), and Zr (16.1 at.%). Whereas, spectrum 2 belonging to major BCC phase (Fig. 5.11d) has higher amount of Zr (25.3 at.%) and Ti (22.3 at.%) as compared to Mo (20.5 at.%), Nb (17.8 at.%), and Ta (14.1 at.%). It can be explained by the concept of mixing enthalpy (ΔH_{ij} $i \neq j$) according to which main dendritic phase with high melting temperature elements (Ta, Mo, and Nb) is formed during the solidification and Ti and Zr are segregated from it due to positive values of ΔH_{Ta-Ti} , ΔH_{Ta-Zr} , ΔH_{Nb-Ti} , and ΔH_{Nb-Zr} (**Takeuchi and Inoue 2005**).

The XRD plot of Fig. 5.12 discloses sharp peaks conforming to major BCC phase (indexed as @) and minor BCC phase (indexed as #) without establishment of any intermetallic compounds. Rapid heating and cooling during the μ -PAAM process prevents formation of intermetallic compound in the multi-track multi-layer depositions of Ti-Ta-Nb-Mo-Zr HEA. Study of microstructure, chemical composition, elemental analysis, and phase analysis of multi-track multi-layer deposition of Ti-Ta-Nb-Mo-Zr HEA confirm the occurrence of major and minor BCC phases. These results are in accordance with the results for depositions of Ti-Ta-Nb-Mo-Zr HEA by casting process (**Wang and Xu, 2017**), SLM process (**Ishimoto et al. 2021**), and by vacuum arc-melting process (**Nagase et al. 2018; Normand et al. 2020; and Shittu et al. 2020**).

5.4 Analysis of Microhardness

Figure 5.13 presents microhardness profile of multi-track multi-layer deposition sample of Ti-Ta-Nb-Mo-Zr HEA. It can be observed that it has an average microhardness value of 520 ± 10 HV which is 20 ± 5 HV higher than the vacuum arc-melted $Ti_{0.5}$ -Nb-Zr-Mo-Ta HEA (**Hua et al. 2021**). It is due to the formation of major BCC phase having fine-dendritic structure. Higher microhardness of μ -PAAM deposited Ti-Ta-Nb-Mo-Zr HEA will impart it better wear resistance according Archard's equation (**Archard 1953**) which states that total

sliding wear debris for a material is inversely proportional to its hardness i.e., sliding wear resistance is higher for material having hardness which enables it to offer higher resistance to removal of its surface asperities during its sliding wear. It can also be noticed from Fig. 5.13 that the Ti-6Al-4V alloy base plate has an average microhardness of 335 ± 8 HV which is in conformance with finding of **Hua et al. (2021)** who reported that microhardness of Ti-6Al-4V alloy is approximately 320 HV.

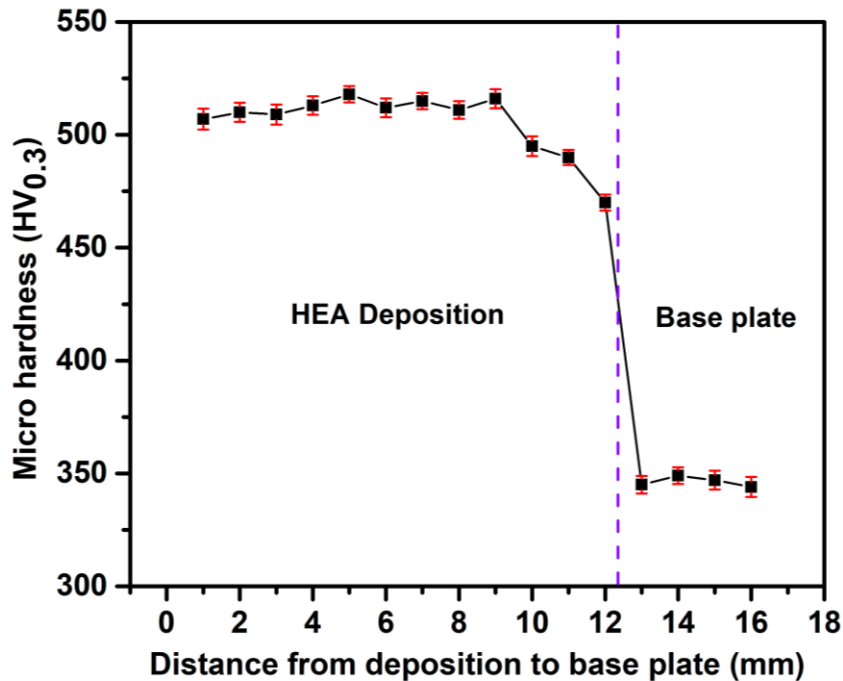


Fig. 5.13: Microhardness profile of multi-track-multi-layer deposition sample of Ti-Ta-Nb-Mo-Zr HEA.

5.5 Results of Compression Test and Fractography

Figure 5.14 shows engineering stress-strain curve under compression for multi-track multi-layer sample of Ti-Ta-Nb-Mo-Zr HEA from which its compressive yield strength, ultimate compressive strength, and compressive strain are found as 1847 ± 25.8 MPa; 1892 ± 15.6 MPa; and $13.53\pm 1.59\%$, respectively. The engineering stress-strain curve of Ti-Ta-Nb-Mo-Zr HEA under compression shows a slight decrease after the yielding. It may be due to dislocation unlocking by solute atoms or ending of short-range order caused by movement of the dislocations. It affects the stacking fault energy which influences the plastic deformation of the HEAs (**George et al. 2019**). Same observation has also been reported by **Guo et al. (2016)** for Ti-Nb-Mo-Zr-Hf HEA, **Liu et al. (2021)** for Ti-Ta-Mo-Nb-V HEA, **Wan et al. (2021)** for Ti-Ta-Nb-Mo-W HEA, and **Li et al. (2022)** for the $\text{Ti}_2\text{-Zr-Hf-V}_{0.5}\text{-Ta}_{0.2}$ HEA. Using the Tabor relationship between microhardness and yield strength (**wang and Xu 2017**) i.e., $\sigma_y = H_v/3$, its estimated compressive yield strength is 1700 ± 32 MPa which is approximately 8% less than its measured value (i.e., 1847 ± 25.8

MPa). **Hori et al. (2019)** reported compressive yield strength of vacuum arc melted equiatomic Ti-Ta-Nb-Mo-Zr HEA as 1132 MPa. **Ishimoto et al. (2021)** reported that SLM deposited and as-cast $\text{Ti}_{1.4}\text{-Nb}_{0.6}\text{-Ta}_{0.6}\text{-Zr}_{1.4}\text{-Mo}_{0.6}$ HEA has compressive yield strength of 1690 ± 78 MPa and 1140 MPa, respectively. It implies that μ -PAAM deposited Ti-Ta-Nb-Mo-Zr HEA has significantly higher compressive yield strength (1847 ± 25.8 MPa) than the SLM deposited (1690 ± 78 MPa), vacuum arc melted (1132 MPa), and as-cast (1140 MPa) Ti-Ta-Nb-Mo-Zr HEA. Remarkably better compressive yield strength of μ -PAAM deposited Ti-Ta-Nb-Mo-Zr HEA is due to its solid solution strengthening achieved by minimizing its elemental segregation. Solid solution strengthening of Ti-Ta-Nb-Mo-Zr HEA is also attributable to significant difference between the elastic modulus of its constituents (**wang and Xu 2017**) whose values are: Mo (329 GPa); Nb (186 GPa); Ti (116 GPa); Ta (105 GPa); and Zr (88 GPa) (**Hua et al. 2021**). Elastic modulus of multi-track multi-layer sample of Ti-Ta-Nb-Mo-Zr HEA is found to be as 130 ± 4 GPa which is less than the as-cast Ti-Ta-Nb-Mo-Zr HEA (153 GPa) measured by **Wang and Xu (2017)** using ultrasonic route. This value is more than 110 GPa elastic modulus of Ti-6Al-4V alloy but much less than 240 GPa and 210 GPa elastic modulus of Co-Cr-Mo alloy and SS316-L alloy respectively (**Hori et al. 2019; Motallebzadeh et al. 2018**). It indicates that μ -PAAM deposited Ti-Ta-Nb-Mo-Zr HEA will reduce stress shielding effect in the knee implants.

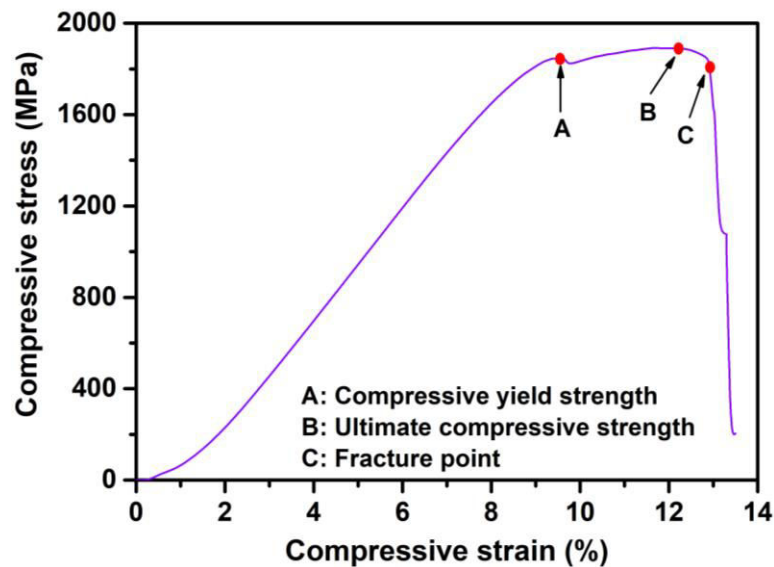


Fig. 5.14: Compressive stress-strain curve for multi-track multi-layer deposition of Ti-Ta-Nb-Mo-Zr HEA.

Figures 5.15a-5.15d presents SEM images of the compression fractured surface morphology of multi-track multi-layer deposition sample of Ti-Ta-Nb-Mo-Zr HEA at different magnifications depicting its fractography at 500x magnification (Fig. 5.15a), 1000x magnification (Fig. 5.15b) for the red color region marked in Fig. 5.15a, 2000x

magnification (Fig. 5.15c) for the yellow color region ‘a’ marked in Fig. 5.15b, and 7000x magnification (Fig. 5.15d) for the yellow color region ‘b’ marked in Fig. 5.15c. It can be observed from these fractography images that the fractured surface of multi-track multi-layer deposition sample of Ti-Ta-Nb-Mo-Zr HEA is predominantly covered by the fan shaped cleavage patterns and shiny plastic tear ridges indicating presence of many large angle grain boundaries (Pineau *et al.* 2016; Senkov *et al.* 2011). The yellow color region ‘a’ marked in Fig. 5.15b and shown in Fig. 5.15c depicts magnified fan shaped patterns. Figure 5.15d depicts river pattern marks and shiny plastic tear ridges. Fractured surface morphology μ -PAAM deposited Ti-Ta-Nb-Mo-Zr HEA reveals its brittle mode of fracture under compression. The same observation has been made by Li *et al.* (2021) for this HEA.

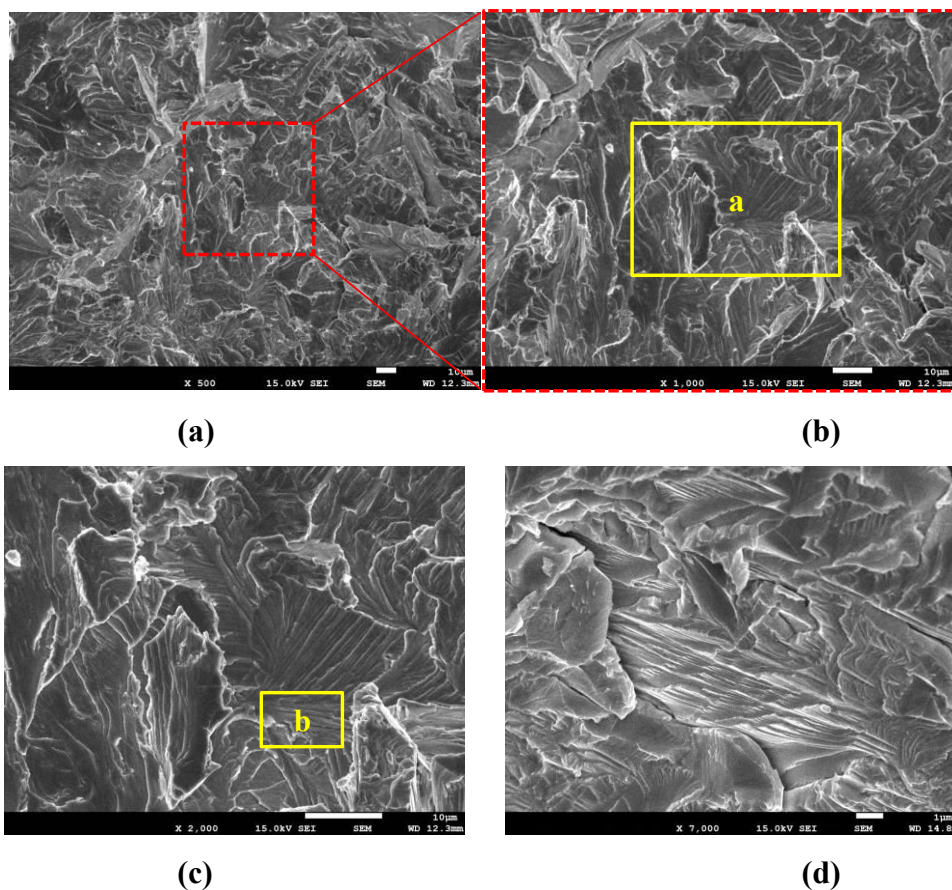
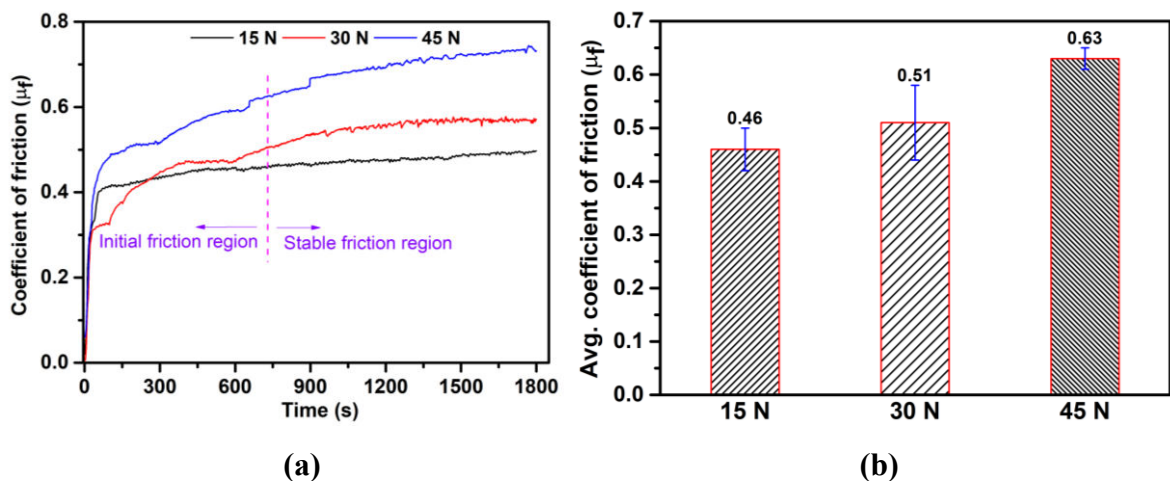


Fig. 5.15: SEM images of compression fractured surface morphology of multi-track multi-layer deposition sample of Ti-Ta-Nb-Mo-Zr HEA at different magnifications: (a) 500x magnification, (b) 1000x magnification for the red color region marked in Fig. 11a, (c) 2000x magnification for the yellow color region ‘a’ marked in Fig. 11b, and (d) 7000x magnification for the yellow color region ‘b’ marked in Fig. 11c.

5.6 Wear Resistance Results

Figure 5.16 presents results of sliding wear for multi-track multi-layer deposition sample of Ti-Ta-Nb-Mo-Zr HEA for the applied load of 15; 30; and 45N depicting change in coefficient of friction (COF) with time (Fig. 5.16a), average COF (Fig. 5.16b) determined

from Fig. 5.16a, worn scar depth profile (Fig. 5.16c), average worn scar depth (Fig. 5.16d) measured from the corresponding worn scar depth profile, and computed values of specific wear rate (Fig. 5.16e). It can be observed from Fig. 5.16a that the COF variation curve can be divided into two regions: initial friction region and stable friction region. The COF increases with time duration of sliding wear in the initial friction region due to an increase in the contact area between the deposition sample and the counter body. It damages the top surface of Ti-Ta-Nb-Mo-Zr HEA deposition but COF stabilizes after approximately 750 seconds of sliding wear duration causing less damage to its top surface. The COF value in this region is higher for the higher value of the applied load. Consequently, computed average COF (Fig. 5.16b) is higher at 45 N applied load (0.63) than 30 N (0.51) and 10 N (0.46) indicating reduction in wear resistance of Ti-Ta-Nb-Mo-Zr HEA deposition with increase in the applied load because it is inversely proportional to average COF. Worn scar depth profile (Fig. 5.16c) is deeper for larger value of the applied load consequently computed average value of worn scar depth (Fig. 5.16d) is maximum for the applied load of 45 N (81 μm) followed by 30 N (68 μm) and 15 N (45 μm) applied load. It can be observed from the computed specific wear rate (Fig. 5.16e) that its maximum and minimum values are observed for applied load of 15 N ($7.29 \times 10^{-4} \text{ mm}^3/\text{N}\cdot\text{m}$) and 45 N ($4.35 \times 10^{-4} \text{ mm}^3/\text{N}\cdot\text{m}$), respectively. Such contrast observation (with reference to Fig. 5.16d) is due to the inverse relationship between the specific wear rate and the applied load (as represented in Eq. 3.5). It implies that change in material volume loss in sliding wear is less than corresponding change in the applied load.



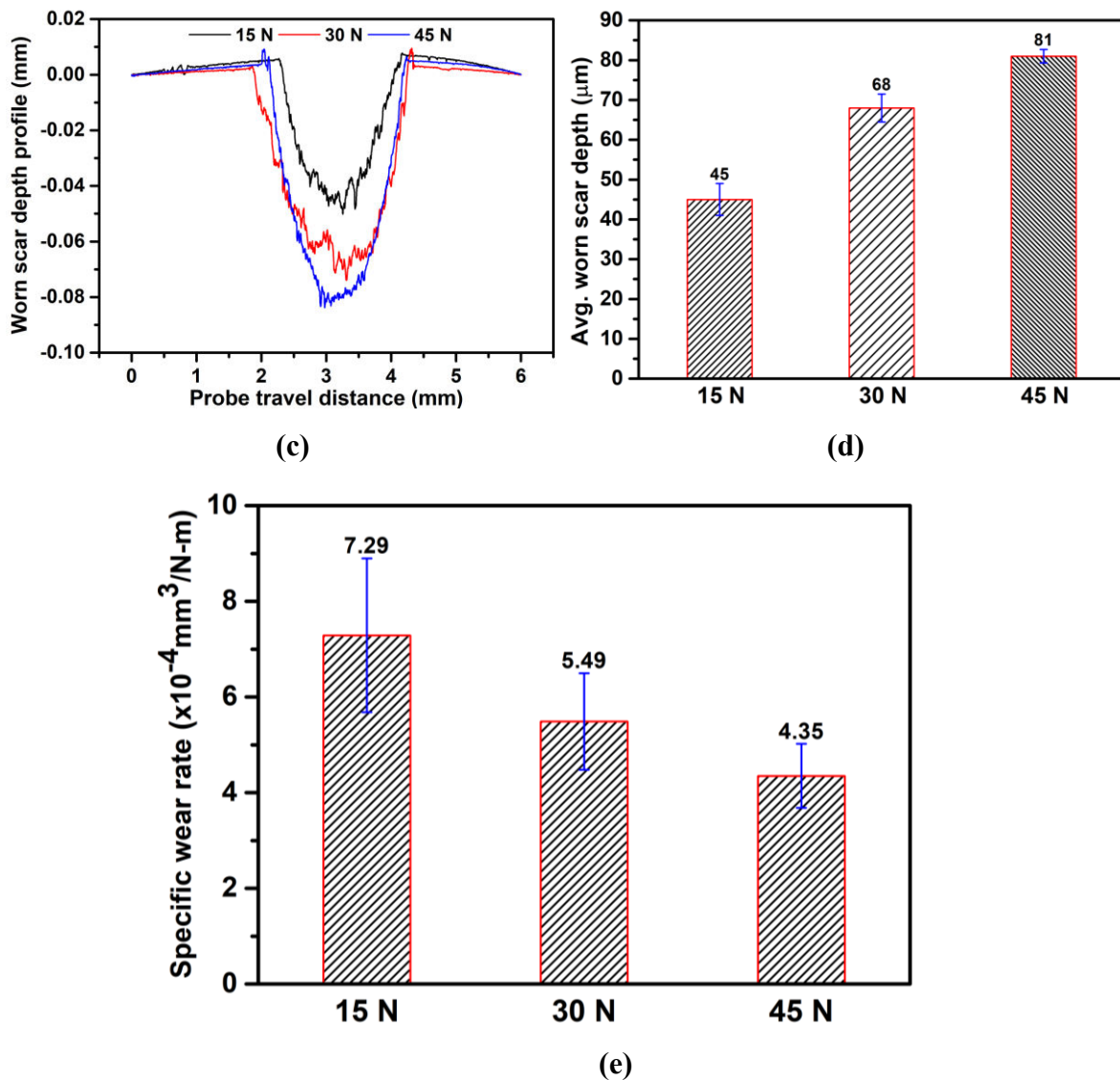


Fig. 5.16: Results of sliding wear for multi-track multi-layer deposition sample of Ti-Ta-Nb-Mo-Zr HEA at different applied load showing: (a) change in COF with time, (b) avg. COF determined from Fig. 12a, (c) worn scar depth profile, (d) avg. worn scar depth computed from worn scar depth profile, and (e) computed values of specific wear rate.

Figure 5.17 presents SEM images of the worn track of multi-track multi-layer deposition sample of Ti-Ta-Nb-Mo-Zr HEA for the applied load of 15 N (Fig. 5.17a), 30 N (Fig. 5.17b), and 45 N (Fig. 5.17c) providing insights to their wear mechanism. Worn track at an applied load of 15 N (Fig. 5.17a) shows combinations of macro and micro-grooves resulting in less wear debris and hence greater wear resistance. Delamination, macro-grooves, and few micro-grooves can be seen in the worn track for the applied load of 30 N (Fig. 5.17b). Worn track at an applied load of 45 N (Fig. 5.17c) shows larger size delamination and macro-grooves removing of more material from the sample. Formation of micro-grooves on deposition surface results from materials separation in the shape of wear debris whereas

macro-grooves and delamination are produced as a result of repetitive ploughing resulting in increased material removal by the spalling mechanism of wear. Table 5.3 presents comparison of sliding wear characteristics of the μ -PAAM deposited Ti-Ta-Nb-Mo-Zr HEA with the comparable HEAs and Ti-6Al-4V alloy.

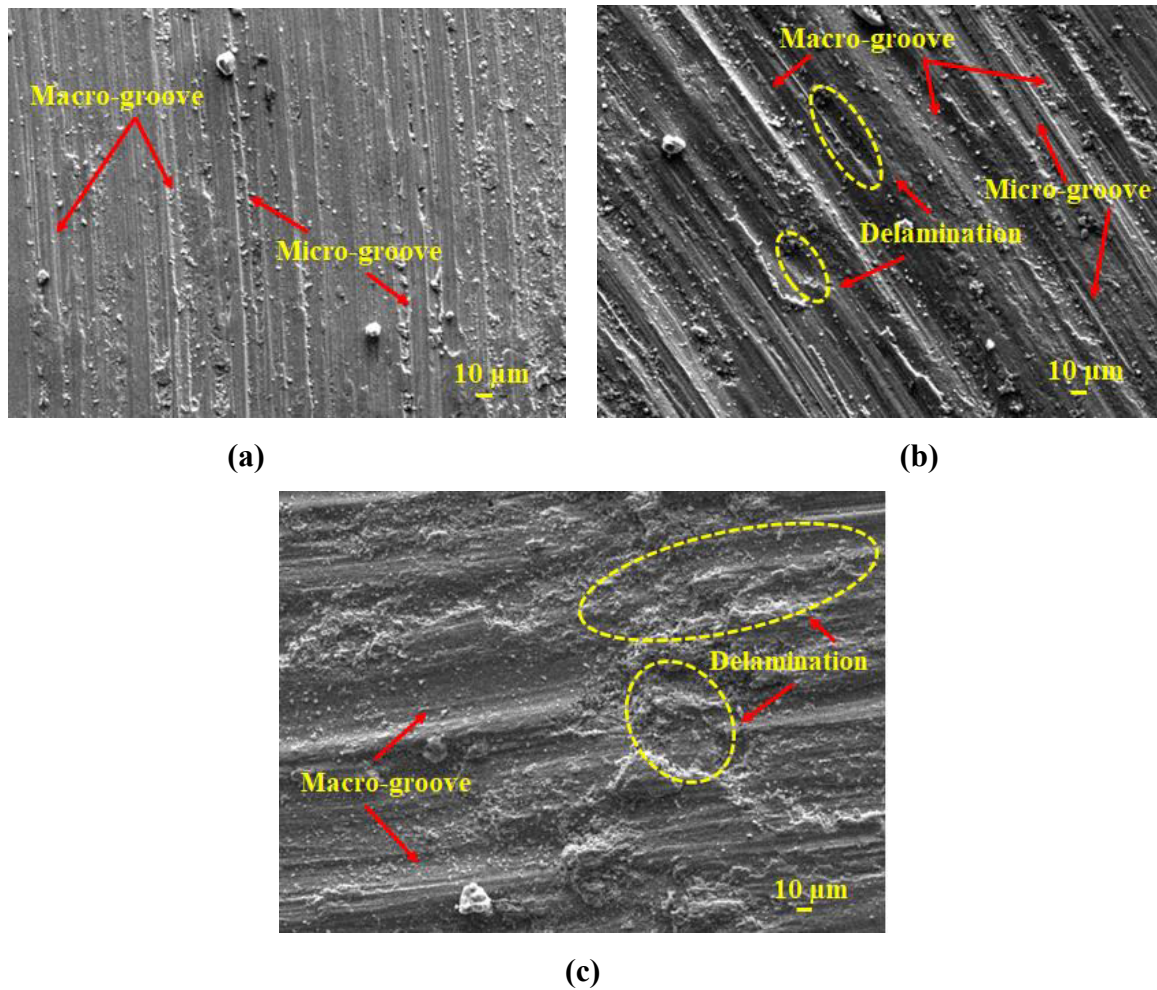


Fig. 5.17: SEM images of the worn track of multi-track multi-layer deposition sample of Ti-Ta-Nb-Mo-Zr HEA for the applied load of: (a) 15 N, (b) 30 N, (c) 45 N.

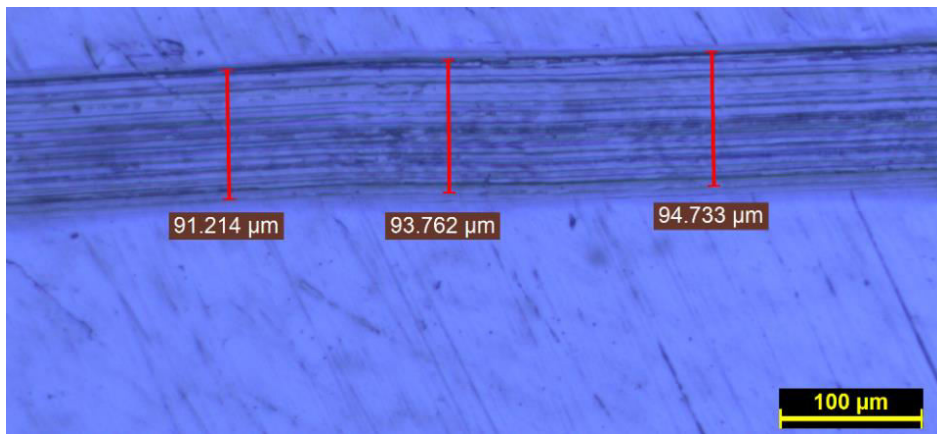
Table 5.3: Comparison of sliding wear characteristics of the multi-track multi-layer sample of Ti-Ta-Nb-Mo-Zr HEA with present HEAs and Ti-6Al-4V alloy.

Materials	Manufacturing process	Applied load	COF	Specific wear rate ($10^{-4} \text{ mm}^3/\text{N}\cdot\text{m}$)	References
Ti-6Al-4V		5 N	0.61	3.50	
Ti ₂ -Nb-Zr-Mo-Ta		5 N	0.84	2.42	
Ti _{1.5} -Nb-Zr-Mo-Ta	Arc melted	5 N	0.94	2.73	Hua <i>et al.</i> (2021)
Ti-Nb-Zr-Mo-Ta		5 N	0.94	2.91	
Ti _{0.5} -Nb-Zr-Mo-Ta		5 N	0.75	2.22	
Ti-Ta-Nb-Mo-Zr		15 N	0.46	7.29	
Ti-Ta-Nb-Mo-Zr	μ -PAAM	30 N	0.51	5.49	<i>Present study</i>
Ti-Ta-Nb-Mo-Zr		45 N	0.63	4.35	

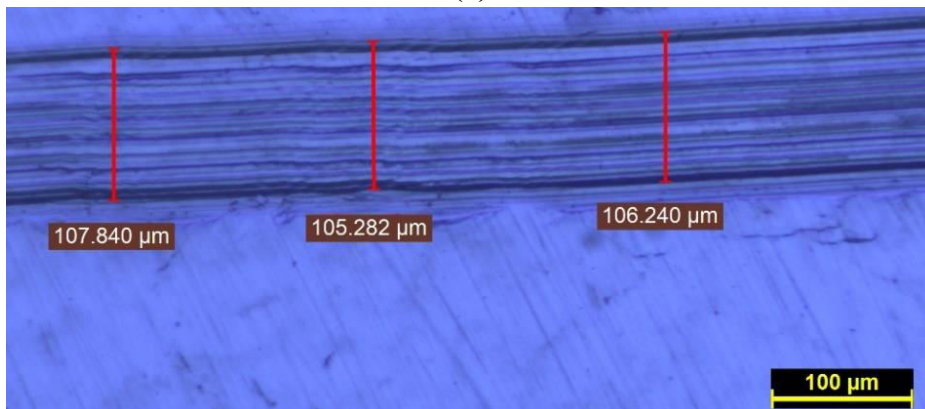
It is evident from the Table 5.3 that at an applied load of 5 N, the COF for the arc melted HEAs varies from 0.75 to 0.94 and it is 0.61 for Ti-6Al-4V alloy. Whereas for an applied load range from 15 to 45 N, it varies from 0.46 to 0.63 in the present study. Specific wear rate of arc melted comparable HEAs and Ti-6Al-4V alloy for an applied load of 5 N is smaller than μ -PAAM deposited Ti-Ta-Nb-Mo-Zr HEA sample for the applied loads of 15, 30, and 45 N.

5.7 Results for Abrasion Resistance

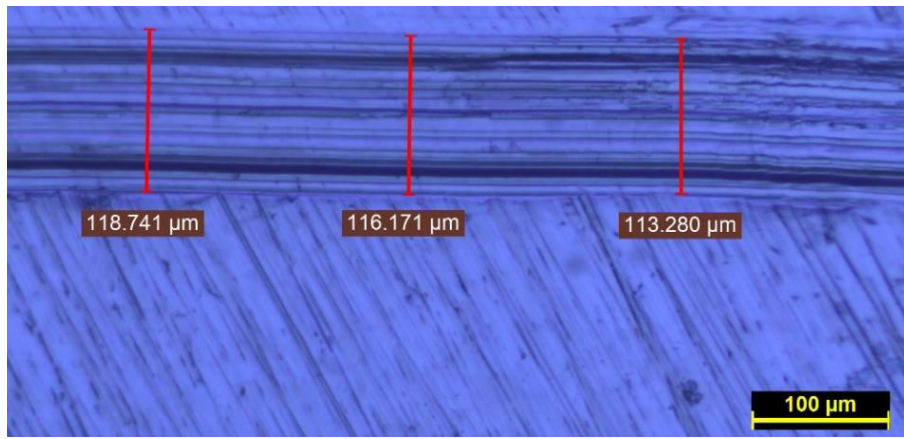
Figure 5.18 shows optical microscopic images of scratch tracks formed on Ti-Ta-Nb-Mo-Zr HEA surface at applied load of 10 N (Fig. 5.18a), 15 N (Fig. 5.18b), and 20 N (Fig. 5.18c). Table 5.4 lists mean value and standard deviation of scratch track width, coefficient of friction, and computed values of scratch hardness number using Eq. 3.6.



(a)



(b)



(c)

Fig. 5.18: Optical micrographs of measurement of scratch track width at different applied load (a) 10 N, (b) 15 N, (c) 20 N.

Table 5.4: Results of abrasion resistance test for Ti-Ta-Nb-Mo-Zr HEA.

Applied load (N)	Mean value (standard deviation) of scratch track width μm	Mean value (standard deviation) of coefficient of friction	Scratch hardness number (GPa)
10	93.24 (1.82)	0.19 (0.04)	2.93
15	106.45 (1.29)	0.22 (0.06)	3.37
20	116.06 (2.73)	0.19 (0.05)	3.78

It can be observed that average value of scratch track width and scratch hardness number (computed using Eq. 3.6) of the developed Ti-Ta-Nb-Mo-Zr HEA (Table 5.4) increase with increase in the applied load. Average value of coefficient of friction first increases from 0.19 to 0.22 when applied load increases to 15 N from 10 N and then decrease to 0.19 for 20 N of applied load. It implies that the developed Ti-Ta-Nb-Mo-Zr HEA has higher abrasion resistance at higher value of the applied load without any considerable change in coefficient friction. This will impart better resistance to wear and tear making it better material for orthopedic implant applications.

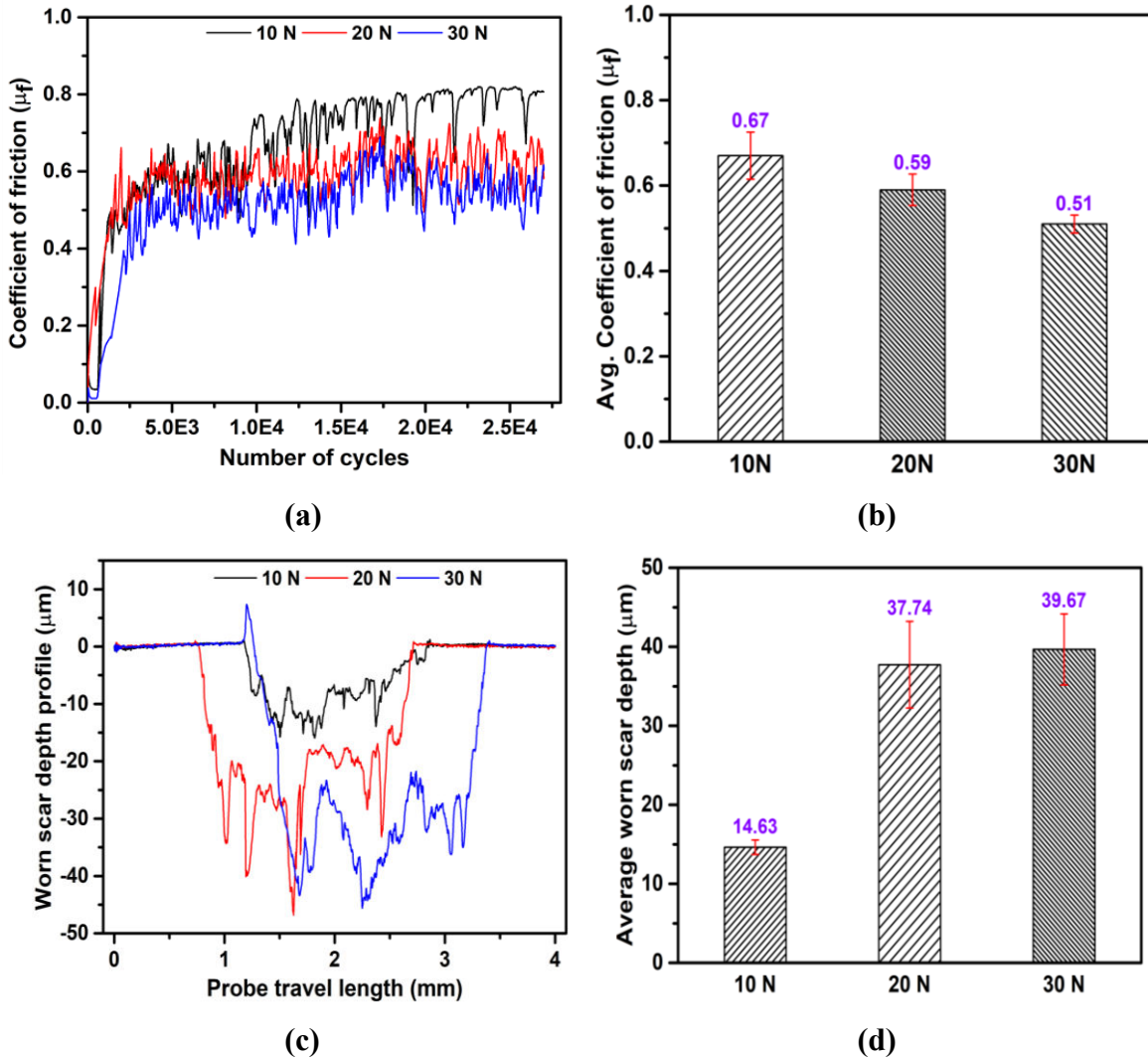
5.8 Findings from Bio-Tribological Behavior of Ti-Ta-Nb-Mo-Zr HEA

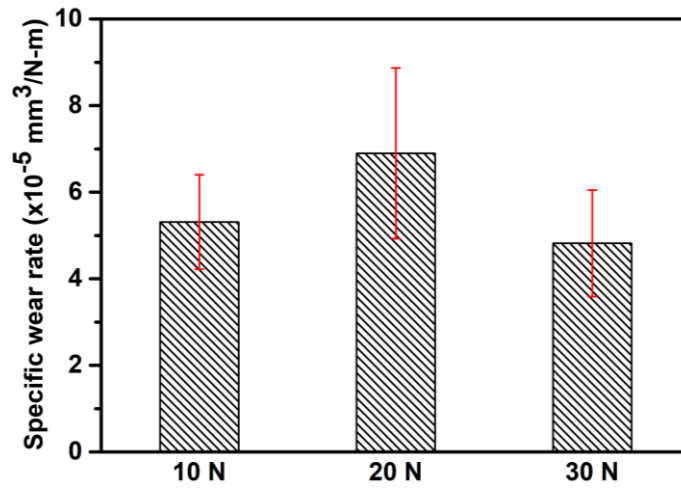
This section describes the results and analysis of dry fretting wear, corrosion, and tribo-corrosion characteristics of multi-track multi-layer deposition Ti-Ta-Nb-Mo-Zr HEA with an objective to demonstrate it as a better knee implant material.

5.8.1 Analysis of Dry Fretting Wear

Figure 5.19 presents results of dry fretting wear of multi-track multi-layer deposition sample of Ti-Ta-Nb-Mo-Zr HEA under the applied load of 10; 20; and 30 N at room temperature. It shows variation in coefficient of friction (COF) with number of fretting cycles which is product of fretting frequency and fretting wear time (Fig. 5.19a), average

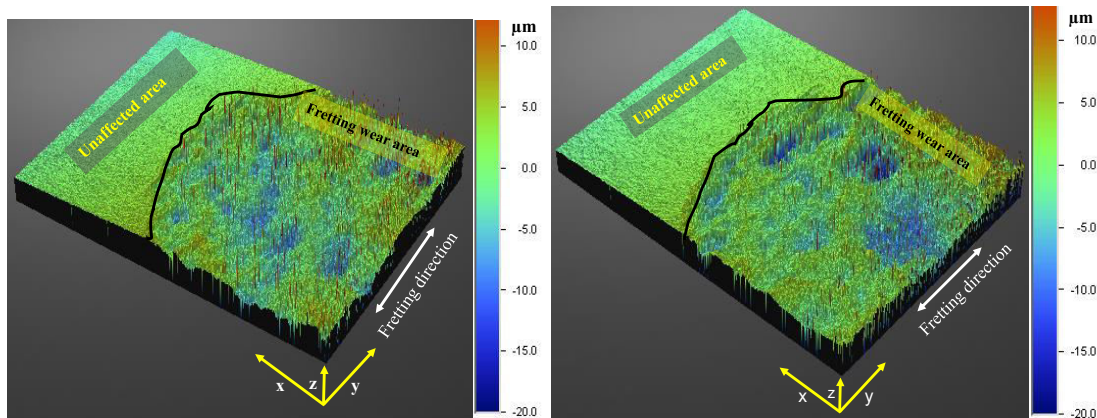
COF (Fig. 5.19b) obtained from the graphs of Fig. 5.19a, change in worn scar depth with probe travel length (Fig. 5.19c), average worn scar depth (Fig. 5.19d) measured from Fig. 5.19c and computed specific wear rate (Fig. 5.19e) for the different applied load. Figure 5.20 depicts 3D surface roughness profiles of worn surface of Ti-Ta-Nb-Mo-Zr HEA after dry fretting wear test at applied load of 10 N (Fig. 5.20a), 20 N (Fig. 5.20b), and 30 N (Fig. 5.20c). Figure 5.21 depicts SEM images of the fretting wear track and their respective worn scar morphology for applied load of 10 N (Fig. 5.21a), 20 N (Fig. 5.21b), and 30 N (Fig. 5.21c).





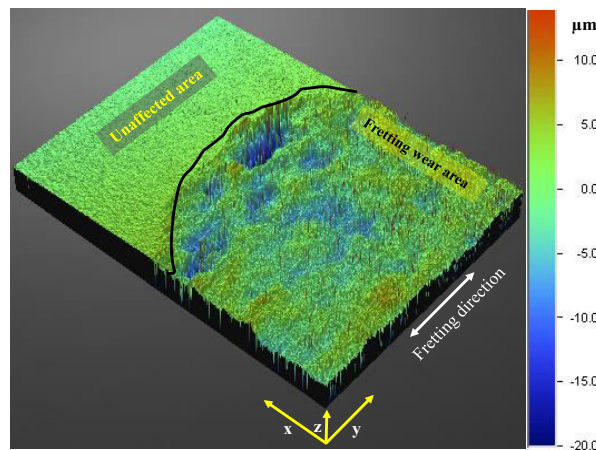
(e)

Fig. 5.19: Fretting wear results for multi-track multi-layer deposition sample of Ti-Ta-Nb-Mo-Zr HEA under different applied load: (a) variation of coefficient of friction with number of cycles, (b) average coefficient of friction, (c) worn scar depth profile with probe travel length, (d) average worn scar depth, and (e) specific wear rate.



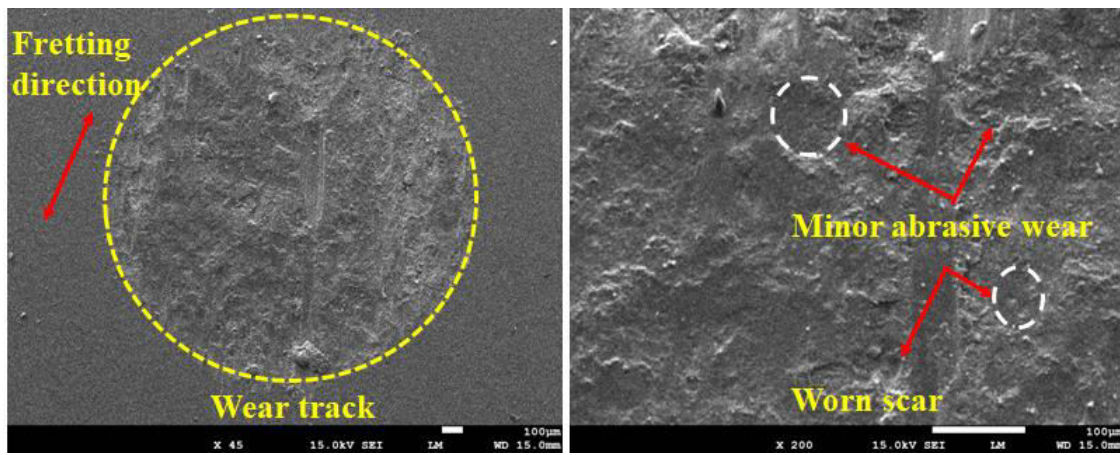
(a)

(b)

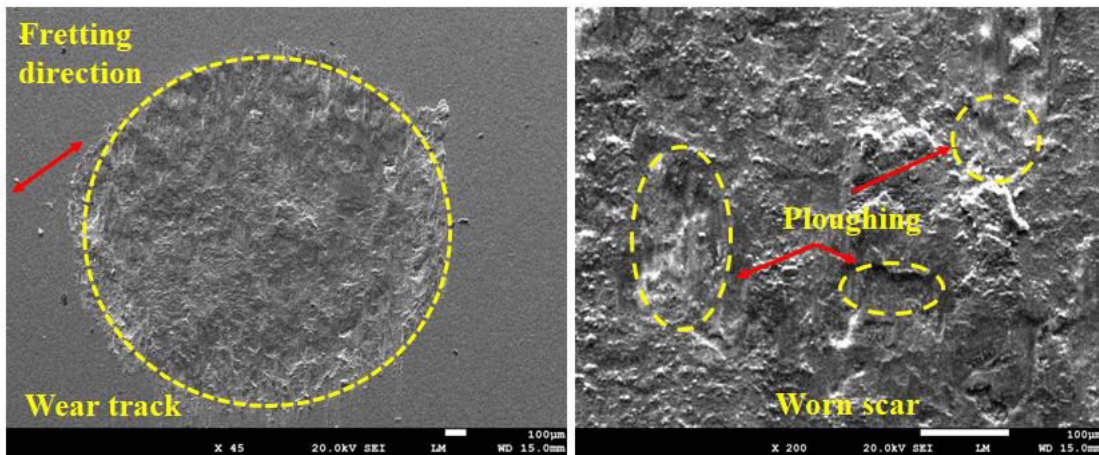


(c)

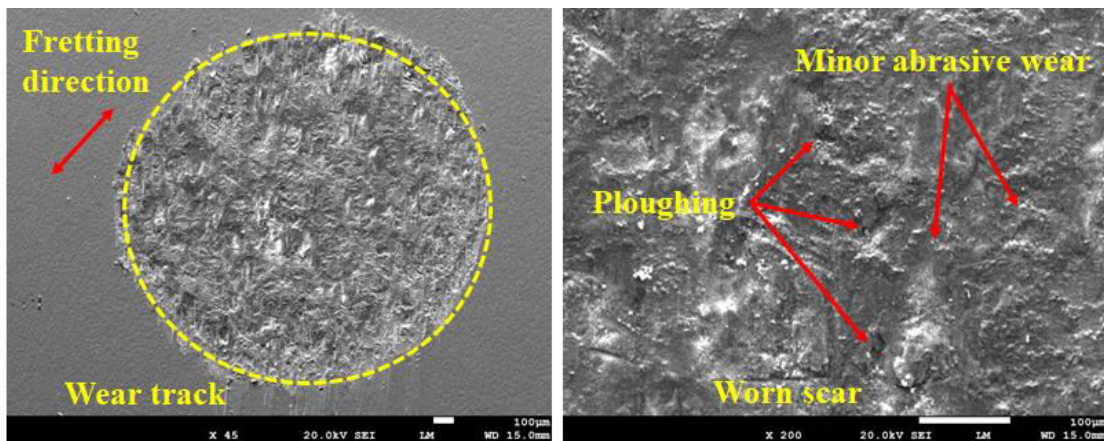
Fig. 5.20: 3D surface roughness profile of worn surface of multi-track multi-layer deposition sample of Ti-Ta-Nb-Mo-Zr HEA in dry fretting wear conducted at applied load of: (a) 10 N, (b) 20 N, (c) 30 N.



(a)



(b)



(c)

Fig. 5.21: SEM images of fretting wear track and worn scar morphology for multi-track multi-layer deposition sample of Ti-Ta-Nb-Mo-Zr HEA for applied load of: (a) 10 N, (b) 20 N, (c) 30 N.

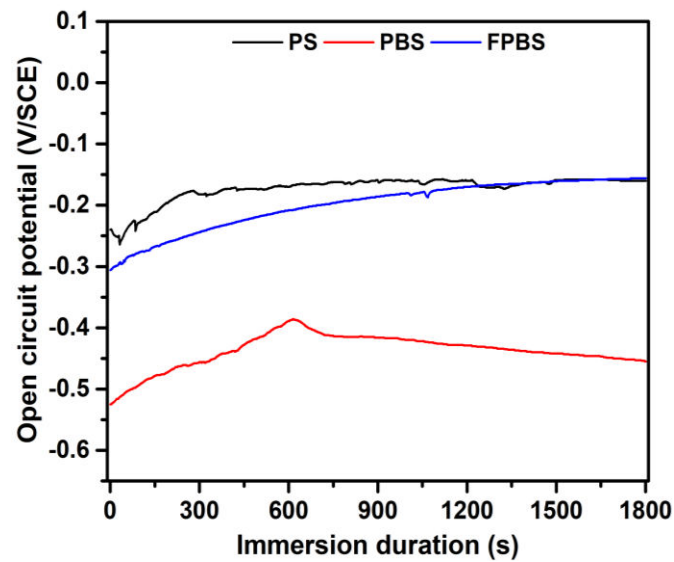
Figure 5.19a shows that COF increases rapidly to 0.4 at the beginning of fretting wear test for different values of applied load. It may be due to uneven surfaces of Ti-Ta-Nb-Mo-Zr HEA test sample and absence of wear track. After 2×10^3 cycles, it stabilizes and varies in

a range of 0.4 to 0.8 may be due to formation of some wear tracks. Average COF decreases with increase in the applied load (Fig. 5.19b). It may be due to rupture of Ti-Ta-Nb-Zr-Mo HEA surface at increased applied load thus producing wear debris. This entrapped debris could act as a small bearing area which may reduce COF. Another possible reason may be self-lubricating properties of Ti-Ta-Nb-Mo-Zr HEA due to its constituent elements such as Ta, Nb, and Mo. **Luo et al. (2021)** have reported similar decreasing trend in COF due to self-lubricating properties of Ta-Nb-W-Mo alloy. **Rustamov et al. (2019)** also observed similar decreasing trend in COF during dry fretting wear of Inconel x-750 alloy. Profiles of worn scar depth on Ti-Ta-Nb-Mo-Zr HEA test samples are U-shaped (Fig. 5.19c) indicating wear volume loss. It can be observed that average worn scar depth (Fig. 5.19d) increases with increase in applied load. Specific fretting wear rate (Fig. 5.19e) is maximum ($6.91 \times 10^{-5} \text{ mm}^3/\text{N-m}$) for the applied load of 20 N followed by at 10 N and 30 N of applied load (5.31×10^{-5} and $4.82 \times 10^{-5} \text{ mm}^3/\text{N-m}$ respectively). Figure 5.20a shows minor variation in 3D surface roughness profile of test sample of Ti-Ta-Nb-Mo-Zr HEA at 10 N applied load in dry fretting wear test with some valleys shown in blue color as compared to its unworn or unaffected surface (shown in green color). Figures 5.20b and 5.20c show more variation in their respective 3D surface roughness profiles at applied loads of 20 N and 30 N showing more deeper valley. It results in larger values of worn scar depth (Fig. 5.19d). Figure 5.21a shows occurrence of minor abrasive wear due to formation of loose wear debris which comes in between the pin and the test sample surface at onset of the dry fretting wear. Morphology of worn scar at applied load of 20 N (Fig. 5.21b) and 30 N (Fig. 5.21c) show ploughing of material from the fretting wear area which occurs due to large scale displacement of material from the surface with or without removing the material. Some minor abrasive wear can also be seen. Dry fretting wear at applied load of 10 N considered as the *control* for tribo-corrosion test due to higher value of COF (0.67), lower value of worn scar depth ($14.63 \mu\text{m}$), and moderate specific wear rate ($5.31 \times 10^{-5} \text{ mm}^3/\text{N-m}$).

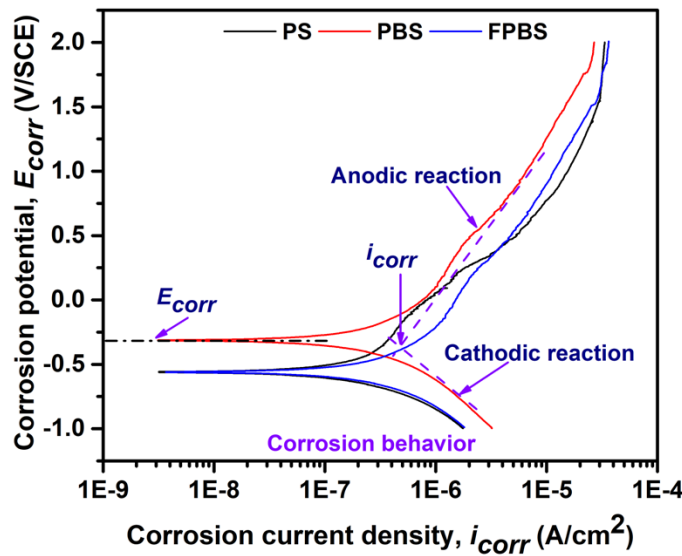
5.8.2 Analysis of Corrosion Behavior in Biofluids

Figure 5.22 presents results for corrosion behavior of multi-track multi-layer deposition sample of Ti-Ta-Nb-Mo-Zr HEA in 7.4 pH value of three human body emulating biofluids namely physiological saline (PS), PBS solution, and 1% fetal bovine serum (FBS) mixed with the PBS solution (FPBS) showing open-circuit potential (OCP) curve (Fig. 5.22a) and Tafel polarization curve (Fig. 5.22b). The OCP shows variation in potential of the working electrode with respect to immersion duration. It indicates corrosion tendency of the working electrode in the chosen corrosive environment i.e., its higher value means higher corrosion tendency and vice-versa. Corrosion potential ' E_{corr} ' is the potential of the working electrode

with respect to corrosion current density ' i_{corr} ' when current is flowing in the corrosion test equipment. Values of OCP and corrosion potential ' E_{corr} ' may or may not be same. Variations in the values of OCP and ' E_{corr} ' are attributed to working electrode, corrosive environment, and experimental apparatus. Corrosion current density ' i_{corr} ' is an important parameter of corrosion analysis which is directly proportional to corrosion rate. Table 5.5 lists corrosion potential ' E_{corr} ' (volts), corrosion current density ' i_{corr} ' ($\mu\text{A}/\text{cm}^2$), and corrosion rate (mm/year) determined from the Tafel polarization curve (Fig. 5.22b) using Tafel extrapolation method. Figure 5.23 shows SEM images of the corroded surfaces of multi-track multi-layer deposition samples of Ti-Ta-Nb-Mo-Zr HEA in PS (Fig. 5.23a), PBS (Fig. 5.23b), and FPBS (Fig. 5.23c) biofluids.



(a)

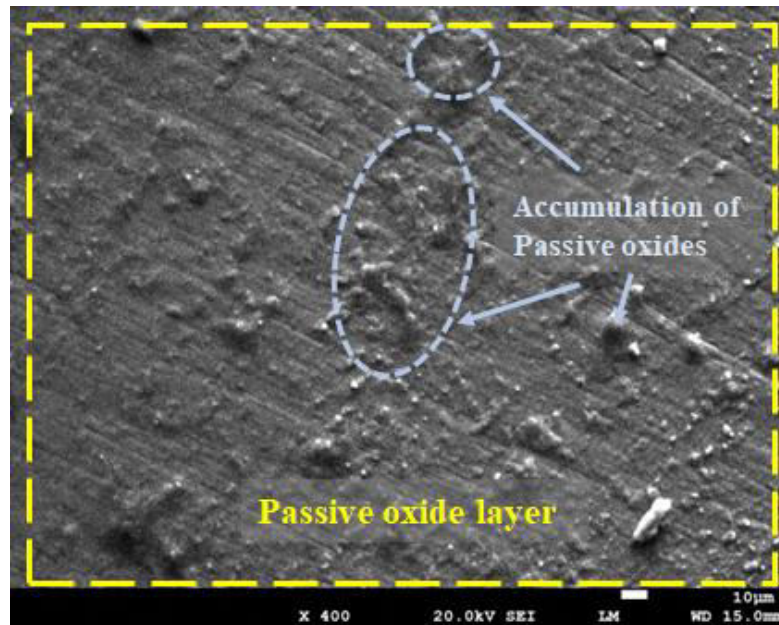


(b)

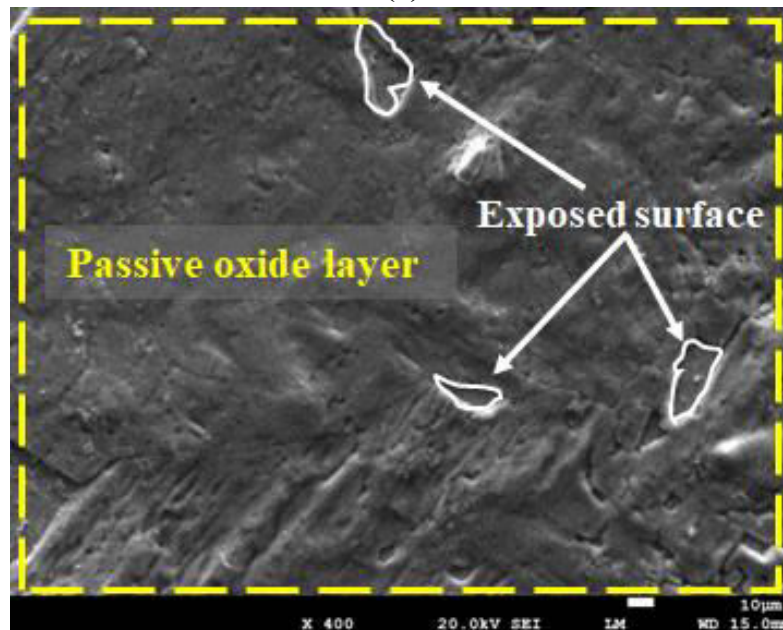
Fig. 5.22: Results for corrosion behavior analysis of multi-track multi-layer deposition sample of Ti-Ta-Nb-Mo-Zr HEA: (a) open circuit potential (OCP) curve, and (b) Tafel polarization curve.

Table 5.5: Corrosion parameters obtained from the Tafel polarization curve for multi-track multi-layer deposition sample of Ti-Ta-Nb-Mo-Zr HEA in three biofluids.

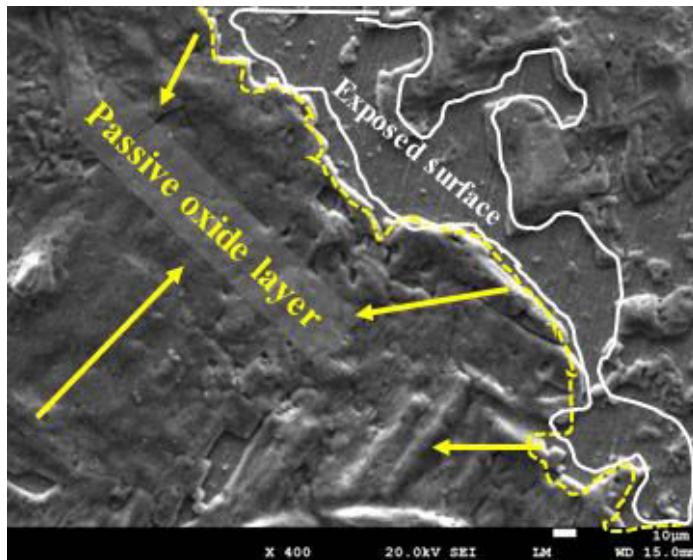
Biofluid	Avg. OCP (volts)	Corrosion potential ' E_{corr} ' (volts)	Corrosion current density ' i_{corr} ' ($\mu\text{A}/\text{cm}^2$)	Corrosion rate (mm/year)
PS	-0.17	-0.58	5.41	0.05
PBS	-0.44	-0.29	7.45	0.06
FPBS	-0.19	-0.58	3.83	0.05



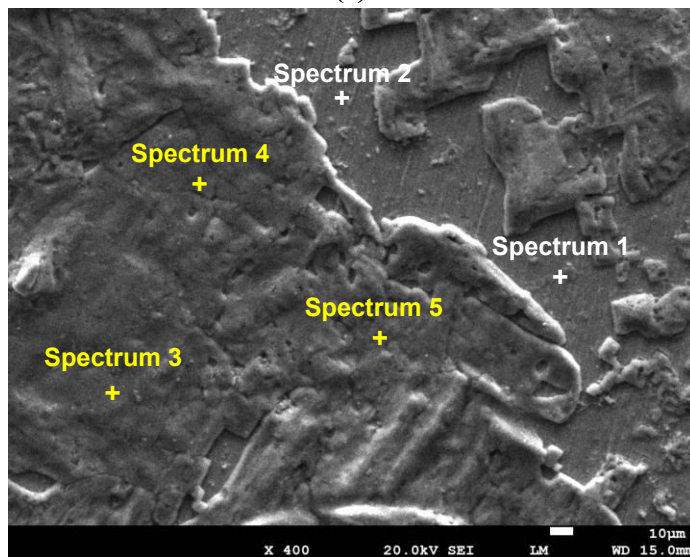
(a)



(b)



(c)



(d)

Fig. 5.23: SEM images of the corroded surface of multi-track multi-layer deposition sample of Ti-Ta-Nb-Mo-Zr HEA in different biofluids: (a) PS, (b) PBS, (c) FPBS, and (d) marked spectrum for its chemical compositions using EDS analysis.

Table 5.6: Chemical compositions (by at. %) of marked spectrums of corroded surface of Ti-Ta-Nb-Mo-Zr HEA in FPBS biofluids.

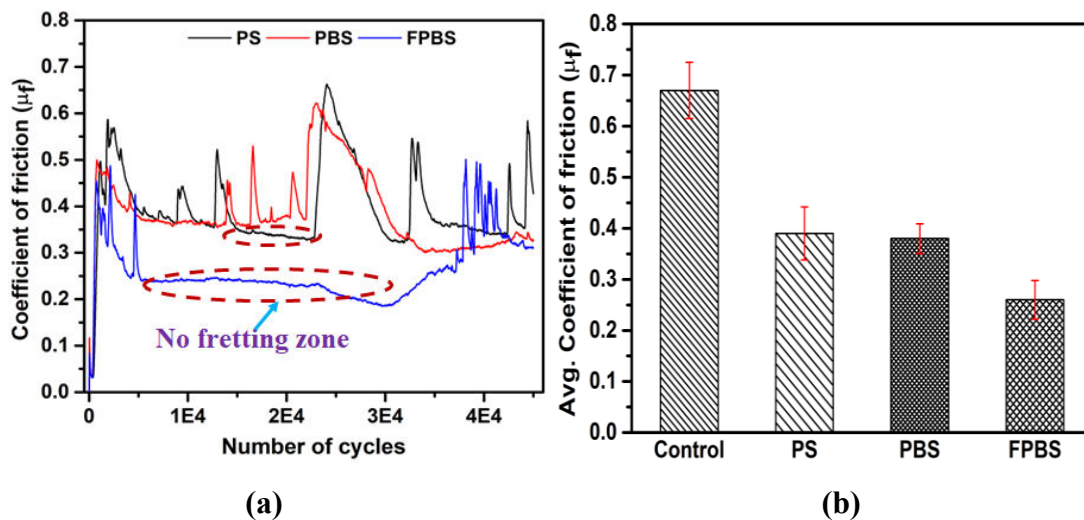
Spectrum	Ti	Ta	Nb	Mo	Zr	O
1	19.5	19.8	20.1	19.9	19.4	1.3
2	19.5	19.4	19.6	20.1	19.6	1.8
3	18.8	17.9	17.7	17.5	16.7	10.7
4	19.1	18.1	17.9	18.4	17.3	9.2
5	18.7	17.7	17.3	18.4	16.5	11.4

Open circuit potential (OCP) of Ti-Ta-Nb-Mo-Zr HEA (Fig. 5.22a) has negative values for the considered immersion durations in PS, PBS and FPBS biofluids at 7.4 pH value. PBS biofluid shows more negative OCP value (-0.44 volts) than FPBS (-0.19 volts) and PS (-0.17 V). It indicates higher corrosive tendency of the exposed surface of the Ti-Ta-Nb-Mo-Zr HEA. But OCP increases gradually with immersion duration and then becomes almost constant after immersion duration of 700 seconds for PBS biofluid and after 1200 seconds for PS and FPBS biofluids (Fig. 5.22a). Such increasing trend of OCP from negative values with immersion duration suggests formation of a passive oxide layer on the exposed surface of Ti-Ta-Nb-Mo-Zr HEA in the biofluids. Passive layer formation tendency on the exposed surfaces is similar to the findings for Ti-22Nb, Ti-22Nb-6Zr alloys by **Wang et al. (2009)**, for Ti-Mo-Nb-Zr alloys by **Nnamchi et al. (2016)** and for Ti-16Nb alloy by **Yilmaz et al. (2019)**. It is evident from Table 5.5 that corrosion potential having maximum value for PS and FPBS (-0.58 volts). Corrosion current density is maximum for PBS biofluid ($7.45 \mu\text{A}/\text{cm}^2$) followed by PS ($5.41 \mu\text{A}/\text{cm}^2$) and FPBS ($3.83 \mu\text{A}/\text{cm}^2$) biofluids. Corrosion rate is found to be almost equal (0.05-0.06 mm/year) in 7.4 pH value of PS, PBS and FPBS biofluids implying that the developed HEA has same corrosion resistance in all biofluids. It can be seen in Fig. 5.22b that the Tafel polarization curves for Ti-Ta-Nb-Mo-Zr HEA in different biofluids are of similar nature with slight differences in their cathodic and anodic reaction regions. There is a wide passive plateau up to 2 volts on anodic side of the Tafel polarization curves indicating no pitting corrosion. It indicates formation of strong passive oxide layers on the exposed surface of Ti-Ta-Nb-Mo-Zr HEA in PS, PBS and FPBS biofluids. Passive oxide layers may consist of TiO_2 , Ta_2O_5 , Nb_2O_5 , NbO_2 , and ZrO_2 which are formed by the constituent elements i.e., Ti, Nb, Zr and Ta imparting excellent corrosion resistance to the developed Ti-Ta-Nb-Mo-Zr HEA in different biofluids. **Bocchetta et al. (2021)** have reported formation of passive layer consisting of TiO_2 , Ta_2O_5 , Nb_2O_5 , NbO_2 , and ZrO_2 in corrosion behavior study of Ti-12Mo-5Ta and Ti-20Nb-10Zr-5Ta alloys imparting these alloys excellent corrosion resistance against the corrosive environment. SEM images of the corroded surface of Ti-Ta-Nb-Mo-Zr HEA in PBS (Fig. 5.23b) and FPBS (Fig. 5.23c) biofluids depict formation of passive oxides layers on the exposed surface except for some regions marked in white color where passive layer is not formed. Formation of passive oxides layers is further confirmed through chemical compositions of marked spectrum (Fig. 5.23d) through EDS analysis as shown in Table 5.6. It can be observed from Table 5.6 those chemical compositions of spectrum 1 and 2 depict oxygen content as 1.3 and 1.8 at. %. Whereas chemical compositions of spectrum 3-5 depict oxygen content varying from 9.2 to 11.4 at. %. These observation from Table 5.6 indicates

that spectrum 1 and 2 belongs to exposed surface (marked in white color in Fig. 5.23c) where inferior passive oxide layer is formed, whereas spectrum 3-5 belongs to strong passive oxides layer (marked in yellow color in Fig. 5.23c) due to higher oxygen content. SEM image for PS biofluid in Fig. 5.23a shows that exposed surface is covered with passive oxide layer and few accumulations of passive oxide layers (marked as a circle). It can be correlated with the corrosion rates in these biofluids which are almost equal (Table 5.5). Formation of passive oxides layer on the exposed surfaces is similar to the findings for Ti-16Nb alloy by **Yilmaz et al. (2019)**, for Ti-22Nb and Ti-22Nb-6Zr alloys by **Wang et al. (2009)**, and for Ti-Mo-Nb-Zr alloys by **Nnamchi et al. (2016)**. Based upon the above findings it can be concluded that developed Ti-Ta-Nb-Mo-Zr HEA has better corrosion resistance than Ti-22Nb, Ti-22Nb-6Zr, Ti-Mo-Nb-Zr, Ti-16Nb, Ti-12Mo-5Ta and Ti-20Nb-10Zr-5Ta alloys (**Wang et al. 2009; Nnamchi et al. 2016; Yilmaz et al. 2019; Bocchetta et al. 2021**) and is potential alternative to the presently used materials for the knee implants.

5.8.3 Analysis of Tribo-Corrosion Behavior in Biofluids

Figure 5.24 presents results of tribo-corrosion behavior of multi-track multi-layer deposition sample Ti-Ta-Nb-Mo-Zr HEA in PS, PBS and FPBS biofluids. It shows variation in COF with number of cycles (Fig. 5.24a), average COF (Fig. 5.24b) obtained from the graphs of Fig. 5.24a, change in worn scar depth with probe travel length (Fig. 5.24c), average worn scar depth (Fig. 5.24d) measured from Fig. 5.24c, computed specific wear rate (Fig. 5.24e), OCP curve (Fig. 5.24f), and Tafel polarization curve (Fig. 5.24g). Table 5.6 lists comparison of parameters of corrosion and tribo-corrosion behavior of Ti-Ta-Nb-Mo-Zr HEA in different biofluids in terms of corrosion potential ' E_{corr} ' (volts), corrosion current density ' i_{corr} ' ($\mu\text{A}/\text{cm}^2$), and corrosion rate (mm/year) determined from their corresponding Tafel polarization curves (Fig. 5.22b and Fig. 5.24g).



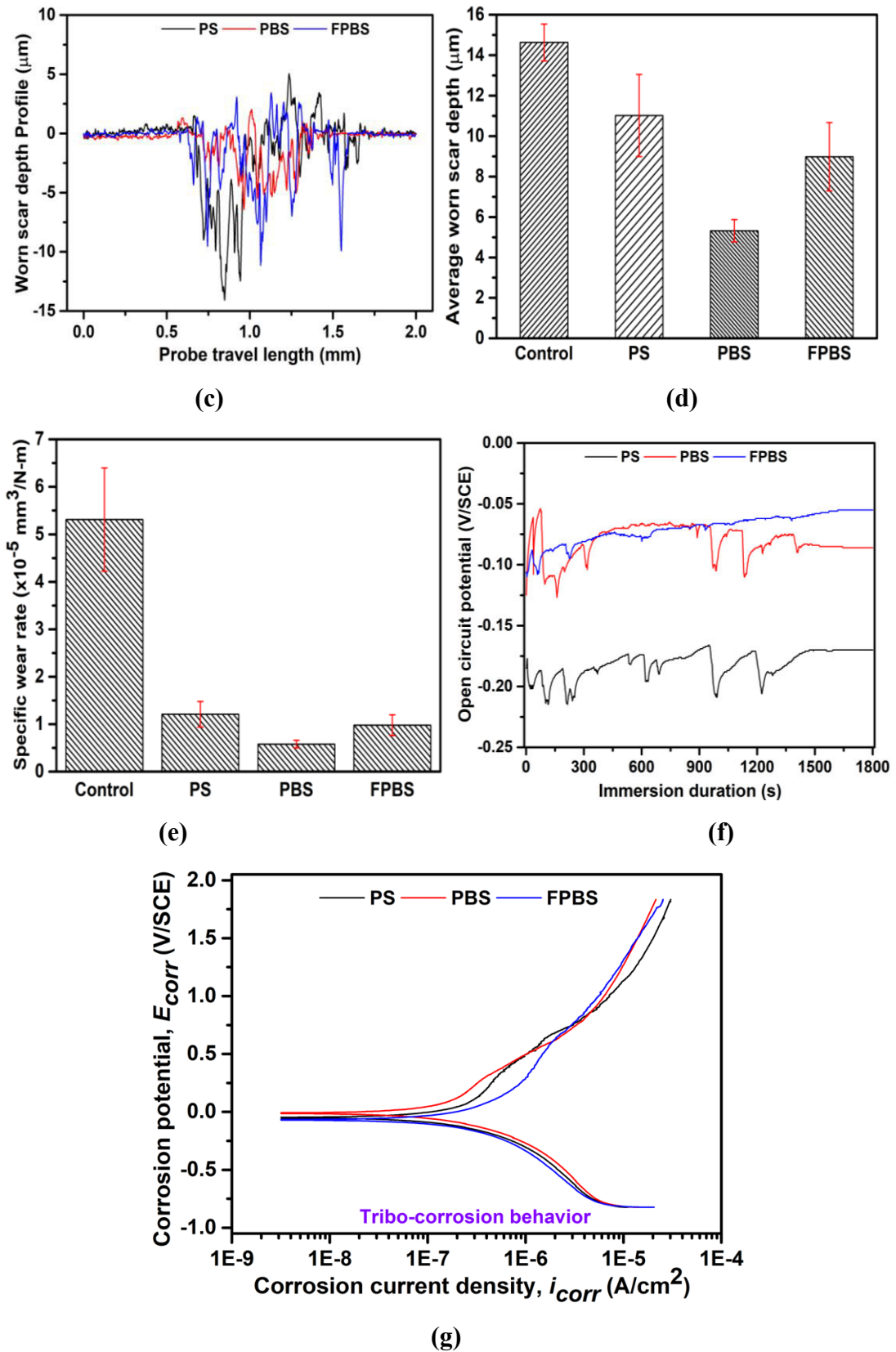


Fig. 5.24: Results for tribo-corrosion of multi-track multi-layer deposition sample of Ti-Ta-Nb-Mo-Zr HEA in different biofluids: (a) variation of coefficient of friction with number of cycles, (b) average coefficient of friction at applied load of 10 N, (c) change in worn scar depth with probe travel length, (d) average worn scar depth, (e) specific wear rate, (f) OCP curve, and (g) Tafel polarization curve.

Table 5.7: Comparison of parameters of corrosion and tribo-corrosion behavior of multi-track multi-layer deposition sample of Ti-Ta-Nb-Mo-Zr HEA in different biofluids determined from their corresponding Tafel polarization curves.

Biofluid	Corrosion			Corrosion rate (mm/yr)	Tribo-corrosion			Corrosion rate (mm/year)
	OCP	' E_{corr} ' (volts)	' i_{corr} ' ($\mu\text{A}/\text{cm}^2$)		OCP	' E_{corr} ' (volts)	' i_{corr} ' ($\mu\text{A}/\text{cm}^2$)	
PS	-0.17	-0.58	5.41	0.05	-0.18	-0.16	1.25	1.05
PBS	-0.44	-0.29	7.45	0.06	-0.08	-0.13	1.61	1.34
FPBS	-0.19	-0.57	3.83	0.05	-0.07	-0.11	1.77	1.43

Following are the observations from Figs. 5.24a-5.24g and Table 5.7 along with their explanations:

- Figure 5.24a shows that COF increases rapidly to 0.6 in PS biofluid and to 0.5 in PBS and FPBS biofluids at the beginning of tribo-corrosion test which may be due to uneven surfaces of test samples of Ti-Ta-Nb-Mo-Zr HEA and absence of wear tracks. As the tribo-corrosion cycles increases then COF decreases and fluctuates in a range of 0.2-0.65 for all the biofluids which may be due to occasional breakage of passive oxide layers. The COF remains constant for a large range of immersion duration for FPBS and for smaller range for PS and PBS biofluids indicating no-fretting zone (i.e., only corrosion taking place) which may be due to slip of the fretting pin on surface of test samples caused by lubricating action of the biofluids, and formation of a strong passive layer of oxides that covers uneven surface of the test samples. The PS biofluid resulted in maximum value of average COF (0.39) and FBPS biofluid yielded its minimum value (0.26) as shown in Fig. 5.24b. It may be due to nature of biofluids used in tribo-corrosion because some biofluids cause frequent removal and formation of passivating oxide layers which produces wear debris and oxides debris. It is worth noting that the presence of biofluids reduces COF by almost 50% in comparison to the control.
- Figure 5.24c depicts zigzag pattern for profiles of worn scar depth unlike U-shaped profile obtained in dry fretting wear test (Fig. 5.19c). Figure 5.24d shows average value of worn scar depth measured from Fig. 5.24c. It results in lesser worn scar depth in presence of biofluids as compared to the control in dry condition. The PS biofluid gave maximum values of worn scar depth (11.02 μm) which is considerably less than the control obtained in dry fretting wear (14.63 μm) due to lubricating action of the biofluids and covering of uneven surfaces of the test samples by the passive layers of oxides. Mechanism of tribo-corrosion worn scar is found to depend on type of biofluid,

stability of passive layer of oxides, applied load, stroke length of the reciprocating pin, number of cycles, and properties of the test sample material (Zhu and Zhou 2011).

- Figure 5.24e depicts specific fretting wear rate (computed using Eq. 3.5) of Ti-Ta-Nb-Mo-Zr HEA in the presence of biofluids in comparison to the control. It has been found that PS biofluid resulted in maximum specific fretting wear rate ($1.20 \times 10^{-5} \text{ mm}^3/\text{N-m}$) which is almost 25% of the specific fretting wear rate of the control ($5.31 \times 10^{-5} \text{ mm}^3/\text{N-m}$). This can be related to average worn scar depth obtained in biofluids (Fig. 5.24d) in which PS biofluid has maximum worn scar depth (11.02 μm) followed by the FPBS (8.98 μm) and PBS (5.32 μm) biofluids.
- Figure 5.24f shows that OCP is fluctuating towards more negative values for PS and PBS biofluids indicating occurrence of mechanical-chemical actions in which fretting wear of the exposed surfaces happen and thin passive layer is removed from the test samples exposing for further corrosion (Niu et al. 2022; Diomidis et al. 2011). Maximum and minimum decrease in OCP happen for PS and FPBS biofluids respectively at 1000 seconds of immersion duration. OCP curves stabilize after 1500 seconds of immersion duration due to re-formation of the passive layer on the worn surfaces (Zha et al. 2020; Benea et al. 2017).
- It can be seen from Fig. 5.24g (Tafel polarization curve) and Table 5.7 that values of OCP (i.e., OCP in PS is -0.18 volts, PBS -0.08 volts, and FPBS -0.07 volts), corrosion potential ' E_{corr} ' and corrosion current density ' i_{corr} ' decrease significantly in tribo-corrosion than those in corrosion of Ti-Ta-Nb-Mo-Zr HEA implying that developed HEA has less corrosive tendency in the presence of biofluids. Higher corrosion rates are found for all biofluids in tribo-corrosion than that in corrosion due to removal of material by the fretting action also. FPBS and PS biofluids showed maximum and minimum values of corrosion rates as 1.43 and 1.05 mm/year respectively in tribo-corrosion behavior. This contrasts with corrosion behavior in which all the biofluids showed the same corrosion rate.
- Overall, it can be concluded that the developed Ti-Ta-Nb-Mo-Zr HEA exhibits better tribo-corrosion resistance than Ti-22Nb, Ti-22Nb-6Zr, Ti-12Mo-5Ta, Ti-20Nb-10Zr-5Ta alloys due to formation of the strong passive oxide layer (Wang et al. 2009; Nnamchi et al. 2016; Yilmaz et al. 2019; Bocchetta et al. 2021).

Figure 5.25 depicts 3D surface roughness profiles of the tribo-corroded surface of multi-track multi-layer deposition sample of Ti-Ta-Nb-Mo-Zr HEA in the PS (Fig. 5.25a), PBS (Fig. 5.25b), and FPBS (Fig. 5.25c) biofluids. The PS biofluid resulted in more variations in surface roughness profile with a greater number of valleys and of more depth (shown in

blue color) than its unaffected surface (shown in green color) as shown in Fig. 5.25a. Whereas, the PBS and FPBS biofluids gave minor variations in surface roughness profiles with a smaller number of valleys and of lesser depth as depicted in Figs. 5.25b and 5.25c. It resulted in lesser values of worn scar depth (Fig. 5.24d) and specific wear rate for FPBS and PBS biofluids than the PS biofluid (Fig. 5.24e).

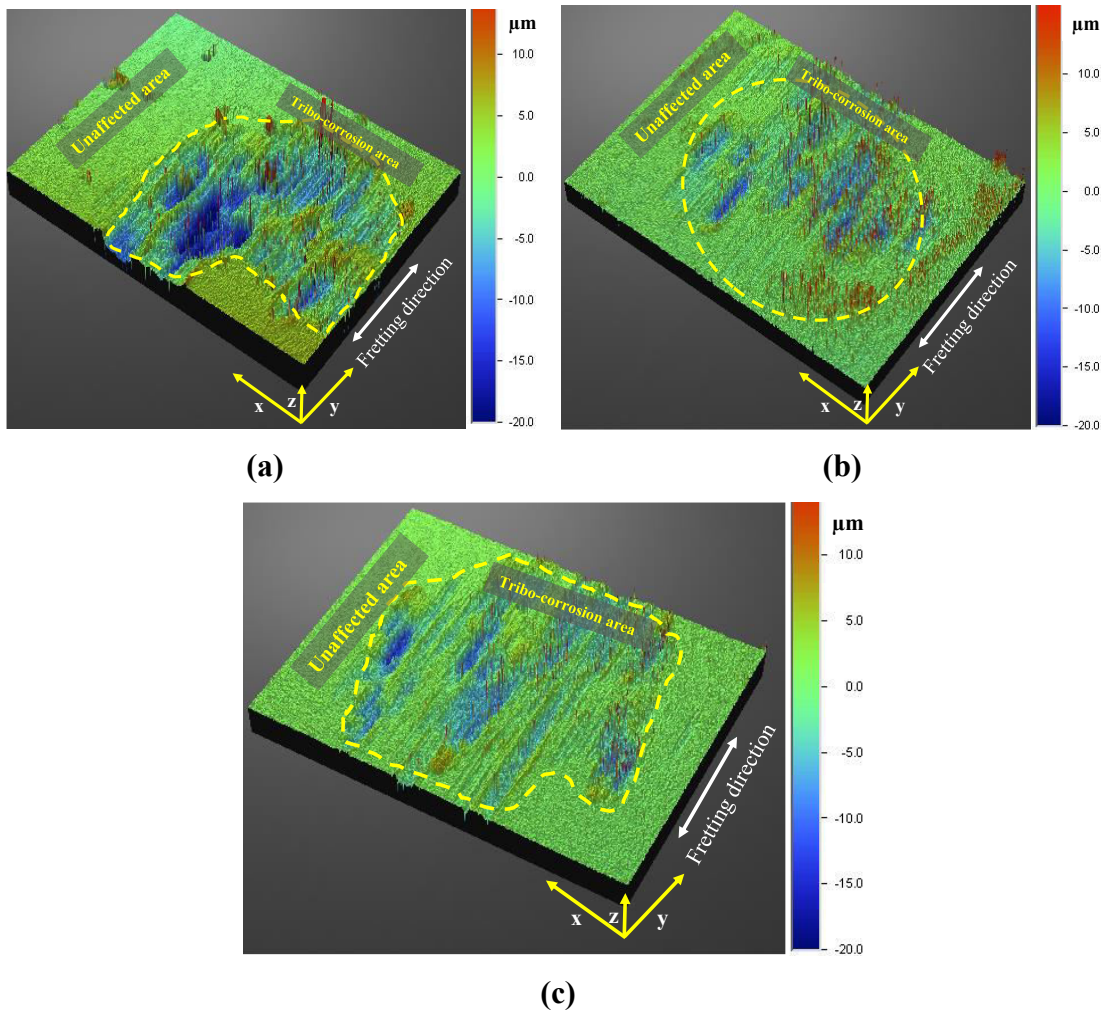
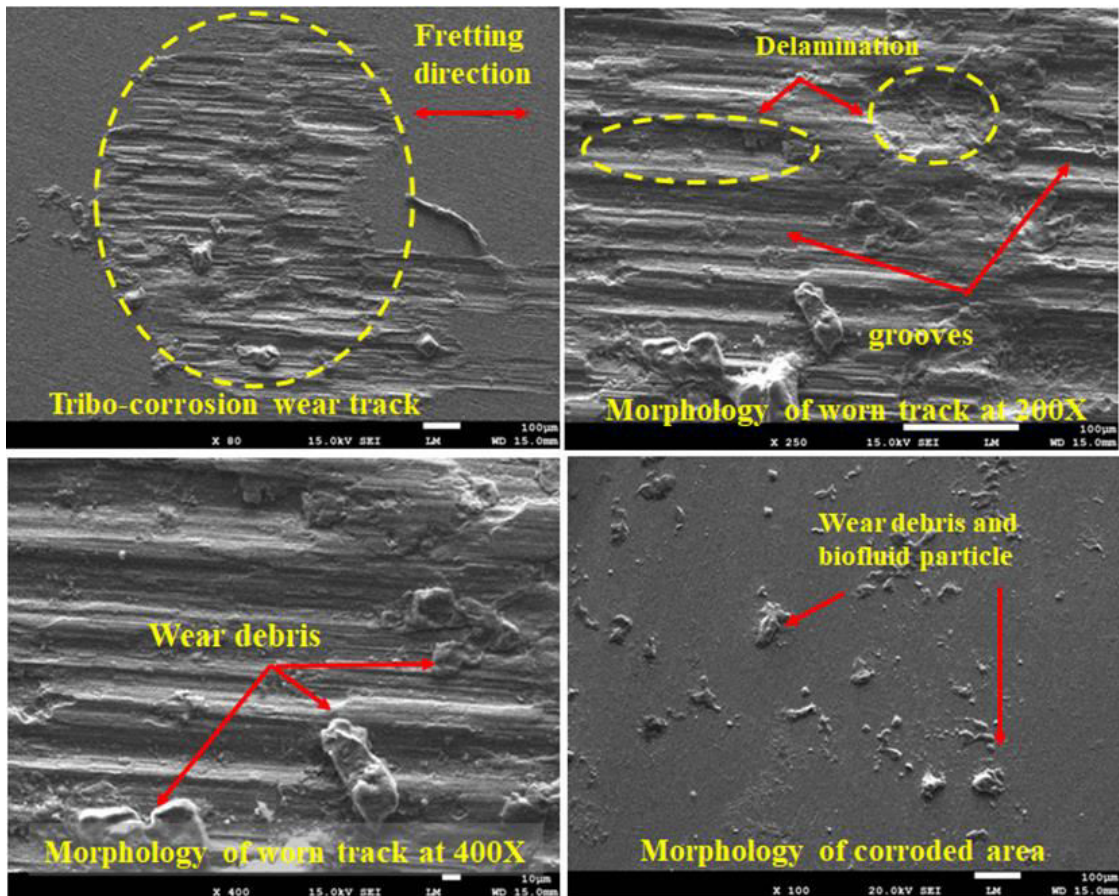


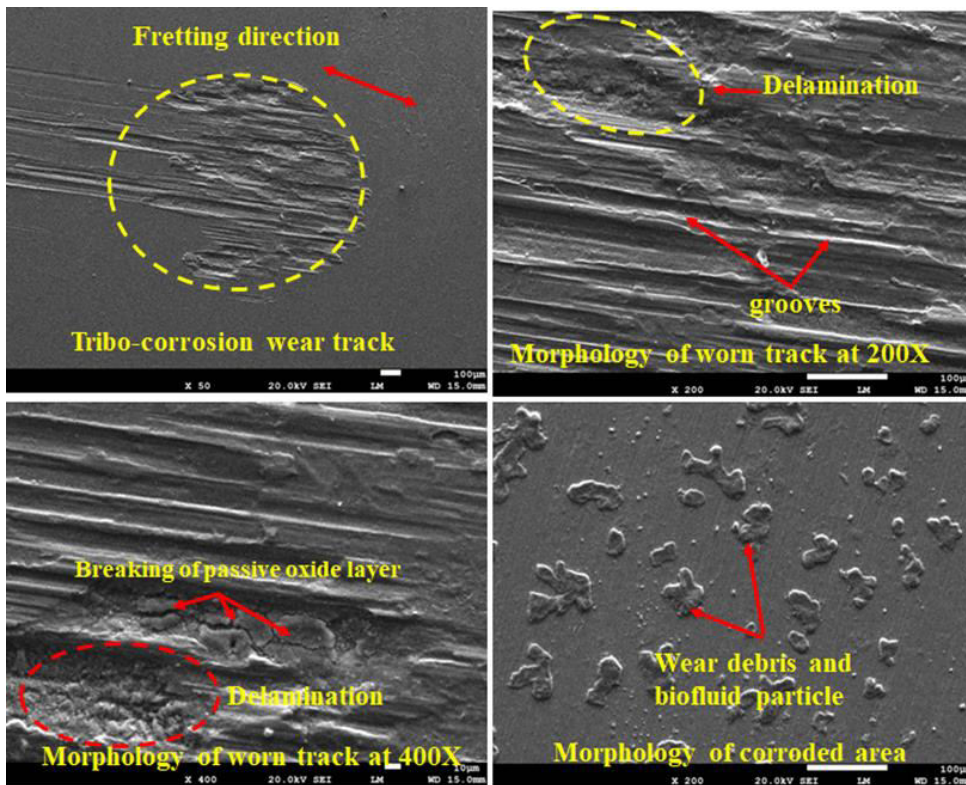
Fig. 5.25: 3D surface roughness profile of tribo-corroded surface of multi-track multi-layer deposition sample of Ti-Ta-Nb-Mo-Zr HEA at 10 N applied load in different biofluids: (a) PS, (b) PBS, and (c) FPBS.

Fig. 5.26 presents SEM images of tribo-corroded surface of Ti-Ta-Nb-Mo-Zr HEA at an applied load of 10 N depicting tribo-corrosion wear track, and morphology of worn track at 200x and 400x magnification and corroded area in the PS (Fig. 5.26a), PBS (Fig. 5.26b), and FPBS (Fig. 5.26c) biofluid. It can be observed from Fig. 5.26a and Fig. 5.26b that slip of fretting pin has occurred in the fretting zone followed by marks of grooves and delamination on the exposed surface in PS and PBS biofluids. Morphology of tribo-corroded surface in PS biofluid shows lesser wear and corrosion debris on the surface after removal of passive layer of oxides. The morphology of worn track in PBS biofluid (Fig.

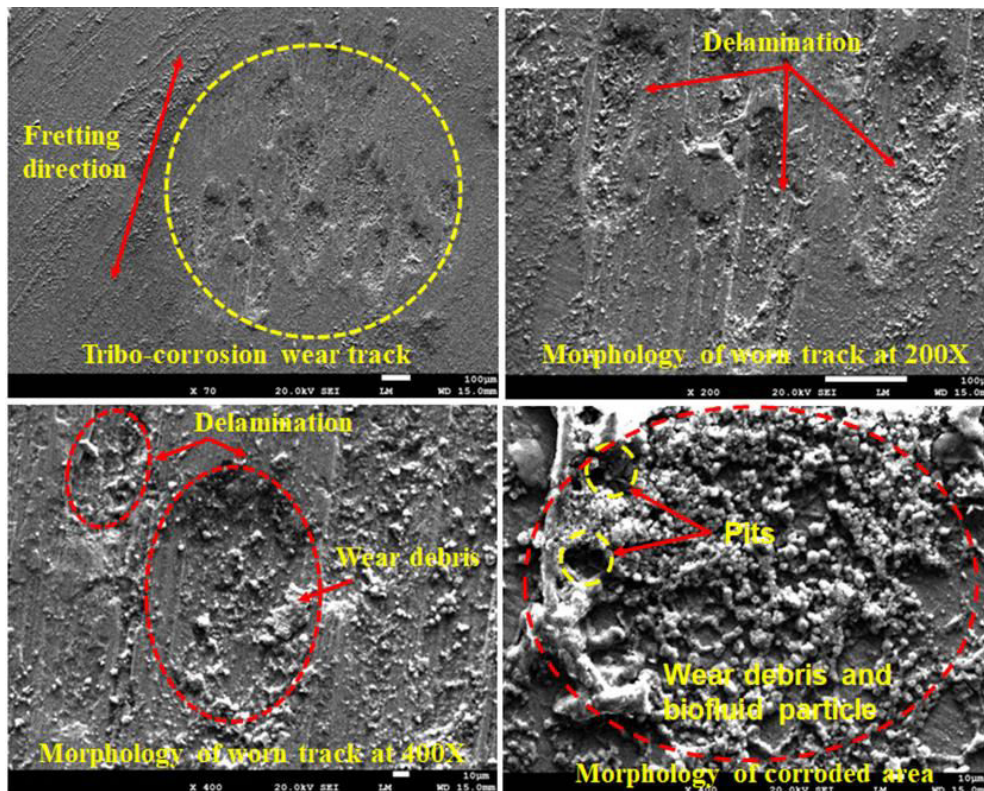
5.26b) at 400x magnification depicts cracks in the delamination due to breakage of the passive layer of oxides. The marked delamination area (Fig. 5.26b) has lesser oxide and wear debris. Tribo-corrosion wear track in FPBS biofluid (Fig. 5.26c) shows absence of slip of the fretting wear pin. More wear debris is seen in morphology of worn track in FPBS biofluid at 400x magnification and some pits, wear debris, and biofluids particles are seen in morphology of the corroded area (Fig. 5.26c). Delamination occurs due to significant relative motion between the entrapped wear debris and the exposed surface which peels off the passive layer of oxides by adhesion (Ureña *et al.* 2019). Grooves are formed due to trapped debris between the pin and the test sample.



(a)



(b)



(c)

Fig. 5.26: SEM images of tribo-corroded surface of multi-track multi-layer deposition sample of Ti-Ta-Nb-Mo-Zr HEA depicting tribo-corrosion wear track and morphology of worn track at 200x and 400x magnification and corroded area in different biofluids: (a) PS, (b) PBS, and (c) FPBS.

The μ -PAAM manufactured Ti-Ta-Nb-Mo-Zr HEA has better corrosion and tribo-corrosion characteristics as compared to arc melted Ti-Zr-Nb-Ta-Mo HEA (Hua et al. 2021), Ti-13Nb-13Zr (Lee et al. 2015), Ti-6Al-4V alloy (Lee et al. 2015; Wang et al. 2019; Hua et al. 2021), Ti-25Nb-3Mo-3Zr-2Sn HEA (Huang et al. 2014) Ti-22Nb alloy (Nnamchi et al. 2016), Ti-22Nb-6Zr alloy (Yilmaz et al. 2019), Ti-12Mo-5Ta alloy (Bocchetta et al. 2021), and Ti-20Nb-10Zr-5Ta HEA (Zhu et al. 2011). Table 5.8 presents comparison of bio-tribological characteristics of the developed Ti-Ta-Nb-Mo-Zr HEA with the existing HEA and other Ti-based alloys. It can be concluded that the tribo-corrosion characteristics of μ -PAAM manufactured Ti-Ta-Nb-Mo-Zr HEA in the biofluids has specific wear rate varying from 0.85×10^{-5} to 1.20×10^{-5} mm³/N-m which is better than the findings of Hua et al. (2021), Wang et al. (2019), Lee et al. (2015), and Huang et al. (2014).

Table 5.8: Comparison of bio-tribological characteristics of the multi-track multi-layer deposition sample of Ti-Ta-Nb-Mo-Zr HEA with existing HEA and Ti based alloys.

Name of material	Manufacturing process	Lubricating condition	Coefficient of friction	Specific wear rate (10^{-5} mm ³ /N-m)	References	
Ti0.5-Zr-Nb-Ta-Mo	Arc melted	Dry	0.75	22.2	Hua et al. (2021)	
Ti-Zr-Nb-Ta-Mo	Arc melted	Dry	0.94	29.1		
Ti1.5-Zr-Nb-Ta-Mo	Arc melted	Dry	0.94	27.3		
Ti2-Zr-Nb-Ta-Mo	Arc melted	Dry	0.84	24.2		
Ti-6Al-4V	Arc melted	Dry	0.61	35		
Ti0.5-Zr-Nb-Ta-Mo	Arc melted	PBS	0.61	15.2		
Ti-Zr-Nb-Ta-Mo	Arc melted	PBS	0.64	18.5		
Ti1.5-Zr-Nb-Ta-Mo	Arc melted	PBS	0.71	22.7		
Ti2-Zr-Nb-Ta-Mo	Arc melted	PBS	0.71	24.5		
Ti-6Al-4V	Arc melted	PBS	0.64	46		
Ti-13Nb-13Zr	hot-rolled	Hank	-	4.44		Lee et al. (2015)
Ti-13Nb-13Zr	warm-rolled	Hank	-	1.05		
Ti-25Nb-3Mo-3Zr-2Sn	Arc melted	PBS	-	29	Huang et al. (2014)	
Ti-25Nb-3Mo-3Zr-2Sn	Arc melted	PBS+BSA	-	27		
Ti-25Nb-3Mo-3Zr-2Sn	Arc melted	PBS+HA	-	32		
Ti-6Al-4V	-	Dry	0.45	6.23	Wang et al. (2019)	
Ti-6Al-4V	-	PS	0.50	8.25		
Ti-6Al-4V	-	SBF	0.54	10.71		
Ti-6Al-4V	-	FBS	0.60	10.90		
Ti-Ta-Nb-Mo-Zr	μ -PAAM	PS	0.39	1.20	Present study	
Ti-Ta-Nb-Mo-Zr	μ -PAAM	PBS	0.38	0.85		
Ti-Ta-Nb-Mo-Zr	μ -PAAM	FPBS	0.26	1.06		

5.9 Concluding Remarks

This chapter presented results of study on aspect ratio of single-track single-layer depositions of equiatomic Ti-Ta-Nb-Mo-Zr HEA and study of *in-vitro* biocompatibility, microstructure and phase evolution, microhardness, compression test and fractography, abrasion resistance and wear characteristics of multi-track multi-layer deposition of Ti-Ta-Nb-Mo-Zr HEA made by μ -PAAM process. Using criterion of uniform and continuous deposition having minimum aspect ratio to identified optimum values of DC power input for μ -plasma power, mass flow rate of feedstock material powder, and deposition head travel speed as 418 W, 1.7 g/min, and 53 mm/min respectively for multi-track multi-layer deposition of Ti-Ta-Nb-Mo-Zr HEA. Average % cell viability decreased with increase in prepared media concentration for Ti-Ta-Nb-Mo-Zr HEA. Overall average values of viability for HeLa, HEK-293, and BHK cells treated in the prepared media for Ti-Ta-Nb-Mo-Zr HEA are 90%; 88%; and 92% respectively. BHK cells showed maximum avg. values of cell viability at each concentration of the prepared media and for each incubation duration. Optical micrographs showed voluminous nature of the HeLa, HEK-293, and BHK cells indicating them being metabolically active and healthy without any apparent physical changes. Overall averaged released amounts of Ti, Ta, Nb, Mo, and Zr ions from Ti-Ta-Nb-Mo-Zr HEA are 37; 26; 57; 38; and 28 ppb respectively. They depend on pH value of the SBF solution, chemical composition of the test sample, and immersion duration. Open circuit potential (OCP) of the developed Ti-Ta-Nb-Mo-Zr HEA has negative values for the considered immersion duration in the SBF solution for its considered pH values. It indicates higher corrosive tendency of the exposed surface of the developed HEA. But OCP showed increasing trend from negative values with immersion duration which suggests formation of passive oxide layer on the exposed surface of Ti-Ta-Nb-Mo-Zr HEA in the SBF solution. Absence of active-passive transition in change from cathodic to anodic reaction in Tafel polarization curves for Ti-Ta-Nb-Mo-Zr HEA for different pH values of SBF solution implies its better corrosion resistance. It due to its constituent element Nb, Zr, and Ta which form strong passive oxide layers of TiO_2 , NbO_2 , ZrO_2 , TaO_2 , and Ta_2O_5 on the exposed surface of the HEA in the SBF as confirmed by EDS results and phase analysis by XRD. Corrosion potential decreased, and corrosion current density and corrosion rate increased with increase in pH value of the SBF solution implying that the developed of Ti-Ta-Nb-Mo-Zr HEA has better corrosion resistance at smaller pH value of the SBF. Microstructure and phase analysis of μ -PAAM deposited Ti-Ta-Nb-Mo-Zr HEA revealed that it consists of major BCC phase having fine dendritic structure and minor BCC phase comprising of inter-dendritic structures. Such phases are likely to impart superior wear resistance to it. It is

confirmed by its microhardness of 520 ± 10 HV which is much higher than the vacuum arc melted Ti-Ta-Nb-Mo-Zr HEA. Chemical composition of μ -PAAM deposited Ti-Ta-Nb-Mo-Zr HEA is slightly different than its alloyed powder. It is confirmed by elemental mapping analysis also. Occurrence of minor segregation of constituents of Ti-Ta-Nb-Mo-Zr HEA is observed due to higher melting temperatures of Ta, Nb, and Mo than Ti and Zr. Elastic modulus, ultimate compressive strength, compressive yield strength, compressive strain of the μ -PAAM deposited Ti-Ta-Nb-Mo-Zr HEA are found as 130 ± 4 GPa; 1892 ± 15.6 MPa; 1847 ± 25.8 MPa; and $13.53 \pm 1.59\%$ respectively which are remarkably better than the vacuum arc melted Ti-Ta-Nb-Mo-Zr HEA. It is due to its solid solution strengthening enabled by minimizing its elemental segregation. Its fractured surface morphology found brittle mode of failure under compression. Average coefficient of friction, worn scar depth, and formation of macro-groove and delamination (due to ploughing action as revealed by SEM images of the worn tracks) increased but specific wear rate decreased with the applied load. Smaller values of applied load resulted in lesser wear debris. Results of bio-tribological characteristics of Ti-Ta-Nb-Mo-Zr HEA revealed that increase in applied load in dry fretting wear decreased coefficient of friction, increased average depth of worn scar and specific wear rate, made worn scar profile U-shaped, and deepened surface roughness valleys. Minor abrasive wear and material ploughing in dry fretting wear zone occurred due to formation of loose wear debris and large-scale material displacement respectively. Corrosion current density of Ti-Ta-Nb-Mo-Zr HEA is maximum in PBS biofluid and minimum in FPBS biofluid and its corrosion rate is almost equal in all the biofluids. Corroded surface micrographs revealed formation of a strong passive layer of TiO_2 , Ta_2O_5 , Nb_2O_5 , NbO_2 , and ZrO_2 on the exposed surface except for some marked regions. Presence of biofluids reduced coefficient of friction by almost 50%, changed pattern of worn scar profile from U-shaped to zigzag, significantly reduced depth of worn scar and specific wear rate than those in dry fretting wear due to their lubricating action and covering of uneven surfaces by the passive layers of oxides. It also significantly reduced values of OCP, corrosion potential, and corrosion current density implying that developed Ti-Ta-Nb-Mo-Zr HEA has less tribo-corrosive tendency in the biofluids. But higher corrosion rate is observed in tribo-corrosion than corrosion due to removal of material by the fretting action also. The FPBS and PS biofluids showed maximum and minimum values of corrosion rates respectively. It contrasts with corrosion characteristics in which all biofluids showed same corrosion rate.

This study found that μ -PAAM process manufactured Ti-Ta-Nb-Mo-Zr HEA has better biocompatibility, microstructure, microhardness, compressive yield and ultimate strength,

wear resistance. It showed higher abrasion resistance at higher load without any considerable change in coefficient of friction which will impart it better resistance to wear and tear. It exhibited better corrosion and tribo-corrosion resistance than Ti-22Nb, Ti-22Nb-6Zr, Ti-12Mo-5Ta, Ti-20Nb-10Zr-5Ta alloys due to formation of strong passive oxide layers. Finding of this work prove that Ti-Ta-Nb-Mo-Zr HEA is a better new class of metallic biomaterials for knee implant applications as compared to the presently used materials.

The *last chapter* summarizes the outcome of the present research by presenting its significant achievements, concluding remarks from findings on development of Co-Cr-Mo-xTi and equiatomic Ti-Ta-Zr-Mo-Nb HEA, and some identified directions for the future research.

Chapter 6

Conclusions and Scope for Future Work

This chapter summarizes the outcome of the present research by presenting its significant achievements, concluding remarks from findings on development of Co-Cr-Mo-xTi and equiatomic Ti-Ta-Zr-Mo-Nb HEA as better metallic materials for knee implants, and some directions identified for the future research.

6.1 Significant Achievements

- Co-Cr-Mo-4Ti alloy is identified as better knee implant material due to its superior biocompatible with respect to cell viability, metallic ion release, and corrosion behavior, lesser density, uniform porous structure, absence of micro-cracks, moderate microhardness, higher yield and ultimate tensile strength, ultimate compressive strength, and moderate value of tensile and compression modulus of elasticity, better wear resistance and abrasion resistance than Co-Cr-Mo-2Ti and Co-Cr-Mo-6Ti alloys.
- Ti-Nb-Zr-Mo-Ta HEA has great potential in overcoming limitations of the presently used knee implant materials and represents a new class of metallic biomaterials for knee implant applications due to its combination of excellent biocompatibility in terms of *in-vitro* evaluation of cell viability, ion release of constituent elements, and corrosion behavior, better microstructure, larger compressive yield strength, smaller value of elastic modulus, higher microhardness, and improved sliding wear resistance. It exhibits better corrosion and tribo-corrosion resistance than Ti-22Nb, Ti-22Nb-6Zr, Ti-12Mo-5Ta, Ti-20Nb-10Zr-5Ta alloys due to formation of strong passive oxide layers. It showed higher abrasion resistance at higher load without any considerable change in coefficient of friction. It will impart it better resistance to wear and tear.
- μ -PAAM process is energy and material efficient, and environment friendly process. It made significant contribution in identification of Co-Cr-Mo-4Ti alloy and Ti-Nb-Zr-Mo-Ta HEA as better knee implant material by minimizing heat affect zone, thermal distortion, segregation of constituents of Ti-Nb-Zr-Mo-Ta HEA, enhancing mechanical properties and bio-tribological characteristics of their depositions. Thus, it has great potential in manufacturing of knee implants from the developed knee implant materials in this work.

6.2 Conclusions

Following are the conclusion made from the work presented in this thesis:

6.2.1 Development of Co-Cr-Mo-xTi Alloy

- Minimum value of aspect ratio of 1.11 and continuous and consistent deposition was obtained for lower μ -plasma power (264 W), and moderate values of mass flow rate of feedstock material powder (2.5 g/min) and deposition head travel speed (50 mm/min). Therefore, it was used for manufacturing multi-layer multi-track depositions of powder of Co-Cr-Mo-xTi alloys.
- Overall average values of cell viability for the optimized deposition samples of Co-Cr-Mo-2Ti; Co-Cr-Mo-4Ti; and Co-Cr-Mo-6Ti alloys are 92%; 95%; and 85% respectively. Addition of Ti to Co-Cr-Mo alloy is advantageous due to formation of intermetallic phase CoTi_2 which is non-cytotoxic to human body and more active in cell growth mechanism.
- Optical micrographs of HeLa cells showed that cells were mutually connected and voluminous in the optimized deposition sample media which indicates that they were metabolically active and samples Co-Cr-Mo-xTi alloys did not have any harmful effects on appearance of HeLa cells.
- Overall averaged released amounts of metallic ions by the optimized deposition samples of Co-Cr-Mo-xTi alloys are 126; 41; 11, and 9 ppb for Co, Cr, Mo, and Ti ion respectively. Addition of Ti to Co-Cr alloys for implant material is advantageous as total release of metallic ions is reduced.
- Co-Cr-Mo-4Ti alloy has minimum values of corrosion potential, corrosion current density, and measured and Tafel curve determined corrosion rates. SEM micrographs of corroded surface showed formation of passive oxides layer on the exposed surface of Co-Cr-Mo-xTi alloys which may consist of TiO_2 formed due to presence of Ti in Co-Cr-Mo-xTi alloys imparting better corrosion resistance than Co-Cr-Mo alloy.
- Co-Cr-Mo-4Ti alloy showed more pores of smaller size and their more uniform distribution which is desirable for knee implant material because it will give better osseointegration with human bones and tissues.
- Microstructure revealed that optimized depositions of Co-Cr-Mo-xTi alloys containing 2% and 4% Ti are porous and free from cracks but Co-Cr-Mo-6Ti alloy optimized deposition is porous, but it has micro-cracks occurred due to residual thermal stresses.
- Phase analysis of Co-Cr-Mo-xTi alloy revealed presence of α -Co phase having FCC crystal structure, ϵ -Co phase having HCP crystal structure, β -titanium phase having

BCC crystal structure, and inter-metallic phases of CoTi_2 and lamellar chromium carbide (i.e., Cr_{23}C_6) at its grain boundaries with relatively higher wt.% of chromium. These findings are confirmed by the phase mapping analysis also.

- Inverse pole figure maps of the optimized depositions did not show any preferential orientation of grains and revealed presence of ϵ -Co phase matrix with traces of grains of chromium carbides and CoTi_2 phase. Phase mapping analysis found that Co-Cr-Mo-4Ti alloy optimized deposition contains minimum % of ϵ -Co phase, maximum % of α -Co, chromium-carbide, and Ti phases.
- Avg. microhardness of optimized deposition of Co-Cr-Mo-2Ti alloy is found to be the highest (i.e., 495 HV) followed by 473 HV for Co-Cr-Mo-4Ti; and 433 HV for Co-Cr-Mo-6Ti alloy optimized depositions.
- Coefficient of friction, specific wear rate, and wear volume are found to increase with increase in % of Ti in Co-Cr-Mo alloys due to decrease in microhardness and increase in porosity. It also increased ploughing and delamination in the worn track.
- Co-Cr-Mo-4Ti alloy has maximum values of yield and ultimate tensile strength, ultimate compressive strength, and moderate value of tensile and compressive modulus of elasticity due to more uniform porous structure, finer grain size, and absence of micro-cracks.
- Co-Cr-Mo-4Ti alloy has minimum value of avg. scratch track width and coefficient of friction, and maximum value of scratch hardness number imparting it better abrasion resistance to it due to presence of fine lamellar carbide phases.

6.2.2 Development of Ti-Ta-Nb-Mo-Zr HEA

Following conclusions can be made from this work:

- Using criterion of uniform and continuous deposition having minimum aspect ratio to the single-track-single-layer depositions of Ti-Ta-Nb-Mo-Zr HEA identified optimum values of μ -plasma power, mass flow rate of feedstock material powder, and deposition head travel speed as 418 W, 1.7 g/min, and 53 mm/min respectively for its multi-track-multi-layer deposition.
- Overall average values of viability for HeLa, HEK-293, and BHK cells treated in the prepared media for Ti-Ta-Nb-Mo-Zr HEA are 90%; 88%; and 92% respectively. Optical micrographs show voluminous nature of the HeLa, HEK-293, and BHK cells indicating them being metabolically active and healthy without any apparent physical change.
- Overall averaged released amounts of Ti, Ta, Nb, Mo, and Zr ions from the developed Ti-Ta-Nb-Mo-Zr HEA are 37; 26; 57; 38; and 28 ppb respectively. They depend on pH

value of the SBF solution, chemical composition of the test sample, and immersion duration.

- Open circuit potential value showed increasing trend from negative values with immersion duration which suggested formation of passive oxide layer on the exposed surface of Ti-Ta-Nb-Mo-Zr HEA in the SBF solution.
- Absence of active-passive transition in change from cathodic to anodic reaction in Tafel polarization curves for Ti-Ta-Nb-Mo-Zr HEA for different pH values of SBF solution implies its better corrosion resistance. It due to its constituent element Nb, Zr, and Ta which form strong passive oxide layers of TiO_2 , NbO_2 , ZrO_2 , TaO_2 , and Ta_2O_5 on the exposed surface of the HEA in the SBF as confirmed by EDS results and phase analysis by XRD.
- Corrosion potential decrease, and corrosion current density and corrosion rate increase with increase in pH value of the SBF solution implying that the developed of Ti-Ta-Nb-Mo-Zr HEA has better corrosion resistance at smaller pH value of the SBF.
- Microstructure and phase analysis of μ -PAAM deposited Ti-Ta-Nb-Mo-Zr HEA revealed that it consists of major BCC phase having fine dendritic structure and minor BCC phase comprising of inter-dendritic structures. Such phases are likely to impart superior wear resistance to it. It is confirmed by its microhardness of 520 ± 10 HV which is much higher than the vacuum arc melted Ti-Ta-Nb-Mo-Zr HEA.
- Chemical composition of μ -PAAM deposited Ti-Ta-Nb-Mo-Zr HEA is slightly different than its alloyed powder. It is confirmed by elemental mapping analysis also. Occurrence of minor segregation of constituents of Ti-Ta-Nb-Mo-Zr HEA is observed due to higher melting temperatures of Ta, Nb, and Mo than Ti and Zr.
- Elastic modulus, ultimate compressive strength, compressive yield strength, compressive strain of the μ -PAAM deposited Ti-Ta-Nb-Mo-Zr HEA are found as 130 ± 4 GPa; 1892 ± 15.6 MPa; 1847 ± 25.8 MPa; and $13.53 \pm 1.59\%$ respectively. Its fractured surface morphology found brittle mode of failure under compression.
- Average coefficient of friction, worn scar depth, and formation of macro-groove and delamination increases but specific wear rate decreases with the applied load. Smaller values of applied load resulted in lesser wear debris.

6.2.3 Bio-Tribological Characteristics of Ti-Ta-Nb-Mo-Zr HEA

Following conclusions can be made from this work:

- Increase in applied load in dry fretting wear decreased coefficient of friction, increased average depth of worn scar and specific wear rate, made worn scar profile U-shaped, and deepened surface roughness valleys. Minor abrasive wear and material ploughing in

dry fretting wear zone occurred due to formation of loose wear debris and large-scale material displacement respectively.

- Corrosion current density of Ti-Ta-Nb-Mo-Zr HEA is maximum in PBS biofluid and minimum in FPBS biofluid and its corrosion rate is almost equal in all the biofluids. Corroded surface micrographs revealed formation of a strong passive layer of TiO_2 , Ta_2O_5 , Nb_2O_5 , NbO_2 , and ZrO_2 on the exposed surface except for some marked regions.
- Coefficient of friction in tribo-corrosion remained constant for a large range of immersion duration for FPBS and for small ranges for PS and PBS biofluids implying no-fretting zone. PS and FBPS biofluids resulted in maximum and minimum values of coefficient of friction respectively.
- Presence of biofluids reduced coefficient of friction by almost 50%, changed pattern of worn scar profile from U-shaped to zigzag, significantly reduced depth of worn scar and specific wear rate than those in dry fretting wear due to their lubricating action and covering of uneven surfaces by the passive layers of oxides.
- Micrographs of tribo-corroded Ti-Ta-Nb-Mo-Zr HEA revealed occurrence of slip of fretting pin in the fretting zone followed by marks of grooves and delamination on the exposed surface in the PS and PBS biofluids. The PS biofluid resulted in lesser wear and corrosion debris after removal of passive layer of oxides whereas FPBS biofluid yielded more wear debris, pits, and biofluids particles. It implies that performance of FPBS biofluid is the better in corrosion but not in tribo-corrosion.

6.3 Directions for Future Work

Following are some directions identified for future research work:

- Further investigation is needed to evaluate in-depth interactions of Co-Cr-Mo-xTi alloys and Ti-Ta-Nb-Mo-Zr HEA with human bones and tissues through *in-vivo* study.
- Bio-corrosion tribo-corrosion characteristics may be explored using cortical bone and tibial bone as counter body.
- Fatigue characteristics of developed Co-Cr-Mo-xTi alloys and Ti-Ta-Nb-Mo-Zr HEA may be explored for better employing lattice structures.
- High quality finishing of additively manufactured knee implant using abrasive flow finishing and electro-chemical finishing processes may be explored.
- Different combinations of Co-Cr-Mo-xTi alloys and Ti-Ta-Nb-Mo-Zr HEA may be explored through CALPHAD modelling and others computational method to get elastic modulus closes to cortical bone.

References

- Acharya, S., Panicker, A. G., Laxmi, D. V., Suwas, S., Chatterjee, K., **2019**. Study of the influence of Zr on the mechanical properties and functional response of Ti-Nb-Ta-Zr-O alloy for orthopedic applications, **Materials and Design**, 164, 107555.
<https://doi.org/10.1016/j.matdes.2018.107555>
- Afzali, P., Ghomashchi, R., Oskouei, R.H., **2019**. On the corrosion behavior of low modulus titanium alloys for medical implant applications: A review. **Metals**, 9, 878.
<https://doi.org/10.3390/met9080878>
- Ali, S., Rani, A.M.A., Baig, Z., Ahmed, S.W., Hussain, G., Subramaniam, K., Hastuty, S., Rao, T.V.V.L.N., **2020**. Biocompatibility and corrosion resistance of metallic biomaterials. **Corrosion Reviews**, 38, 381-402. <https://doi.org/10.1515/correv-2020-0001>
- AlMangour, B., Luqman, M., Grzesiak, D., Al-Harbi, H., Ijaz, F., **2020**. Effect of processing parameters on the microstructure and mechanical properties of Co–Cr–Mo alloy fabricated by selective laser melting. **Materials Science and Engineering: A**, 792, 139456. <https://doi.org/10.1016/j.msea.2020.139456>
- Alvarado, J.V., Maldonado, R.J., Marxuach, J., Otero, R., **2003**. Biomechanics of Hip and Knee Prostheses, 1-20.
- Amanov, A., **2021**. Effect of post-additive manufacturing surface modification temperature on the tribological and tribocorrosion properties of Co-Cr-Mo alloy for biomedical applications. **Surface & Coatings Technology**, 421, 127378.
<https://doi.org/10.1016/j.surfcoat.2021.127378>
- Amuzuga, P., Suchier, Y., Lefebvre, F., **2018**. Optimization of fretting resistance of modular stem. **Procedia Engineering**, 213, 104-116.
<https://doi.org/10.1016/j.proeng.2018.02.012>
- Archard, J. F., **1953**. Contact and rubbing of flat surfaces, **Journal of Applied Physics**, 24:981-988. <https://doi.org/10.1063/1.1721448>
- Asgharzadeh, S.H., Ayatollahi, M.R., Asnafi, A., **2017**. To reduce the maximum stress and the stress shielding effect around a dental implant–bone interface using radial functionally graded biomaterials. **Computer Methods in Biomechanics and Biomedical Engineering**, 20, 750-759.
<https://doi.org/10.1080/10255842.2017.1299142>
- ASTM Standard G31, **2012**. Standard practice for laboratory immersion corrosion testing of metals. **ASTM International**, West Conshohocken, PA.
<http://dx.doi.org/10.1520/G0031-72R04>

- Au, A.G., James Raso, V., Liggins, A.B., Amirfazli, A., **2007**. Contribution of loading conditions and material properties to stress shielding near the tibial component of total knee replacements. **Journal of Biomechanics**, 40, 1410-1416.
<https://doi.org/10.1016/j.jbiomech.2006.05.020>
- Bairagi, D., Mandal, S., **2022**. A comprehensive review on biocompatible Mg-based alloys as temporary orthopedic implants: Current status, challenges, and future prospects. **Journal of Magnesium and Alloys**, 10, 627–669.
<https://doi.org/10.1016/j.jma.2021.09.005>
- Bal, B., Garino, J., Ries, M., Rahaman, M., **2007**. A review of ceramic bearing materials in total joint arthroplasty. **Hip International**, 17, 21-30.
- Banerjee, R., Genc, A., Hill, D., Collins, P., Fraser, H., **2005**. Nanoscale TiB precipitates in laser deposited Ti-matrix composites. **Scripta Materialia**, 53, 1433-1437.
<https://doi.org/10.1016/j.scriptamat.2005.08.014>
- Barucca, G., Santecchia, E., Majni, G., Girardin, E., Bassoli, E., Denti, L., Gatto, A., Iuliano, L., Moskalewicz, T., Mengucci, P., **2015**. Structural characterization of biomedical Co–Cr–Mo components produced by direct metal laser sintering. **Materials Science and Engineering: C**, 48, 263-269.
<https://doi.org/10.1016/j.msec.2014.12.009>
- Benea, L., Dănilă, E., Ponthiaux, P., **2017**. Porous TiO₂-ZrO₂ thin film formed by electrochemical technique to improve the biocompatibility of titanium alloy in physiological environment. **IOP Conference Series: Materials Science and Engineering**, 174, 6-12. <https://doi.org/10.1088/1757-899X/174/1/012044>
- Ben-Nissan, B., Choi, A.H., Roest, R., Latella, B.A., Bendavid, A., **2015**. Adhesion of hydroxyapatite on titanium medical implants, in: M. Mucalo (Ed.), **Hydroxyapatite (Hap) for Biomedical Applications**, Woodhead Publishing, Sawston (UK), pp. 21-51. <https://doi.org/10.1016/B978-1-78242-033-0.00002-X>
- Bergschmidt, P., Ellenrieder, M., Bader, R., Kluess, D., Finze, S., Schwemmer, B., Mittelmeier, W., **2016**. Prospective comparative clinical study of ceramic and metallic femoral components for total knee arthroplasty over a five-year follow-up period, **The Knee**, 23, 871-876. <https://doi.org/10.1016/j.knee.2016.06.001>
- Billi, F., Sangiorgio, S.N., Aust, S., Ebramzadeh, E., **2010**. Material and surface factors influencing backside fretting wear in total knee replacement tibial components. **Journal of Biomechanics**, 43, 1310-1315.
<https://doi.org/10.1016/j.jbiomech.2010.01.015>

- Bocchetta, P., Chen, L.Y., Tardelli, J.D.C., Dos Reis, A.C., Almeraya-Calderón, F., Leo, P. **2021**. Passive layers and corrosion resistance of biomedical Ti-6Al-4V and β -Ti alloys. *Coatings*, 11, 487. <https://doi.org/10.3390/coatings11050487>
- Bolmaro, R., Parau, A.C., Pruna, V., Surmeneva, M.A., Constantin, L.R., Avalos. M., et al. **2019**. Investigation of cast and annealed Ti25Nb10Zr alloy as material for orthopedic devices. *Journal of Materials Research and Technology*, 8, 3399-3414. <https://doi.org/10.1016/j.jmrt.2019.06.006>
- Bonnin, M.P., Basiglini, L., Archbold, H.A., 2011. What are the factors of residual pain after uncomplicated TKA? *Knee Surgery, Sports Traumatology, Arthroscopy*, 19, 1411-1417. <https://doi.org/10.1007/s00167-011-1549-2>
- Bourne, R.B., Chesworth, B.M., Davis, A.M., Mahomed, N.N., Charron, K.D., 2010. Patient satisfaction after total knee arthroplasty: who is satisfied and who is not? *Clinical Orthopaedics and Related Research*, 468, 57-63. <https://doi.org/10.1007/s11999-009-1119-9>
- Bullens, P.H., Van Loon, C.J., De Waal Malefijt, M.C., Laan, R.F., Veth, R. P. 2001. Patient satisfaction after total knee arthroplasty: A comparison between subjective and objective outcome assessments. *The Journal of Arthroplasty*, 16, 740-747. <https://doi.org/10.1054/arth.2001.23922>
- Cabrini, M., Carrozza, A., Lorenzi, S., Pastore, T., Testa, C., Manfredi, D., et al. **2022**. Influence of surface finishing and heat treatments on the corrosion resistance of LPBF-produced Ti-6Al-4V alloy for biomedical applications. *Journal of Materials Processing Technology*, 308, 117730. <https://doi.org/10.1016/j.jmatprotec.2022.117730>
- Calignano, F., Manfredi, D., Ambrosio, E.P., Biamino, S., Lombardi, M., Atzeni, E., Salmi, A., Minetola, P., Iuliano, L., Fino, P., **2017**. Overview on additive manufacturing technologies. *Proceedings of the IEEE*, 105, 593-612. <https://doi.org/10.1109/JPROC.2016.2625098>
- Carr, B.C., Goswami, T., **2009**. Knee implants- Review of models and biomechanics, *Materials & Design*, 30, 398-413. <https://doi.org/10.1016/j.matdes.2008.03.032>
- Castro, D., Jaeger, P., Baptista, A. C., Oliveira, J. P., **2021**, An overview of high-entropy alloys as biomaterials, *Metals*, 11, 648. <https://doi.org/10.3390/met11040648>
- Cheng, B., Wei, F., Teh, W.H., Lee, J.J., Meng, T.L., Lau, K.B., Chew, L.T., Zhang, Z., Cheong, K.H., Ng, C.K., Wang, P., Tan, C.C., Ramamurty, U., **2022**. Ambient pressure fabrication of Ni-free high nitrogen austenitic stainless steel using laser

- powder bed fusion method, **Additive Manufacturing**, 55, 102810.
<https://doi.org/10.1016/j.addma.2022.102810>
- Cheng, Z., Li, Y., Xu, C., Liu, Y., Ghafoor, S., Li, F., 2020. Incremental sheet forming towards biomedical implants: a review. **Journal of Materials Research and Technology**, 9, 7225-7251. <https://doi.org/10.1016/j.jmrt.2020.04.096>
- Chu T., 1999. An investigation on contact stresses of New Jersey Low Contact Stress (NJLCS) knee using finite element method. **Journal of Systems Integration**, 9, 187–199.
- Correa, D.R.N., Rocha, L.A., Donato, T.A.G., Sousa, K.S.J., Grandini, C.R., Afonso, C.R.M., et al. 2020. On the mechanical biocompatibility of Ti-15Zr-based alloys for potential use as load-bearing implants. **Journal of Materials Research and Technology**, 9, 1241–1250. <https://doi.org/10.1016/j.jmrt.2019.11.051>
- Cui, A., Li, H., Wang, D., Zhong, J., Chen, Y., Lu, H., 2020. Global, regional prevalence, incidence and risk factors of knee osteoarthritis in population-based studies, **Clinical Medicine**, 29-30, 100587. <https://doi.org/10.1016/j.eclinm.2020.100587>
- Culliford, D.J., Maskell, J., Beard, D.J., Murray, D.W., Price, A.J., Arden, N.K., 2010. Temporal trends in hip and knee replacement in the United Kingdom, **The Journal of bone and joint surgery. British volume**, 92, 130-135. <https://doi.org/10.1302/0301-620X.92B1.22654>
- Cvijovic´ -Alagic´ , I., Cvijovic´ , Z., Rakin, M., 2019. Damage behavior of orthopedic titanium alloys with martensitic microstructure during sliding wear in physiological solution. **International Journal of Damage Mechanics**, 28, 1-20.
<https://doi.org/10.1177/1056789518823049>
- Davids, W.J., Chen, H., Nomoto, K., Wang, H., Babu, S., Primig, S., Liao, X., Breen, A., Ringer, S.P., 2021. Phase transformation pathways in Ti-6Al-4V manufactured via electron beam powder bed fusion. **Acta Materialia**, 215, 117131.
<https://doi.org/10.1016/j.actamat.2021.117131>
- DebRoy, T., Wei, H., Zuback, J., Mukherjee, T., Elmer, J., Milewski, J., Beese, A., Heid, A.W., De, A., Zhang, W., 2018. Additive manufacturing of metallic components—process, structure and properties. **Progress in Materials Science**, 92, 112-224.
<https://doi.org/10.1016/j.pmatsci.2017.10.001>
- Delgado-Ruiz, R., Romanos, G., 2018. Potential causes of titanium particle and ion release in implant dentistry: a systematic review. **International Journal of Molecular Sciences**, 19, 3585. <https://doi.org/10.3390/ijms19113585>

- Diomidis, N., Mischler, S., More, N.S., Roy, M., Paul, S.N. **2011**. Fretting-corrosion behavior of β titanium alloys in simulated synovial fluid. **Wear**, 271, 1093-1102. <https://doi.org/10.1016/j.wear.2011.05.010>
- Doerfler, D., Gurney, B., Mermier, C., Rauh, M., Black, L., Andrews, R., 2016. High-velocity quadriceps exercises compared to slow-velocity quadriceps exercises following total knee arthroplasty: a randomized clinical study. *Journal of Geriatric Physical Therapy*, 39, 147-158. <https://doi.org/10.1519/JPT.0000000000000071>
- Dong, Y., Zhang, Z., Dong, W., Hu, G., Wang, B., Mou, Z., **2020**. An optimization method for implantation parameters of individualized TKA tibial prosthesis based on finite element analysis and orthogonal experimental design. **BMC Musculoskeletal Disorders**, 21, 165. <https://doi.org/10.1186/s12891-020-3189-5>
- Eisenbarth, E., Velten, D., Müller, M., Thull, R., Breme, J., **2004**. Biocompatibility of beta-stabilizing elements of titanium alloys. **Biomaterials**, 25, 5705-5713. <https://doi.org/10.1016/j.biomaterials.2004.01.021>
- Espallargas, N., Torres, C., Munoz, A.I., **2015**. A metal ion release study of CoCrMo exposed to corrosion and tribo-corrosion conditions in simulated body fluids. **Wear**, 332-333, 669-678. <https://doi.org/10.1016/j.wear.2014.12.030>
- Evans, N.T., Torstrick, F.B., Lee, C.S.D., Dupont, K.M., Safranski, D.L., Chang, W.A., Gall, K., **2015**. High-strength, surface-porous polyether-ether-ketone for load-bearing orthopedic implants. **Acta Biomaterialia**, 13, 159-167. <https://doi.org/https://doi.org/10.1016/j.actbio.2014.11.030>
- Fallahnezhad, K., Feyzi, M., Ghadirinejad, K., Hashemi, R., Taylor, M., **2022**. Finite element-based simulation of tribocorrosion at the head-neck junction of hip implants. **Tribology International**, 165, 107284. <https://doi.org/10.1016/j.triboint.2021.107284>
- Festas, A.J., Ramos, A., Davim, J.P., **2019**. Medical devices biomaterials- A review. **Proceedings of IMechE, Part L: Journal of Materials Design and Applications**, 234, 218-228. <https://doi.org/10.1177/1464420719882458>
- Fikeni, L., Annan, K.A., Seerane, M., Mutombo, K., Machaka, R., **2019**. Development of a biocompatible Ti-Nb alloy for orthopaedic applications. **IOP Conference Series: Materials Science and Engineering**, 655, 012022. <https://doi.org/10.1088/1757-899X/655/1/012022>
- Fischer, H.B., Simanski, C.J., Sharp, C., Bonnet, F., Camu, F., Neugebauer, E.A., Rawal, N., Joshi, G.P., Schug, S.A., Kehlet, H., 2008. A procedure-specific systematic review and consensus recommendations for postoperative analgesia following total knee

- arthroplasty. *Anaesthesia*, 63, 1105-1123. <https://doi.org/10.1111/j.1365-2044.2008.05565.x>
- Frosch, S., Nüsse, V., Frosch, K., Lehmann, W., Buchhorn, G., **2021**. Osseointegration of 3D porous and solid Ti–6Al–4V implants-Narrow gap push-out testing and experimental setup considerations. **Journal of the Mechanical Behavior of Biomedical Materials**, 115, 104282. <https://doi.org/10.1016/j.jmbbm.2020.104282>
- Galati, M., Iuliano, L., **2018**. A literature review of powder-based electron beam melting focusing on numerical simulations. **Additive Manufacturing**, 19, 1-20. <https://doi.org/10.1016/j.addma.2017.11.001>
- Garcia-Mendez, M.C., Urrutia-Baca, V.H., Cuao-Moreu, C.A., Lorenzo-Bonet, E., Alvarez-Vera, M., Ortiz-Martinez, D.M., et al. **2021**. In vitro biocompatibility evaluation of a new Co-Cr-B alloy with potential biomedical application. **Metals**, 11:1-17. <https://doi.org/10.3390/met11081267>
- Geetha, M., Singh, A.K., Asokamani, R., Gogia, A.K., **2009**. Ti based biomaterials, the ultimate choice for orthopaedic implants-A review. **Progress in Materials Science**, 54, 397-425. <https://doi.org/10.1016/j.pmatsci.2008.06.004>
- Geng, H., Li, J., Xiong, J., Lin, X., Zhang, F., **2017**. Optimization of wire feed for GTAW based additive manufacturing. **Journal of Materials Processing Technology**, 243, 40-47. <https://doi.org/10.1016/j.jmatprotec.2016.11.027>
- George, E.P., Raabe, D., Ritchie, R.O., **2019**. High-entropy alloys, **nature reviews materials**, 4, 515–534. <https://doi.org/10.1038/s41578-019-0121-4>
- Ghiban, A., Ghiban, B., Bortun, C.M., Buzatu, M., **2014**. Structural investigations in CoCrMo(Ti) welded dental alloys, **Revista De Chimie**, 65, 1314-1318.
- Gong, L., Dong, J., **2014**. Patient's personality predicts recovery after total knee arthroplasty: A retrospective study. *Journal of Orthopaedic Science*, 19, 263-269. <https://doi.org/10.1007/s00776-013-0505-z>
- Gradzka-Dahlke, M., Dabrowski, J.R., Dabrowski, B., **2007**. Modification of mechanical properties of sintered implant materials on the base of Co-Cr-Mo alloy. **Journal of Materials Processing Technology**, 1-3, 199-205. <https://doi.org/10.1016/j.jmatprotec.2007.11.034>
- Gueye, M., Ammar-Merah, S., Nowak, S., Decorse, P., Chevillot-Biraud, A., et al., **2020**. Study of the stability under in vitro physiological conditions of surface silanized equimolar HfNbTaTiZr high-entropy alloy: A first step toward bio-implant applications. **Surface and Coatings Technology**, 385, 125374. <https://doi.org/10.1016/j.surfcoat.2020.125374>

- Guo, N.N., Wang, L., Luo, L.S., Li, X.Z., Chen, R.R., Su, Y.Q., Guo, J.J., Fu, H.Z., **2016**. Hot deformation characteristics and dynamic recrystallization of the MoNbHfZrTi refractory high-entropy alloy, **Materials Science and Engineering A**, 651, 698–707. <https://doi.org/10.1016/j.msea.2015.10.113>
- Gupta, K.P., **2001**. The Co-Cr-Ti System (Cobalt-Chromium-Titanium). **Journal of Phase Equilibria**, 22, 52-60. <https://doi.org/10.1361/105497101770339292>
- Gupta, K.P., **2005**. The Co-Cr-Mo (Cobalt-Chromium-Molybdenum) System. **Journal of Phase Equilibria and Diffusion**, 26, 87-92. <https://doi.org/10.1007/s11669-005-0071-y>
- Hallab, N., Jacobs, J., **2011**. Implant Debris: clinical data and relevance, **Comprehensive Biomaterials**, 97-107. <https://doi.org/10.1016/B978-0-08-055294-1.00207-5>
- Hallab, N.J., Anderson. S., Stafford, T., Glant, T., Jacobs, J.J., **2005**. Lymphocyte responses in patients with total hip arthroplasty, **Journal of Orthopaedic Research**, 23, 384-391. <https://doi.org/10.1016/j.orthres.2004.09.001>
- Hamilton, D.F., Burnett, R., Patton, J.T., Howie, C.R., Moran, M., Simpson, A.H., Gaston, P., **2015**. Implant design influences patient outcome after total knee arthroplasty: a prospective double-blind randomised controlled trial. *The Bone & Joint Journal*, 97, 64-70. <https://doi.org/10.1302/0301-620X.97B1.34254>
- Hannouche, D., Hamadouche, M., Nizard, R., Bizot, P., Meunier, A., Sedel, L., **2005**. Ceramics in total hip replacement. **Clinical Orthopaedics and Related Research**, 430, 62-71.
- Harsten, A., Kehlet, H., Toksvig-Larsen, S. **2013**. Recovery after total intravenous general anaesthesia or spinal anaesthesia for total knee arthroplasty: A randomized trial. **British Journal of Anaesthesia**, 111, 391-399. <https://doi.org/10.1093/bja/aet104>
- Hasani, F.J.A., **2020**. Effect of cobalt addition on the cytotoxicity and cell attachment of titanium alloys. **Systematic Reviews in Pharmacy**, 11, 804-813. <https://doi.org/10.31838/srp.2020.5.119>
- Hazlehurst, K., Wang, C.J., Stanford, M., **2013**. Evaluation of the stiffness characteristics of square pore CoCrMo cellular structures manufactured using laser melting technology for potential orthopedic applications. **Materials & Design**, 51, 949-955. <https://doi.org/10.1016/j.matdes.2013.05.009>
- Hedberg, Y.S., Qian, B., Shen, Z., Virtanen, S., Wallinder, I.O., **2014**. In vitro biocompatibility of CoCrMo dental alloys fabricated by selective laser melting. **Dental Materials**, 30, 525-534, <https://doi.org/10.1016/j.dental.2014.02.008>

- Hernandez-Vaquero, D., Noriega-Fernandez, A., Suarez-Vazquez, A., **2010**. Total knee arthroplasties performed with a mini-incision or a standard incision. Similar results at six months follow-up. **BMC Musculoskelet Disorder**, 11, 27.
<https://doi.org/10.1186/1471-2474-11-27>
- Hirota, K., Mitani, K., Yoshinaka, M., Yamaguchi, O., **2005**. Simultaneous synthesis and consolidation of chromium carbides (Cr_3C_2 , Cr_7C_3 and Cr_{23}C_6) by pulsed electric-current pressure sintering. **Materials Science and Engineering: A**, 399, 154-160.
<https://doi.org/10.1016/j.msea.2005.02.062>
- Hjalmarsson, L., Smedberg, J.I., Wennerberg, A., **2011**. Material degradation in implant-retained cobalt-chrome and titanium frameworks. **Journal of Oral Rehabilitation**, 38, 61-71. <https://doi.org/10.1111/j.1365-2842.2010.02127.x>
- Hori, T., Nagase, T., Todai, M., Matsugaki, A., Nakano, T., **2019**. Development of non-equiatom Ti-Nb-Ta-Zr-Mo high-entropy alloys for metallic biomaterials, **Scripta Materialia**, 172:83–87, <https://doi.org/10.1016/j.scriptamat.2019.07.011>
- Hua, N., Wang, W., Wang, Q., Ye, Y., Lin, S., Zhang, L., et al. **2021**. Mechanical, corrosion, and wear properties of biomedical Ti-Zr-Nb-Ta-Mo high entropy alloys. **Journal of Alloys and Compound**, 861, 157997.
<https://doi.org/10.1016/j.jallcom.2020.157997>
- Huang, P., Lopez, H. F., **1999**. Strain induced ϵ -martensite in a Co-Cr-Mo alloy: grain size effects. **Materials Letters**, 39, 244-248. [https://doi.org/10.1016/S0167-577X\(99\)00021-X](https://doi.org/10.1016/S0167-577X(99)00021-X)
- Huang, W., Wang, Z., Liu, C., Yu, Y., **2014**. Wear and electrochemical corrosion behavior of biomedical Ti-25Nb-3Mo-3Zr-2Sn alloy in simulated physiological solutions, **Journal of Bio- and Tribo-Corrosion**, 1:1. <https://doi.org/10.1007/s40735-014-0001-9>
- Hunter, D.J., Zeinstra, S.B., **2019**. Osteoarthritis, **The LANCET**, 393, 1745–1759.
[https://doi.org/10.1016/S0140-6736\(19\)30417-9](https://doi.org/10.1016/S0140-6736(19)30417-9)
- Hussein, A.H., Gepreel, M.A.H., Gouda, M.K., Hefnawy, A.M., Kandil, S.H., **2016**. Biocompatibility of new Ti-Nb-Ta base alloys. **Materials Science and Engineering: C**, 61, 574-578. <https://doi.org/10.1016/j.msec.2015.12.071>
- Hylkema, T.H., Stevens, M., Selzer, F., Amick, B.A., Katz, J.N., Brouwer, S., **2019**. Activity impairment and work productivity loss after total knee arthroplasty: a prospective study, **The Journal of Arthroplasty**, 34, 2637-2645.
<https://doi.org/10.1016/j.arth.2019.06.015>

- Idil A.S., Donaldson, N., **2018**. The use of tungsten as a chronically implanted material, **J. Neural Eng.** 15, 021006. <https://doi.org/10.1088/1741-2552/aaa502>
- Ingarao, G., Priarone, P.C., **2020**. A comparative assessment of energy demand and life cycle costs for additive- and subtractive-based manufacturing approaches. **Journal of Manufacturing Processes**, 56, 1219–1229. <https://doi.org/10.1016/j.jmapro.2020.06.009>
- Ishfaq, K., Abdullah, M., Mahmood, M. A., **2021**. A state-of-the-art direct metal laser sintering of Ti6Al4V and AlSi10Mg alloys: Surface roughness, tensile strength, fatigue strength and microstructure. **Optics & Laser Technology**, 143, 107366. <https://doi.org/10.1016/j.optlastec.2021.107366>
- Ishimoto, T., Ozasa, R., Nakano, K., Weinmann, M., Schnitter, C., et al., **2021**. Development of TiNbTaZrMo bio-high-entropy alloy (BioHEA) super-solid solution by selective laser melting, and its improved mechanical property and biocompatibility. **Scripta Materialia**, 194, 113658. <https://doi.org/10.1016/j.scriptamat.2020.113658>
- Jhavar, S., Jain, N. K., Paul, C. P., **2014a**. Development of micro-plasma transferred arc (μ -PTA) wire deposition process for additive layer manufacturing applications. **Journal of Materials Processing Technology**, 214, 1102-1110. <https://doi.org/10.1016/j.jmatprotec.2013.12.016>
- Jhavar, S., Jain, N. K., Paul, C. P., **2014b**. Enhancement of deposition quality in microplasma transferred arc deposition process. **Materials and Manufacturing Process**, 29, 1017-1023. <https://doi.org/10.1016/j.jmatprotec.2013.12.016>
- Jhavar, S., Paul, C.P., Jain, N.K., **2016**. Micro-plasma transferred arc additive manufacturing for die and mold surface remanufacturing. **Journal of the Minerals Metals & Materials Society**, 68, 1801-1809. <https://doi.org/10.1007/s11837-016-1932-z>
- Kajima, Y., Takaichi, A., Kittikundecha, N., Nakamoto, T., Kimura, T., Nomura, N., Kawasaki, A., Hanawa, T., Takahashi, H., & Wakabayashi, N., **2018**. Effect of heat-treatment temperature on microstructures and mechanical properties of Co–Cr–Mo alloys fabricated by selective laser melting. **Materials Science and Engineering: A**, 726, 21-31. <https://doi.org/10.1016/j.msea.2018.04.048>
- Kajima, Y., Takaichi, A., Kittikundecha, N., That, H.L., Cho, H.H.W., Tsutsumi, Y., Hanawa, T., Wakabayashi, N., Yoneyama, T., **2021**. Reduction in anisotropic response of corrosion properties of selective laser melted Co-Cr-Mo alloys by post-heat treatment, **Dental Materials**, 37, e98-e108. <https://doi.org/10.1016/j.dental.2020.10.020>

- Kassapidou, M., Hjalmarsson, L., Johansson, C.B., Johansson, P.H., Morisbake, E., Wennerberg, A., Stenport, V.F., **2020**. Cobalt-chromium alloys fabricated with four different techniques: Ion release, toxicity of released elements and surface roughness. **Dental Materials**, 36, e352-e363. <https://doi.org/10.1016/j.dental.2020.08.012>
- Katz, J.L., **1980**. Anisotropy of Young's modulus of bone. **Nature**, 283, 106-107. <https://doi.org/10.1038/283106a0>
- Kilmametov, A.R., Ivanisenko, Y., Straumal, B.B., Gornakova, A.S., Mazilkin, A.A., Hahn, H., **2018**. The $\alpha \rightarrow \omega$ transformation in titanium-cobalt alloys under high-pressure torsion. **Metals**, 8, 1. <https://doi.org/10.3390/met8010001>
- Kim, T., See, C.W., Li, X., Zhu, D., **2020**. Orthopedic implants and devices for bone fractures and defects: Past, present and perspective, **Engineered Regeneration**, 1, 6-18. <https://doi.org/10.1016/j.engreg.2020.05.003>
- Kim, T.K., Chang, C.B., Kang, Y.G., Kim, S.J., Seong, S.C., **2009**. Causes and Predictors of Patient's Dissatisfaction After Uncomplicated Total Knee Arthroplasty. *The Journal of Arthroplasty*, 24, 263-271. <https://doi.org/10.1016/j.arth.2007.11.005>
- Kim, T.K., Park, K.K., Yoon, S.W., Kim, S.J., Chang, C.B., Seong, S.C., **2009**. Clinical value of regular passive ROM exercise by a physical therapist after total knee arthroplasty, **Knee Surgery, Sports Traumatology, Arthroscopy**, 17, 1152–1158. <https://doi.org/10.1007/s00167-009-0731-2>
- Kircher, R.S., Christensen, A.M., Wurth, K.W., **2009**. Electron beam melted (EBM) Co-Cr-Mo alloy for orthopedic implant applications. <http://dx.doi.org/10.26153/tsw/15119>
- Kloppenburger, M., Berenbaum, F., **2020**, Osteoarthritis year in review 2019: epidemiology and therapy. **Osteoarthritis and Cartilage**, 28, 242-248. <https://doi.org/10.1016/j.joca.2020.01.002>
- Kohn, D., **2011**. Porous coatings in orthopedics, **Comprehensive Biomaterials**, 65-77. <https://doi.org/10.1016/B978-0-08-055294-1.00201-4>
- Kong, W., Cox, S.C., Lu, Y., Villapun, V., Xiao, X., Ma, W., et al. **2021**. The influence of zirconium content on the microstructure, mechanical properties, and biocompatibility of in-situ alloying Ti-Nb-Ta based β alloys processed by selective laser melting. **Materials Science and Engineering: C**, 131. <https://doi.org/10.1016/j.msec.2021.112486>
- Krishna, B.V., Bose, S., Bandyopadhyay, A., **2007**. Low stiffness porous Ti structures for load bearing implants, **Acta Biomaterialia**, 3, 997-1006. <https://doi.org/10.1016/j.actbio.2007.03.008>

- Kumar, P., Jain, N. K., **2020**. Effect of material form on deposition characteristics in micro-plasma transferred arc additive manufacturing process. **CIRP Journal of Manufacturing Science and Technology**, 30, 195-205.
<https://doi.org/10.1016/j.cirpj.2020.05.008>
- Kwak, T.Y., Yang, J.Y., Heo, Y.B., Kim, S.J., Kwon, S.Y., Kim, W.J., Lim, D.H., **2021**. Additive manufacturing of a porous titanium layer structure Ti on a Co-Cr alloy for manufacturing cementless implants. **Journal of Materials Research and Technology**, 10, 250-267. <https://doi.org/10.1016/j.jmrt.2020.11.080>
- Laheurte, P., Prima, F., Eberhardt, A., Gloriant, T., Wary, M., et al., **2010**. Mechanical properties of low modulus β titanium alloys designed from the electronic approach. **Journal of the Mechanical Behavior of Biomedical Materials**, 3, 565-573.
<https://doi.org/10.1016/j.jmbbm.2010.07.001>
- Laitinen, M., Nieminen, J., Reito, A., Pakarinen, T.K., Suomalainen, P., Pamilo, K., Parkkinen, J., Lont, T., Eskelinen, A., **2017**. High blood metal ion levels in 19 of 22 patients with metal-on-metal hinge knee replacements: A cause for concern. **Acta Orthopaedica**, 88, 269-274. <http://dx.doi.org/10.1080/17453674.2017.1283846>
- Lee, D.H., Lee, S.H., Song, E.K., Seon, J.K., Lim, H.A., Yang, H.Y., **2017**. Causes and clinical outcomes of revision total knee arthroplasty, **Knee Surgery & Related Research**, 29, 104-109. <https://doi.org/10.5792/ksrr.16.035>
- Lee, T., Mathew, E., Rajavaman, S., Manivasagam, G., Singh, A.K., Lee, C.S., **2015**. Tribological and corrosion behaviors of warm and hot-rolled Ti-13Nb-13Zr alloys in simulated body fluid conditions. **International Journal of Nanomedicine**, 10, 207-212. <https://doi.org/10.2147/IJN.S79996>
- Levine, M., McElroy, K., Stakich, V., Cicco, J., **2013**. Comparing conventional physical therapy rehabilitation with neuromuscular electrical stimulation after TKA. **Orthopedics**, 36, e319-324. <https://doi.org/10.3928/01477447-20130222-20>
- Lewallen, E.A., Riestler, S.M., Bonin, C.A., Kremers, H.M., Dudakovic, A., Kakar, S., Cohen, R.C., Westendorf, J.J., Lewallen, D.G., **2015**. Biological strategies for improved osseointegration and osteoinduction of porous metal orthopedic implants. **Tissue Engineering. Part B, Reviews**, 21, 218-230.
<https://doi.org/10.1089/ten.teb.2014.0333>
- Li, B. Q., Lu, X., **2019**. A Biomedical Ti-35Nb-5Ta-7Zr alloy fabricated by powder metallurgy. **Journal of Materials Engineering and Performance**, 28, 5616-5624.
<https://doi.org/10.1007/s11665-019-04294-7>

- Li, B. Q., Xie, R. Z., Lu, X., **2020**. Microstructure, mechanical property and corrosion behavior of porous Ti-Ta-Nb-Zr. **Bioactive Materials**, 5, 564-568.
<https://doi.org/10.1016/j.bioactmat.2020.04.014>
- Li, C., Ma, Y., Yang, X., Hou, M., **2021**. New TiTaNbZrMo high-entropy alloys for metallic biomaterials. **Materials Research Express**, 8, 105403.
<https://doi.org/10.1088/2053-1591/ac2f0b>
- Li, H., Wang, M., Lou, D., Xia, W., Fang, X., **2020**. Microstructural features of biomedical cobalt-chromium-molybdenum (Co-Cr-Mo) alloy from powder bed fusion to aging heat treatment. **Journal of Materials Science & Technology**, 45, 146-156.
<https://doi.org/10.1016/j.jmst.2019.11.031>
- Li, H.F., Zheng, Y.F., **2016**. Recent advances in bulk metallic glasses for biomedical applications. **Acta Biomaterialia**, 36, 1-20.
<http://dx.doi.org/10.1016/j.actbio.2016.03.047>
- Li, T., Lu, Y., Li, Z., Wang, T., Li, T., **2022**. Hot deformation behavior and microstructure evolution of non-equimolar Ti₂ZrHfV_{0.5}Ta_{0.2} refractory high-entropy alloy, **Intermetallics**, 146, 1–11. <https://doi.org/10.1016/j.intermet.2022.107586>
- Li, X., Wang, X., Zhang, J., Wang, B., Breisch, M., Hartmaier, A., Rostotskyi, I., Voznyy, V., Liu, Y., **2022**. Experimental investigation of laser surface texturing and related biocompatibility of pure titanium. **The International Journal of Advanced Manufacturing Technology**, 119, 5993-6005. <https://doi.org/10.1007/s00170-022-08710-6>
- Liu, P., Lu, F.F., Liu, G.J., Mu, X.H., Sun, Y.G., Zhang, Q.D., Wang, W.G., Guo, W.S., **2021**. Robotic-assisted unicompartmental knee arthroplasty: a review, **Arthroplasty**, 3, 15. <https://doi.org/10.1186/s42836-021-00071-x>
- Liu, Q., Wang, G., Liu, Y., Sui, X., Chen, Y., Luo, S., **2021**. Hot deformation behaviors of an ultrafine-grained MoNbTaTiV refractory high-entropy alloy fabricated by powder metallurgy, **Materials Science and Engineering: A**, 809, 1–10.
<https://doi.org/10.1016/j.msea.2021.140922>
- Liu, Y., Gilbert, J.L., **2018**. The effect of simulated inflammatory conditions and Fenton chemistry on the electrochemistry of CoCrMo alloy, **Journal of Biomedical Materials Research Part B: Applied Biomaterials**, 106, 209-220.
<https://doi.org/10.1002/jbm.b.33830>
- Liu, Y.J., Li, S. J., H.L., Wang, Hou, W.T., Hao, Y.L., Yang, R., Sercombe, T.B., Zhang, L.C., **2016**. Microstructure, defects and mechanical behaviour of beta-type titanium

- porous structures manufactured by electron beam melting and selective laser melting. **Acta Materialia**, 113, 56-67. <https://doi.org/10.1016/j.actamat.2016.04.029>
- Liu, Y.J., Wang, H.L., Li, S.J., Wang, S. G., Wang, W.J., Hou, W.T., Hao, Y.L., Yang, R., Zhang, L.C., **2017**. Compressive and fatigue behaviour of beta-type titanium porous structures fabricated by electron beam melting, **Acta Materialia**, 126, 58-66. <https://doi.org/10.1016/j.actamat.2016.12.052>
- Lu, X., Wu, Z., Xu, K., Wang, X., Wang, S., Qiu, H., Li, X., Chen, J., **2021**. Multifunctional coatings of titanium implants toward promoting osseointegration and preventing infection: recent developments, **Frontiers in Bioengineering and Biotechnology**, 9, 783816. <https://doi.org/10.3389/fbioe.2021.783816>
- Lu, Y., Wu, S., Gan, Y., Li, J., Zhao, C., Zhuo, D., Lin, J., **2015**. Investigation on the microstructure, mechanical property and corrosion behavior of the selective laser melted CoCrW alloy for dental application, **Materials Science and Engineering: C**, 49, 517-525. <https://doi.org/10.1016/j.msec.2015.01.023>
- Łukaszczyk, A., Zimowski, S., Pawlak, W., Dubiel, B., Moskalewicz, T., **2021**. Microstructure, micro-mechanical and tribocorrosion behavior of oxygen hardened Ti-13Nb-13Zr alloy, **Materials**, 14:2088. <https://doi.org/10.3390/ma14082088>
- Luo, D., Zhou, Q., Ye, W., Ren, Y., Greiner, C., He, Y., et al. **2021**. Design and characterization of self-lubricating refractory high entropy alloy-based multilayered films. **ACS Applied Materials & Interfaces**, 13, 55712-55725. <https://doi.org/10.1021/acsmi.1c16949>
- Lupone, F., Padovano, E., Ostrovskaya, O., Russo, A., Badini, C., **2021**. Innovative approach to the development of conductive hybrid composites for selective laser sintering. **Composites Part A: Applied Science and Manufacturing**, 147, 106429. <https://doi.org/10.1016/j.compositesa.2021.106429>
- Lützner, J., Günther, K.P., Postler, A., Morlock, M., **2020**. Metal ion release after hip and knee arthroplasty-causes, biological effects and diagnostics. **Zeitschrift für Orthopädie und Unfallchirurgie**, 158, 369-382. <http://dx.doi.org/10.1055/a-0929-8121>
- Lyons, R., Newell, A., Ghadimi, P., Papakostas, N., **2021**. Environmental impacts of conventional and additive manufacturing for the production of Ti-6Al-4V knee implant: a life cycle approach, **The International Journal of Advanced Manufacturing Technology**, 112, 787–801. <https://doi.org/10.1007/s00170-020-06367-7>

- Ma, R., Tang, S., Tan, H., Lin, W., Wang, Y., Wei, J., Zhao, L., Tang, T. **2014**. Preparation, characterization, and in vitro osteoblast functions of a nano-hydroxyapatite/polyetheretherketone biocomposite as orthopedic implant material. **International journal of nanomedicine**, 9, 3949-3961.
<https://doi.org/10.2147/IJN.S67358>
- Mann, M.A., Smith, K., Banack, H.R., Tanzer, M. **2013**. Changing Surgeons Improves Outcome of Subsequent Primary Total Joint Arthroplasty in Previously Dissatisfied Patients. **The Journal of Arthroplasty**, 28, 736-739.
<https://doi.org/10.1016/j.arth.2012.12.014>
- Mantrala, K.M., Das, M., Balla, V.K., Rao, C.S., Rao, V.V.S.K., **2015**. Additive manufacturing of Co-Cr-Mo alloy: influence of heat treatment on microstructure, tribological, and electrochemical properties. **Frontiers in Mechanical Engineering**, 1, 2. <https://doi.org/10.3389/fmech.2015.00002>
- Maratt, J.D., Lee, Y., Lyman, S., Westrich, G.H., **2015**. Predictors of Satisfaction Following Total Knee Arthroplasty. **The Journal of Arthroplasty**, 30, 1142-1145.
<https://doi.org/10.1016/j.arth.2015.01.039>
- Mathiou, C., Pouliou, A., Georgatis, E., Karantzalis, A. E., **2018**. Microstructural features and dry - Sliding wear response of MoTaNbZrTi high-entropy alloy. **Materials Chemistry and Physics**, 210, 126-135.
<https://doi.org/10.1016/j.matchemphys.2017.08.036>
- Matkovi'c, T., Slokar, L., Matkovi'c, P., **2006**. Structure and properties of biomedical Co-Cr-Ti alloys. **Journal of Alloys and Compounds**, 407, 294-298.
<http://dx.doi.org/10.1016/j.jallcom.2005.06.025>
- McKeever, D.C., **1985**. The Classic: Tibial Plateau Prosthesis, **Clinical Orthopaedic Related Research**, 192, 3-12.
- Mergulhão, M.V., Neves M.D., **2018**. Characteristics of biometallic alloy to additive manufacturing using selective laser melting technology, **Journal of Biomaterials and Nanobiotechnology**, 9, 89-99. <https://doi.org/10.4236/jbnb.2018.91008>
- Mergulhão, M.V., Neves, M.D.M.D., **2018**. Characteristics of biometallic alloy to additive manufacturing using selective laser melting technology. **Journal of Biomaterials and Nanobiotechnology**, 9, 89-99. <https://doi.org/10.4236/jbnb.2018.91008>
- Mergulhão, M.V., Podestá C.E., Neves, M., **2017**. Investigation of mechanical, microstructural and thermal behavior of CoCrMo alloy manufactured by selective laser melting and casting techniques.
<https://doi.org/10.26678/ABCM.COBEP2017.COF2017-1286>

- Merola, M., Affatato, S., **2019**. Materials for hip prostheses: a review of wear and loading considerations. **Materials**, 12, 495. <https://doi.org/10.3390/ma12030495>
- Mirhosseini, N., Crouse, P., Schmidh, M., Li, L., Garrod, D., **2007**. Laser surface micro-texturing of Ti-6Al-4V substrates for improved cell integration. **Applied Surface Science**, 253, 7738-7743. <https://doi.org/10.1016/j.apsusc.2007.02.168>
- Miyoshi, S., Takahashi, T., Ohtani, M., Yamamoto, H., Kameyama, K., **2002**. Analysis of the shape of the tibial tray in total knee arthroplasty using a three-dimension finite element model. **Clinical Biomechanics**, 17, 521-525. [https://doi.org/10.1016/S0268-0033\(02\)00064-5](https://doi.org/10.1016/S0268-0033(02)00064-5)
- Moffet, H., Tousignant, M., Nadeau, S., Mérette, C., Boissy, P., Corriveau, H., Marquis, F., Cabana, F., Ranger, P., Belzile, É., Dimentberg, R., **2015**. In-home telerehabilitation compared with face-to-face rehabilitation after total knee arthroplasty: a noninferiority randomized controlled trial. **The Journal of Bone and Joint Surgery**, 97, 1129-1141. <https://doi.org/10.2106/JBJS.N.01066>
- Motallebzadeh, A., Yagci, M. B., Bedir, E., Aksoy, C. B., Canadinc, D., **2018**. Mechanical properties of TiTaHfNbZr high-entropy alloy coatings deposited on NiTi shape memory alloy substrates, **Metallurgical and Materials Transactions A**, 49, 1992-1997. <https://doi.org/10.1007/s11661-018-4605-4>
- Mu, J., Wang, H., Qin, B., Zhang, Y., Chen, L., Zeng, C., **2021**. Improved wear and corrosion resistance of biological compatible TiZrNb films on biomedical Ti6Al4V substrates by optimizing sputtering power. **Surface Coatings and Technology**, 428, 127866. <https://doi.org/10.1016/j.surfcoat.2021.127866>
- Mukherjee, S., Dhara, S., Saha, P., **2015**. Enhancing the biocompatibility of Ti6Al4V implants by laser surface microtexturing: an in vitro study. **The International Journal of Advanced Manufacturing Technology**, 76, 5-15. <http://dx.doi.org/10.1007/s00170-013-5277-2>
- Naert, I., **2017**. 7.24 Materials in fixed prosthodontics for indirect dental restorations, **Comprehensive Biomaterials II**, 467-481. <https://doi.org/10.1016/B978-0-08-100691-7.00244-5>
- Nag, S., Samuel, S., Puthucode, A., Banerjee, R., **2009**. Characterization of novel borides in Ti-Nb-Zr-Ta + 2B metal-matrix composites. **Materials Characterization**, 60, 106-113. <https://doi.org/10.1016/j.matchar.2008.07.011>
- Nagase, T., Todai, M., Hori, T., Nakano, T., **2018**. Microstructure of equiatomic and non-equiatomic Ti-Nb-Ta-Zr-Mo high-entropy alloys for metallic biomaterials. **Journal of Alloys and Compounds**, 753, 412-421. <https://doi.org/10.1016/j.jallcom.2018.04.082>

- Narayanan, D., Liu, M., Kuttolamadom, M., Castaneda, H., **2022**. Identification and development of a new local corrosion mechanism in a Laser Engineered Net Shaped (LENS) biomedical Co-Cr-Mo alloy in Hank's solution. **Corrosion Science**, 207, 110599. <https://doi.org/10.1016/j.corsci.2022.110599>
- Nath, B., Raza, A., Sethi, V., Dalal, A., Ghosh, S.S., Biswas, G., **2018**. Understanding flow dynamics, viability and metastatic potency of cervical cancer (HeLa) cells through constricted microchannel. **Nature: Science Reports**, 8, 17357. <http://dx.doi.org/10.1038/s41598-018-35646-3>
- Navarro, M., Michiardi, A., Castaño, O., Planell, J.A., **2008**. Biomaterials in orthopaedics, **Journal of The Royal Society Interface**, 5, 1137-1158. <http://doi.org/10.1098/rsif.2008.0151>
- Naylor, J.M., Hart, A., Mittal, R., Harris, I., Xuan, W. **2017**. The value of inpatient rehabilitation after uncomplicated knee arthroplasty: A propensity score analysis. **Medical Journal of Australia**, 207, 250-255. <https://doi.org/10.5694/mja16.01362>
- Neto, A.J.F., Panzeri, H., Neves, F.D., Prado, R.A.D., Mendonça, G., **2006**. Bond strength of three dental porcelains to Ni-Cr and Co-Cr-Ti alloys. **Brazilian Dental Journal**, 17, 24-28. <https://doi.org/10.1590/s0103-64402006000100006>
- Niinomi, M., **2007**. Fatigue characteristics of metallic biomaterials. **International Journal of Fatigue**, 29, 992-1000. <https://doi.org/10.1016/j.ijfatigue.2006.09.021>
- Niu, D., Zhang, C., Sui, X., Lu, X., Zhang, X., Wang, C., et al. **2022**. Microstructure, mechanical properties and tribo-corrosion mechanism of (CrNbTiAlVMo)_xNi_{1-x} coated 316 L stainless steel in 3.5 wt% NaCl solution. **Tribology International**, 173, 107638. <https://doi.org/10.1016/j.triboint.2022.107638>
- Nnamchi, P.S., Obayi, C.S., Todd, I., Rainforth, M.W., **2016**. Mechanical and electrochemical characterisation of new Ti-Mo-Nb-Zr alloys for biomedical applications. **Journal of the Mechanical Behavior of Biomedical Materials**, 60, 68-77. <https://doi.org/10.1016/j.jmbbm.2015.12.023>
- Noble, P.C., Conditt, M.A., Cook, K.F., Mathis, K.B., **2006**. The John Insall Award: Patient expectations affect satisfaction with total knee arthroplasty. **Clinical Orthopaedics and Related Research**, 452, 35-43. <https://doi.org/10.1097/01.blo.0000238825.63648.1e>
- Normand, J., Moriche, R., García-Garrido, C., Sepúlveda, F.R.E., Chicardi, E., **2020**. Development of a Ti-Nb-Ta-Mo-Zr-based high-entropy alloy with low young's modulus by mechanical alloying route. **Metals**, 10, 1-15. <https://doi.org/10.3390/met10111463>

- Nová, K., Novák, P., Dvorský, D., **2017**. Influence of alloying elements on the mechanical properties of a cobalt-based alloy produced with powder metallurgy. **Materials and Technology**, 51, 443-447. <https://doi.org/10.17222/mit.2016.054>
- Ocampo, C.M., Juarez, R., Rodriguez, A.S., **2002**. Effect of fcc-hcp phase transformation produced by isothermal aging on the corrosion resistance of a Co-27Cr-5Mo-0.05C alloy. **Metallurgical and Materials Transactions A**, 33, 2229-2235. <https://doi.org/10.1007/s11661-002-0054-0>
- Okazaki, Y., Gotoh, E., Nishimori, M., Katsuda, S., Manabe, T., Kobayashi, K., **2005**. Osteocompatibility of stainless steel, Co-Cr-Mo, Ti-6Al-4V and Ti-15Zr-4Nb-4Ta alloy implants in rat bone tissue. **Materials Transactions**, 46, 1610-1617. <https://doi.org/10.2320/matertrans.46.1610>
- Oladokun, A., Pettersson, M., Bryant, M., Engqvist, H., Persson, C., Hall, R., et al. **2015**. Fretting of CoCrMo and Ti6Al4V alloys in modular prostheses. **Tribology-Materials Surfaces & Interfaces**, 9, 165-173. <https://doi.org/10.1179/1751584X15Y.0000000014>
- Oliveira, J.P., Gouveia, F.M., Santos, T.G., **2022**. Micro wire and arc additive manufacturing (μ -WAAM). **Additive Manufacturing Letters**, 2, 100032. <https://doi.org/10.1016/j.addlet.2022.100032>
- Ozan, S., Lin, J., Zhang, Y., Li, Y., Wen, C., **2020**. Cold rolling deformation and annealing behavior of a β -type Ti-34Nb-25Zr titanium alloy for biomedical applications, **Journal of Materials Research and Technology**, 9, 2308-2318. <https://doi.org/10.1016/j.jmrt.2019.12.062>
- Paris, H., Mokhtarian, H., Coatanéa, E., Museau, M., Ituarte, I.F., **2016**. Comparative environmental impacts of additive and subtractive manufacturing technologies, **CIRP Annals**, 65, 29-32. <https://doi.org/10.1016/j.cirp.2016.04.036>
- Parvizi, J., Nunley, R.M., Berend, K.R., Lombardi, A.V., Ruh, EL., Clohisy, J.C., Hamilton, W.G., Della, V.C.J., Barrack, R.L., **2014**. High level of residual symptoms in young patients after total knee arthroplasty. **Clinical Orthopaedics and Related Research**, 472, 133-137. <https://doi.org/10.1007/s11999-013-3229-7>
- Petit, C., Maire, E., Meille, S., Adrien, J., Kurosu, S., & Chiba, A. **2016**. CoCrMo cellular structures made by Electron Beam Melting studied by local tomography and finite element modelling. **Materials Characterization**, 116, 48-54. <https://doi.org/10.1016/j.matchar.2016.04.006>

- Pilliar, R.M., Lee, J.M., Maniopoulos, C., **1986**. Observations on the effect of movement on bone ingrowth into porous-surfaced implants. **Clinical Orthopaedics and Related Research**, 208, 108-13. <https://pubmed.ncbi.nlm.nih.gov/3720113/>
- Pineau, A., Benzerga, A.A., Pardoën, T., **2016**. Failure of metals I: Brittle and ductile fracture, **Acta Materialia**, 107, 424-483. <https://doi.org/10.1016/j.actamat.2015.12.034>
- Popescu, G., Ghiban, B., Popescu, C. A., Rosu, L., Truscă, R., et al., **2018**. New TiZrNbTaFe high-entropy alloy used for medical applications, **IOP Conference Series: Materials Science and Engineering**, 400, 022049. <https://doi.org/10.1088/1757-899X/400/2/022049>
- Priya, P., Mercer, B., Huang, S., Aboukhatwa, M., Yuand, L., Chaudhuri, S., **2020**. Towards prediction of microstructure during laser based additive manufacturing process of Co-Cr-Mo powder beds. **Materials & Design**, 196, 109117. <https://doi.org/10.1016/j.matdes.2020.109117>
- Priyadarshini, B., Rama, M., Chetan., Vijayalakshmi U., **2019**. Bioactive coating as a surface modification technique for biocompatible metallic implants: a review. **Journal Asian Ceram Society**, 7, 397-406. <https://doi.org/10.1080/21870764.2019.1669861>
- Raducanu, D., Vasilescu, E., Cojocaru, V. D., Cinca, I., Drob, P., et al., **2011**. Mechanical and corrosion resistance of a new nanostructured Ti-Zr-Ta-Nb alloy, **Journal of the Mechanical Behavior of Biomedical Materials**, 4, 1421-1430. <https://doi.org/10.1016/j.jmbbm.2011.05.012>
- Rahimizadeh, A., Nourmohammadi, Z., Arabnejad, S., Tanzer, M., Pasini, D., **2018**. Porous architected biomaterial for a tibial-knee implant with minimum bone resorption and bone-implant interface micromotion. **Journal of the Mechanical Behavior of Biomedical Materials**, 78, 465-479. <https://doi.org/10.1016/j.jmbbm.2017.11.041>
- Rahman, S.S., Ashraf, M.Z.I., Bashar, M.S., Kamruzzaman, M., Amin, A.K.M.N., Hossain, M.M., **2017**. Crystallinity, surface morphology, and chemical composition of the recast layer and rutile-TiO₂ formation on Ti-6Al-4V ELI by wire-EDM to enhance biocompatibility. **The International Journal of Advanced Manufacturing Technology**, 93, 3285-3296 <http://dx.doi.org/10.1007/s00170-017-0772-5>
- Ramsden, J., Allen, D., Stephenson, D., Alcock, J., Peggs, G., Fuller, G., Goch, G., **2007**. The Design and Manufacture of Biomedical Surfaces. **CIRP Annals**, 56, 687-711. <https://doi.org/10.1016/j.cirp.2007.10.001>

- Reiner, T., Sorbi, R., Müller, M., Nees, T., Kretzer, J.P., Rickert, M., et al. **2020**. Blood metal ion release after primary total knee arthroplasty: a prospective study. **Orthopaedic Surgery**, 12, 396-403. <https://doi.org/10.1111/os.12591>
- Ren, L., Gu, H., Wang, W., Wang, S., Li, C., Wang, Z., Zhai, Y., Ma, P., **2020**. The Microstructure and properties of an Al-Mg-0.3Sc alloy deposited by wire arc additive manufacturing. **Metals**, 10, 320. <https://doi.org/10.3390/met10030320>
- Robinson, R.P., **2005**, The early innovator of today's resurfacing condylar knees. **Journal of Arthroplasty**, 20, 2–26.
- Rogal, L., Ikeda, Y., Lai, M., Körmann, F., Kalinowska, A., Grabowski, B., **2020**. Design of a dual-phase hcp-bcc high entropy alloy strengthened by ω nanoprecipitates in the Sc Ti-Zr-Hf-Re system. **Materials & Design**, 192, 108716. <https://doi.org/10.1016/j.matdes.2020.108716>
- Ruiz, R.D., Romanos, G., **2018**. Potential causes of titanium particle, and ion release in implant dentistry: a systematic review. **International Journal of Molecular Sciences**, 19, 3585. <http://dx.doi.org/10.3390/ijms19113585>
- Rustamov, I.A., Sabirova, O.S., Wang, Z., Wang, Y., **2019**. Fretting wear behavior and damage mechanisms of Inconel x-750 alloy in dry contacts. **Advances in Materials Science and Engineering**, 2019. <https://doi.org/10.1155/2019/7079819>
- Ryu, D.J., Jung, A., Ban, H.Y., Kwak, T.Y., Shin, E.J., Gweon, B., Lim, D., Wang, J.H., **2021**. Enhanced osseointegration through direct energy deposition porous coating for cementless orthopedic implant fixation, **Nature: Scientific Reports**, 11, 22317. <https://doi.org/10.1038/s41598-021-01739-9>
- Sato, T.D.O., Hansson, G.-Å., Coury, H.J.C.G., **2010**. Goniometer Crosstalk Compensation for Knee Joint Applications. **Sensors**, 10, 9994-10005. <https://doi.org/10.3390/s101109994>
- Sawant, M.S., Jain, N.K., **2017**. Investigations on wear characteristics of Stellite coating by micro-plasma transferred arc powder deposition process, **Wear**, 378-379, 155-164. <https://doi.org/10.1016/j.wear.2017.02.041>.
- Sawant, M.S., Jain, N.K., **2018a**. Investigations on additive manufacturing of Ti-6Al-4V by μ -plasma transferred arc powder deposition process. **Transactions of ASME: Journal of Manufacturing Science and Engineering**, 140, 081014. <https://doi.org/10.1115/1.4040324>
- Sawant, M.S., Jain, N.K., **2018b**. Evaluation of Stellite coatings by μ -PTA powder, laser and PTA deposition processes, **Materials and Manufacturing Processes**, 33, 1043-1050. <https://doi.org/10.1080/10426914.2017.1364764>

- Sawant, M.S., Jain, N.K., Nikam, S.H., **2019**. Theoretical modelling and finite element simulation of dilution in micro-plasma transferred arc additive manufacturing of metallic materials. **International Journal of Mechanical Sciences**, 164, 105166. <https://doi.org/10.1016/j.ijmecsci.2019.105166>
- Sawant, M.S., Jain, N.K., Palani, I.A., **2018c**. Influence of dimple and spot-texturing of HSS cutting tool on machining of Ti-6Al-4V. **Journal of Materials Processing Technology**, 261, 1–11. <https://doi.org/10.1016/j.jmatprotec.2018.05.032>
- Sawy, A.A.E., Shaarawy, M.A., **2014**. Evaluation of metal ion release from Ti-6Al-4V and Co-Cr-Mo casting alloy: in-vivo and in-vitro study, **Journal of Prosthesis**, 23, 89-97. <https://doi.org/10.1111/jopr.12067>
- Schoon, J., Ort, M.J., Huesker, K., Geissler, S., Rakow, A., **2019**. Diagnosis of metal hypersensitivity in total knee arthroplasty: a case report. **Frontiers in Immunology**, 10, 1-8. <https://doi.org/10.3389/fimmu.2019.02758>
- Scott, C.E., Bugler, K.E., Clement, N.D., MacDonald, D., Howie, C.R., Biant, L.C., **2012**. Patient expectations of arthroplasty of the hip and knee. **The Journal of Bone and Joint Surgery**, 94, 974-981. <https://doi.org/10.1302/0301-620X.94B7.28219>
- Scott, C.E., Howie, C.R., MacDonald, D., Biant, L.C., **2010**. Predicting dissatisfaction following total knee replacement: a prospective study of 1217 patients. **The Journal of bone and joint surgery. British volume**, 92, 1253-1268. <https://doi.org/10.1302/0301-620X.92B9.24394>
- Scuderi, G.R., Bourne, R.B., Noble, P.C., Benjamin, J.B., Lonner, J.H., Scott, W.N. **2011**. The new knee society knee scoring system. **Clinical Orthopaedics and Related Research**, 470, 3-19. <https://doi.org/10.1007/s11999-011-2135-0>
- Senkov, O.N., Wilks, G.B., Scott, J.M., Miracle, D.B., **2011**. Mechanical properties of Nb₂₅Mo₂₅Ta₂₅W₂₅ and V₂₀Nb₂₀Mo₂₀Ta₂₀W₂₀ refractory high-entropy alloys. **Intermetallics**, 19, 698-706. <https://doi.org/10.1016/j.intermet.2011.01.004>
- Shaik, N.B., Mantrala, K.M., Bakthavatchalam, B., Gillani, Q.F., Rehman, M.F., Behera, A., Rajak, D.K., Pruncu, C.I., **2021**. Corrosion behavior of LENS deposited Co-Cr-Mo alloy using bayesian regularization-based artificial neural network (BRANN), **Journal of Bio and Tribo-Corrosion**, 7, 116. <https://doi.org/10.1007/s40735-021-00550-3>
- Shi, Z., Liu, M., Atrens, A., **2010**. Measurement of the corrosion rate of magnesium alloys using Tafel extrapolation. **Corrosion Science**, 52, 579-588. <http://dx.doi.org/10.1016/j.corsci.2009.10.016>
- Shittu, J., Pole, M., Cockerill, I., Sadeghilaridjani, M., Reddy, L.V.K., Manivasagam, G., et al. **2020**. Biocompatible high-entropy alloys with excellent degradation resistance in a

- simulated physiological environment. **ACS Applied Bio Materials**, 3, 8890-8900.
<https://doi.org/10.1021/acsabm.0c01181>
- Sidun, J., Dąbrowski, J.R., **2018**. The method of fretting wear assessment with the application of 3D laser measuring microscope. **Advances in Intelligent Systems and Computing**, 623, 369-377. https://doi.org/10.1007/978-3-319-70063-2_39
- Singh, J.A., Lewallen, D.G., **2013**. Medical and psychological comorbidity predicts poor pain outcomes after total knee arthroplasty. **Rheumatology (Oxford)**, 52, 916-923.
<https://doi.org/10.1093/rheumatology/kes402>
- Singh, R., Dahotre, N.B., **2007**. Corrosion degradation and prevention by surface modification of biometallic materials. **Journal of Materials Science: Materials in Medicine**, 18, 725-751. <https://doi.org/10.1007/s10856-006-0016-y>
- Sivakumar, B., Pathak, L.C., Singh, R., **2018**. Fretting corrosion response of boride coated titanium in Ringer's solution for bio-implant use: elucidation of degradation mechanism. **Tribology International**, 127, 219-230.
<https://doi.org/10.1016/j.triboint.2018.06.013>
- Sola, A., Nouri, A., **2019**. Microstructural porosity in additive manufacturing: The formation and detection of pores in metal parts fabricated by powder bed fusion, **Journal of Advanced Manufacturing and Processing**, 1, 1-21.
<https://doi.org/10.1002/amp2.10021>
- Spencer, J., Dickens, P., Wykes, C., **1998**. Rapid prototyping of metal parts by three-dimensional welding. Proceedings of the Institution of Mechanical Engineers. **Part B: Journal of Engineering Manufacture**, 212, 175-182.
<https://doi.org/10.1243/0954405981515590>
- Straumal, B.B., Gornakova, A.S., Kilmametov, A.R., Rabkin, E., Anisimova, N.Y., Kiselevskiy, M.V., **2021**. β -Ti-based alloys for medical applications, **Russian Journal of Non-Ferrous Metals**, 62, 54-63. <https://doi.org/10.3103/S1067821221010156>
- Straumal, B.B., Korneva, A., Kilmametov, A.R., Dobrzynska, L.L., Gornakova, A.S., Chulist, R., et al. **2019**. Structural and mechanical properties of Ti-Co alloys treated by high pressure torsion. **Materials**, 12, 426. <https://doi.org/10.3390/ma12030426>
- Surmeneva, M.A., Surmenev, R.A., Chudinova, E.A., Koptioug, A., Tkachev, M.S., Gorodzha, S.N., Rännar, L.E., **2017**. Fabrication of multiple-layered gradient cellular metal scaffold via electron beam melting for segmental bone reconstruction, **Materials & Design**, 133, 195-204. <https://doi.org/10.1016/j.matdes.2017.07.059>
- Takeuchi, A., Inoue, A., **2005**. Classification of bulk metallic glasses by atomic size difference, heat of mixing and period of constituent elements and its application to

- characterization of the main alloying element. **Materials Transactions**, 46, 2817-2829. <https://doi.org/10.2320/matertrans.46.2817>
- Tamayo, J.A., Riascos, M., Vargas, C.A. Baena, L.M., **2021**. Additive manufacturing of Ti6Al4V alloy via electron beam melting for the development of implants for the biomedical industry. **Heliyon**, 7, e06892. <https://doi.org/10.1016/j.heliyon.2021.e06892>
- Tan, X., Kok, Y., Tan, Y.J., Descoins, M., Mangelinck, D., Tor, S.B., Leong, K.F., Chua, C.K., **2015**. Graded microstructure and mechanical properties of additive manufactured Ti-6Al-4V via electron beam melting, **Acta Materialia**, 97, 1-16. <https://doi.org/10.1016/j.actamat.2015.06.036>
- Tang, H.P., Zhao, P., Xiang, C.S., Liu, N., Jia, L., **2018**. Ti-6Al-4V orthopedic implants made by selective electron beam melting, in: F.H. Froes, M. Qian (Eds.), *Titanium in Medical and Dental Applications*. Woodhead Publishing, **Sawston (UK)**, pp. 239-249. <https://doi.org/10.1016/B978-0-12-812456-7.00011-1>
- Tanzi, MC., Farè, S., Candiani, G., **2019**. *Biomaterials and Applications, Foundations of Biomaterials Engineering*, **Academic Press**. pp. 199-287. <https://doi.org/10.1016/C2015-0-05967-6>
- Taunton, M.J., **2021**. What's new in adult reconstructive knee surgery, **The Journal of Bone and Joint Surgery**, 103, 97-105. <http://dx.doi.org/10.2106/JBJS.20.01753>
- Teoh, S.H., **2000**. Fatigue of biomaterials: A review. **International Journal of Fatigue**, 22, 825-837. [https://doi.org/10.1016/S0142-1123\(00\)00052-9](https://doi.org/10.1016/S0142-1123(00)00052-9)
- Terakubo, M., Oh, J., Kirihara, S., Miyamoto, Y., Matsuura, K., Kudoh, M., **2005**. Freeform fabrication of titanium metal by 3D micro welding. **Materials Science and Engineering A**, 402, 84-91. <https://doi.org/10.1016/j.msea.2005.04.025>
- Tian, L., Tang, N., Ngai, T., Wu, C., Ruan, Y., Huang, L., Qin, L., **2019**. Hybrid fracture fixation systems developed for orthopaedic applications: A general review. **Journal of Orthopaedic Translation**, 16, 1-13. <https://doi.org/10.1016/j.jot.2018.06.006>
- Tower, S.S., Cho, C.S., Bridges, R.L., Gessner, B.D., **2021**. Prevalence of cobalturia among adults with joint replacements. **JAMA Network Open**, 4, 8-11. <https://doi.org/10.1001/jamanetworkopen.2021.21758>
- Tüten, N., Canadinc, D., Motallebzadeh, A., Bal, B., **2019**. Microstructure and tribological properties of TiTaHfNbZr high-entropy alloy coatings deposited on Ti-6Al-4V substrates. **Intermetallics**, 105, 99-106. <https://doi.org/10.1016/j.intermet.2018.11.015>

- Twiggs, J.G., Wakelin, E.A., Fritsch, B.A., Liu, D.W., Solomon, M., Parker, D., Klasan, A., Miles, B., **2019**. Clinical and statistical validation of a probabilistic prediction tool of total knee arthroplasty outcome, **The Journal of Arthroplasty**, 34, 2624-2631. <https://doi.org/10.1016/j.arth.2019.06.007>
- Ureña, J., Tabares, E., Tsipas, S., Jiménez-Morales, A., Gordo, E., **2019**. Dry sliding wear behaviour of β -type Ti-Nb and Ti-Mo surfaces designed by diffusion treatments for biomedical applications. **Journal of the Mechanical Behavior of Biomedical Materials**, 91, 335-344. <https://doi.org/10.1016/j.jmbbm.2018.12.029>
- Van Hove, R.P., Sierevelt, I.N., Van Royen, B.J., Nolte, P.A., **2015**. Titanium-Nitride Coating of Orthopaedic Implants: A Review of the Literature, **BioMed Research International**, 2015, 485975. <https://doi.org/10.1155/2015/485975>
- Von Hintze, J., Niemeläinen, M., Sintonen, H., Nieminen, J., Eskelinen, A., **2021**. Outcomes of the rotating hinge knee in revision total knee arthroplasty with a median follow-up of 6.2 years. **BMC Musculoskeletal Disorders**, 22, 1-9. <https://doi.org/10.1186/s12891-021-04205-9>
- Von Keudell, A., Sodha, S., Collins, J., Minas, T., Fitz, W., Gomoll, A.H., **2014**. Patient satisfaction after primary total and unicompartmental knee arthroplasty: an age-dependent analysis. **Knee**, 21, 180-194. <https://doi.org/10.1016/j.knee.2013.08.004>
- Vrancken, B., Thijs, L., Kruth, J. P., Humbeeck, J.V., **2014**. Microstructure and mechanical properties of a novel b titanium metallic composite by selective laser melting, **Acta Materialia**, 68, 150-158. <https://doi.org/10.1016/j.actamat.2014.01.018>
- Wallace, I.J., Worthington, S., Felson, D.T., Jurmain, R.D., Wren, K.T., Maijanen, H., Woods, R.J., Lieberman, D.E., **2017**. Knee osteoarthritis has doubled in prevalence since the mid-20th century, **PNAS**, 114, 9332-9336. <https://doi.org/10.1073/pnas.1703856114>
- Wan, Y., Mo, J., Wang, X., Zhang, Z., Shen, B., Liang, X., **2021**. Mechanical properties and phase stability of WTaMoNbTi refractory high-entropy alloy at elevated temperatures, **Acta Metallurgica Sinica**, 34, 1585–1590. <https://doi.org/10.1007/s40195-021-01263-9>
- Wang, B.L., Zheng, Y.F., Zhao, L.C., **2009**. Electrochemical corrosion behavior of biomedical Ti-22Nb and Ti-22Nb-6Zr alloys in saline medium. **Materials and Corrosion**, 60, 788-794. <https://doi.org/10.1002/maco.200805173>
- Wang, C., Zhang, G., Li, Z., Zeng, X., Xu, Y., Zhao, S., et al. **2019**. Tribological behavior of Ti-6Al-4V against cortical bone in different biolubricants. **Journal of the**

- Mechanical Behavior of Biomedical Materials**, 90, 460-471.
<https://doi.org/10.1016/j.jmbbm.2018.10.031>
- Wang, R., Qin, G., Zhang, E., **2020**. Effect of Cu on martensite transformation of CoCrMo alloy for biomedical application. **Journal of Materials Science & Technology**, 52, 127-135. <https://doi.org/10.1016/j.jmst.2020.04.012>
- Wang, S. P., Xu, J., **2017**. TiZrNbTaMo high-entropy alloy designed for orthopedic implants: as-cast microstructure and mechanical properties. **Materials Science and Engineering C**, 73, 80-89. <https://doi.org/10.1016/j.msec.2016.12.057>
- Wang, X., Zhang, L., Guo, Z., Jiang, Y., Tao, X., Liu, L., **2016**. Study of low-modulus biomedical β -Ti-Nb-Zr alloys based on single-crystal elastic constants modeling. **Journal of the Mechanical Behavior of Biomedical Materials**, 62, 310-318.
<http://dx.doi.org/10.1016/j.jmbbm.2016.04.040>
- Wang, Z., Tang, S.Y., Scudino, S., Ivanov, Y.P., Qu, R.T., Wang, D., et al. **2021**. Additive manufacturing of a martensitic Co-Cr-Mo alloy: Towards circumventing the strength-ductility trade-off. **Additive Manufacturing**, 37, 101725.
<https://doi.org/10.1016/j.addma.2020.101725>
- Wegener, K., Spierings, A. B., Teti, R., Caggiano, A., Knüttel, D., et al., **2021**. A conceptual vision for a bio-intelligent manufacturing cell for selective laser melting, **CIRP Journal of Manufacturing Science and Technology**, 34, 61-83.
<https://doi.org/10.1016/j.cirpj.2020.11.009>
- Wei, D., Koizumi, Y., Chiba, A., Ueki, K., Ueda, K., Narushima, T., et al. **2018**. Heterogeneous microstructures and corrosion resistance of biomedical Co-Cr-Mo alloy fabricated by electron beam melting (EBM). **Additive Manufacturing**, 24, 103-114. <https://doi.org/10.1016/j.addma.2018.09.006>
- Williams, D. F., **2008**. On the mechanisms of biocompatibility. **Biomaterials**, 29, 2941-2953. <https://doi.org/10.1016/j.biomaterials.2008.04.023>
- Williams, D.F. (editor) **1987**. Definitions in biomaterials: *Proceedings of Consensus Conference of the European Society for Biomaterials (Vol. 4)*, Elsevier Science Limited.
- Williams, D.P., Price, A.J., Beard, D.J., Hadfield, S.G., Arden, N.K., Murray, D.W., Field, R.E., **2013**. The effects of age on patient-reported outcome measures in total knee replacements. **The Bone & Joint Journal**, 95, 38-44. <https://doi.org/10.1302/0301-620X.95B1.28061>
- Willmann, G., **2000**. Ceramic femoral head retrieval data. **Clinical Orthopedics and Related Research**, 379, 22-28. <https://doi.org/10.1097/00003086-200010000-00004>

- Xiang, S., Yuan, Y., Zhang, C., Chen, J., **2022**. Effects of process parameters on the corrosion resistance and biocompatibility of Ti-6Al-4V parts fabricated by selective laser melting, **ACS Omega**, 7, 5954-5961. <https://doi.org/10.1021/acsomega.1c06246>
- Xiang, S., Zhao, Y., Li, Z., Feng, B., Weng, X., **2019**. Clinical outcomes of ceramic femoral prosthesis in total knee arthroplasty: a systematic review. **Journal of Orthopaedic Surgery and Research**, 14, 57. <https://doi.org/10.1186/s13018-019-1090-4>
- Xin, X.Z., Xiang, N., Chen, J., Wei, B., **2012**. In vitro biocompatibility of Co–Cr alloy fabricated by selective laser melting or traditional casting techniques, **Materials Letters**, 88, 101-103. <https://doi.org/10.1016/j.matlet.2012.08.032>
- Xu, F., Lv, Y., Liu, Y., Shu, F., He, P., Xu, B., **2013**. Microstructural evolution and mechanical properties of Inconel 625 alloy during pulsed plasma arc deposition process. **Journal of Materials Science & Technology**, 29, 480-488. <https://doi.org/10.1016/j.jmst.2013.02.010>
- Yan, R., Luo, D., Huang, H., Li, R., Yu, N., Liu, C., Hu, M., Rong, Q., **2018**. Electron beam melting in the fabrication of three-dimensional mesh titanium mandibular prosthesis scaffold. **Nature: Scientific Reports**, 8, 750. <https://doi.org/10.1038/s41598-017-15564-6>
- Ye, Y. X., Liu, C. Z., Wang, H., Nieh, T. G., **2018**. Friction and wear behavior of a single-phase equiatomic TiZrHfNb high-entropy alloy studied using a nanoscratch technique, **Acta Materialia**, 147, 78-89. <https://doi.org/10.1016/j.actamat.2018.01.014>
- Yılmaz, E., Çakıroğlu, B., Gökçe, A., Findik, F., Gulsoy, H.O., Gulsoy, N., et al. **2019**. Novel hydroxyapatite/graphene oxide/collagen bioactive composite coating on Ti16Nb alloys by electrodeposition. **Materials Science and Engineering:C**, 101, 292-305. <https://doi.org/10.1016/j.msec.2019.03.078>
- Yu, S.Y., Scully, J.R., Vitus, C.M., **2001**. Influence of niobium and zirconium alloying additions on the anodic dissolution behavior of activated titanium in HCl solutions. **Journal of the Electrochemical Society**, 148, B68. <https://doi.org/10.1149/1.1337605>
- Yuan, L., Ding, S., Wen, C., **2019**. Additive manufacturing technology for porous metal implant applications and triple minimal surface structures: A review. **Bioactive Materials**, 4, 56-70. <https://doi.org/10.1016/j.bioactmat.2018.12.003>
- Yuan, Y., Wu, Y., Yang, Z., Liang, X., Lei, Z., et al., **2019**. Formation, structure and properties of biocompatible TiZrHfNbTa high-entropy alloys, **Materials Research Letters**, 7, 225-231. <https://doi.org/10.1080/21663831.2019.1584592>

- Zahoor, S., Saleem, M.Q., Kader, W.A., Ishfaq, K., Shehzad, A., Ghani, H.U., Hussain, A., Usman, M., Dawood, M., **2019**. Improving surface integrity aspects of AISI 316L in the context of bioimplant applications. **The International Journal of Advanced Manufacturing Technology**, 105, 2857-2867. <https://doi.org/10.1007/s00170-019-04444-0>
- Zareidoost, A., Yousefpour, M., **2020**. A study on the mechanical properties and corrosion behavior of the new as-cast TZNT alloys for biomedical applications, **Materials Science and Engineering: C**, 110, 110725. <https://doi.org/10.1016/j.msec.2020.110725>
- Zha, L., Li, H., Wang, N., **2020**. In situ electrochemical study of the growth kinetics of passive film on TC11 alloy in sulfate solution at 300 °C/10 MPa. **Materials**, 13, 1135. <https://doi.org/10.3390/ma13051135>
- Zhang, C., Chen, F., Wang, Q., Liu, Y., Shen, Q., Zhang, L., **2023**. Additive manufacturing and mechanical properties of TC4/Inconel 625 functionally graded materials by laser engineered net shaping. **Materials Science and Engineering: A**, 862, 144370. <https://doi.org/10.1016/j.msea.2022.144370>
- Zhang, Y., Chen, Y., Li, P., Male, A.T., **2003**. Weld deposition-based rapid prototyping: a preliminary study. **Journal of Materials Processing Technology**, 135, 347-357. [https://doi.org/10.1016/S0924-0136\(02\)00867-1](https://doi.org/10.1016/S0924-0136(02)00867-1)
- Zhao, X., Niinomi, M., Nakai, M., Ishimoto, T., Nakano, T., **2011**. Development of high Zr-containing Ti-based alloys with low Young's modulus for use in removable implants, **Materials Science and Engineering: C**, 31, 1436-1444. <https://doi.org/10.1016/j.msec.2011.05.013>
- Zhou, R., Roy, A., Silberschmidt, V.V., **2019**. A crystal-plasticity model of extruded AM30 magnesium alloy. **Computational Materials Science**, 170, 109140. <https://doi.org/10.1016/j.commatsci.2019.109140>
- Zhu, M.H., Zhou, Z.R., **2011**. On the mechanisms of various fretting wear modes. **Tribology International**, 44, 1378-1388. <https://doi.org/10.1016/j.triboint.2011.02.010>

Appendix A: Details of the Equipment Used in Evaluation and Characterization of the Responses

A1: Leica Stereo Microscope (IIT Indore)



Make	Leica Microsystems, Germany
Model	<i>EZ4HD</i>
Full frame image acquisition	2048 × 1536 pixels, 3.1 megapixels
Pixel size	3.2 μm × 3.2 μm

A2: Scanning Electron Microscope (IIT Indore)



Make	JEOL Ltd., Japan
Model	<i>JSM-7610F</i>
Resolution	1.0 nm @ 15 kV 1.5 nm @ 1 kV 4.0 nm @ 15 kV
Acceleration Voltage	0.1 – 30 kV
Magnification	25x – 19,000 x (LM mode) 130x – 1,000,000 (SEM mode)
Stages	Computer-controlled 5-axis (X, Y, R, T, Z) motor drive (with backlash connection) Stage X = 70 mm, Y = 50 mm and Z = 50 mm, T = -5° to + 70°, R = 360°

A3: Microhardness Testing Machine (IIT Indore)



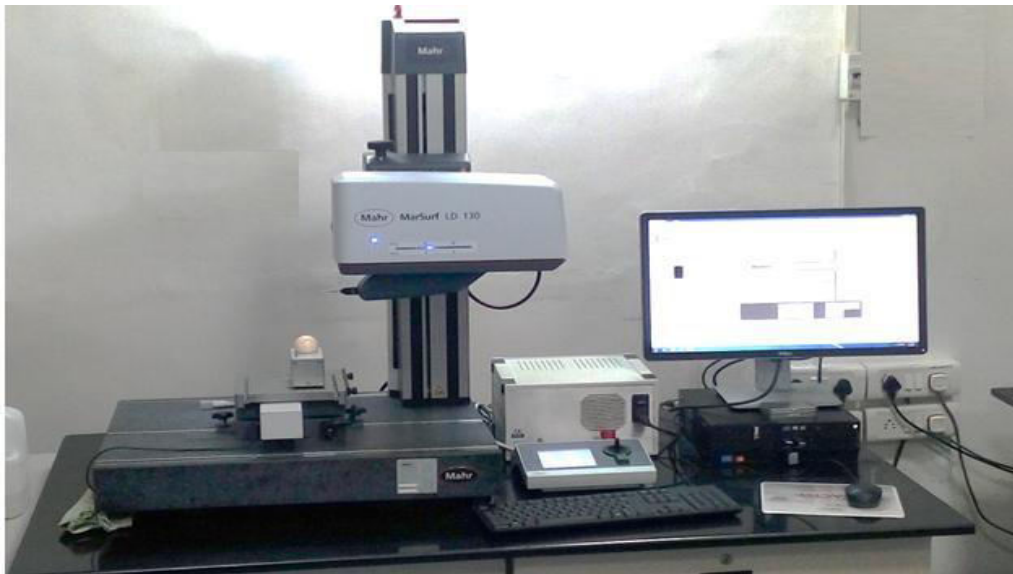
Make	Walter UHL Technische Mikroskopie GmbH, Germany.
Model	<i>VMH002 V</i>
Load Range	1 grams – 2000 grams
Type of indenter	Diamond square base hexagonal Pyramid



A4: Tensile Testing Machine (IIT Indore)

Make	Tinius Olsen USA
Model	<i>H50KL</i>
Load Range	1-50 kN
Clearance Between Columns	405 mm
Testing Speed Range	0.001 to 500 mm/min

A5: 3D-Surface roughness-cum-contour tracing equipment (IIT Indore)



Make	Mahr GmbH, Germany
Model	<i>MarSurf LD 130</i>
Resolution	0.8 nm
Positioning speed	0.02 mm/s to 200 mm/s
Traversing lengths	0.1 mm - 130 mm

A6: X-ray Diffraction (XRD) (IIT Indore)



Make	Malvern Panalytical Empyrean, Netherland
Attachments	Capillary spinner, Micro-diffraction spinner, 3-axes (chi,phi,z) cradle with optional manual x,y platform, 5-axes (chi,phi,x,y,z) cradle, Programmable XYZ stage, High-throughput stage, Multipurpose sample stage
X-ray generator	A 4kW sealed tube x-ray generator Max. voltage 60kV, Max. current 100mA, with Cu target
High-accuracy theta-theta goniometer	Maximum usable range – $-111 < 2\theta < 168^\circ$, Smallest addressable increment – 0.0001° , Maximum angular speed – 15 deg/s, Angular resolution (FWHM on LaB6) – 0.026°
Detectors	0D Scintillation Counter (point detector), 1D Semiconductor Detector D/tex Ultra (linear detector)

Appendix B: Details of the Equipment Used in Evaluation and Characterization of the Responses

Finite element analysis (FEA) of tibial tray of knee implant was done by the ANSYS software using material properties (Listed in Table B1) of the optimized deposition of Co-Cr-Mo-2Ti, Co-Cr-Mo-4Ti, and Co-Cr-Mo-6Ti alloys and static load to determine Von-Mises stresses and total deformation. Three-dimensional computer aided design model of tibial tray was developed as shown in Fig. B1. Its dimensions are 60 mm length; 10 mm tip diameter; 13 mm base diameter at tibial base stem junction; and 5 mm thickness. FEA of the tibial tray used 8906 elements and 2714 nodes during the meshing using following boundary and loading conditions: (i) materials of the optimized depositions are isotropic and homogeneous, (ii) outer surface of the tibial tray is fixed in all the directions, and (iii) two compressive loads of 1000 N each are applied symmetrically at two points 38 mm apart from the stem center. Load value was selected based on the previously described FEA analysis (**Dong et al. 2020**).

Table B1: Material properties used in FEM analysis for tibial tray.

Material	Density (g/cm ³)	Yield strength (MPa)	Poisson's ratio
Co-Cr-Mo-2Ti	8.097	774 (6.7)	0.32
Co-Cr-Mo-4Ti	7.772	789 (7.9)	0.32
Co-Cr-Mo-6Ti	7.198	734 (5.8)	0.32

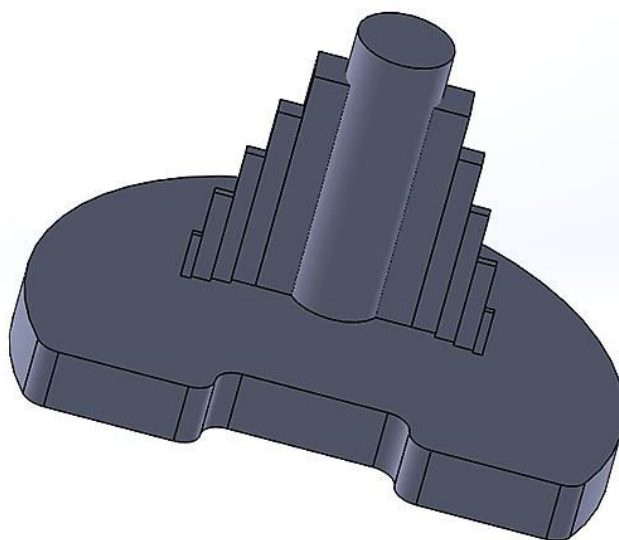
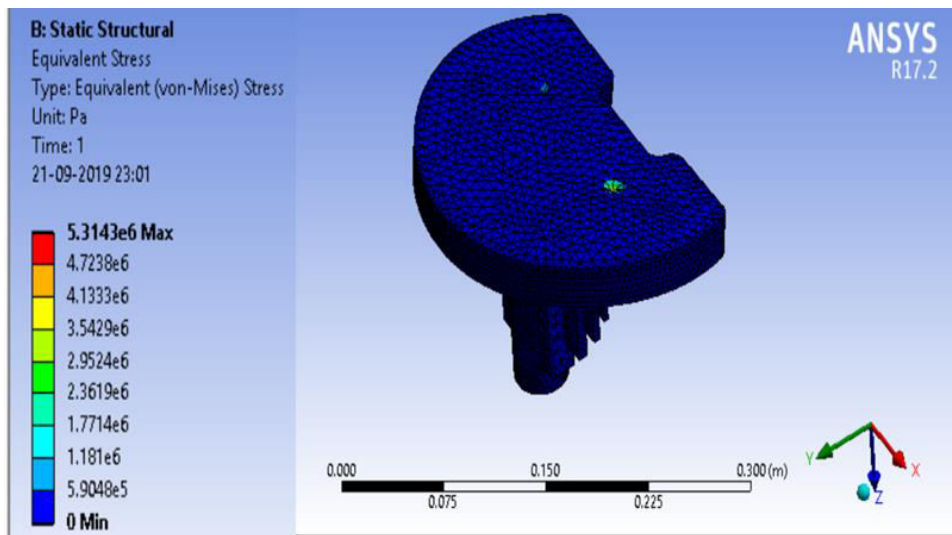
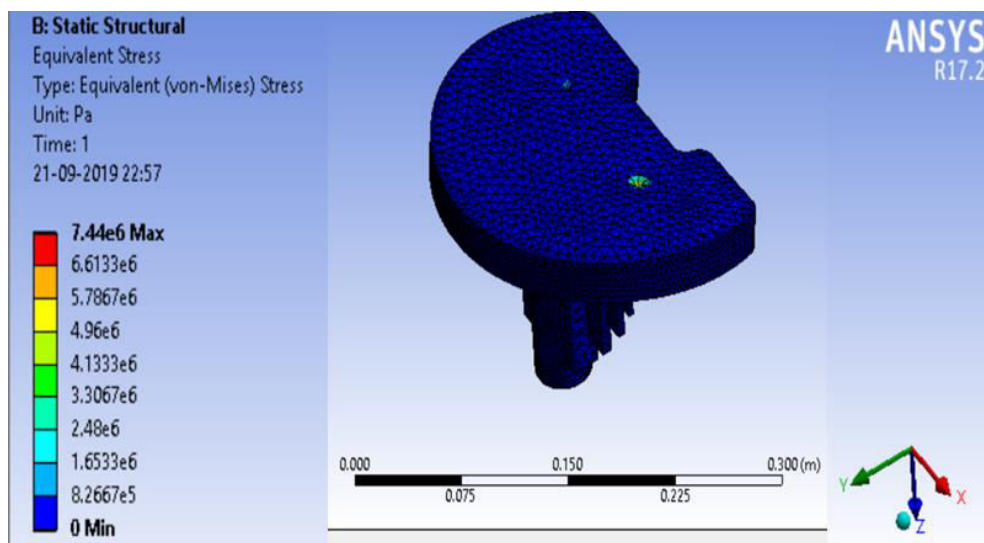


Fig. B1: 3D model of tibial tray used in its finite element analysis.

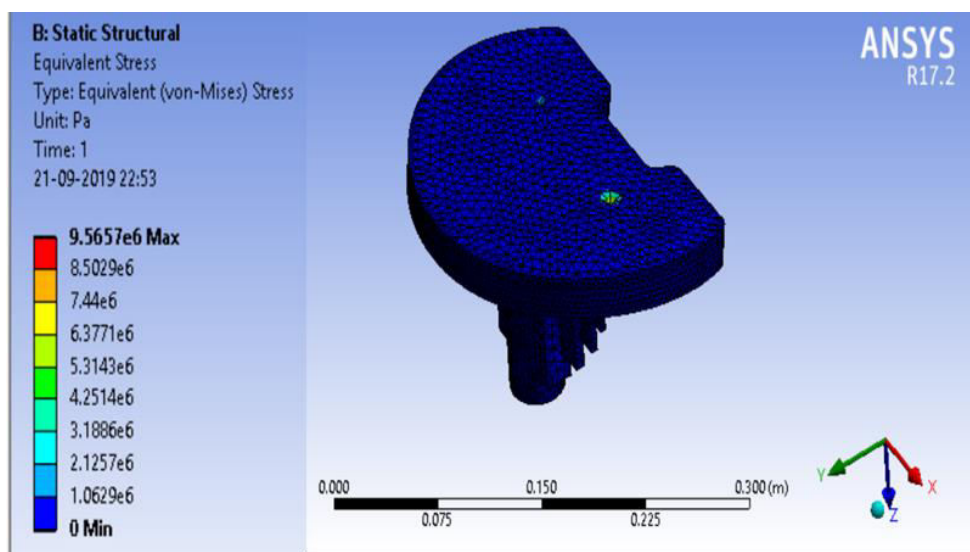
Figure B2 shows Von-Mises equivalent stress and Fig. B3 depicts FEA predicted total deformation for the tibial tray made of Co-Cr-Mo-2Ti alloy (Figs. B2a, B3a); Co-Cr-Mo-4Ti alloy (Figs. B2b, B3b); and Co-Cr-Mo-6Ti alloy (Figs. B2c, B3c). Table B2 summarizes maximum values of Von-Mises equivalent stress and total deformation obtained from Figs. B2 and B3.



(a)

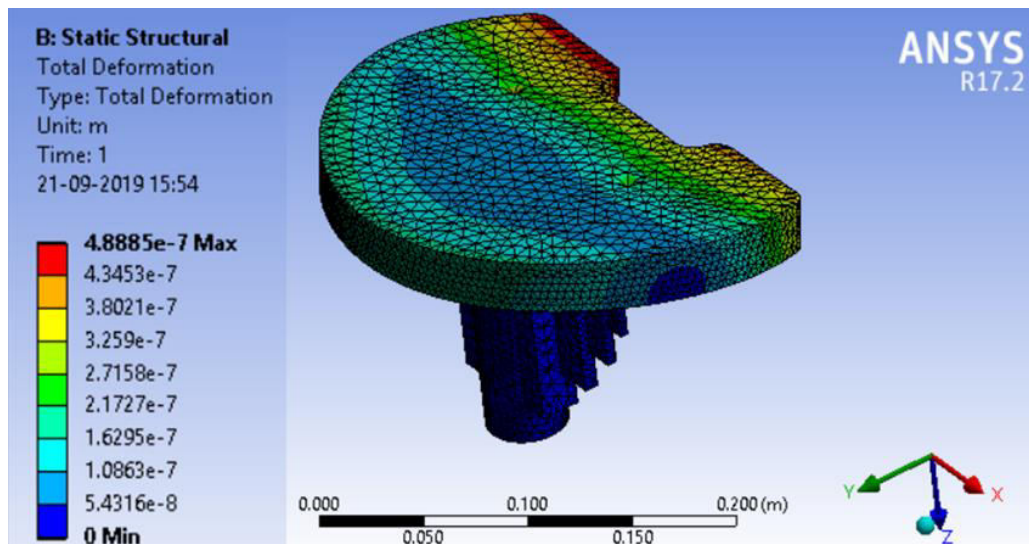


(b)

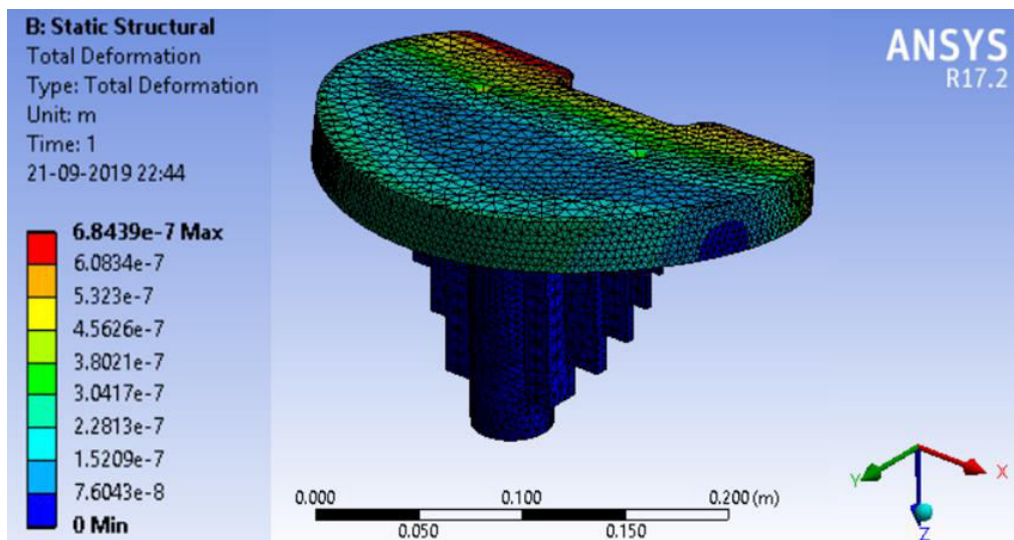


(c)

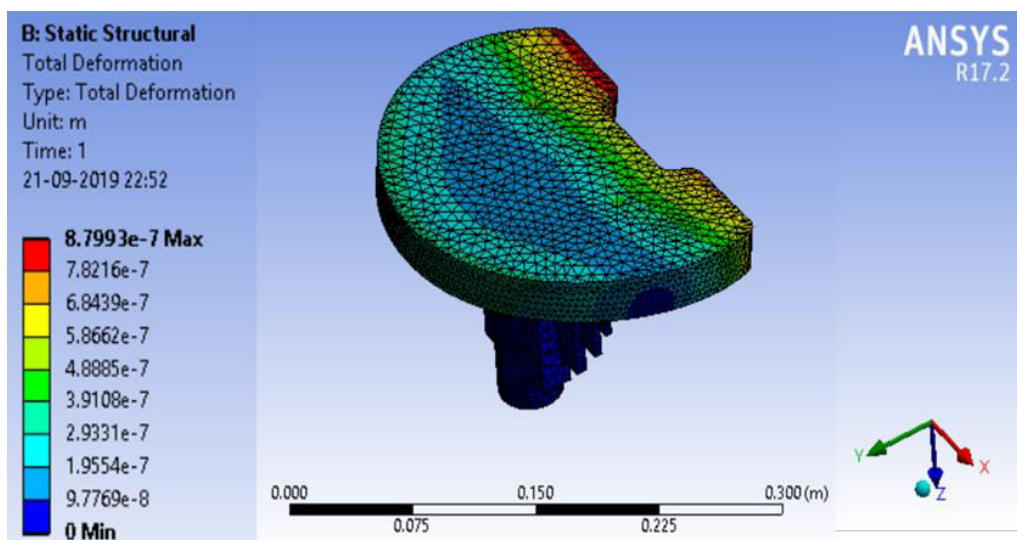
Fig. B2: Von-Mises equivalent stress predicted by FEA for tibial tray made of (a) Co-Cr-Mo-2Ti, (b) Co-Cr-Mo-4Ti, and (c) Co-Cr-Mo-6Ti alloy.



(a)



(b)



(c)

Fig. B3: Total deformation predicted by FEA for tibial tray made of (a) Co-Cr-Mo-2Ti, (b) Co-Cr-Mo-4Ti, and (c) Co-Cr-Mo-6Ti alloy.

Table B2: Maximum values of Von-Mises equivalent stress and total deformation predicted by FEA of tibial tray made of Co-Cr-Mo-2/4/6Ti alloys.

Alloy	Maximum Von-Mises equivalent stress (GPa)	Maximum value of total deformation (μm)
Co-Cr-Mo-2Ti	5.31	48.88
Co-Cr-Mo-4Ti	7.44	68.43
Co-Cr-Mo-6Ti	9.56	87.99

It can be observed from Figs. B2 and B3, and Table B2 that maximum value of Von-Mises equivalent stress and total deformation are increasing with increase in wt.% of Ti in Co-Cr-Mo alloy. Maximum values of total deformation in tibial tray of Co-Cr-Mo-2/4/6Ti alloys are much less 150 μm as mentioned by **Pillar et al. (1986)** minimizing their micromotion. These findings are consistent with **Miyoshi et al. (2002)** who have compared maximum value of Von-Mises stress for tibial tray with and without cut slots and found that tibial tray component with a cut-out slot had a more considerable Von-Mises stress. They also found maximum total deformation of tibial tray was 73 μm . Constraints of present FEA of tibial tray are assumption about tibial tray materials being homogenous and isotropic. It also did not consider porosity therefore further dynamic study is required for knee implant including tibial bone and femoral bone for better understanding of knee implant functioning. Concept of Von-Mises equivalent stress and total deformation can be useful but absolute total deformation values should be used with caution.

FEA of tibial tray revealed that equivalent Von-Mises's stress and total deformation increase with increase in wt.% of Ti in Co-Cr-Mo alloy. Maximum total deformation is 88 μm in Co-Cr-Mo-6Ti alloy which is much less 150 μm reported in the literature. This will minimize micromotion of tibial tray.

Appendix C: SEM micrographs of Co-Cr-Mo-xTi alloys used for EDS analysis.

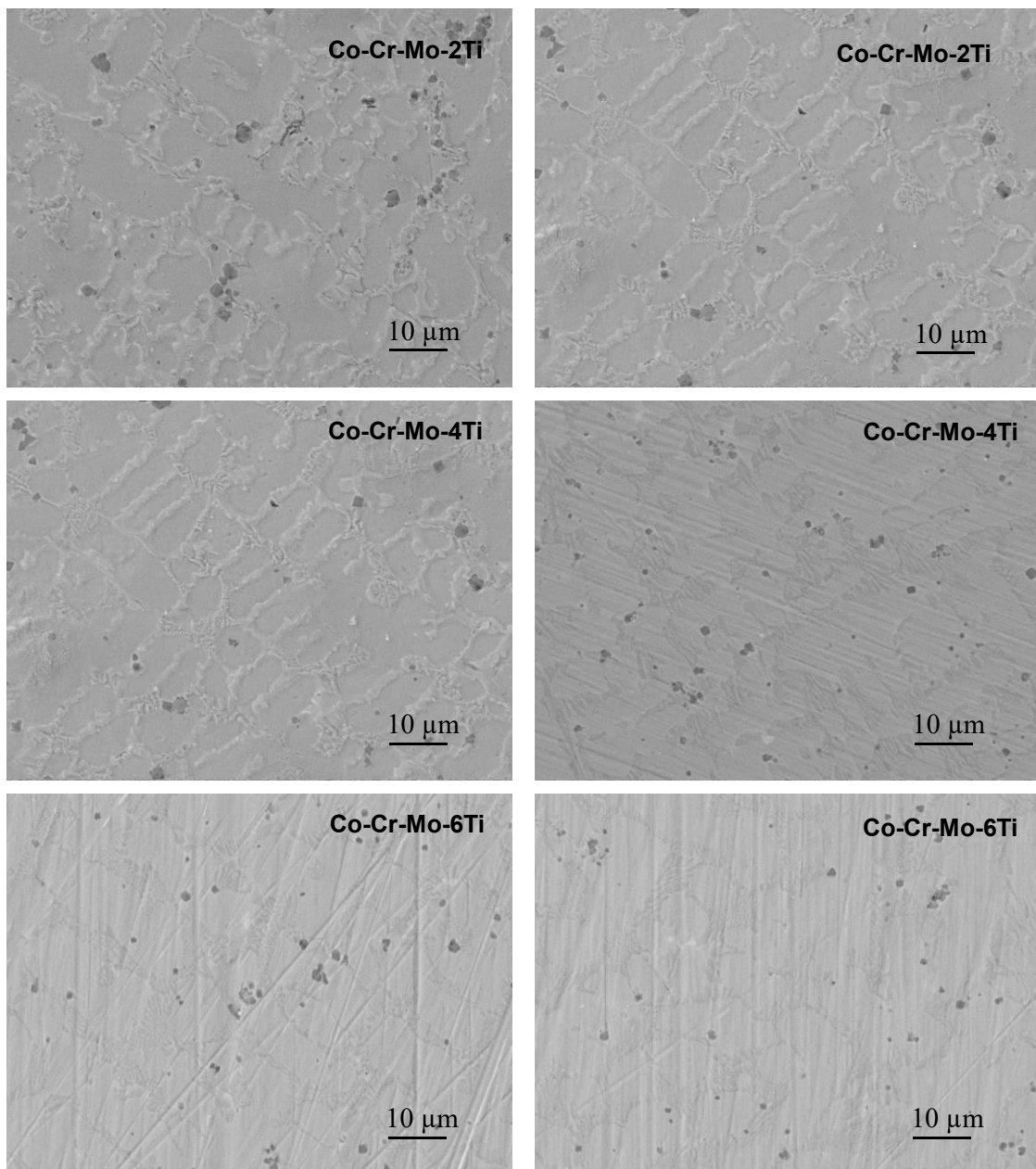


Fig. C1: SEM micrographs of Co-Cr-Mo-xTi alloys used for EDS analysis.